THERMODYNAMICS OF ELECTROSORPTION-BASED SEPARATION PROCESSES AND CYCLES

A Dissertation
Presented to
The Academic Faculty

By

Daniel A. Moreno

In Partial Fulfillment
of the Requirements for the Degree
Doctor of Philosophy in the
Woodruff School of Mechanical Engineering

Georgia Institute of Technology

August 2019

THERMODYNAMICS OF ELECTROSORPTION-BASED SEPARATION PROCESSES AND CYCLES

Approved by:

Dr. Marta Hatzell, Advisor
School of Mechanical Engineering
Georgia Institute of Technology

Dr. Sheldon Jeter
School of Mechanical Engineering
Georgia Institute of Technology

Dr. Tequila Harris
School of Mechanical Engineering
Georgia Institute of Technology

Dr. Hailong Chen
School of Mechanical Engineering
Georgia Institute of Technology

Dr. Sotira Yiacoumi
School of Civil & Environmental Engineering
Georgia Institute of Technology

Date Approved: April 19, 2019

The price of success is hard work, dedication to the job at hand, and the determination that whether we win or lose, we have applied the best of ourselves to the task at hand.

Vince Lombardi

I dedicate this thesis to all of the members of my family, whose love and care have enabled me to excel in my pursuits and get to where I am in my career and in my life. Thanks so much for all the help and support.

ACKNOWLEDGEMENTS

Firstly, I would like to deeply thank my advisor, Dr. Marta Hatzell, for all of the help and guidance that she provided me along the way. I am very grateful for the motivation that she provided which enabled me to work to my fullest potential beyond what I could have imagined, and for her timely and detailed feedback on all of my work, and for all of the opportunities both inside and outside of Georgia Tech that she provided and assisted me with. It has definitely been a very challenging and rewarding experience.

Secondly, I would like to thank my committee members, Dr. Sheldon Jeter, Dr. Tequila Harris, Dr. Hailong Chen, and Dr. Sotira Yiacoumi, for their review and evaluation of my Ph.D. work. Each has provided me with unique ideas and suggestions based on their individual expertise which has contributed greatly to the broader aims and finer details of my research.

Thirdly, I would like to greatly thank two other instructors, the lovely Dr. Roxanne Moore and the good Dr. Cassandra Telenko, for providing encouragement and a vision for my future career path through all of the great conversations we had, in particular relating to teaching and education. Both have been wonderful inspirational role models and have made my pursuit of the Ph.D. a more positive and happier experience. I'm so glad to have met and talked to them while on this journey.

Additionally, I owe a big thanks to all of my colleagues in the WATER Lab who have provided me with incredible support and encouragement, professionally as well as personally. In particular I would like to thank my fellow graduate students Carol (Yu-Hsuan) Liu, Yousuf Bootwala, Carlos Fernandez, Jeonghoon Lim, and Rodrigo Caceres.

Finally, a special thanks to my family. Mom, Dad, and Aimee have provided incredible moral support along this entire journey through my Ph.D.. I am very thankful for all of the encouraging conversations we have had and ensuring that I am doing well physically as well as mentally.

TABLE OF CONTENTS

LIST OF TABLES

LIST OF FIGURES

SUMMARY

Understanding the thermodynamics associated with ion mixing and separation processes is important in order to meet the rising demand for clean energy and water production. State-of-the-art separations technologies such as reverse osmosis and thermal-based distillation methods desalinate through processes that occur at elevated pressure and/or temperature. This can result in an increase in the energy requirements or system footprint. Several electrochemical-based technologies such as capacitive deionization (CDI) and capacitive mixing (CapMix) are also capable of achieving desalination and energy production through ion separation and mixing processes, yet experimental investigations suggest energy conversion is inefficient. Here, a theoretical investigation of reversible and irreversible CapMix and CDI cycles aims to explore the irreversibilities that prevent CDI from operating efficiently. Analogies drawn between heat engines and blue engines aim to provide insight into designing optimal separation and mixing cycles and processes. In addition to examining efficiencies for CapMix and CDI, an analysis of the theoretical and experimental heat of electroadsorption provides knowledge regarding how field-assisted sorption technologies compare to passive-sorption technologies.

Here, we will explore the origin of low thermodynamic efficiency in CDI systems, through evaluating theoretically the electrochemical separations process and complete electrochemical swing cycle. We will also explore engineering approaches which may enable CDI to move beyond batch-mode operations through the use of flow electrodes. Chapter 1 will provide an introduction and background, and Chapter 2 will provide a literature review. In Chapter 3, the energetic and exergetic efficiency will be compared for a Carnot-analog and conventional CDI cycle. In Chapter 4, we will explore the thermodynamic efficiency of capacitive mixing (CapMix) cycles for energy generation. In Chapter 5, we explore the effect of temperature on CDI and CapMix cycle efficiency. In Chapter 6, we evaluate the performance stability of CDI operated in a continuous mode using flow electrodes. Chap-

ter 7 will detail a theoretical and experimental analysis which aims to define the heat of electroadsorption.

CHAPTER 1
INTRODUCTION AND BACKGROUND

1.1 Motivation

As the world‘s population grows, demand for clean, safe water is increasing. By 2025, up to 1.8 billion people ($> 20\%$ of global population) could be living in regions with water scarcity (Fig. 1.1) [1, 2]. In the absence of a reliable fresh water source, emphasis will need to focus on developing treatment strategies for nontraditional sources of water (wastewater, brackish water, or seawater) in order to augment our freshwater supply. Seawater desalination is effective, but is energy intensive, requiring 3–4 kWh of energy per m^3 of desalinated water [3]. Furthermore, pumping energy requirements restrict desalination to regions with access to seawater. Since the United States is not primarily a coastal country, it is unlikely that seawater desalination will be able to meet all continental water needs (municipal, industrial, agricultural).

Wastewater is typically dilute in nature, however, public perception complicates the use of wastewater in a variety of applications [4]. In addition, with the growth in emerging contaminants, new treatment strategies are needed to guarantee the safety of reused wastewater [5]. Brackish water is a particularly ideal alternative feed source when compared with waste and seawater, as it is characterized by low inherent salt concentrations (1000 to 10000 ppm) [6]. Thus, treatment of brackish water is less energy intensive when compared to seawater desalination (0.5–1 kWh per m^3 of desalted water). Brackish water is also not as geographically limited, as it is found in a variety of locations across the United States.

Brackish water can be used either directly (without treatment) or can be treated. For some applications (cooling water, hydraulic fracturing, aquaculture), direct use of brackish

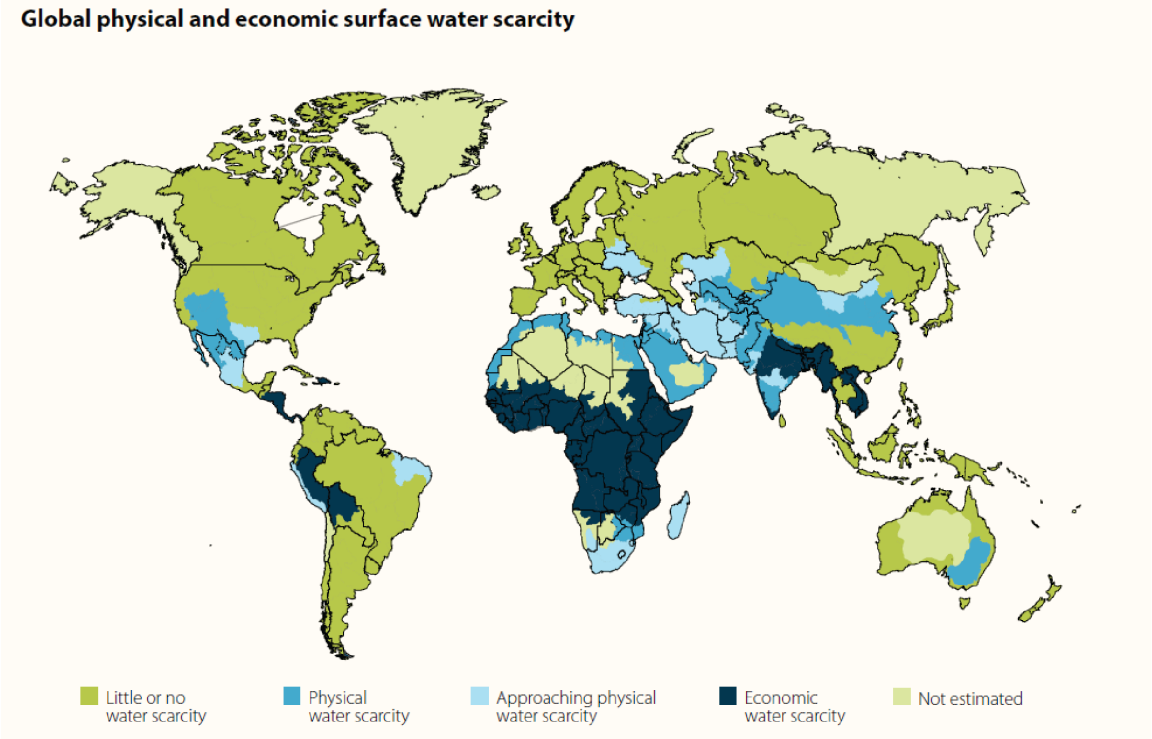

Figure 1.1: Global physical and economic surface water scarcity [2]

water rather than freshwater is one immediate means to reduce global freshwater usage. However, if brackish water is going to be used to meet water demands associated with the agricultural, industrial, or municipal sectors, treatment will be required.

In the agricultural sector, there is a large opportunity to use alternative water sources to meet irrigation needs. Irrigation practices currently account for 37% of all fresh water withdrawals and 80% of fresh water consumption in the United States[7]. The salinity requirements for irrigation vary depending on crop, but typically must be less than 1400 ppm. Higher salt concentrations can be toxic to plants, or may result in rapid moisture loss from soils. The requirements for irrigation water are strict, but the requirements are still significantly less restrictive than drinking water requirements (30-400 ppm)[8]. Therefore, treatment strategies capable of reducing brackish water salinity to below 1400 ppm could aid in eliminating freshwater usage at agricultural sites. Treated brackish water could also be used at power generation facilities which operate using a Rankine Cycle, and in manufacturing processes which have moderate water quality requirements. Thus, a primary

motivation of this dissertation is in understanding and developing new treatment strategies and technologies which may enable the use of brackish water rather than freshwater.

1.2 Water-Energy Nexus

Growth in global domestic product, population, and the mounting issues associated climate change, have all contributed to concern regarding the water-energy nexus [9]. Energy demand is projected to increase by 30% by 2035 [2], and water withdrawals and consumption could increase by 20% and 85%. The global water demand for non-energy water uses is also increasing, and is projected to increase by over 40% by 2030 [2]. Growth in water treatment in both developing and developed countries may also increase the energy consumed by water treatment processes by $15-25\%$ [10].

The major challenge of the water-energy nexus is ensuring a sufficient supply of water and energy without sacrificing either commodity. However, the current interdependence between water and energy systems prevents this from being possible. This promotes the need to develop new ways to decouple our energy and water systems. Ultimately, this will require that water treatment and desalination processes operate using energy which is produced on or near the water treatment site, and not from the electrical grid. If systems can be decoupled, both systems will be able to operate in a more resilient manner.

When implementing these changes, care must be taken to also ensure that environmental preservation is considered in order to meet the goals of COP21, the global agreement on reduction of climate change, reached in 2015 [11]. For instance, most current desalination and water treatment processes are powered by fossil fuels. Therefore in addition to adding strain to the electrical grid, increased water treatment also accounts for a growing amount of global CO_2 emissions [12]. Therefore, when developing decoupled energy and water systems, integrating renewable energy sources (solar, wind, hydro) is essential.

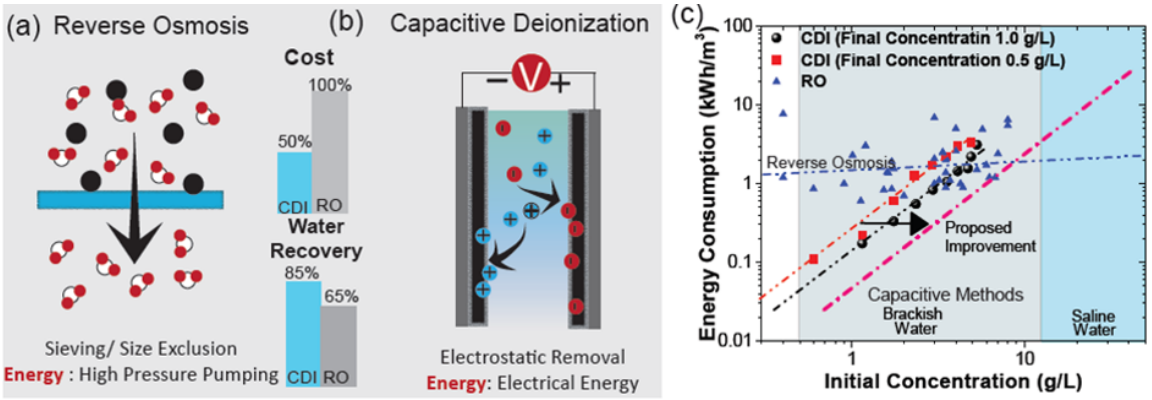

Figure 1.2: (a) RO is the current state of the art for desalination and relies on pressure (b) CDI, an emerging technology, relies on voltage to separate salt from water (c) Energy consumption of RO vs. CDI.

1.3 Direct Renewable Integration with Deionization (Electrochemical Separations)

When moving toward effective strategies for integrating renewable energy with desalination, there are a range of scenarios. Each differs primarily in the cost of electricity and water which are commonly referred to as the levelized cost of electricity (LCOE) and levelized cost of water (LCOW).

For brackish water treatment, ultrafiltration (UF) is the preferred desalination technology (not RO). Today, nearly all brackish water RO and UF processes are powered by fossil fuels. However, one could imagine that they could be coupled with a variety of renewable energy technologies (e.g. Photovoltaics - PV, concentrated solar power - CSP, or wind). Since the primary means of separation is pressure, the electrical energy generated from a renewable would need to stored and then delivered to a pump. Therefore, a chief challenge with integrating renewable with UF is that of energy storage. In addition, multiple energy conversion processes may promote significant energy losses.

An alternative to UF for brackish water treatment is capacitive deionization (CDI). CDI has lower desalination efficiencies, but has greater water recovery and lower costs (Figure 1.2a-c) [13]. A primary advantage of CDI is that it can be directly connected to renewable energy, as it is an energy storage device (i.e. supercapacitor). This limits the number

of required energy conversion processes and the number of required system components. Therefore, electrochemical separations devices like capacitive deionization provide a direct means to obtain clean desalted water using renewable electrons. The proposed research in this thesis will focus on investigating and improving thermodynamic limitations of capacitive deionization, so that it can be utilized as an integrated deionization device powered by renewable intermittent energy.

CHAPTER 2
LITERATURE REVIEW

2.1 State-of-the-Art Desalination Technologies

Desalination technologies are commonly split into thermal and membrane/filtration-based technologies (Figure 2.1). Pressure-based desalination technologies include reverse osmosis (RO), nanofiltration (NF), and ultrafiltration (UF). There are a number of thermal-based desalination technologies, but the most abundantly utilized are multi-stage flash distillation (MSF) and multiple effect distillation (MED). An emerging class of desalination technologies falls in the category of electrochemical based. These include electrodialysis (ED), membrane capacitive deionzation (MCDI), capacitive deionization (CDI) and Faradaic capactive deionization (FaCDI). Today, however, over 90% of all desalination plants operate using thermal or pressure-based technologies.

2.1.1 Multiple Effect Desalination (MED)

In multiple effect desalination (MED), saline water is evaporated in stages at relatively low temperature (top brine temperature 70^{o}C) and low pressure (0.3 bar)[14]. The low operational temperature allow for reduced operating costs, low thermal energy consumption, and reduced scaling risks. The evaporated steam goes into the next stage to heat and evaporate more water, essentially reusing the energy from the previous stage. During this process, the temperature and pressure of each successive stage will gradually decrease. Some of the advantages of MED include low cost and low energy consumption. However, the loss in pressure across each stage requires additional pumping in order to maintain equilibrium with the atmosphere.

MED has not been as industrially competitive with multi-stage flash distillation because

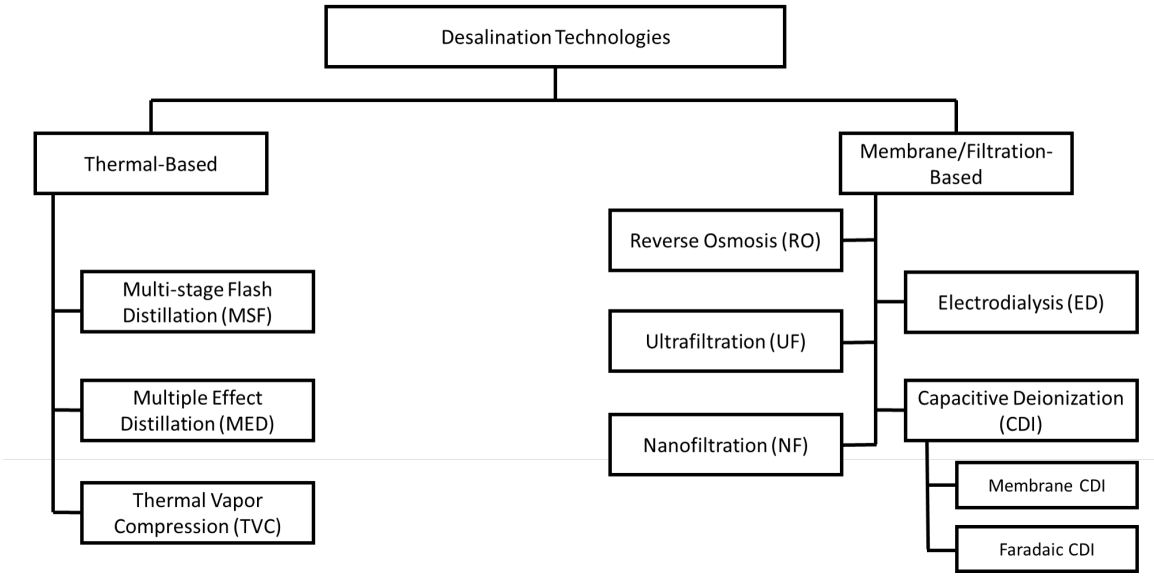

Figure 2.1: Example of some different desalination technologies.

of large capital and operational expenditures [15]. However, recent technological advances have enabled lower specific energy requirements. According to some researchers, this may enable MED to more readily compete with other thermally-driven cycles [16].

2.1.2 Multiple-Stage Flash Distillation (MSF)

The multiple-stage flash distillation (MSF) process involves the flashing of water into steam in multiple heat exchanger stages [17]. Similar to MED, the pressures at each stage are set to correspond to the boiling points of the water-salt solutions at a given temperature. This process operates in three stages: Heat rejection, brine heating, and recovery, in which the vapor condenses back to water with salt concentration removed. When the saline water flows into the stage of reduced pressure, it flashes immediately into a vapor, until the brine solution has reached its saturation temperature. The steam that condenses back into water becomes the desalinated (distilled) water which is then further purified to the point where it can reach a more potable state [18].

Similar to MED, MSF has certain limitations. While higher temperatures can enable higher efficiencies, issues arise with scaling. Fouling of the brine heater has been cited as

a concern at high temperatures [19]. Additionally, the CO_2 emissions of MSF range higher than the emissions for MED. These emissions can be reduced by about 30% if combined with cogeneration in steam plants [20] (Table 2.1).

2.1.3 Reverse Osmosis (RO)

One of the most widely used desalination technologies in today's industry, for both sea-waters and lower concentration brackish waters, is reverse osmosis (RO) [21]. The RO process applies a pressure gradient in order to remove salt ions from solution [22]. With RO, applying an increased pressure on the concentrated side of semi-permeable membranes drives water across the membrane. Other molecules, including salt ions (Na^+ and Cl^-), do not pass through the membrane, resulting in an increased volume of diluted water. The energy demand for RO (3-4 kWh/m^3 of water) is minimal compared to prior technologies such as MSF (55-80 kWh/m^3) [23]. To provide the amount of energy required for MSF, 100 power plants per day would be needed to produce drinking water for the entire global population (approx. 8 billion).

Growth in RO has significantly increased due to increased membrane development, pressure recovery, and nanofiltration-based treatments [24]. Since RO does not require input of thermal energy in addition to electrical energy, this reduces the associated energy consumption and costs. CO_2 emissions for RO are also minimal (Table 2.1), which has made it ideal for meeting COP21 regulations.

Limitations to RO that hinder greater use for it include membrane cost and vulnerability, which will take more research and development before, it can be used to facilitate commercial production. Additionally, if the degree of contamination of water to be purified is higher, extensive pretreatment processes will be required which will ultimately drive costs of RO much higher than the thermal-based processes [25] . This is particularly true at higher concentrations due to a higher number of total dissolved solids (TDS).

Table 2.1: Summary of operational and performance parameters of different desalination processes. Adapted from [26].

	MSF	MED	RO
Thermal Energy (kWh/m^3)	40-65	53-70	N/A
Electrical Energy (kWh/m^3)	2.0 - 2.5	2.5 - 5.0	4 - 6
Cost of Water ($\$/m^3$)	0.52 - 1.01	0.56 - 1.75	0.26 - 0.54
Environmental Impact	Discharge at 10-15°C hotter than ambient; TDS increase of 15-20%	Discharge at 10-15°C hotter than ambient; TDS increase of 15-20%	Discharge at ambient; TDS increase of 50-80%
CO_2 emissions (kg/m^3)	7.0 17.6	15.6 25.0	1.7 2.8

2.2 Electrochemical Separations-Based Technologies

2.2.1 Electrodialysis (ED)

Desalination via electrodialysis (ED) involves the input in the form of electric current, separated by fluid channels, with an anion and cation exchange membrane placed in alternating order (Figure 2.1) [27]. During the ED desalination processes, ions migrate toward the oppositely charged electrode through membranes of the same charge. As a result, one stream has its overall concentration reduced, while the other has its concentration increased. ED has existed on the market for decades, currently accounting for over 6% of all desalination technologies used today [28]. This percentage has been steadily growing since the start of the century [29]. Its main usefulness is for brackish water, particularly, concentrations below a TDS of 3000 ppm (approx. 50 mM) [30]. Some of its other applications are in the food industry, such as for the treatment of dairy goods, various juices, and sugar [31].

Despite some advantages over RO, MED, and MSF, ED has some limitations to its usage. For instance, since it involves the removal of the ions in the solution rather than the solvent, ionic species with less charge, higher weight, or lower ion mobility will be more difficult to remove. Also, if the salt concentration is particularly low, ED will be

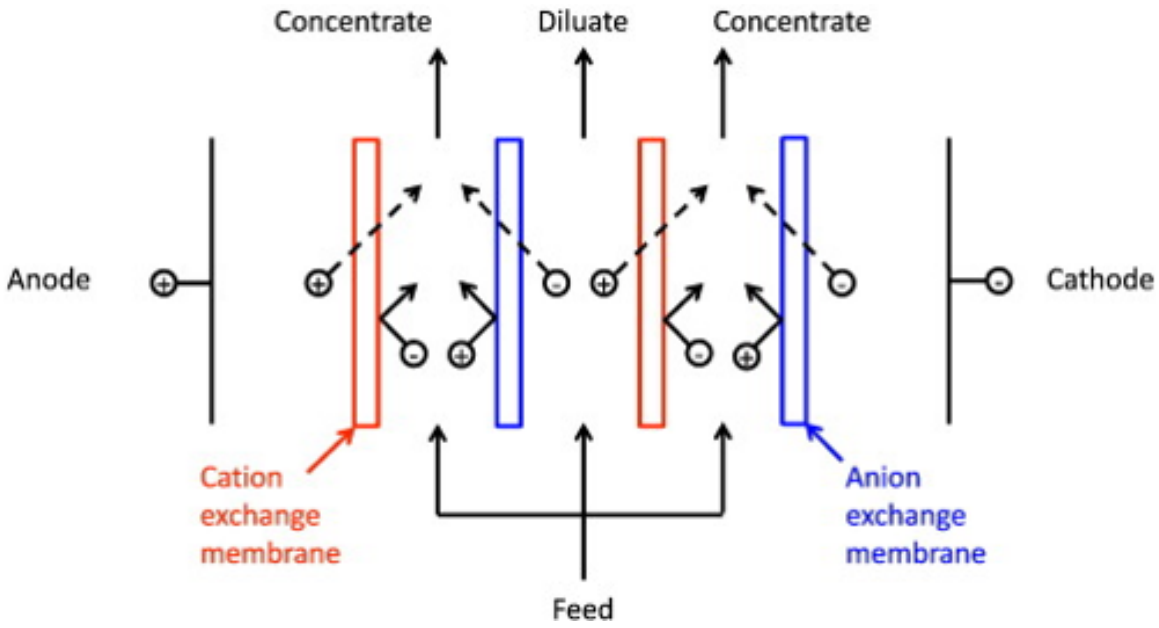

Figure 2.2: Process of electrodialysis (ED) [32].

less economical because cell resistance grows significantly at lower concentrations when the electrical conductivity approaches zero. Some ED systems have thus focused on the integration of ED with RO, in which both systems operate in their most efficient operating ranges, minimizing capital costs [33].

2.2.2 Capacitive Deionization (CDI)

Capacitive deionization (CDI) processes involve the use of an electrochemical capacitor which adsorbs salt ions as the cell is charged and stores them within an electrode (Figure 2.3). Thus, during charging, as salt ions are removed, the inlet concentration C_0 is reduced to a diluate concentration C_L at the outlet stream. Then, during discharging, salt ions stored in the electrode are released back into the effluent stream, resulting in an increased outlet brine concentration C_H. This discharging process can recover some of the energy that is expended during charging, which is a key point of interest in reducing energy consumption in CDI research.

CDI first originated as an electrochemical demineralization concept proposed by Blair and Murphy [34], who claimed that electrochemical demineralization could be achieved

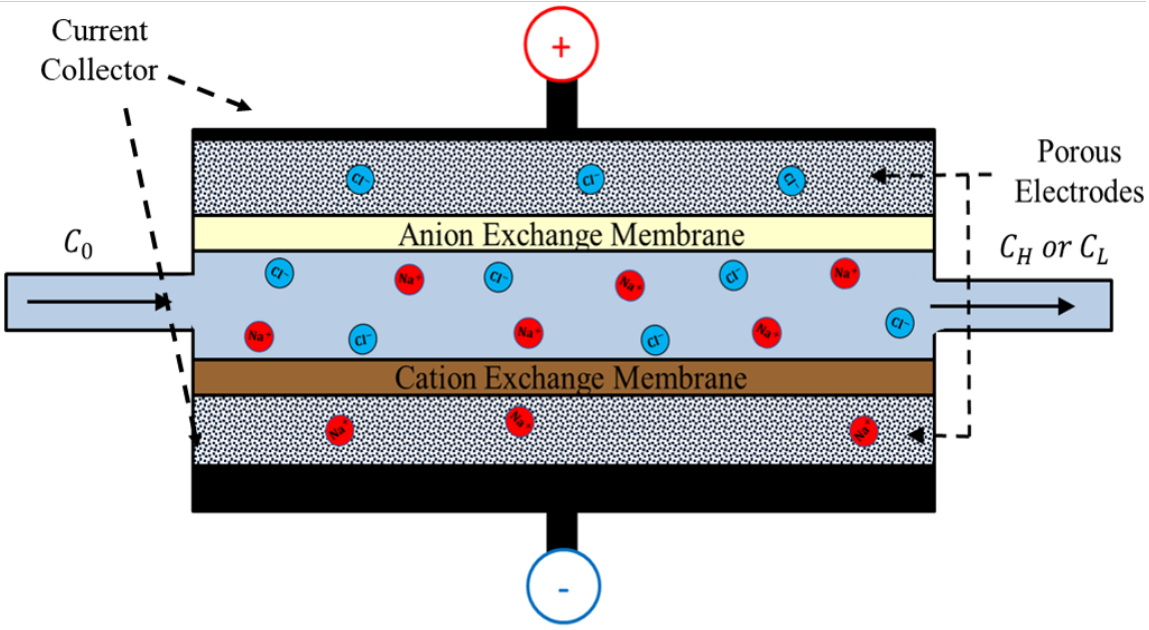

Figure 2.3: Process of capacitive deionization (CDI).

through Faradaic-like reactions between ions and surface chemical groups. Murphy also developed mathematical models in order to enhance knowledge of salt concentration distribution during this electrochemical demineralization process [35] . In the 1970s new discoveries in CDI suggested ion removal by a capacitor-like mechanism, and also that performance was in fact limited by the presence of Faradaic reactions [36] . This theory led to the development of potential-modulated ion sorption, and later, the formation of an electric double layer (EDL) at the electrode-electrolyte interface that governed the removal of salt ions [37]. This led to increasing interest in understanding the surface interaction of the EDL with the porous carbon electrode [38].

Despite these new advances, CDI studies were nearly nonexistent for almost two decades, primarily due to limitations in carbon electrodes to improve salt removal performance. One innovation that arose during this time was the development of a more precise separation method between desalinated water and concentrate. This four-step cycle, termed electrochemical parametric pumping, consisted of two separate charge/discharge stages, as well as axial pumping of the solution in and out of a storage tank [39].

In the 1990s, Farmer developed a new CDI device using aerogels, which led to improvements in desalination capabilities due to their improved surface area and conductivity [40]. Additionally, Farmer reported that a desalination voltage of 1.2 V was optimal, setting a trend that would continue throughout many CDI experiments. The performance of CDI remained limited; results had demonstrated a maximum salt adsorption limit of 95% salt removal for a feed of only 100 μS/cm (approximately 1 mM) [41].

Increased interest in different types of carbon materials/compositions to expand ion storage capabilities (Figure 2.4) arose as a result of this initial study. Ordered mesoporous carbons [42] with higher specific surface area were found to attain higher adsorption capacities. Carbide-derived carbons have also been used to attain much narrower micropores with smaller size distributions, which led to an even higher desorption capacity, removing up to 15 mg/g NaCl [43]. Carbon nanotubes, while of greater interest in a variety of other fields due to their excellent mechanical and thermal properties, have also emerged as being of interest in the CDI field due to their versatility [44]. This is due to the structure of the carbon nanotubes, which could promote ion transport. Despite the initially smaller specific surface area (evaluated through TEM and X-ray diffraction) [45], improved salt adsorption capacity (SAC) has been demonstrated [46]. Additionally, single-walled structures have shown better performance than multi-walled nanotubes [47].

In summary, previous studies have highlighted that specific surface area is not the only significant factor in improving salt removal performance. Additionally, all of the electrodes mentioned thus far are limited by total surface area, making their reliability for desalinating higher concentration streams much more challenging.

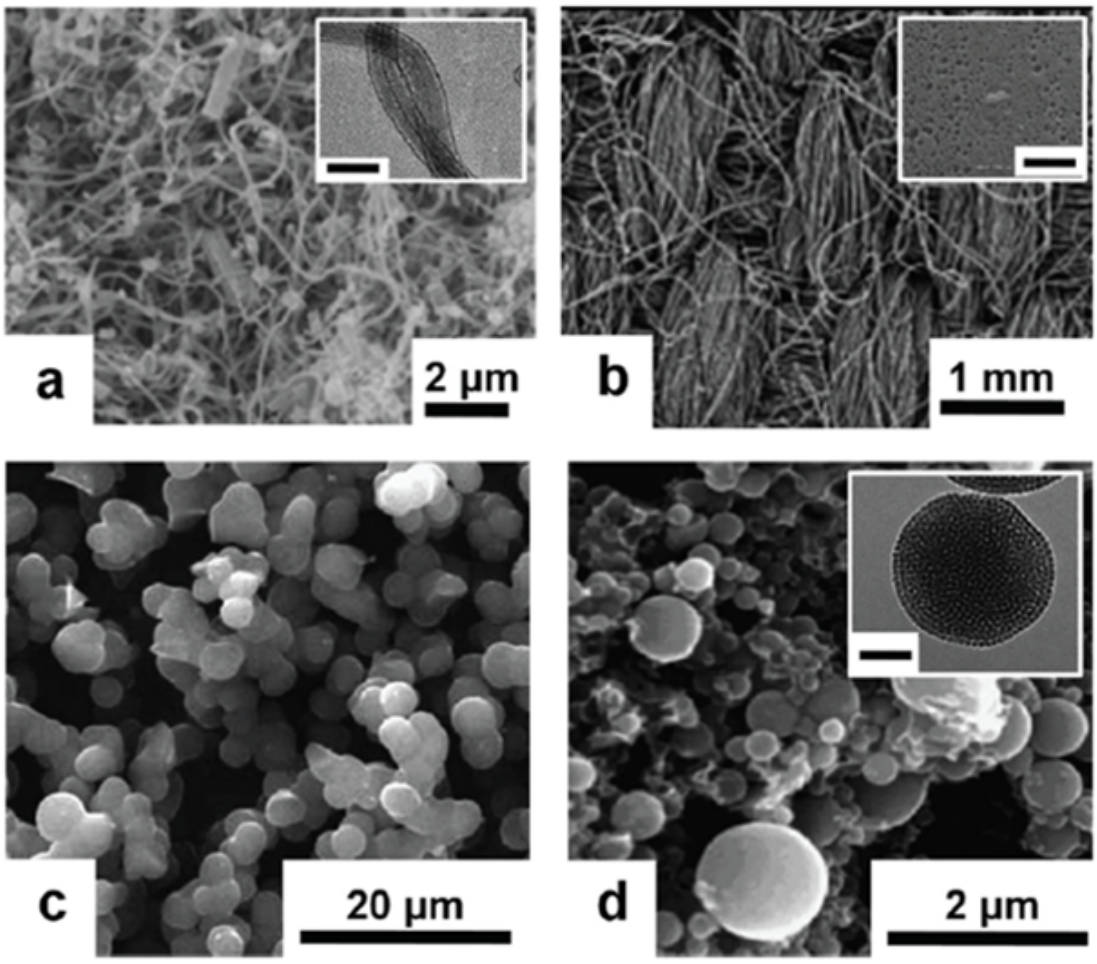

Figure 2.4: Various carbon materials used in prior CDI studies: a) carbon nanotube and nanofiber composite, b) activated carbon cloth, c) carbon aerogel, d) ordered mesoporous carbon [28].

2.3 Thermodynamics Considerations For Desalination Technologies

As desalination is energy intensive, many studies continue to focus on the means through which this energy consumption can be reduced. Regardless of the method through which desalination is done, there will always be a minimum theoretical energy of work input required to drive the desalination process. Normally, the energy consumed in these desalination processes is several times greater than the minimum energy of separation, with the values approaching that minimum energy at higher (seawater) concentrations [48]. As with

all real-world systems, irreversibilities will exist which cause the additional work required to increase, compensating for such losses.

Some desalination processes are primarily heat driven, whereas others are entirely work driven. It is important to distinguish between work and heat in the evaluation of thermodynamic desalination processes. Work can be fully converted into heat, but heat cannot convert fully into work, leading to multiple sources of irreversibilities for all of the desalination technologies. This provides a motivation for pursuing further studies into the role of the second law of thermodynamics on desalination processes. Many studies also focus on exergy-based analyses, taking into account both thermodynamic and economic perspectives [49, 50].

All desalination processes can essentially be modeled as simple thermodynamic systems (Figure 2.5), with cycle processes, input/output fluxes, and heat/work transfers. While a similar analysis can be developed for the energy flows into and out of the system, the exact mechanisms of entropy generation (and thus exergetic losses) vary per desalination technology.

In any open system, the first law of thermodynamics, given in transient form, is:

$$\frac{dU}{dt} = \dot{Q} + \dot{W} + \sum_i \dot{H}_i - \sum_o \dot{H}_o \tag{2.1}$$

where $\dot{Q}$ represents heat input, $\dot{W}$ represents work input, and $\dot{H}_{\mathrm{i}}$ and $\dot{H}_{\mathrm{o}}$ are the input and output extensive rates of enthalpy transfers into and out of the system. In this case and in all other cases examined, we will neglect the contribution of kinetic energy and potential energy to the system, unless otherwise stated. The second law of thermodynamics follows as:

$$\frac{dS}{dt} = \frac{\dot{Q}}{T_0} + \sum_i \dot{S}_i - \sum_o \dot{S}_o + \dot{S}_{gen} \tag{2.2}$$

Combining the first and second laws by using boundary temperature T_0 to multiply the

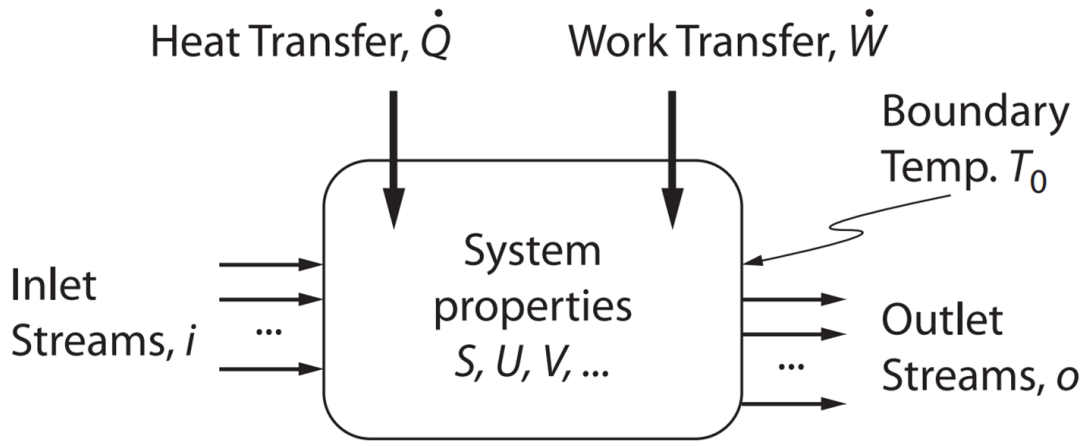

Figure 2.5: Simple open thermodynamic system [48].

second law of thermodynamics, the heat transfer terms cancel. If we make an additional assumption for a steady-state process, we are then left with:

$$0 = \dot{W} + \sum_i \dot{G}_i - \sum_o \dot{G}_o - T_0 \dot{S}_{gen} \tag{2.3}$$

where the Gibbs free energies are defined as:

$$\dot{G} = \dot{H} - T_0 \dot{S} \tag{2.4}$$

The system is reversible when $\dot{S}_{\text{gen}}$ is zero. In this case we find the reversible work associated with a stream changing from inlet to outlet. With Gibbs energy defined, we can also consider the chemical potential for the system. The Gibbs energy, as an extensive property, can be written as a weighted sum of partial molar properties of a species:

$$\dot{G} = \sum_i \frac{\partial G}{\partial N_i} N_i \tag{2.5}$$

This partial molar term we define as the chemical potential μ. We can write the chemical

potential as:

$$\mu_i = \mu_i^o + RTln(a_i) \tag{2.6}$$

where a_i represents activity based on the species i in the solution. Activity is sometimes thought of as a thermodynamic concentration; a change in energy based on changes as a component is added to a mixture, relative to some external reference. As the activity is based on molar concentration, it can be written in terms of either mole fraction x, molality b, or concentration C:

$$a = \gamma x = \gamma \frac{b}{b_{ref}} = \gamma \frac{C}{C_{ref}} \tag{2.7}$$

where γ represents the mean activity coefficient, x is the mole fraction, b represents the solution molality, and C represents concentration. The subscript ref denotes the reference state that molality or concentration is measured relative to.

Generally, the activity coefficients depend on a number of factors, such as the molecular characteristics of ions immersed in solution, its concentration in the solution, and the temperature of the solution. The Debye-Huckel theory [51], based on electrostatics and statistical mechanics, is the most fundamental method of determining activity coefficients, valid for molalities of up to 0.01 mol/kg:

$$ln(\gamma) = -|z_+ z_-| \Big(\frac{e^3 (2 N_A \rho_{water})^{(1/2)}}{8\pi(\epsilon_r \epsilon_0 k_B T)^{(3/2)}} \Big) \tag{2.8}$$

where z_+ and z_- represent the charge numbers for the cation and anion, e is the elementary charge, N_A is Avogardo's number, ϵ is permittivity of free space, ϵ_r is relative permittivity of the solvent, k_B is Boltzmann's constant, and ρ_{water} is the density of water. The ionic

strength I is determined by the solution molality b as well as ionic charge (valence) z:

$$I = 0.5 \sum_i (b_i {z_i}^2) \tag{2.9}$$

To expand this model, the Davies model [52] includes additional ionic strength-dependent terms not accounted for from Debye-Huckel theory. While the maximum molality is increased to 0.1 mol/kg, the model makes immediate assumptions about operating temperature of 25°C:

$$\log \gamma = 0.5|z_+ z_-|\Big(\frac{\sqrt{I}}{1+\sqrt{I}} - 0.20I\Big) \tag{2.10}$$

Possibly the most accurate model for determining activity coefficients is the Pitzer model, which considers short-range interactions between solute pairs/triplets in the model. Calculation of the model is much more involved, but when high concentrations (sea water) are considered, the Pitzer model is most accurate [48]. The Pitzer model is detailed further in the Appendix, Section A.2.

2.3.1 Thermal-based separations

Thermal distillation processes are driven by a heat source with a temperature T_H. The inlet solution to be distilled, the brine, and pure solvent are all at a temperature T_L. Since heat is used as the input energy instead of work, the input heat Q_H is considered for evaluation of distillation efficiency. The Gibbs energy of mixing for the distillation process is defined as [53]:

$$\dot{W}_{least} = \dot{m}_p g_p + \dot{m}_b g_b - \dot{m_{sw}} g_{sw} \tag{2.11}$$

where g represents intensive Gibbs energies (g = h - Ts), and subscripts denote the product concentration, brine concentration b, and seawater concentration. These similar concepts are used in processes involving separation of chemicals as well.

Second law efficiency is then given as:

$$\eta = \frac{\dot{W}_{least}}{\dot{Q}_{in}}\left(1 - \frac{T_C}{T_H}\right) \tag{2.12}$$

where (1 - T_C/T_H) is the familiar Carnot efficiency. The derivation is extremely similar to the value previously shown and determined from thermodynamics.

In one recent example for a single-effect distiller (Figure 2.6), the boiling point is dependent on both the minimum and maximum molar fractions of the salt concentrations considered during the distillation process. This allows for a relation similar to the Carnot law only involving the boiling points at different salt concentrations:

$$\frac{\dot{W}_{least}}{\dot{Q}_{in}} \leq 1 - \frac{T_{bp}(C_{min})}{T_{bp}(C_{max})} \tag{2.13}$$

As the boiling elevation typically only sees about a 1°C rise for a seawater concentration (0.6 M) [54], this greatly restricts the maximum efficiencies that can be obtained through distillation processes. In most studies, distillation efficiencies are very low, approaching only 5% at a maximum [55, 56, 57, 58]. One of the reasons for this is the large amount of heat energy that is required to perform the boiling of the salt water solution during the distillation process. Additionally, multiple sources of exergetic losses occur within MED including pressure drop during throttling of a liquid, flow through an expansion device when phase change does not occur, and isentropic inefficiency of pumps and compressors [48]. Also, as thermal-based processes, the thermal efficiency is restricted by the Carnot efficiency, which gets smaller if temperature differences are decreased. However, input heat for MED or MSF can still be used for alternative desalination processes, such as using a thermoelectric plant to generate electrical energy which can be used for membrane-based or electrochemical-based technologies [59].

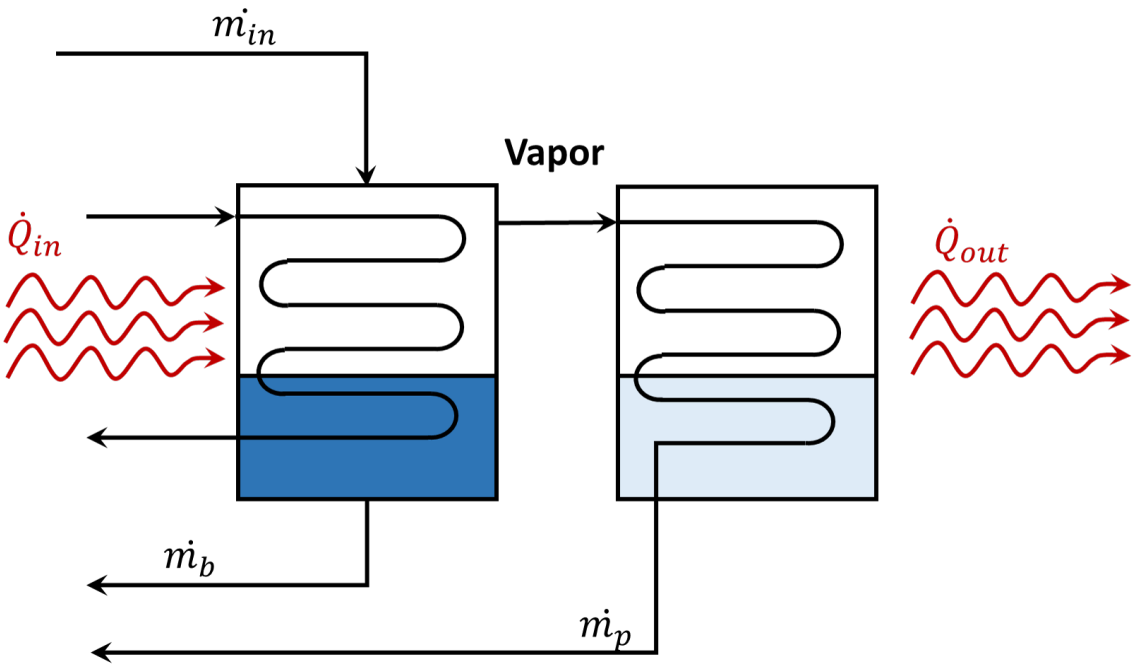

Figure 2.6: Schematic of a single-effect distiller. Adapted from [53].

2.3.2 Pressure-based separations

For a simple reverse osmosis system (RO) similar to the one in Figure 2.7, the relevant first law and second law energy balances are given as:

$$\dot{m}_p h_p + \dot{m}_p h_b - \dot{m}_{in} h_{in} = \dot{Q} \tag{2.14}$$

$$\dot{m}_p s_p + \dot{m}_p s_b - \dot{m}_{in} s_{in} = \dot{S}_{gen} + \frac{\dot{Q}}{T_0} \tag{2.15}$$

Due to the pressure changes within the system, some heat transfer will need to be accounted for in order to maintain isothermal conditions at temperature T_0.

Upon inspection of the input parameters to the input system with realistic values, the energy balance leads to second law efficiency of about 30%. The primary sources of irreversibility losses within the RO modules are the pressurization (expansion) process for the brine and for water purification. The pressure drop leads to diffusion of water which serves

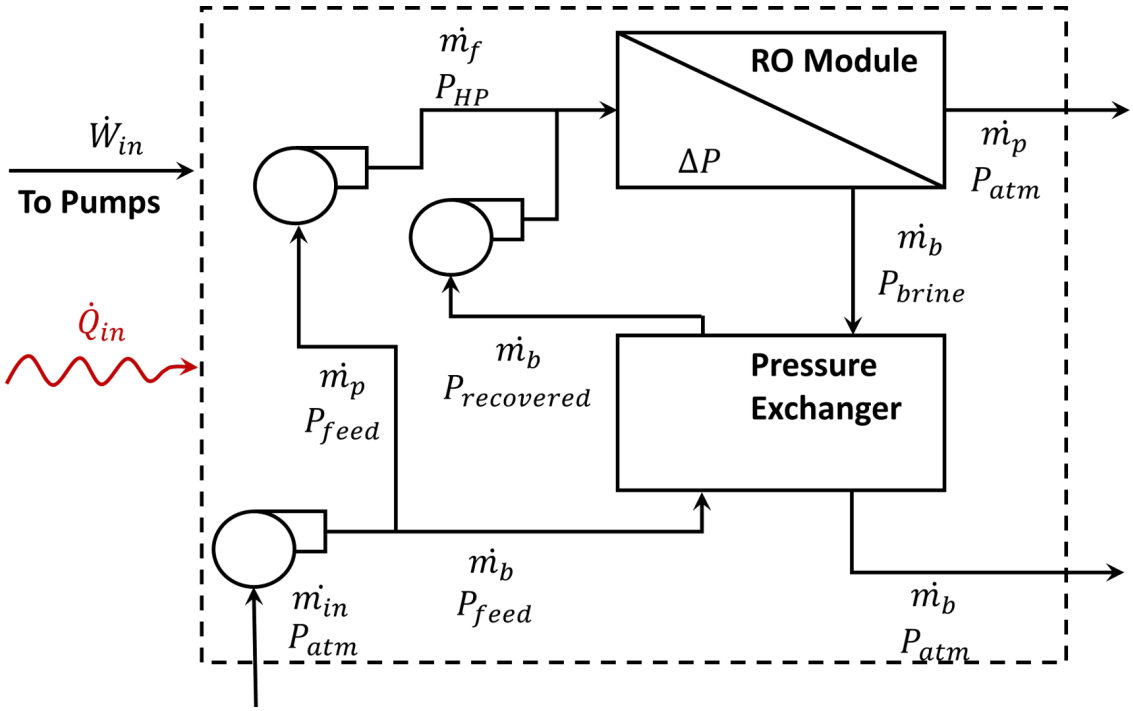

Figure 2.7: Schematic of a single stage RO system. Adapted from [48].

as the main irreversibility source.

Generally, for RO systems, the second law efficiency is higher than in thermal plants, reaching values of up to 30 - 35% [60, 61, 56]. Much of the irreversibility in reverse osmosis systems comes the brine concentration formation. Thus, operating RO systems with a higher number of stages to ease the transition may reduce some of the irreversibility. Additionally, batch processing on the seawater can help to reduce differences between the hydraulic and osmotic pressure. Different semi-batch and batch operations could help to significantly reduce energy requirements for RO [18, 62].

2.3.3 Electrochemical-based separations

Electrodialysis (ED)

Electrodialysis systems, similar to thermodynamic and pressure-based separations-based technologies, can be simplified through only considering mass streams into/out of an open system, along with work and heat exchange. Considering the system defined by Figure 2.8,

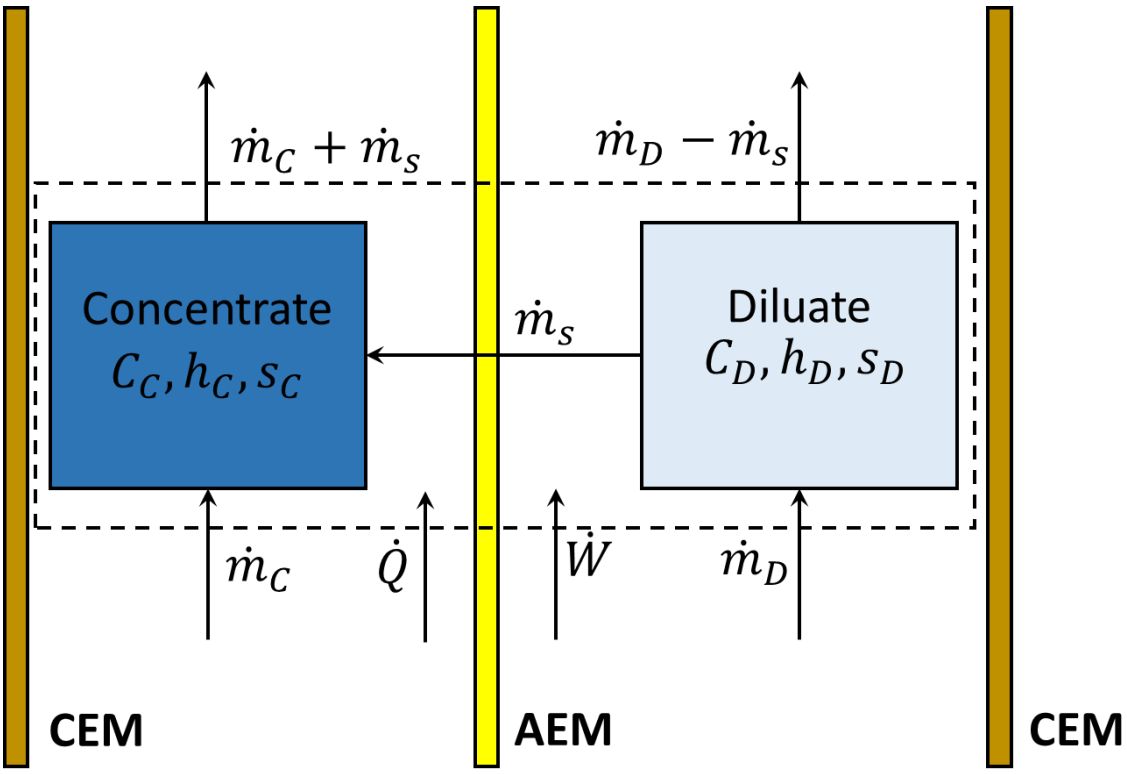

Figure 2.8: Portion of an ED cell showing its basic thermodynamic analysis. Adapted from [32].

the first and second laws of thermodynamics are written as:

$$\dot{m}_s(h_c - h_d) = \dot{W} + \dot{Q} \tag{2.16}$$

$$\dot{m}_s(s_c - s_d) = \frac{\dot{Q}}{T_0} + \dot{S}_{gen} \tag{2.17}$$

The entropy generation sources can be quantified using the pressure drop of the fluid through an electrodialysis channel. Assuming a fully isothermal system, this pressure loss is given by:

$$\dot{S}_{gen} = \frac{Q}{T}\Delta P + \frac{I}{T}\Delta V \tag{2.18}$$

The entropy is due to both pressure drop within the channel (viscous losses) and the

losses due to the voltage drop (transport losses). Transport losses arise mainly as a result of transport limitations within the ED stack. Here we approximate this transport loss as a function of potential gradients within the ED stack based on concentration gradients, assuming the two are linearly proportional to one another [32]. At lower concentrations, the low solution conductivity increases resistance which would account for most of the exergetic losses. If the solution concentration is increased, exergy destruction can be reduced, but the resistance of the membranes remains, since higher salinity differences generate additional spontaneous diffusion.

Losses are also present due to viscous effects, which are higher when the cell current or feed stream velocity are lowered. At lower operating speeds, this presents challenges with lower Reynolds numbers and inconsistent mixing, common in electrochemical fluid flow systems. In systems with lower concentration, the viscous losses become more prevalent since corresponding current values are lower. Thus, designing the cell's geometry to minimize the transport-based losses are important to offset the larger viscous losses where the channel length is smaller.

When considering the design of ED systems, membranes present a challenge not only thermodynamically due to entropy generation, but also economically at larger scales. If the membrane costs can be reduced, then ED can be operated at a larger area, potentially consuming less energy than RO [63, 64, 65]. Some studies already claim that energy consumption can be reduced over RO at brackish concentrations (< 35 mM) if considered under certain representative designs. Furthermore, multistaging is another design consideration that could reduce energy demand if membrane area can be made economically viable.

Capacitive Deionization (CDI)

The thermodynamics of capacitive deionization (CDI) has been explored similarly to ED, taking into account an inlet stream that is separated into a brine and diluate concentration with relevant work and heat inputs [66]. The energy balance leads to the same general

equation previously shown for electrodialysis. Here, we will once again remove the additional contribution of heat generated (assuming small current/resistance values), we can write the energy balance as:

$$\dot{W}_{in} = T(\dot{S}_{in} - \dot{S}_{out}) \tag{2.19}$$

Here we have cancelled the enthalpy terms, upon assuming that the cycle is isothermal and isobaric. We can apply a molar balance (mass balance equivalent) for the inlet and outlet streams:

$$\phi_0 C_0 = \phi_C C_C + \phi_D C_D \tag{2.20}$$

where $\phi_{\,0}$, $\phi_{\,\mathrm{C}}$, and $\phi_{\,\mathrm{D}}$ denote the total volumetric flow rates of the inlet, concentrate, and diluate streams. By using these terms to substitute for entropy values between the inlet and outlet streams, in terms of the concentrations, volumetric flow rates, and universal gas constant, R:

$$\dot{W}_{in} = nRT(\phi_0 C_0 ln(C_0) - \phi_C C_C ln(C_C) - \phi_D C_D ln(C_D)) \tag{2.21}$$

where n is the van't Hoff factor that is used for chemical separations. We can then define an appropriate recovery ratio for the amount of inlet volume diluted. Then, if assuming a 1:1 salt such as NaCl, we can write n = 2 and then the following expression for the theoretical minimum mixing energy:

$$\Delta\dot{G}_{mix} = 2RT\Big[\frac{C_0}{\alpha} ln\Big(\frac{C_0 - \alpha C_D}{C_0(1-\alpha)}\Big) - C_D ln\Big(\frac{C_0 - \alpha C_D}{C_D(1-\alpha)}\Big)\Big] \tag{2.22}$$

Compared to electrodialysis, CDI exhibits much of the same governing physics regarding fluid and electrochemical transport, only that charge is first stored within electrodes to form the diluate during charging, then released during discharging to form the concentrate.

The exergetic efficiency of CDI has been examined extensively in a recent study. In addition to the potential (transport) losses, the same pressure losses are taken into account as from the ED case. The study finds the maximum exergetic efficiency of around 16% for an experimental study of concentration 5 mM; however; theoretical analysis (Chapter 4) showed that this exergetic efficiency can be increased to over 30% under ideal conditions at higher operating currents.

Thermodynamics of Electrochemical Adsorption Processes

Thermodynamic principles can be used to determine the adsorption capabilities of electrochemical-based processes. Isotherms are commonly used for gas sorption processes [67], but they can also be applicable to liquid solutions, varying as a function of concentration C. Of the models that exist to predict the variation of electroadsorption as a function of equilibrium concentration, the two most commonly cited in literature are the Langmuir isotherm and the Freundlich isotherm.

The Langmuir isotherm model, while initially developed for gas-solid adsorbent pairs [67], is also applicable to liquid solutions, in which adsorption varies as a function of concentration at equilibrium, C_{eq}, typically given in mg/L. The Langmuir model assumes fully homogeneous, monolayer adsorption with no interaction of the adsorbed species in the plane of the surface. Furthermore, the model imposes a limit to the maximum quantity of total adsorption by the adsorbate. The governing equation for the Langmuir adsorption isotherm is given as:

$$q_e = q_{max} \frac{K_L C}{1 + K_L C} \tag{2.23}$$

where K_L is the Langmuir constant, given in units of q_{max} represents this maximum adsorption. The concentration C is determined as the equilibrium concentration for the adsorption process. In continuous mode processes this can be assumed as the inlet concentration, but if the process is done in batch mode with a finite volume constantly circulated during

adsorption, the equilibrium concentration is given as the average between inlet and dilute concentration.

A second isotherm that can be used to determine ion sorption capabilities is the Freundlich isotherm. This model extends beyond monolayer adsorptions of the Langmuir model and assumes that multiple layers exist through which sorbent can be stored within sorbate. Unlike the Langmuir model, however, the Freundlich isotherm is semi-empirical [68] and does not have a direct theoretical basis behind its values. The Freundlich isotherm is preferred when lower concentrations of solute are used [69], and commonly for desalination it is directly compared with the Langmuir adsorption process. The Freundlich isotherm is given as a power relation:

$$q_e = K_L C^{1/n} \tag{2.24}$$

where K_F is a constant, related to heat of adsorption, given in units of $(L/mg)^{1/n}$, and 1/n is a constant power parameter, which indicates the heterogeneity of the solution and indicates the tendency for which the sorbent readily adsorbs.

For desalination processes, the adsorption isotherms can be developed by examining salt removal with experimental operating conditions as the control and the initial feed concentration as the variable (Figure 2.9A). A plot of C vs. q can be fitted to the Langmuir and/or Freundlich adsorption isotherms to predict the extent to which monolayer or multilayer adsorption holds under the given conditions based on R^2 values [69]. The chosen equilibrium constant K_{eq} is then multiplied by appropriately related parameters to make its value dimensionless. Regardless of which isotherm is used, it is important to perform this unit conversion correctly, as it has been cited as a source of error in various adsorption isotherm literature [70].

When operating over a range of temperatures, isotherms can be used to further identify further characteristics of the adsorption process (Figure 2.9B). The equilibrium constant

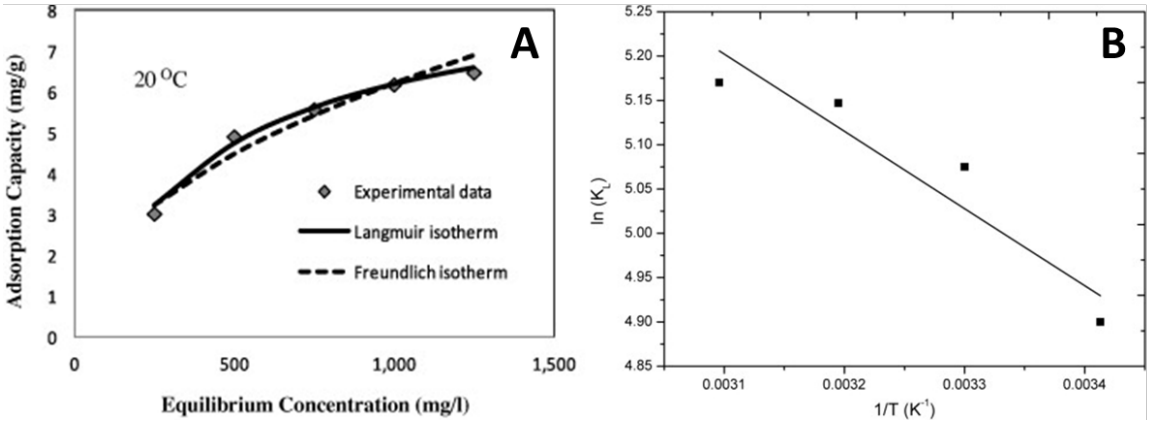

Figure 2.9: (A) Plot of a CDI electrosorption at one temperature, with curves showing fits to Langmuir and Freundlich adsorption isotherms. (B) van't Hoff plot for ion electrosorption, showing linear fit to determine enthalpy/entropy of adsorption. Data taken from [71].

K_{eq} can be related to the Gibbs free energy of adsorption by [72]:

$$ln(K_{eq}) = -\frac{\Delta G}{RT} \tag{2.25}$$

When $\Delta G < 0$, the process is said to be spontaneous; positive values are considered non-spontaneous. The Gibbs energy can also be used to calculate related enthalpies and entropies of adsorption:

$$\Delta G = \Delta H - T\Delta S \tag{2.26}$$

The relationship between ΔG, ΔH, and ΔS can be plotted as a linear variation with T. More specifically, the variation of $\ln(K_{eq})$ vs. 1/T can be used to determine ΔH and ΔS via linear regression. Thus, ΔH and ΔS can be used to further characterize the adsorption process. If ΔH is positive, it is indicative of an endothermic reaction; if it is negative, it is indicative of an exothermic reaction. Furthermore, the magnitude of the enthalpy of adsorption allows for prediction of characteristics for some adsorption processes: If the enthalpy values are below 84 kJ/mol, the adsorption is considered physiosorption; whereas values from approximately 80 - 420 kJ/mol are considered chemisorption [67, 71]. Alter-

natively, it has been suggested that a chemisorption process can occur if the ΔH values are negative, regardless of their magnitude[73]. The entropy of adsorption indicates the affinity between sorbent and sorbate. If the value is higher, there is more favorable adsorption due to greater degrees of freedom from the sorbate. If the entropy value is negative, the activity of sorbent at the solid-liquid interface is reduced, essentially making the adsorption process more difficult [74].

The determination of ΔH and ΔS experimentally has been done for salt water desalination on various electrodes, for NaCl sorbent as well as other ions in aqueous solutions [73, 71]. However, the breadth of experimental data collected is limited since ranges of both concentrations and temperatures are required to determine a single ΔH and ΔS value. As a result, the viability of exploring fundamental adsorption processes with different values/ranges of multiple parameters is further challenged. Computational studies can relieve the arduous task of running large numbers of experiments, and more importantly, can easily assess the sensitivity of ΔH, ΔG, and ΔS to a wide range of operating conditions.

Thermodynamics for Blue Refrigeration

In thermodynamics, it is well known that work can be extracted if there is an energy transfer of heat as it flows from a hot medium to a colder medium [75], commonly known as heat engines. Conversely, in order to reverse the flow of heat to maintain cooler temperatures in one space and a warmer temperature in the other, work needs to be added into the system as this process does not occur spontaneously, a concept known as refrigeration (Figure 2.15A). Thermodynamic concepts have been examined and applied to desalination studies [48], such as reverse osmosis [76], even dating back to 1971 [77].

For capacitive deionization/mixing purposes, one can imagine two reservoirs with different ion concentrations (2.10b). If ions diffuse from high concentration to low concentration, energy can be extracted from the salinity gradient through processes known as capacitive mixing (CapMix) or reverse electrodialysis (RED) [78, 79]. Energy extracted

by this means is sometimes called as blue energy, a term first coined in the mid-2000s by research & development programs in the Netherlands [80]. Cycle operation in the reverse mode, or blue refrigeration, essentially drives the process of CDI to keep a fresher reservoir at a low concentration.

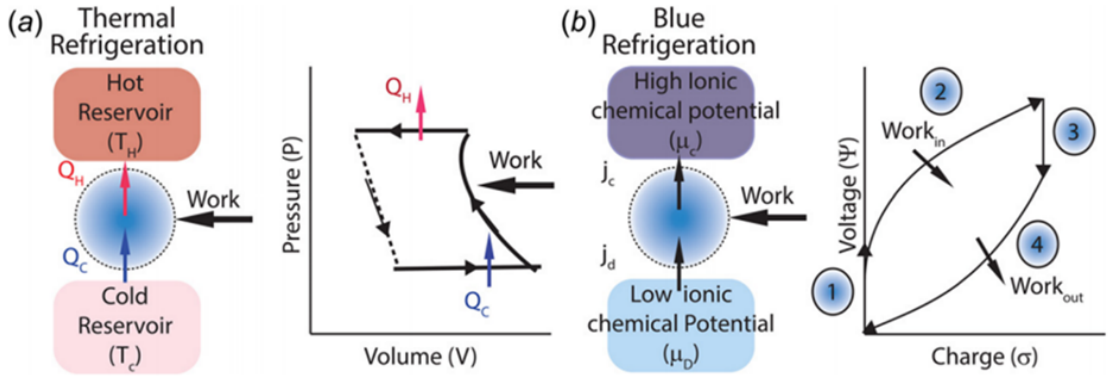

Figure 2.10: (a) Traditional refrigerator, in which work is consumed to move heat from a cold reservoir to a hot reservoir, (b) Blue refrigerator, where ions are transferred from a low ionic chemical potential solution to a high chemical potential solution [81].

The first published work on a cycle for a capacitive mixing system came in 2009, when Brogioli performed a 4-stage cycle with 2 stages of constant voltage and 2 stage constant feed stream concentration [82] . While small scale and proof-of-concept, the study claimed reasonably competitive performances with membrane-based methods, and provided insight into EDL considerations to take into account in blue cycles. Direct analogies between thermodynamic and electrochemical terms to draw an equivalent for desalination were the focus of van Roij′s work [83], which are illustrated in Figure 2.11. For example, van Roij concluded that Brogiolis cycle was equivalent to a Stirling engine in thermodynamics. However, in order to maximize efficiency of the cycle, one should use a constant temperature and constant entropy process, otherwise well-known as the Carnot cycle [75].

The variables in Figure 2.11 are defined as follows: From (a), μ is the chemical potential of the cell (relative to a reference concentration), N is the number of ions present in the cell, ϕ is the cell voltage, and Q represents surface charge in the cell. In (b), T represents

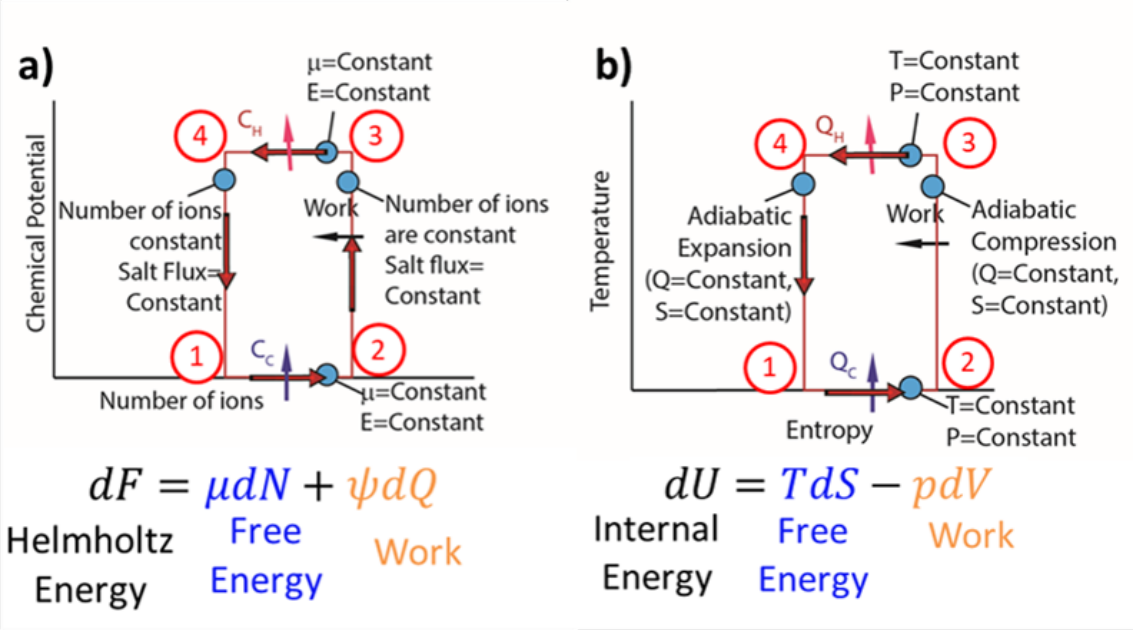

Figure 2.11: (a) Electrochemical analog of (b) traditional Carnot thermodynamic cycle for capacitive deionization.

temperature, S is the extensive entropy (relative to reference temperature and pressure at each state), p is the system pressure, and V is its volume.

From published work in [83], temperature is actually analogous to the chemical potential, which varies logarithmically with concentration. Entropy is proportional to the total number of ions present within the solution volume of interest. In 2011 Boon and van Roij had simulated this cycle for comparison, and when compared with Brogioli′s cycle, had resulted in an improved work output per number of ions exchanged throughout the cycle [84]. While not as straightforward to constrain number of ions in practicality, simulating this condition can facilitate operation of overall system efficiency and/or energy consumption.

Several studies have performed CDI under various four-stage processes, both computationally and experimentally [40, 84, 82, 85, 86, 87, 88]. There has now been increasing interest in how proposed operational conditions of the cycle can affect desalination performance and appropriate analogies to thermodynamic cycles.

2.4 Electric Double Layer (EDL) Theory

The electric double layer (EDL) is a structure that forms on the surface of a solid at its interface with an electrolyte. Understanding the composition of the electrolyte is crucial to understanding how the electric potential varies within the electrolyte and ultimately, within the cell. EDLs have not only gained considerable attention for CDI applications but also other electrochemical technologies as well, such as batteries or in electrowetting [89]. When applying an external potential through the cell, the electric field within the electrolyte causes a buildup of charges at the surface of the solid electrode.

The concept of the EDL was first proposed in 1853, when Helmholtz discovered that charged electrodes attract counter-ions within the electrolyte solution but repel co-ions [90]. The Helmholtz model was able to effectively describe the solid-liquid interface, but did not make any considerations about variable capacitance or take into account effects such as diffusion or the exact composition of the layers used. Gouy and Chapman expanded upon this model by incorporating a diffuse layer to account for the fact that the ions are not static, and that capacitance did in fact vary with ion concentration and applied potential [91]. Due to the assumption that ion movement could govern random thermal motion, Maxwell-Boltzmann statistics could explain the exponential decrease in the potential distribution through the electrolyte. More specifically, this potential distribution is governed by the Poisson-Boltzmann equation developed by Gouy and Chapman [89].

One of the limitations of Gouy-Chapman (GC) was that the theory did not consider ion size, as there is a finite amount of space for ions to adhere to the surface. At higher concentrations or charges, GC theory breaks down. Stern corrected this in 1947 by combining the theories of Helmholtz and Gouy-Chapman. He concluded that some ions adhere to the electrode (Stern layer), while some form the GC diffuse layer [92]. The Gouy-Chapman Stern (GCS) theory for EDLs accounted for the sizes of the ions, but still treated these charges as point charges [89]. Additionally, GCS theory is only accurate as long as the

double layers within the pores do not overlap. This is determined by evaluating the Debye length for the EDL, a measure of how far double layer effects propagate into the solution. As the Debye length increases at lower concentrations to nearly 10 nm, and pore sizes typically range from 2-4 nm, additional considerations need to be made in order to account for this overlap [93].

Since the majority of CDI studies focus on lower salt concentrations, it became necessary to refine this model to account for this discrepancy. The refined model, called modified Donnan (mD), accounted for the effects of overlapping EDLs [94] (Figure 2.12). The primary physical additions to this model were a micropore concentration and an excess chemical potential from inter-ion interactions. This model has been dubbed the improved modified Donnan model (i-mD). Recently, the excess chemical potential term has been adapted as a physical parameter, which allows for inclusion of mD theory in higher concentration ranges [93]. Additional EDL models developed in more recent years include GCS-CS (Carnahan-Starling) [95], which enabled more realistic characterizations at higher concentrations, and modified Poisson-Boltzmann theory for unequal radii [96], facilitating predictions for charge separation.

From a modeling perspective, there is much interest in understanding EDL due to its significant influence on desalination cycles. During charging, ions build up on the electrolyte surface and form a layer of finite thickness [66, 84]. Temperature and concentration each have a significant effect on EDL characteristics as well [97]. Ensuring reliable considerations for EDL modeling is crucial to determining accurate performance in mixing and CDI cycles.

2.5 Electric Double Layer Capacitor Modeling

Electrochemical capacitors typically consist of two porous electrodes (parallel plates) with a conductive electrolyte (salt) in between contacting the electrodes (Figure 2.14A). As the surface area increases and the distance between the capacitors decreases, the general

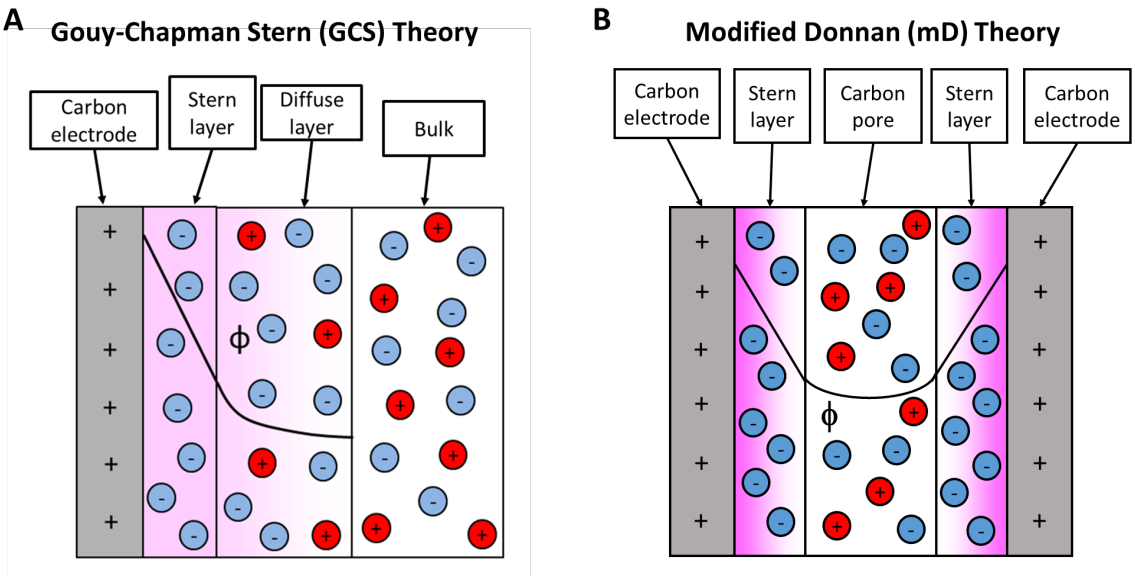

Figure 2.12: Illustration of EDL models for (A) Gouy-Chapman Stern (GCS) and (B) modified Donnan (mD) theories. [93].

capacitance of the EDL decreases.

One important advantage of EDLCs is that they can exhibit a varying range of energy storage techniques. Whereas capacitors are used for higher power and batteries for higher energy, electrochemical capacitors can achieve higher capacity with a higher surface area (Figure 2.13), motivating many studies which use porous electrodes. Since EDLCs do not exhibit chemical reactions or phase change, the life cycle capabilities can last up to millions of cycles [98]. However, the power of EDLCs is not as strong as pure capacitors, since ionic conductivity through the separators limits the discharging rates. As was previously stated, EDLCs using carbon-based electrodes have been commonplace for several decades [99]. Research has been conducted into investigating metal oxides in EDLCs, due to properties such as high capacitance, lower resistance, e.g. RuO_2 and MnO_2 [100].

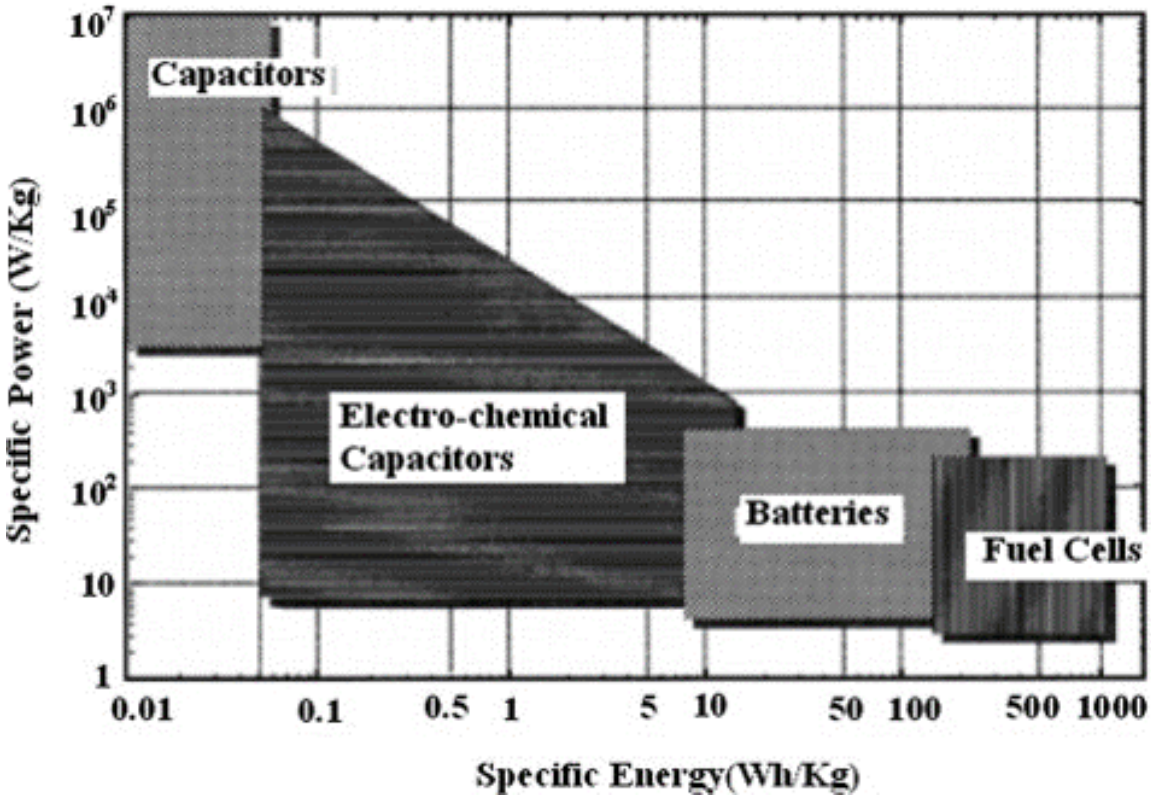

Figure 2.13: Ragone chart of different electrochemical energy storage devices [98].

Perhaps the most primitive model of the EDLC would be the classical equivalent circuit (Figure 2.14B). This model consists of a capacitor C and a resistor R_P in parallel with another resistor in series R_C [101]. While some capacitors can be evaluated and connected to this model through EIS techniques, most experimental EDLCs do not accurately fit this classical model. One of the more accurate and well-known circuit models for EDLCs today is the de Levie transmission line model [102] (Figure 2.14C). De Levie's model assumed that the electrode pores within the EDLC could be modeled as a transmission line, containing both resistances and capacitances to estimate the effects on the double layer responses to various input. The model makes several simplifying assumptions, such as neglecting gradients of concentration and solution resistivity within the electrode and a conductivity for the electrode that is infinitely high (i.e. metallic-like electrode).

Models for EDLCs have been categorized into either direct charging of the EDL alone, or the entire performance of the capacitor as a whole. The modeling of the EDLC was first

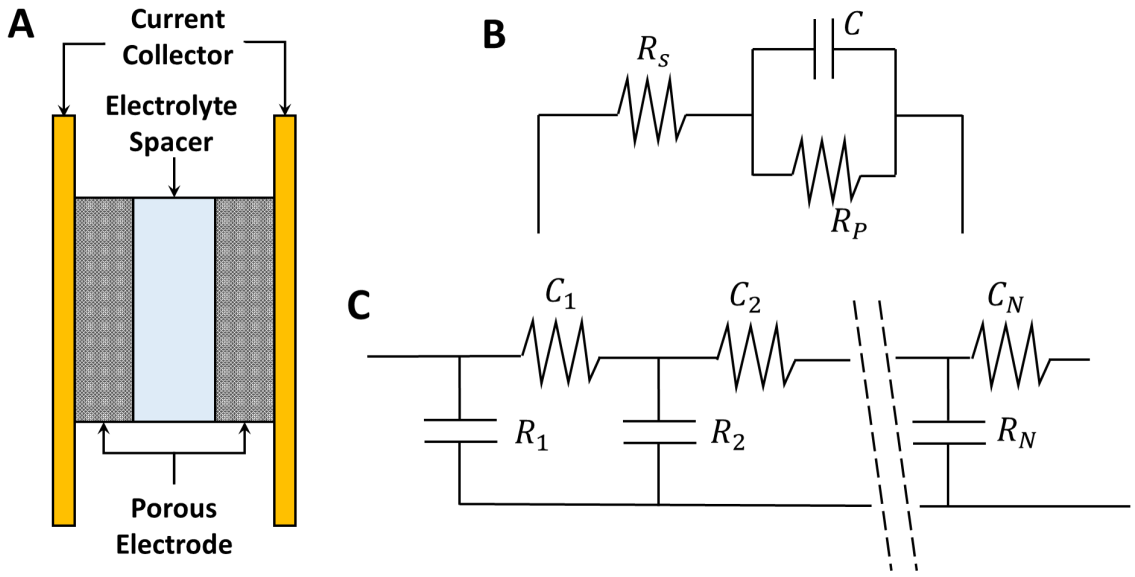

Figure 2.14: (A) Setup of a typical EDLC, (B) simplified circuit model, (C) de Levie transmission line model.

motivated by Pillay and Nerman who examined constant charge operation, taking into account the side reactions of hydrogen and oxygen evolutions that limit efficiency [103]. The model made assumptions of small overpotentials and thus used linear kinetics to examine performance.

Porous electrode theory assumes that the current density $i_{cell} = I/A_{cell}$ is divided into two components, each of which accounts for the current distribution in both a matrix and the solution phases of the porous electrode:

$$i_{cell} = i_1 + i_2 \tag{2.27}$$

These currents can be related by the gradient of the potential ϕ within the electrode phase:

$$i_1 = -\sigma \frac{\partial \phi}{\partial x} \tag{2.28}$$

$$i_2 = -\kappa \frac{\partial \phi}{\partial x} \tag{2.29}$$

where the carbon matrix has current distribution i_1 and conductivity σ, and its surrounding solution has current distribution i_1 and conductivity κ, at any given time. The two currents are related to double layer capacitance by:

$$\frac{\partial \imath_1}{\partial x} = -\frac{\partial \imath_2}{\partial x} = -aC_{dl}\frac{\partial \eta}{\partial t} + i_F a \tag{2.30}$$

where the first term on the right-hand side of the equation represents the contribution to the capacitive current from the EDL, while the second term considers Faradaic contributions to the current, if Faradaic interactions are considered. The overall double-layer capacitance C_{dl} can be assumed to be equal to the Stern layer capacitance. The specific electrode surface area a, in units of m^{-1} is given in terms of electrode porosity ϵ and pore diameter d:

$$a = \frac{3(1-\epsilon)}{d} \tag{2.31}$$

If Faradaic current i_F is considered, then the Butler-Volmer kinetic equation can be used to relate its value to the cell overpotential η:

$$i_{\text{cell}} = i_0\Big(exp(\frac{\alpha_C F\eta}{RT}) - -exp(\frac{\alpha_A F\eta}{RT})\Big) \tag{2.32}$$

One of the first full-scale porous EDLC models was developed in 1999, which simulated an EDLC under both a constant current discharge and looked at EIS [104]. By employing both operating regimes for the models, EDLC model behavior under different operating conditions could be predicted and related to the overall energy and power density performance of the EDLC. There were clear tradeoffs as the cell components were varied; for instance, larger electrode thicknesses could increase energy density but limited power density. Additionally, if lower currents were used, the operating efficiency could be im-

proved, as the lower current allows for sources of irreversibility, such as resistive losses and Joule heating, to be reduced during cycling operation.

The effect of temperature on the performance of EDLCs was also carefully examined following initial experimental observations [105]. As temperature decreases during cycling, it was shown that effective cycle resistance increased and capacitance decreased, as a result of the decreased ion mobility and solvent viscosity when temperature was decreased at lower temperatures. At higher temperatures, resistance can be increased while capacitance decreases, but this would result in lower cycling stability. Thermal models for EDLCs have employed the heat diffusion equation to model temperatures within the electrolyte:

$$\rho C_P \frac{\partial T}{\partial t} = -A\nabla(k\nabla T) + \dot{Q_{rev}} + \dot{Q_{irr}} \tag{2.33}$$

where A represents the cross-sectional area of the EDLC, ρ represents its density, C_P its specific heat, and k its thermal conductivity. The irreversible heat generation term $\dot{Q}_{\text{irr}}$ is the familiar Joule heating (I^2R), and the reversible heat generation $\dot{Q}_{\text{rev}}$ is based on entropic changes of ions when the EDL forms [106]. This is especially important when below-ambient temperatures are used, as changes in the EDL resistance and capacitance are strongest there. Many previous models did not fully account for both the spatial variations of temperature within the EDL and the irreversible heating term [106]. Incorporating both considerations enabled more accurate temperature profiles for the EDLCs relevant to literature [106, 107].

Up until this point, the capacitors discussed have been studied predominantly on short term scales (order of milliseconds), with maximum temperature rises of only up to a few degrees. The principles of supercapacitors to store and release energy are important for forming the basis of capacitive mixing (CapMix) to generate energy, and its inverse, CDI, to separate ions from solutions for desalination. When operating EDLCs on the time and geometric scales for CapMix and CDI, the operating conditions must be adjusted accordingly, but the fundamentals of charge storage remain intact when considering transport and

thermodynamics.

2.6 Flow Electrode CDI - Motivations & Limitations

One of the more recent innovations in CDI arose due to the limited surface area of the electrodes used, which can lead to saturation of the cell [108]. One solution to this involves increasing the electrode area using a flowable electrode slurry (Figure 2.15). In this configuration, the storage of the electrode is no longer limited and is able to flow through the system continuously. The concept of flow electrode CDI demonstrated a significant improvement in salt removal for a higher saline concentration than typical CDI [109].

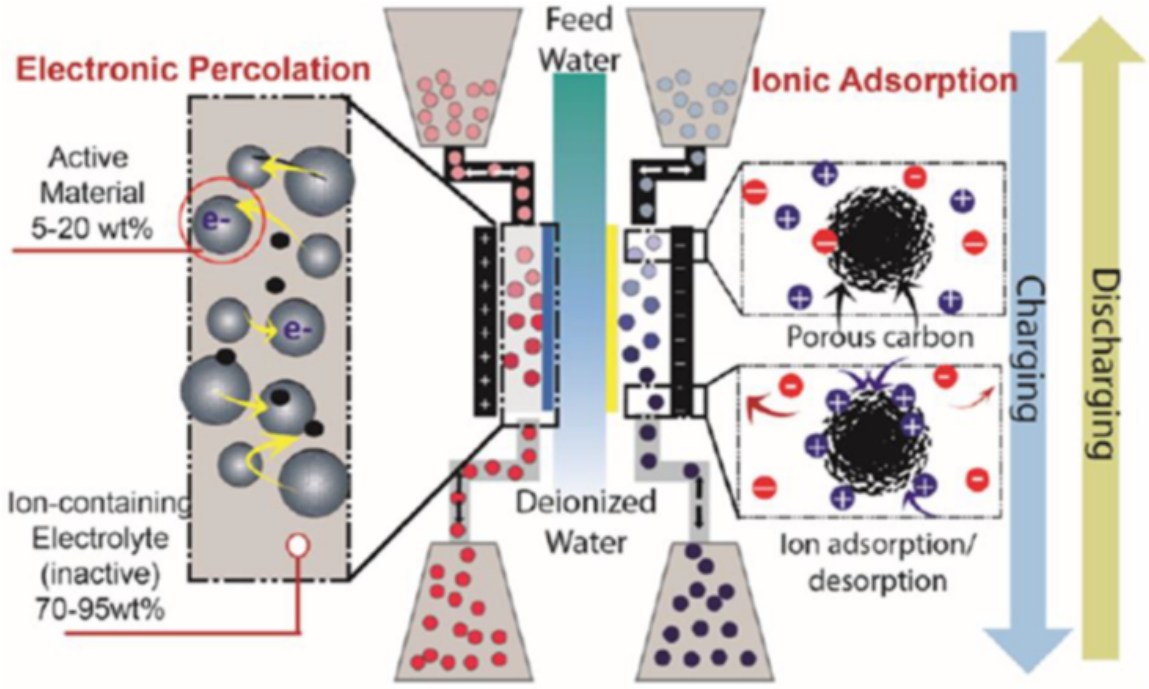

Figure 2.15: Typical architecture for flowable CDI, utilized for large-scale energy storage [110].

Recent advances in FCDI technology have focused on energy recovery, flow electrode optimization, and cell design. Expansions of FCDI to include neutralization deionization (ND) and capacitive energy harvesting have also been recently explored [111, 112]. FCDI is among one of the major breakthrough technologies for large-scale energy storage and management. One of the primary issues with the technology is that while an increased

amount of carbon weight percent leads to better desalination performance, the viscosity increases exponentially within the carbon loading [112], which can lead to severe clogging of the FCDI system. FCDI systems should thus take care in using electrodes appropriate to minimize clogging of the tubing [110]. Even if clogging does not occur, higher fluid viscosity requires higher pumping power, which reduces the overall system efficiency.

Therefore, it is important to determine methods of effective desalination without always having to resort to higher concentrations. One method involved the oxidation of the flow electrodes using nitric acid (HNO_3), in order to improve energy storage properties due to greater wettability and surface accessibility in ions [110]. Another study [113] proposed the combination of carbon spheres (CS) wrapped by highly conductive reduced graphene oxide sheets (rGO) to increase conductivity, accelerating the percolation of charge in the flowable electrodes. Additionally, surface-modified spherical carbon was added to ion-selective functional groups for each electrode, promoting electrostatic repulsion to reduce fluid viscosity [114]. Xu [115] proposed an asymmetric FCDI cell to improve desalination by expanding the applied voltage range to 1.8 V. This greatly increased the systems salt removal efficiency as well as mean electrosorption rate as shown on Kim-Yoon plots [116].

In addition to modifying material considerations and properties for the electrode, it is also necessary to look at the concentration of the electrolyte as well when evaluating FCDI performance. The flow electrode-supporting electrolyte has received less attention with the majority of researchers using various concentrations (0 to 0.5 M) of sodium chloride [109, 110, 111, 112, 117, 79, 113, 114, 115, 116, 118, 119, 120, 121]. Increasing the salt concentration should reduce ohmic resistance and thus improve performance, yet it has been shown that desalination efficiency only increases up until $\approx$0.4 M sodium chloride (E_{cell} 1.2V), and decreases beyond this point due to transport of ions into the feed [121]. Higher saline electrolytes (0.5 M Na_2SO_4) were further investigated, and shown to improve desalination rate, but only at elevated voltages ($E_{cell} > 1.5V$). This indicates that the supporting electrolytes play a critical role in mediating transport, in addition to minimizing

ohmic-based losses.

CHAPTER 3
EVALUATING EFFICIENCY OF CARNOT AND CONVENTIONAL CAPACITIVE DEIONIZATION CYCLES

Brackish water treatment characteristically suffers from low efficiency. Overcoming this challenge requires a fundamental understanding regarding the energetics of both the ion removal process and the trajectory of the complete deionization cycle. Evaluating the processes and cycles in tandem can elucidate potential sources of inefficiency (entropy production), and may promote new operational schemes leading to higher efficiency low saline separations. Here, using a Gouy-Chapman-Stern model we elucidate the efficiency of two capacitive deionization cycles. In the first cycle, electroadsorption occurs as the cell voltage increases, which resembles processes employed experimentally. In the second cycle, a theoretical Carnot-like electroadsorption process occurs while maintaining a constant number of ions (N=constant). We show that the projected thermodynamic efficiency of both cycles exhibited similar efficiency which range from 2-4.5%, while operating with a low saline feed (C_{feed}= 20 mM) stream. However, at elevated feed concentrations (100 mM), the Carnot-like electroadsorption process resulted in a significant improvement in thermodynamic efficiency (30%), when compared with the conventional electroadsorption process (15%). While the Carnot-like electroadsorption process is not technically feasible, it may serve as a benchmark for understanding thermodynamic limits associated with low saline separations achieved through electrosorption.

3.1 Introduction

The inextricable connection between water and energy promotes investigations that reduce energy consumption during desalination processes. Moving toward the use of low saline brackish water as a feed solution is one simple approach to achieve low specific energy con-

sumption (SEC) desalination. This is because the theoretical minimum energy required for separating brackish waters ($\leq$0.3 kWh/m^3) is significantly less than that required for seawater separations (3-10 kWh/m^3)[122, 123]. Brackish water separation is also increasingly favorable in remote or inland regions which do not have reliable access to seawater[124].

A growing interest beyond attaining low SEC is achieving high desalination efficiency. The efficiency by which desalination technologies are evaluated are based on thermodynamic principles or exergy considerations. The thermodynamic energy efficiency (TEE) provides information regarding how far a technology is from the theoretical minimum, whereas exergetic efficiencies (ExE) provide guidance on how far a technology is away from a practical minimum, based on chemical exergy changes. The TEE has primarily been the guiding tool to measure the efficiency of reverse osmosis (RO), with efficiencies improving from only 5% in the 1970s to over 50% today [125, 126]. It should be noted that achieving 100% is not practically possible; therefore little gains in terms of energy efficiency can be made through solely improving reverse osmosis for seawater desalination. This is one reason why there is greater interest in mitigating energy consumption in alternative water treatment processes such as pre or post treatment[3].

Despite the near ideal performance, RO does not maintain this efficiency when moving toward low saline solutions (brackish water)[64]. The SEC for brackish water RO decreases[127, 128, 129], but the corresponding decrease in the Gibbs free energy of mixing is greater. This low efficiency is often overlooked, as there is a greater emphasis on SEC. Furthermore, exergetic efficiencies for brackish water RO are less than 10%[60, 130, 131], with the highest reported value of 16% [61]. This is why historically alternative technologies (electrodialysis and capacitive deionzation) are discussed for brackish water treatment[132, 133, 134, 135, 136]. Most capacitive deionization cycles yield efficiencies in the range of 1-5% with feed solutions of on the order of 20 mM [66, 137, 133, 138, 139]; however, the aim of these investigations was not on optimizing TEE. In more recent efforts which aimed to improve TEE, maximum values of 9% were shown to be possible[140].

Here, we aim to analyze the expected thermodynamic and exergetic efficiency of two different capacitive deionization cycles. In the first cycle, electroadsorption and desorption occur as the cell voltage is incrementally increased. This cycle is practically feasible as one can execute the cycle experimentally. The second cycle is purely theoretical, and is based on prior definitions of a Carnot-like chemical cycle for capacitive mixing[141]. In the second cycle, salt removal occurs while maintaining a fixed number of ions (N=constant). By examining both cycles, we aim to discern if the electroadsorption processes within a given desalination cycle (Carnot or conventional) can limit the maximum efficiency. Furthermore, we aim to better describe thermodynamic limitations associated with dilute solution separations.

3.2 Theory

The desalination cycle employed in most capacitive deionization studies includes four consecutive processes. However, just like with thermal energy systems, these cycles can operate using different modes. Thus, achieving ion removal is possible by various different processes [142, 81, 86]. Here, we investigate two thermodynamic deionization cycles.

In the first cycle, we employ four processes which can be executed in a conventional CDI system. Process one consists of deionization up to a set voltage V_{max}. Next in process two, as the feed is switched to a brine the electrodes continue to be charged at fixed voltage (iso-V - switch). In process three, the electrodes are discharged while the concentration decreases. Then in process four, the electrodes are brought back to the initial conditions (C_{feed} replaces C_{brine}) using a constant voltage process (iso-V - switch). Since this cycle operates using conventional processes, we term this the conventional cycle (Figure 3.1a and b). Evaluating energy consumption will take place through the use of V-σ curves (Figure 3.1e).

In the second cycle, we employ processes which are analogous to a Carnot refrigeration cycle. The Carnot cycles for thermal systems represent the ideal (reversible) cycle. It is

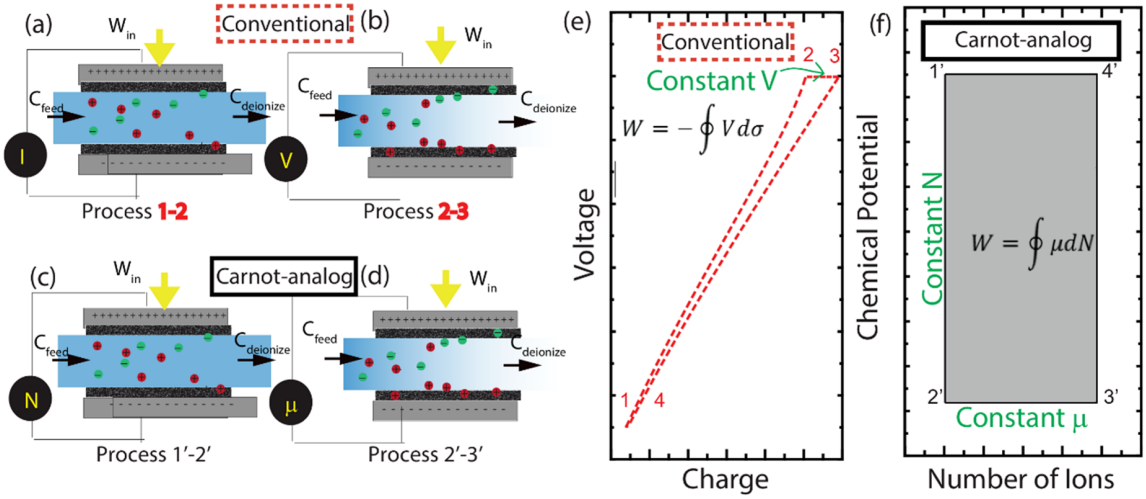

Figure 3.1: (a) Ion removal in the IV cycle occurs through a constant current (iso-I) process followed by a (b) constant voltage (iso-V) process. (c) Ion removal in the Nμ (Carnot-like) cycle occurs through a constant number of ions (iso-N) process followed by (d) a constant chemical potential (iso-μ) process. (e) The trajectory of the cycles is evaluated on a voltage versus charge (σ), or (f) chemical potential (μ) versus number of ions (N) diagram.

well known that Carnot cycles cannot be executed in reality, but the theoretical insight provides guidance on how far a real cycle is away from an ideal system. The chemical Carnot cycle was previously described in prior work[141]. Briefly, process one is described by deionization at a constant number of ions (iso-N), process two is described by deionization at constant chemical potential (iso-μ), process three is described by resalination at constant number of ions (iso-N), and process four is described by another resalination step at constant chemical potential (iso-μ) (Figure 3.1c and d). We will refer to this cycle as the Carnot cycle, and energy consumption will be detailed on the μ-N diagram (Figure 3.1f).

For both cycles, we assume a quasi-equilibrium condition, which implies that the cycle operates on an infinitesimally slow flow rate to minimize irreversibilities. This greatly simplifies the model since it eliminates the need to specify time dependent parameters, such as current and flow rate. Additionally, considerations regarding cell geometry are not considered, since all quantities here will be evaluated on a per area or per volume basis. The model also does not consider Faradaic losses due to side reactions or resistive losses due to components such as membranes or contacts.

In order to describe various iso-property (μ, N, V, C, T, σ) processes for a given capacitive deionization cycle a description for the electric double layer is needed. Here we employed the well documented Gouy-Chapman-Stern (GCS) model to describe the electric double layer dynamics necessary for ion removal[66]. In each of the simulations the maximum voltage V_{max} was limited to 1.2 V. In addition, the feed (C_{feed}) remained constant while the deionized concentration (C_{min}=$C_{deionized}$) and water recovery ratio α=$V_{deionized}$/V_{feed} were varied. In order to maintain an ion balance during the cycle, the resulting brine concentration C_{brine} is determined by:

$$C_{brine} = \frac{C_{feed} - \alpha C_{min}}{1 - \alpha} \tag{3.1}$$

Since the Carnot analog cycle is constrained to limits of only two concentrations, the high concentration is the brine C_{brine} and the low concentration is the diluate C_{min}. The chemical potential in the cell at any point is:

$$\mu = RTln(\frac{C}{C_{ref}}) \tag{3.2}$$

where T is temperature, R is the universal gas constant, and C_{ref} represents a reference concentration, taken to be 1 M [141]. The total number of ions in the cell (per electrode area) N is:

$$N = \Gamma + CL_eN_{av} \tag{3.3}$$

where N_{av} is Avogadro's constant, L_e represents the pore length between carbon particles (pore volume/pore area), taken in this study to be 4 nm, and Γ is the excess surface charge. Γ is determined as a function of both the electrode surface charge σ and additional crossover charge σ^*:

$$\Gamma = \sqrt{\sigma^2 + \sigma^{*2}} - \sigma^* \tag{3.4}$$

$$\sigma^* = \frac{1}{2\pi\lambda_B\lambda_D} \tag{3.5}$$

where the Debye and Bjerrum lengths for the electrolyte, λ_B and λ_D determine the crossover charge[66]. Crossover charge is defined as the charge at which attractive forces from counter ions and repulsive forces from co-ions are balanced [143]. When crossover charge exceeds surface charge, the increase in counter ions exceeds the decrease in concentration of co-ions, resulting in a net increase in number of ions adsorbed [144]. If surface charge is smaller, then Γ is directly proportional to σ. The diffuse layer voltage difference ΔV_D is given by:

$$\Delta V_D = 2V_T sinh^{-1}\Big(\sigma\sqrt{\frac{\pi\lambda_B}{2C_{feed}N_{av}}}\Big) \tag{3.6}$$

The thermal voltage V_T is defined as V_T = RT/F, where F is Faraday's constant. For the Stern layer voltage ΔV_{st}, Gauss law is used for a 1:1 electrolyte (as in the case with NaCl):

$$\Delta V_{st} = \sigma e / C_{st} \tag{3.7}$$

where C_{st} is the Stern capacity and *e* is the elementary charge. Previous studies using GCS models have assumed a constant Stern capacity around 0.2 F/m^2. [**biesheuvel2009dynamicadsorptionmo** 145]

Assuming a symmetric cell configuration, the diffuse and Stern layer potentials can be summed and then doubled to provide the total voltage ΔV_{cell} through the cell:

$$\Delta V_{cell} = 2V_T(\Delta V_{st} + \Delta V_D) \tag{3.8}$$

For CDI cycles, thermodynamic energy efficiency (TEE) is the ratio of the Gibbs energy of mixing ΔG_{mix} to the input cycle work W_{cycle}[146, 147], measured by $\oint$ V dσ. To equate units with the Gibbs energy of mixing, σ is represented as a volumetric-based charge after

dividing by 2x the pore length L_e. For any generic separations process, the Gibbs energy of mixing is defined as [148]:

$$\Delta G_{mix} = nRT\Big[\frac{C_0}{\alpha} ln\Big(\frac{C_0 - \alpha C_{min}}{C_0(1-\alpha)}\Big) - C_{min} ln\Big(\frac{C_0 - \alpha C_{min}}{C_{min}(1-\alpha)}\Big)\Big] \tag{3.9}$$

$$\eta_{TEE} = \frac{\Delta G_{mix}}{W_{cycle}} \tag{3.10}$$

where n is the van't Hoff Factor, which for $1:1$ electrolytes assumes a value of 2. Thus, taking relevant limits, mixing energy should maximize when C_{min} is lowest and when α is highest.

In the case of Carnot analog cycle, the GCS theory imposes constraints on the allowable values for α and C_{min} (Figure A.1). These limitations occur in the recharging stage, in order to maintain the constant number of ions condition. The limit varies with the chosen feed concentration, water recovery ratio, and maximum allowable voltage. As a result, recovery ratios above the allowable range are not computed. Detail on how this limit was found is included in Supporting Information.

Chemical exergy of a feed can be calculated using electrolytic solution models (which use feed concentration references as seawater), or Szargut models (which use lithosphere as the reference). In an ideal mixture, molar chemical exergy can be calculated as a function of concentration of water as well as the salt solution:

$$e_{sol}^{Ch} = \sum_i x_i e_i^{Ch} + RT \sum_i x_i ln x_i \tag{3.11}$$

where x_i is the mole fraction of the species considered, and e^{Ch} is standard molar chemical exergy of this species. Here, the Szargut model for exergy calculation reduces to only considering the activities and molar concentrations of H_2O and NaCl:

$$B_{ch}^{s} = n_{H_2O} e_{H_2O} + n_{NaCl} e_{NaCl} + RT(n_{H_2O} ln(a_{H_2O}) + n_{NaCl} ln(m_{NaCl}\gamma_{NaCl})) \tag{3.12}$$

where n_i represents the molar concentration of each species, m_{NaCl} is the molality of NaCl solution (in mol/kg of solvent) and activity coefficients are given as a_{H_2O} for H_2O and γ_{NaCl} for NaCl[50]. Changes in chemical exergy will be accounted for during both the charging and discharging stages. Exergy will be evaluated using the Szargut model[149], while activity coefficients will be evaluated using the Pitzer model[150]. This is discussed in further detail in the Appendix (also see Figure A.2 for comparative plots of chemical exergy changes at varying concentrations).

Exergy efficiency (here referred to as ExE) is determined as the ratio of the chemical exergy change during charging and discharging, to the input electrical exergy B_{el}, which we take as the equivalent of the input work (W_{cycle}):

$$\eta_{ExE} = \Delta B_{ch}/\Delta B_{el} = \Delta B_{ch}/W_{cycle} \tag{3.13}$$

3.3 Results and Discussion

3.3.1 Impact of capacitive desalination cycle

Differences in the energetics of a complete capacitive deionization cycle is indicated by a change in the area of a V-σ or μ-N diagram. The larger the area represents a cycle with greater energy consumption (Figure 3.1e and f). Experimentalists are able to easily evaluate V-σ diagrams through extrapolating experimental voltage and current (charge) data, whereas in practice μ-N diagrams cannot be measured as easily since the total number of ions in the cell cannot be precisely determined. However, from the differential form of the Helmholtz free energy (dF=μdN+Vdσ), one can easily see that for a complete thermodynamic cycle where a system returns to the initial state (no net change in energy dF=0), the two integrals are equal in magnitude and opposite in sign (μdN=-Vdσ). Therefore, both profiles are effective for evaluating total energy consumed during a capacitive deionization cycle (Figure A.3).

By fixing the initial and final conditions (C_{feed}=20 mM, V_{max}=1.2 V, and C_{min}=1 mM),

of a desalination cycle, the measured energy consumption can be normalized per the same number of ions removed, independent of the cycle trajectory (thermodynamic cycle). Here, the fixed conditions equate to a desalination test with 75% salt removal and 50% water recovery (conditions commonly employed by experimentalists). For these conditions, the energy or area of both the V-σ (Figure 3.2a) and μ-N (Figure 3.2b) graphs was slightly greater for the Carnot analog than for the conventional operation. For this scenario, the energy consumed was 0.96 kWh/m^3 (93 kT/ion) for the Carnot cycle, whereas only 0.48 kWh/m^3 (47 kT/ion) was consumed through the conventional operation.

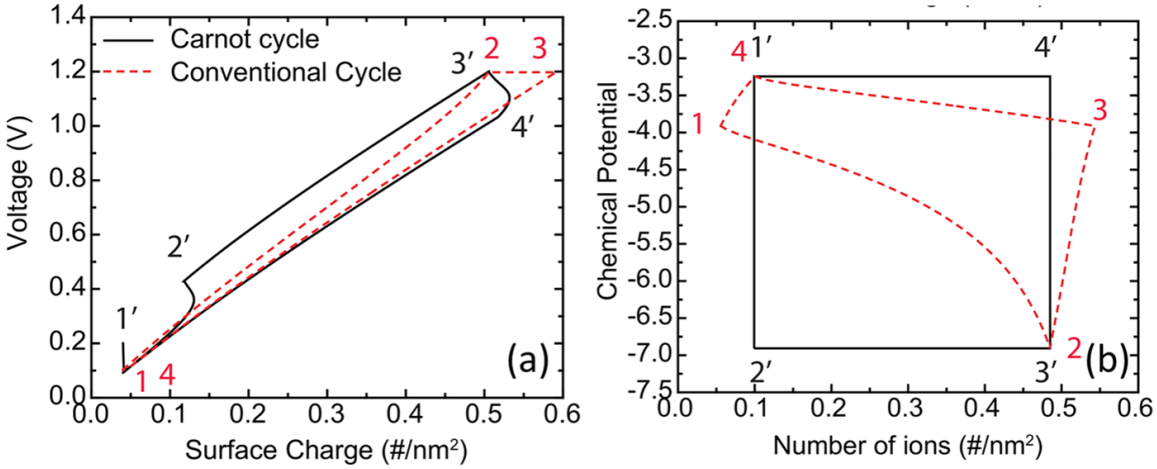

Figure 3.2: (a and b) N-μ and I-V capacitive deionization desalination cycles represented by a V-σ, and μ-N diagrams. Numbers represent each process within the desalination cycle. For both cycles the C_{feed} used is 20 mM, with a C_{min} of 1 mM and α = 0.5.

The greater energy consumed during the complete cycle can be attributed to either increased energy consumption during charging, or to a reduction in energy recovery during discharging. For the individual deionization process (not the entire cycle) the energy is indicated by the area under the 1-2-3 curve and 1'-2'-3' on Figure 3.2. This energy for ion removal is 8.7 kWh/m^3 for the conventional operation and 7.9 kWh/m^3 for the Carnot analog. Thus, the Carnot analog did consume less energy during the deionization process than when the cycle had operated conventionally, indicating that adsorption is indeed more ideal, albeit small. Thus the reduction in cycle energy consumption is due to the conventional operation recovering a larger portion of that energy. The corresponding thermodynamic efficiency for the conventional operation and Carnot analog was TEE=3.6% and TEE=1.8%. The thermodynamic efficiency appears low, but this is in line with other reported values[138, 139, 133, 137]. As the cycles studied here operate without transient or geometric considerations, we are limited in the full range of explorable design parameters. Employing these additional capabilities while tending to optimal operating conditions can allow for an increase in efficiencies [140].

3.3.2 Impact of feed water concentration

To evaluate the effect of the various boundary conditions, the TEE was measured for both the Carnot analog and the conventional operation as the water recovery (α) and percent of salt removed ($\Delta C/C_{feed}$) was varied (Figure 3.3). In all tests, the starting concentration C_0 remained fixed at either 20 mM or 100 mM, maximum cell voltage V_{max} was constrained to 1.2 V, and minimum cell voltage V_{min} was 0.1 V. With the 20 mM feed, increasing the percent of salt removed, and water recovery resulted in a greater TEE irregardless of cycle (Figure 3.3a and b). The TEE again was on average two times greater for the conventional operation than for the Carnot cycle, but never exceeded 4%. While the percent of salt removal had a significant effect on the apparent maximum thermodynamic efficiency, the water recovery did not. Increasing the water recovery (α) from 25% to 75% only increased

the TEE by 0.5% for the conventional operation, and 2% for the Carnot cycle. The increase observed at higher salt removal is due to a greater Gibbs energy of mixing needed for the cycle, which grows faster than the required cycle work.

When the feed increased from 20 mM to 100 mM, the TEE increased by nearly four times. With the Carnot cycle, the constant number of ions criteria could not be maintained at high percent salt removal or higher concentrations. To overcome this model limitation, additional boundary conditions with respect to the minimum concentration and water recovery were placed on each simulation, taking into account the input voltage (discussed in greater detail in Appendix; see Figure A.1 and A.4). It should also be noted that most CDI systems do not operate with 100 mM salt solutions, as the limited available surface area would likely result in salt removal of only 1% to 50% depending on the size of the system. However, the aim in investigating these conditions was to evaluate the thermodynamics of the separations process, as there is a greater amount of thermodynamic separations data available at higher concentrations. Furthermore, with the development of CDI with unlimited surface area (e.g. flow electrodes), capacitive deionization technologies are beginning to evaluate more concentrated saline solutions[151, 152].

With 100 mM feed solutions, the TEE increases substantially from only 5% at 20 mM to 20% at 100 mM (Figure 3.3c and d). In addition to the increase in efficiency, the Carnot analog achieves higher TEE at corresponding salt removal rates and water recovery. This is because for this concentration range, the Carnot cycle operates at nearly optimal conditions. The higher conditions allow for the minimum cell charge to approach zero during discharge (with the constant number of ions criteria), which substantially reduces the total cycle work consumed. At higher concentration ranges ($\geq$ 100 mM), the theoretical efficiency even begins to approach 100% (Figure 3.4a). The conventional operating cycle, on the other hand, achieves maximum efficiencies of around 5-10% (Figure 3.4b).

The effect of feed water concentration (Figure A.5), shows that there is a sharp increase in the TEE for the Carnot analog if high water recovery is possible, with TEE approaching

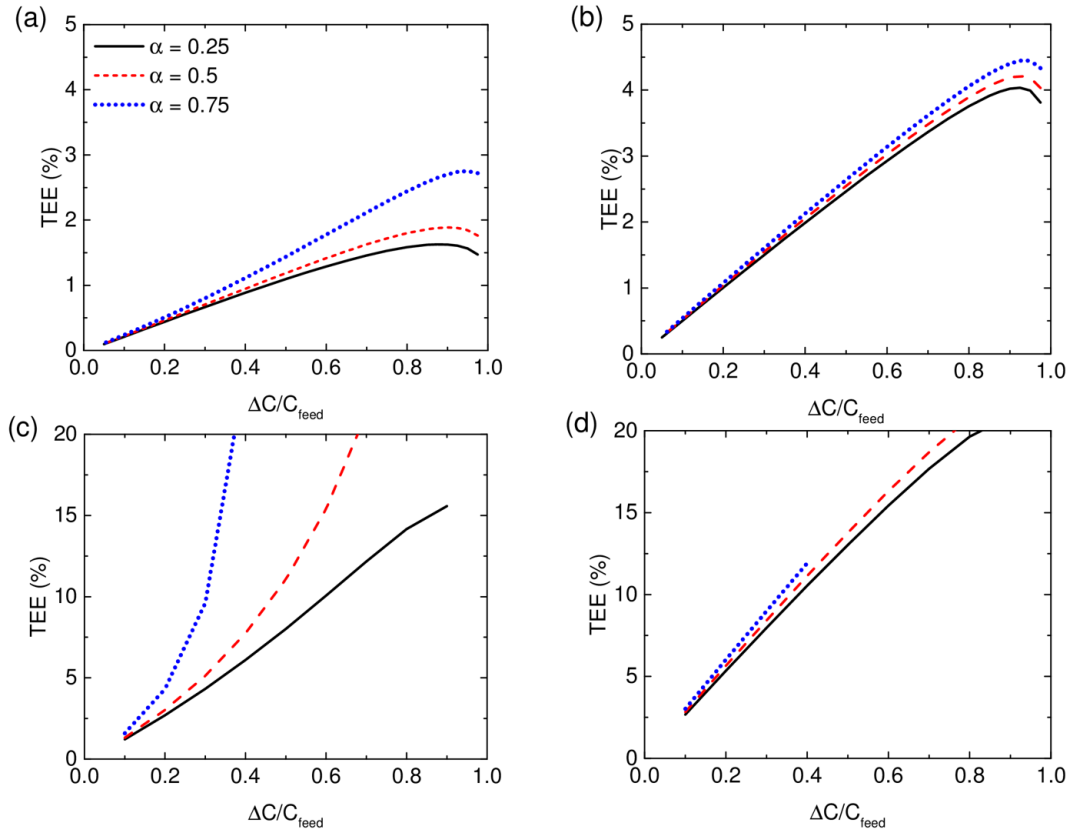

Figure 3.3: Evaluation of thermodynamic energy efficiency with C_{feed}= 20 mM feed (a) Carnot analog, and (b) conventional mode. Efficiency measured with C_{feed}= 100 mM feed (c) Carnot analog and (d) conventional mode cycle.

30%. Unlike the Carnot analog (Figure A.5a), the conventional operation does not show a dependence on water recovery (Figure A.5b). The stronger dependence for the Carnot analog is an indicator that the cycle is approaching its near-ideal limiting case at a higher concentration. Thus, moving to even higher salinity feed streams would increase the theoretical limit to above 50% which is in line with observed TEE found in most state-of-the-art membrane-based technologies. At higher concentration, it also becomes apparent that the Carnot analog and conventional electrosorption process differ. With the same concentration limits, the Carnot analog exceeds the traditional cycle's efficiency of ≈15% by over 2x.

For the cycle limits established, the effect on charge over the various concentrations

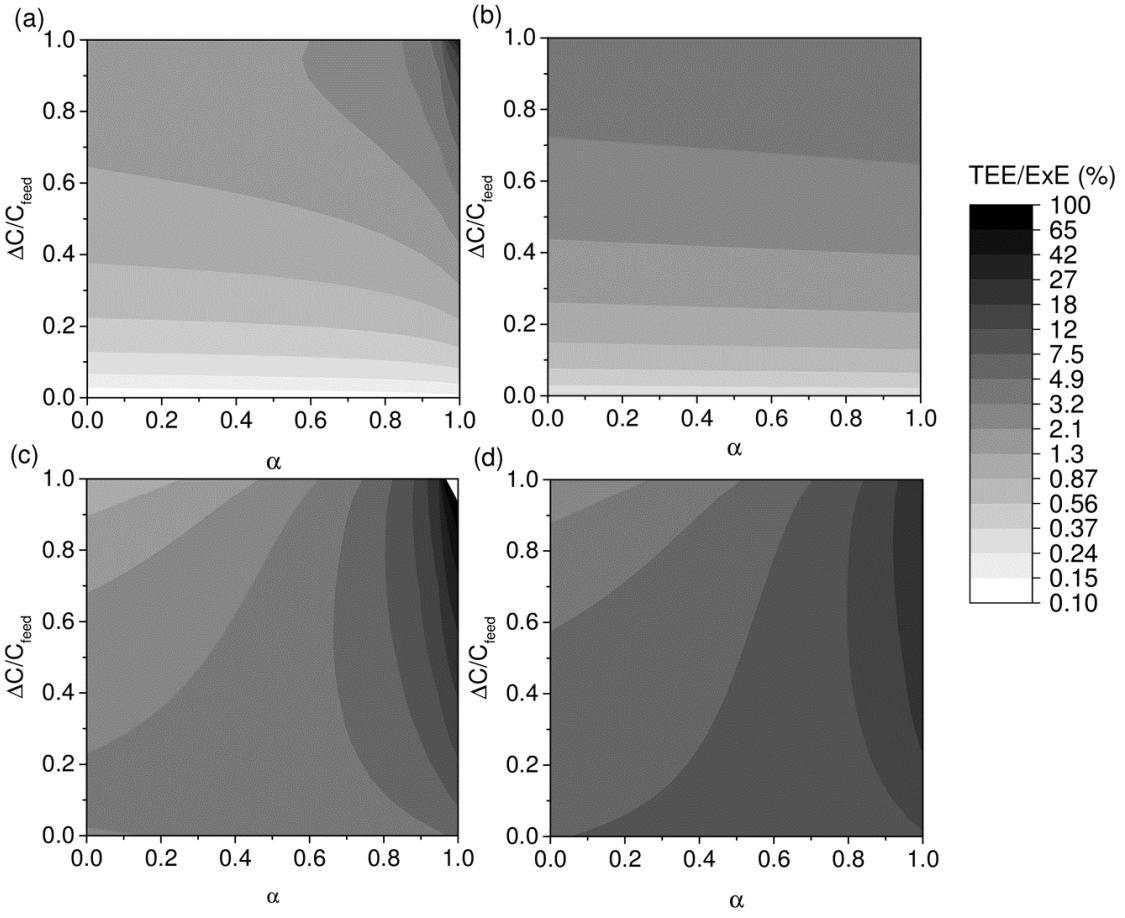

Figure 3.4: Contour plots of thermodynamic energy efficiency (TEE) and exergetic efficiency (ExE) as a function of water recovery ratio α and salt removal ratio $\Delta C/C_{feed}$. In all cases shown here C_{feed} = 20 mM. (a) TEE, Carnot analog cycle, (b) TEE, conventional mode cycle, (c) ExE, Carnot analog cycle, (d) ExE, conventional mode cycle.

was also examined. Charge for the surface, crossover, and total excess charge are nearly the same magnitude in all cases (Figure A.6). As a result, efficiencies are not affected by charge, but rather by deviations within these values during cycling which change the work required to operate (See Figure 3.1b).

3.3.3 Exergetic efficiency of capacitive deionization cycles

Similar to TEE, exergetic efficiency (ExE) for the conventional cycle exceeded those of the Carnot analog using the baseline conditions (C_{feed}=20 mM, C_{min}=1 mM, V_{cell}=1.2 V, α=50%). ExE also generally increased with salt removal at high and low water recoveries,

for both the conventional cycle and the Carnot analog (Figure A.7). For this nominal test case, the maximum value for ExE observed was 12%, at a nearly 80% salt removal for the conventional cycle (Figure A.7b). This is comparable to the maximum values observed in prior studies on MCDI [50, 61]. As this study was computational and assumed to run infinitely slow, additional exergy losses that did not need to be considered for this study (i.e. pumps) would need to be accounted for in experiments, and would lower exergetic performance. However in both cycles, the ExE (Figure 3.4c and d) efficiency increased with an increase in water recovery and generally with increased salt removed. Furthermore, theoretical ExE values approached 100% for the Carnot cycle and 30% for the conventional operation mode.

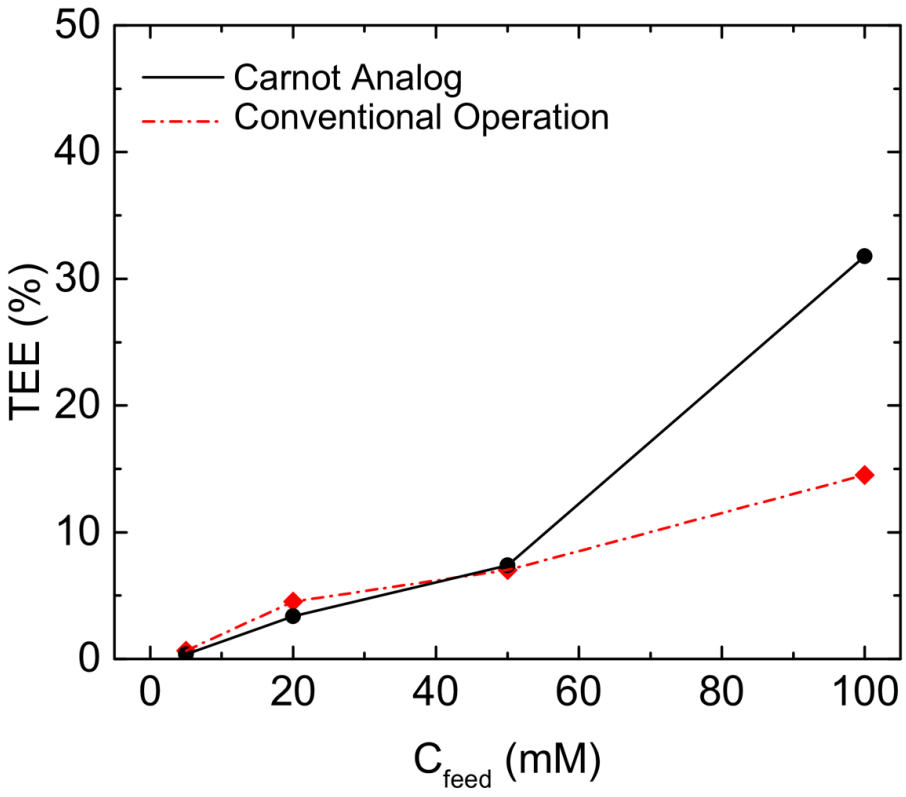

Figure 3.5: Reported values of thermodynamic efficiency (TEE) from various prior studies. The dashed lines indicate the trends determined from this work, for both types of cycles analyzed. Evaluation of thermodynamic energy efficiency (TEE) at varying initial feed concentrations for a diluate value of C_d = 5 mM and water recovery α = 0.5.

3.4 Conclusions

Various system properties and processes contribute to the observed thermodynamic and exergetic efficiency of a capacitive deionization cycle. Here, we evaluate two deionization cycles. One mimics an executable approach whereby ion removal occurs during charging with constant voltage switching, the other is a Carnot analog cycle where ion removal occurs while maintaining a constant number of ions. Under low saline conditions the energetics associated with voltage regulated electroadsorption were slightly more favorable, and resulted in predicted thermodynamic efficiencies that approach 2-5%. However, when feed solutions were increased to 100 mM the energetics of constant N electroadsorption was favored over the conventional approach, and the maximum thermodynamic efficiencies approached 37% (Figure 3.5). In all simulations, thermodynamic efficiencies improved as C_{feed}, and ΔC (C_{feed}–C_{min}) increased. A survey of experimental capacitive deionization system performance will reveal that actual desalination performance data is far below these values ($\leq$ 1 %) for CDI and ($\leq$ 3%) for membrane CDI. However, this is due to the low effective surface area available in lab scale systems, which limit the operation to low C_{feed}, ΔC, and only 50% water recovery. As experimentalists begin to further explore the CDI operational space, increased TEE may be observed. Interestingly, this is similar to trends observed with thermal heat engines, whereby increasing the T_0 and maximizing ΔT results in higher thermodynamic efficiencies, due to an increase in the theoretical Carnot limit. When evaluating the CDI TEE to a Carnot analog, at low feed concentrations, the actual cycle performs similarly to that of a Carnot analog. This indicates that while efficiencies are low, limitations may exist which prevent substantial improvements. However, efficiency improvements are increased if the feed stream concentration increases.

CHAPTER 4
USING THERMODYNAMICS PRINCIPLES TO OPTIMIZE PERFORMANCE OF CAPACITIVE MIXING CYCLES FOR SALINITY GRADIENT ENERGY GENERATION

4.1 Abstract

Understanding the thermodynamics associated with ion mixing and separation processes is important in order to meet the rising demands for clean energy and water production. Several electrochemical-based technologies such as capacitive deionization (CDI) and capacitive mixing (CapMix) are capable of achieving desalination and energy production through ion mixing and separation processes, yet experimental investigations suggest energy conversion occurs with low thermodynamic efficiency. Here, we explore the maximum attainable efficiency for several different CapMix cycles. All investigated cycles are analogous to well documented heat engine cycles. In order to analyze CapMix cycles, we develop a physics-based model of the electric double layer based on the Gouy-Chapman-Stern theory. Evaluating CapMix cycles for energy generation revealed that cycles where ion mixing occurs at constant concentration and switching occurs at constant charge (a cycle analogous to the Stirling engine) attained the highest overall electrical energy efficiency (39%). This electrical energy efficiency is nearly 300% greater than the electrical energy efficiency of the Otto, Diesel, Brayton, and Atkinson analog cycles where ion mixing occurs while maintaining a constant number of ions. Additionally, the maximum chemical to electrical energy efficiency was 89% with a maximum work output of 0.5 kWh per m^3 of solution mixed (V=1.0V) using this same Stirling cycle. Here the salinity gradient was C_H=600 mM and C_L= 1 mM, the minimum dilute value evaluated (ΔG_{mix}=0.56 kWh/m^3). The effect of voltage was also examined at C_H = 600 mM (seawater) and C_L = 20 mM

(river water). CapMix cycles operated at lower voltage (V<1.0V), resulted in an increase in electrical energy efficiency to about 25%; however, this was at the expense of a reduction (50x) in net electrical energy extracted from the same mixing process (0.01 kWh per m^3). In addition, the chemical to electrical energy efficiency reduced to 2%.

4.2 Introduction

The increasing electrification of energy and water systems promotes investigations on technologies, which convert energy directly into electricity. This is in contrast with most modern energy systems (heat engines), where power production occurs through converting thermal energy into mechanical energy prior to electricity generation (Figure 4.1a) [75]. While effective, the numerous conversion processes promote excess loss. In addition, the maximum obtainable efficiency is limited by the temperature of a thermal reservoir (Carnot limitation). Another well-documented limitation with power generation systems is that they produce a significant amount of carbon emissions. This promotes the development of higher efficiency energy systems, which convert chemical energy directly to electricity. Chemical to electrical energy conversion processes occur primarily using electrochemical-based technologies, and extract work based on the flow of ions (Figure 4.1b). Various approaches exist; however, capacitive-based technologies have emerged as a potential low cost approach for generating energy through ion mixing processes. In CapMix energy is generated through reversibly storing and releasing ions within an electric double layer (EDL) at a high surface area charged electrode [141, 83]. Controlled ion mixing occurs through charging the electrodes in a high concentration stream (C_H), and discharging the electrodes in a second low concentration stream (C_L). In a low concentration stream, the diffuse portion of the EDL expands, resulting in a reduction in electrode capacitance. As a result, there is net electrical energy generation over the cycle (Figure 4.1).

Experimental investigations of CapMix have only investigated one cycle. The CapMix cycle occurs using four processes. In process 1-2, electrodes are charged (constant voltage)

in the C_H solution (e.g. constant concentration). In process 2-3, a C_L solution replaces the C_H solution (constant). In process 3-4, the electrodes are discharged (constant-voltage). Finally, in process 4-1, the C_L solution is replaced by the C_H (constant charge) (Figure 4.1) [84, 82, 135, 85, 86, 142, 66, 153]. Here we will theoretically examine the operations of CapMix for ion mixing using thermodynamic principles. While previous investigations have focused on exploring the thermodynamic limits associated with Carnot and Stirling-based analog cycles, we aim to extend this to investigate Otto, Diesel, Brayton, Atkinson, and Ericsson analogs [84]. Fundamentally, we will seek to explore the effect operational modes have on maximizing efficiency and work output from CapMix cycles.

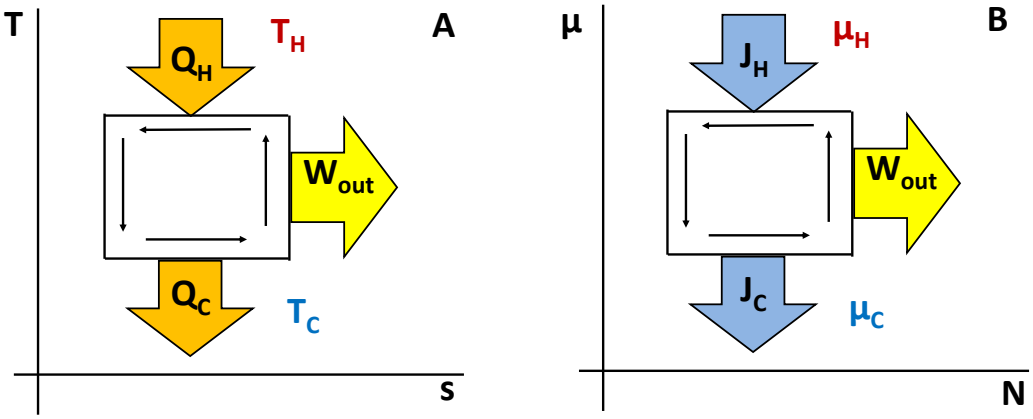

Figure 4.1: (a) Thermodynamic heat engine cycle, (b) Blue engine cycle.

4.3 Methodology

Most theoretical heat engine analyses evaluate energy production through cycles comprised of four processes. Often these processes take place while keeping system properties constant. For instance, processes take place under isothermal (iso-T), isentropic (iso-s), isochoric (iso-V), and isobaric (iso-P) conditions where T, s, V, and P refer to temperature, entropy, volume and pressure. When considering electrochemical properties, instead of evaluating T, s, V and P, we evaluate the four analogous properties: chemical potential μ,

number of ions N, charge σ, and voltage V_{cell} [83]. Consequently, here we will be interested in evaluating processes that take place under iso-μ, iso-N, iso-σ, and iso-V_{cell} conditions. Since the thermal analog for voltage is the negative of pressure, this indicates that a mixing cycle will operate in the counterclockwise direction when viewed on a V_{cell}-σ diagram [84, 82, 154].

The chemical potential μ varies as a function of both concentration and temperature, which in this study is determined using

$$\mu = k_B T ln(\frac{C}{C_{ref}}) \tag{4.1}$$

where k_B is Boltzmanns constant and C_{ref} is a reference temperature to the environment, here taken as 1 M [84]. Here, since all simulations take place under standard conditions (temperature and pressure), all constant chemical potential processes are also constant concentration processes. The total number of ions in the cell (per electrode area), N, is

$$N = \Gamma + C L_e N_{av} \tag{4.2}$$

where N_{av} is Avogadros constant, L_e represents the pore length between carbon particles (pore volume/pore area), taken in this study as 4 nm, and Γ is the excess surface charge. Γ is determined as a function of both the electrode surface charge σ and additional crossover charge σ

$$\Gamma = \sqrt{\sigma^2 + \sigma^{*2}} - \sigma^* \tag{4.3}$$

$$\sigma^* = \frac{1}{2\pi \lambda_B \lambda_D} \tag{4.4}$$

where the Debye and Bjerrum lengths for the electrolyte, λ_B and λ_D, determine the crossover charge σ* [84]. Crossover charge is defined as the charge at which attractive

forces from counter ions and repulsive forces from co-ions are balanced [143]. When crossover charge exceeds surface charge, the increase in counter ions exceeds the decrease in concentration of co-ions, resulting in a net increase in number of ions adsorbed [144]. As surface charge decreases, Γ becomes directly proportional to σ. The diffuse layer voltage difference Δ V_D is

$$\Delta V_D = 2V_T sinh^{-1}\Big(\sigma\sqrt{\frac{\pi\lambda_B}{2C_{feed}N_{av}}}\Big) \tag{4.5}$$

with thermal voltage V_T defined as V_T = RT/F, where F is Faradays constant. For the Stern layer voltage ΔV_{st}, the Gauss‘ law is used for a 1:1 electrolyte (as in the case with NaCl):

$$\Delta V_{st} = \sigma e / C_{st} \tag{4.6}$$

where C_{st} is the Stern capacity and e is the elementary charge. For C_{st}, we will use values from previous studies with Gouy-Chapman-Stern models which have assumed a constant Stern capacity around 0.08 F/m_2 [155, 156]. Assuming a symmetric cell configuration, summing and doubling the Stern and diffuse layer potentials yields the total voltage through the cell V_{cell}

$$\Delta V_{cell} = 2V_T(\Delta V_{st} + \Delta V_D) \tag{4.7}$$

The interdependence of the four properties (μ, N, σ, V_{cell}) to one another are most clearly displayed on a μ-N or V_{cell}-σ diagram which is analogous to a T-s and P-V-based diagrams commonly used to evaluate thermal-based processes (Figure 4.2a and b). T-s diagrams contain lines of constant pressure (isobars), and P-V diagram contains lines of constant temperature (isotherms). Here, we plot both lines of constant charge (iso-σ) and voltage (iso-V_{cell}) on the V_{cell}- σ diagram, and lines of constant concentration (iso-C) and number of ions (iso-N) on the μ-N diagram. The iso-V_{cell} and iso-σ lines are nearly identi-

cal (black and blue dashed lines), and at lower concentrations begin to align with an iso-N processes (vertical line) (Figure 4.2a). At low concentrations (e.g. C $<$ 100 mM), the area of a Carnot cycle, which represents work output, does not change substantially. As a reminder, the Carnot cycle for blue energy systems employs two iso-σ (charge/discharge) processes (process 1-2 and 3-4), and two iso-N switching processes (process 2-3 and 4-1) (Figure 4.1). The chemical potential μ is nondimensionalized by dividing it by room temperature (T = 298 K) and Boltzmanns constant (Figure 4.2). When the concentration is large (C$>$100 mM), N grows exponentially with respect to chemical potential. This allows for an increase in the area of the Carnot cycle, and highlights the benefits of operating a cycle under Carnot-like conditions[86, 66, 154].

For CapMix, we will simulate various combinations of iso-σ,V_{cell},μ,N processes at a range of salinity gradients (e.g. ΔC) and aim to evaluate the efficiency by which chemical mixing energy is converted to electrical energy. The cycle efficiency is defined here as the energy efficiency η_E. η_E is defined as the net cycle work output $E_{net} = \oint V_{cell} d\sigma$ to the input work E_{in} consumed during the charging stage only:

$$\eta_E = \frac{E_{net}}{E_{in}} \tag{4.8}$$

We verify the appropriate energy balance during the cycle by considering not only the electrical work gained or lost during each process, but also the change in free (chemical) energy, given as μdN. Over the entire cycle, the integrals μdN and Vdσ should sum to 0, indicating appropriate energy balance is reached [84]. To evaluate effectiveness of ions exchanged within the cell, we will compare the net output work E_{net} to the maximum range of the number of ions during the cycle:

$$W'_N = \frac{E_{net}}{\Delta N} \tag{4.9}$$

where Δ N represents the range between the maximum and minimum number of ions

values obtained during the cycle. We will also evaluate the thermodynamic efficiency η_{th} for the CapMix process by comparing the net cycle work to the maximum obtainable energy from the mixing:

$$\Delta G_{mix,CM} = -2RT\Big(\frac{C_{avg}}{\phi} ln(x_{avg}) - (C_{min}) ln(x_{min}) - \frac{1-\phi}{\phi} C_{max} ln(x_{max})\Big) \quad (4.10)$$

where ϕ is the volume fraction of low concentration water that is used during the CapMix process. The mole fractions x_M, x_L, and x_H all correspond to the concentrations of salt in the solution divided by the molar concentration of water or 55.5 M. In this study we will always assume this value as ϕ = 0.5, meaning that the same amount of water is mixed during both of the switching stages. We will also assume activity coefficients as unity values as an additional simplification. Then, the second law efficiency η_{th} is given as:

$$\eta_{th} = \frac{E_{net}}{\Delta G_{mix}} \quad (4.11)$$

Stages with a constant number of ions are analogous to isentropic process in thermodynamics, or, in the case of reversible cycles, also analogous to adiabatic (no heat transfer) processes. To develop fully reversible cycles, we will run the cycles under infinitely slow conditions by linearly scaling a chosen parameter during each process from the initial state to the desired value at the next state (e.g. maximum voltage or minimum concentration). This is traditionally done for thermodynamic processes to eliminate irreversibilities due to transients [75]. We will develop analogies for seven thermodynamic cycles: Otto, Diesel, Brayton, Atkinson, Ericsson, Stirling, and Carnot. We provide the analog thermodynamic properties for each cycle (Table 1). In the CapMix process 1-2 the cycle is charged using a iso-μ (Ericsson, Stirling, Carnot cycles) or iso-N (Otto, Diesel, Brayton, Atkinson cycles) process, until Vmax (Vmax= 1 V). Next in Process 2-3, switching from C_H to C_L occurs at iso-V (Diesel, Brayton, Atkinson, Ericsson), iso-σ (Otto, Diesel, Stirling. Atkinson),

or iso-N (Carnot). If voltage is not constant, the cell voltage can increase during Process 2-3. Hence, a cutoff voltage for process 2-3 was set as 1.0 V. In process 3-4 the cycle is discharged through a iso-μ (Ericsson, Stirling, Carnot cycles) or a iso-N (Otto, Diesel, Brayton, Atkinson cycles) process until the minimum voltage V_{min} (V_{min}=0.1 V). The cell concentration will gradually increase during this discharging stage. Finally, in Process 4-1, switching from CL back to CH occurs at iso-V (Diesel, Brayton, Atkinson, Ericsson), iso-σ (Otto, Diesel, Stirling, Atkinson), or iso-N (Carnot). We will evaluate and compare the performance dependence of each of the cycles (Table 4.1) as a function of ranges in concentration ($\Delta C = C_H - C_L$) and voltage ($\Delta V = V_{max} - V_{min}$).

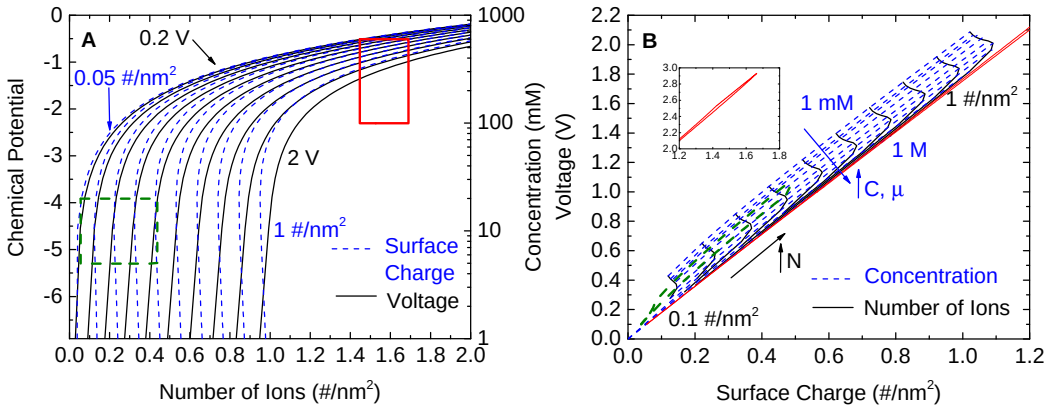

Figure 4.2: (a) -N diagram with Iso-μ and iso-N lines. (b) V_{cell}- σ diagram with iso-N and iso-C lines. Red solid and green dashed box designate Carnot cycle at high concentration (red solid) and low concentration (green dashed).

Table 4.1: Equivalent constant cycling conditions for thermodynamic and blue energy harvesting.

Cycle	Constant Terms (Thermodynamic)	Constant Terms (Electrochemical)
Otto	S,V	N,σ
Diesel	S, V (low T), P (high T)	N, σ (low μ), V_{cell} (high μ)
Brayton	S, P	N, V_{cell}
Atkinson	S, P (low T), V (high T)	N, V_{cell} (low μ), σ (high μ)
Ericsson	T, P	μ, V_{cell}
Stirling	T, V	μ, σ
Carnot	T, S	μ, N

4.4 Results and Discussion

For all CapMix cycles, increasing the ΔC resulted in a clear increase in the net work (Figure 4.3a and b). With C_H = 600 mM the maximum extracted work ranged from an average 0.01 - 0.2kWh per m^3 depending on the choice of C_L=1-500mM (Figure 4.3a)), averaged over all of the different cycles. With C_H = 1 M the maximum extracted work increased slightly to 0.03 - 0.3 kWh per m_3 for C_L=1-900 mM (Figure 4.3b), again averaged per the type of cycle. This increase in extracted work is due to an increase in available energy released due to mixing (G_{mix}). For instance the theoretical energy released from mixing C_H=600 mM with C_L=100mM (ΔC=500 mM) is 0.27 kWh per m^3, whereas the theoretical energy released from mixing C_H=1M with C_L=500 mM (ΔC=500 mM) is 0.1 kWh per m^3 (Figure 4.3b).

As $\Delta C \rightarrow C_H$, iso-μ charge/discharge (Process 1-2 and 3-4) employed in the Ericsson, Stirling and Carnot cycles are more advantageous for work output than charge/discharge processes which take place under iso-N conditions (Otto, Diesel, Brayton, Atkinson). This is due to the large hysteresis (separation) between charge and discharge profiles attainable with the iso-μ process when compared to profiles projected with iso-N processes. Large hysteresis results in a larger area as projected on a Vcell-σ or μ-N diagram (Figure 4.3a and b). With C_H = 600 mM and ΔC=599 mM, this maximum extracted work (e.g. area of cycle curve) is 0.49 kWh/m^3 for the Stirling cycle. This was followed by 0.42 kWh/m^3 for the Ericsson cycle, 0.18 kWh/m^3 for the Carnot cycle and Otto cycle, 0.22 kWh/m^3 Diesel, 0.17kWh/m^3 Brayton, and 0.08 kWh/m^3 Atkinson cycles (Figure 4.4a). When a brine solution is considered for high concentration, a slight increase in the work output is observed, but the trends remain intact (Figure 4.3b). Net work outputs are (in kWh/m^3): 0.51 (Stirling), 0.43 (Ericsson), 0.16 (Carnot), 0.19 (Otto), 0.18 (Brayton), 0.23 (Diesel), 0.10 (Atkinson).

That the Carnot cycle did not result in the greatest net work output is counterintuitive,

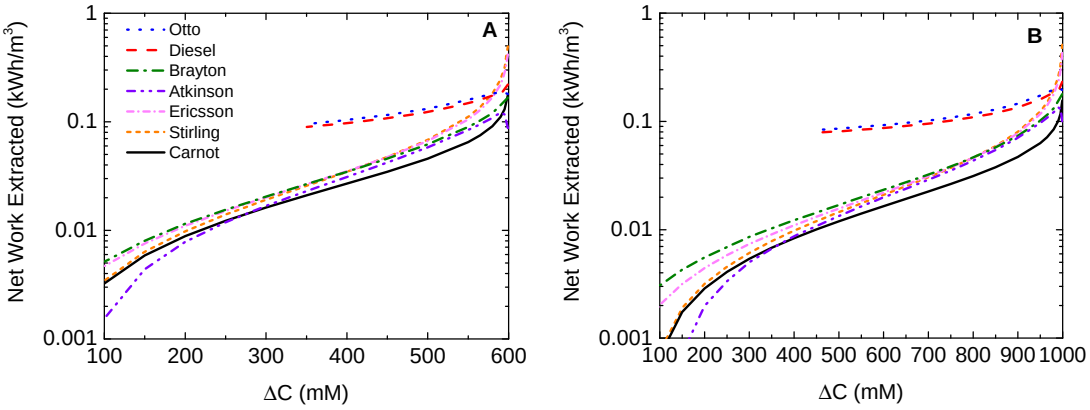

Figure 4.3: Net cycle work as a function of the range C between the maximum concentration C_H and minimum concentration C_L (a) C_H = 600 mM, (b) C_H = 1 M.

as the Carnot cycle is typically the most efficient thermodynamic cycle for heat engines. The lower Carnot cycle performance is attributed to the trajectory of a iso-N process with respect to V_{cell} (Figure 4.3b). During an iso-N switching stage (process 2-3 and 4-1), the cell voltage continues to rise until the maximum voltage occurs (a fixed boundary condition). Upon reaching the maximum voltage, in order to maintain the constant N, the charge must decrease (Eq. 4.2). As a result, the charge in the cell is lower for the Carnot cycle at the beginning of the discharge process than it is for the Stirling cycle. This results in less energy recovery during Process 3-4. Additionally, after discharge, the iso-N line limits the minimum voltage that the cell can achieve before beginning the next switch stage. As a result, the work extracted during the discharge process reduces when compared to discharging to the constant voltage stage as is done in the Ericsson cycle. By comparison, as ΔC decreases, the difference in net work output between cycles reduces. At most, the cycles differ only by as much as 20% for $\Delta C < 300$ mM.

Evaluating the cycle efficiencies yields similar trends. For the C_H=600 mM, the first law (electrical) efficiency approached a maximum of 38% (Stirling), 31% (Ericsson), 16% (Diesel), 13% (Otto) 10% (Brayton), and 5% (Atkinson) (Figure 4.4a). The efficiencies decrease rapidly when $\Delta C < 400$ mM, which is due to the decreased thermodynamic work

potential obtainable from mixing (ΔG_{mix}). Increasing C_H to 1 M, the maximum efficiencies obtained changed only slightly: 22% (Stirling), 17% (Ericsson), 8% (Otto), 6% (Brayton), 0.1% (Carnot), 9% (Diesel), 3% (Atkinson).

The Stirling cycle outperformed the Ericsson cycle, which we attribute to the fact that constant charging stage does not require any additional input work, and the constant charge, switch process enables higher discharge voltage, improving the net work output. The Carnot cycle stands out as an anomaly again, exhibiting lower efficiency values of 0.3% (Figure 4.4a).

This demonstrates one of the challenges in operating under a constant number of ions as a switching stage. The Stirling and Ericsson cycles also exhibit maximum thermodynamic efficiency (percent of maximum available mixing energy converted to electrical energy). Both approach a maximum thermodynamic efficiency of 80% (C_H=600 mM and ΔC=599 mM), while the Carnot cycle approaches 50% (Figure 4.4b). Thus, each cycle operates irreversibly as all thermodynamic efficiencies remained below 100%. However, as $\Delta C \rightarrow C_H$, the Stirling, Ericsson, and Carnot cycles appear to approach 100%, which would indicate a perfectly reversible system.

With the exception of the Atkinson and Brayton cycles, the second law efficiencies also demonstrate a second maximum when C_L approaches C_H ($\Delta C \rightarrow 0$). This depicts the exponential decline in the ΔG_{mix}, which reduces to zero as the $\Delta C \rightarrow 0$. In this limit despite the second law efficiency approaching 100%, the work output also decreases to a not useful level. Thus, it is theoretically possible through cycle operation to obtain over 50% of the theoretical energy from mixing, despite current technologies that only capture at best 50% of the ΔG_{mix} [157, 158].

For the Otto and Diesel cycles, there is a limit to the minimum ΔC by the Gouy–Chapman–Stern theory; if operating under a constant number of ions, charging the cell to a certain voltage requires some removal of the initial salt concentration to maintain the iso-N condition. Thus, reducing the salt removal any further would not be possible, and would

result in net work outputs larger than the Gibbs energy of mixing (Figure 4.4b).

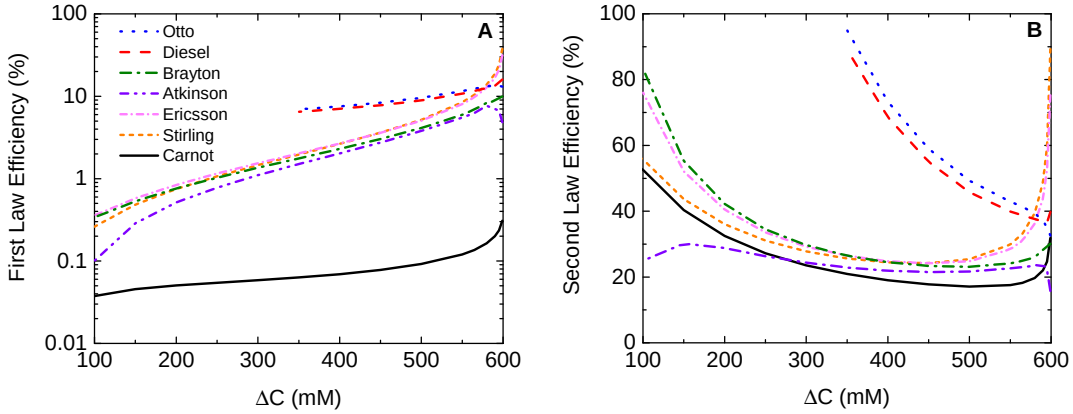

Figure 4.4: Effect of concentration range on efficiency with a seawater concentration (C_H = 600 mM) as the maximum value. (a) first law efficiency, (b) second law efficiency.

The benefits of the Carnot cycle operation are more clearly pronounced when examining the ratio of work output per number of ions exchanged, W‘/ΔN, or effectiveness. When diluting to brackish concentrations (C_H = 600 mM, C_L = 100 mM, ΔC = 500 mM), ΔN varies by 15% when iso-σ or iso-V_{cell} conditions are employed. For most other cycles, this large range in number of ions greatly reduces the W‘/ΔN. As a result, the W‘/ΔN for all non-Carnot cycles only reaches 0.1 $\pm$ 0.05 kWh•nm^2/# •m^3 for C_L = 20 mM and up to 0.2 $\pm$ 0.1 kWh•nm ^{2}/#•m^3 in the limit of low values of C_L. However, when employing iso-μ charging/discharging with iso-N switching, the W/ΔN increases by approximately 10x (from 0.3 to 3.5 kWh•nm^2/#•m^3) for Carnot when compared to all other cycles (Figure 4.5). The second highest value of 0.3 kWh•nm^2/#•m^3 for W/ΔN was obtained by the Stirling cycle. This reaffirms one of the previously cited advantages of the Carnot-like mixing engine. Thus, while the Carnot cycle first law efficiency may have been low from an energy perspective, it displayed more benefits when considering the effective usage of ions within the cell, especially when operating at higher concentration ranges.

One notable feature is that in the Otto and Diesel cycles, the number of ions grows asymptotically as $\Delta C \rightarrow 0$. This is indicative of the limitations (Eq. 4.2). The maximum

voltage set in the cycle inherently requires a minimum number of ions be removed during the charging stage. If the amount removed in this charging stage is close to the desired minimum concentration C_L, then the switching stage is not necessary and the number of ions will subsequently change minimally. This is since the lines for constant charge and voltage are nearly parallel to the constant number of ions lines at low concentrations (Figure 4.2a). Such operations are of minimal interest, as they will not generate energy. Nevertheless, as with the minimum observed for second law efficiency, we make note of this additional unique trait during these cycle operations.

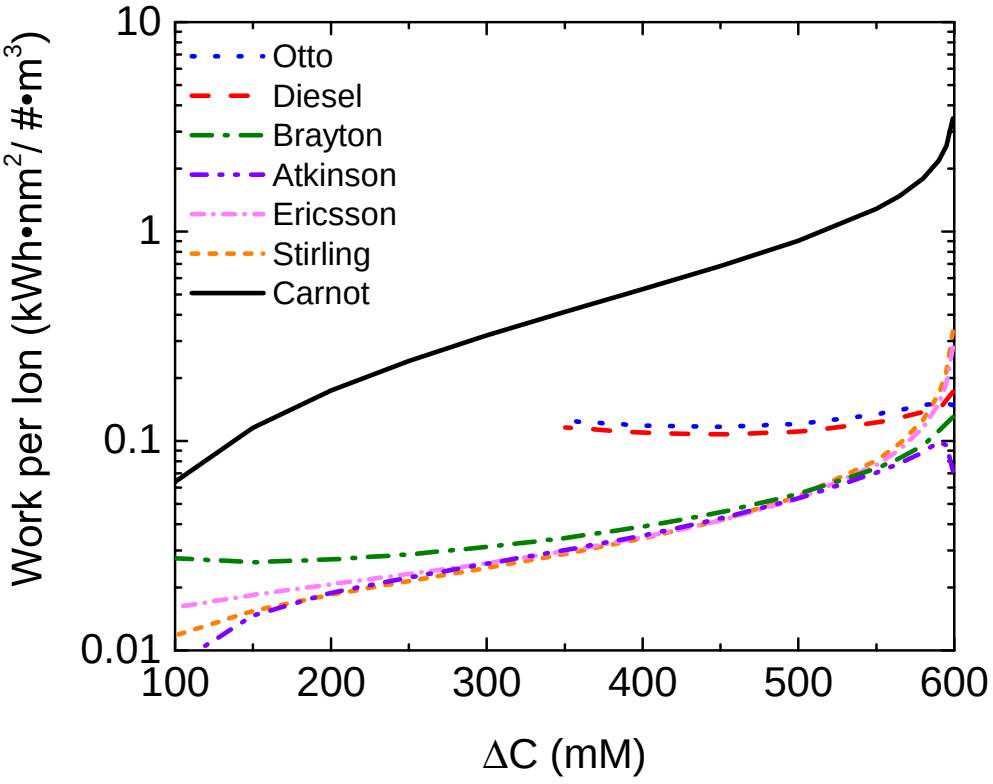

Figure 4.5: Net cycle work per number of ions exchanged as a function of range ΔC between maximum concentration C_H = 600 mM and minimum concentration C_L.

Lastly, we vary the input voltage ratio while maintaining all other appropriate cycle parameters. Since the cycle assumes an infinitely slow operation, C_H, C_L, and ΔC remain fixed at 600 mM, 20 mM and 580 mM. For mixing seawater with river water, the increase

for net work extracted grows proportionally, employing a iso-μ charging/discharging over the range of ΔV simulated (0.1 V $< \Delta$V $<$ 1.1 V).

For all ranges of ΔV the Otto/Stirling $>$ Diesel/Ericsson $\rightarrow$ Brayton/Atkinson $>$ Carnot cycles (Figure 4.6a). This suggests that in addition to higher concentration ranges, the Carnot cycle should operate when considering higher voltage ranges as well. Additionally, at this concentration range selected, a notable benefit in Otto/Diesel cycle operations showed in the lower voltage ranges.

When examining cycle efficiencies as a function of voltage,the lower voltage ranges predominantly demonstrate the highest first law efficiencies. Instead of continuously increasing to 100%, it seems that some of the cycles actually demonstrate clear peak values. For example, the Stirling cycle approaches a maximum of 18% efficiency, but the Ericsson cycles only show a maximum at about 15% at a ΔV of around 0.3 V (Figure 4.6b). The Otto cycle more clearly highlights the benefits of constant charge switching when coupled with a constant number of ions. Its efficiency grows to a maximum of 23%, 5% higher under any other under the same concentration and voltage ranges. Some of the other cycles lower maximum efficiencies of around 0.2 V before beginning to decrease in the limit of ΔV (17% for Diesel cycle, 16% for Atkinson cycle, 15% for Brayton cycle). The Carnot cycle, however, is the only one that increases when consuming more voltage during the charging stage. Despite this, all of the other cycle efficiencies remain at least 2x as large as the maximum Carnot cycle efficiency. Thus, it is possible that tailoring the cycle could enable operations at higher voltages and/or increases in energy efficiency to a point where the Carnot operation could surpass the other cycles.

Since concentration ranges remain the same when sweeping a voltage range, the thermodynamic efficiency is exactly proportional to the net cycle work (Eq. 4.11). Compared to the previous cycles with V_{max} fixed at 1 V (ΔV = 0.9 V), if the voltage range were expanded, it could reach maximum efficiency of over 50% when operating a mixing Stirling engine (Figure 4.6c). A caveat to operating here is that since we only account for cell

voltage after the initial charging stage, the additional 0.1-0.2 V incurred during constant charge switching would push V_{cell} above the operating threshold for electrolysis. While most studies for CapMix have typically operated under lower voltage ranges, this should be considered if the operating range is to be expanded [84, 82].

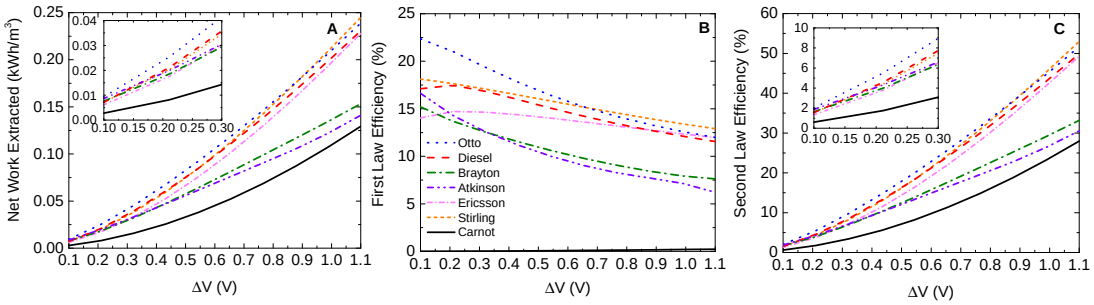

Figure 4.6: Net cycle work as a function of the voltage range ΔV. Effect of varying voltage range ΔV between minimum (initial) cycle voltage at Stage 1 and maximum cycle voltage at Stage 2. (a) Net cycle work, (b) first law efficiency, (c) second law efficiency. C_H = 600 mM, C_L = 20 mM.

4.5 Conclusions

Simulating different operation for CapMix cycles suggested certain ways for optimizing performance. The cycles demonstrated a maximum efficiency and net work output when charging at constant chemical potential (concentration) and constant charging switching (Stirling engine). This maximized the overall recoverable energy (η_{th}= 38%, η_{th} = 89%) while eliminating additional input energy during switching (Net work output = 0.3 kWh/m^3). Benchmark efficiencies for suitable brackish water ranges still yielded work output values from 0.03 0.2 kWh/m^3 (20 mM $< C_L <$ 200 mM). When raising the maximum concentration from a seawater value to a more concentrated solution, energy extracted on average could increase by up to 5%, although the Carnot cycle actually experienced a decrease from this larger concentration range. Overall, the efficiency and work output values for cycles with constant chemical potential charging (analogous to isothermal processes in a heat engine) were significantly higher than the analogous operation of more traditional

thermodynamic cycles in the limit of low concentrations.

While a Carnot-like operation with constant switching mode does not recover energy as effectively (Maximum work output = 0.18 kWh/m^3), its efficiency per number of ions exchanged during cycling is higher (3.3 kWh$nm^2/\#$m^3), over 10x greater than maximum for all other cycles). The increase in work output per number of ions is attributed to the substantial change in the number of ions during an iso-σ or iso-V process. As ΔV $\rightarrow$ 0, the cycles yielded less energy output, but the Otto cycle attained an energy efficiency of 23%, approximately a 25% improvement over the Stirling/Ericsson/Carnot cycles when C_H = 600 mM and C_H = 20 mM. Through thermodynamic principles, we have defined an extensive range of operating conditions and parameters for EDL capacitors. The results obtained provide unique insight into the conditions that cycles should operate at, depending on the desired system criteria (work output, energy efficiency, thermodynamic efficiency). Developing these types of analogies can improve our understanding and performance of a wide range of cyclic energy processes.

CHAPTER 5
EFFICIENCY OF THERMALLY ASSISTED CAPACITIVE MIXING AND DEIONIZATION SYSTEMS

5.1 Abstract

The temperature of an input solution to an environmental technology can vary greatly depending on numerous industrial and environmental factors. For capacitive mixing (CapMix) and deionization (CDI)-based technologies which rely on charge storage within an electric double layer (EDL), this temperature dependence affects energy output and energy consumption. Yet, how temperature-dependent EDL properties impact the thermodynamic efficiency for energy conversion and ion separations is less known. Here, we evaluate how isothermal, non-isothermal and variable temperature profiles impact the thermodynamic efficiency of CDI and CapMix cycles operated under both reversible and irreversible (current dependent) conditions. For CapMix (C_{HC}=600mM, C_{LC}=20 mM, ϕ=50%), reversible system operation resulted in an optimal efficiency of 43% when $T_{HC} \neq T_{LC}$. For CDI (C_{feed}=20mM, $C_{diluate}$=5 mM, α=50%), optimal thermodynamic efficiencies are attained through the use of non-isothermal ($T_{feed} \neq T_{brine}$) or variable temperature operation, and approached 10%. The introduction of current–based irreversibilities (25 mA), however, reduces the maximum attainable CapMix and CDI thermodynamic efficiency to 25% and 3.2% (25 mA).

5.2 Introduction

Capacitive mixing (CapMix) is a technology which generates energy through controlling spontaneous ionic mixing between two solutions (sea and river water). Conversely, capacitive deionization (CDI) is a technology which consumes energy in order to separate ionic

species in a feed stream into two streams (diluate and brine/concentration). Both technologies are electrochemical in nature, and use highly porous supercapacitor-based electrodes to generate energy or desalinate water. Thus, optimized ion structuring within the electric double layer (EDL) of a supercapacitor is essential for effective desalination from CDI and energy production from CapMix[105, 66, 136, 159, 160]. Extensive investigations have aimed to describe EDL phenomena (desolvation, screening, ion packing) responsible for improving charge storage–based processes (electroadsorption/desorption) through theory and experiments[161, 152, 162]. Despite these extensive investigations, much of the current focus on charge storage within the EDLs is limited by the assumption that charge storage occurs isothermally.

It is well known that numerous factors contribute to thermal fluctuations which produce non-isothermal operations. This in turn alters the ion structuring and by extension charge storage dynamics within the EDL[163, 106]. Thus, the temperature of a CapMix and CDI cell impacts the system performance (energy consumption, energy generation, thermodynamic efficiency). Within energy storage, thermal properties have been intensely investigated due to the role joule heating plays in materials aging [164, 165, 166, 167, 107, 105, 168]. Additionally, thermal energy harvesting from EDL capacitors has been suggested through leveraging the thermogalvanic effect[169, 154]. The thermogalvanic effect within CapMix systems has been experimentally and theoretically investigated, with performance increasing when the seawater is warm and the river water is cool[142, 170]. This improved performance was attributed to a thermally–induced double layer expansion process in concert with the concentration–induced double layer expansion. This work was also highlighted as a means to reduce energy consumption in CDI cells[142, 86]. However, prior computational work has emphasized the importance of infinitely slow cycle operation, where irreversibilities are minimal. Accounting for transients could demonstrate variations with temperature due to effects of resistance and diffusion that had not previously been seen.

Here, we investigate how thermal properties can aid in minimizing electrical energy required for CDI or maximizing electrical energy produced through CapMix. In the first scenario, we examine systems where all four stages of the separations and mixing cycles occur on one isotherm (T=20-80°C). Next, we examine the case whereby different cycle stages (charging, discharging, solution switching) are operated on two separate isotherms. Finally, we examine the scenario whereby cycles stages occur with a variable temperature profile (charging, discharging, solution switching) approximating Carnot-like cycles which operate under constant chemical potential conditions (iso-μ). Each scenario is evaluated in terms of the total electrical energy produced/consumed (CapMix/CDI) and the thermodynamic efficiency.

5.3 Methodology

5.3.1 CapMix and CDI Thermodynamic cycle operation

The investigated CDI cycle consists of four stages and closely resembles experiments where charging and discharging occurs at constant current (Figure 5.1A). The first stage (Process 1-2), consists of a solution switching stage, where the maximum brine concentration is replaced by a minimum diluate concentration. The second stage (process 2-3), consists of a charging stage where the chemical potential was held constant (mimicking a Carnot-like process). The second stage was complete once a maximum set voltage was reached. Stage two represents the desalination process. The third stage (process 3-4), consists of a constant charging phase (no current). This stage is complete once the concentration reaches the predefined brine concentration. The fourth stage (process 4-1), consists of a discharging stage where the chemical potential was held constant (mimicking a Carnot-like process). The fourth stage was complete once a minimum set voltage was reached. Stage four represents the resalination process.

The CapMix cycle consisted of four stages, which also resembled processes employed experimentally. The four stages were similar to those described above. The main differ-

ence was that in CapMix charging occurred in the maximum concentration (i.e. Seawater, HC) and discharging occurred in the minimum concentration (i.e. river water, LC) (Figure 5.1B). The cycle started with a maximum concentration (C_{HC}), and the electrodes were held at a constant chemical potential until the cell reached the maximum charging voltage (process 1-2). Then, the solution was switched to the minimum concentration (C_{LC}). This resulted in an increase in the total cell voltage due to the EDL expansion process (process 2-3). Thus, when discharging (process 3-4), the higher voltages enabled net energy recovery. Finally, the high concentration (C_{HC}) was reintroduced during a constant charge switching stage (process 4-1). Note that, in Figure 5.1, both the CapMix and the CDI cycles are operated in a continuous (single-pass) mode during all four stages, and the processes are only depicted in a cyclic manner to demonstrate the energy transfers of work and heat.

In order to introduce thermal effects into the aforementioned cycles, we investigated three modes of operation. In the first mode, the entire cycle was operated under isothermal conditions (stages 1-4). We investigated cycles operated at (T = 20, 50, 80°C). In the second mode, we investigated cycles where operations occurred on two isotherms. Specifically we investigated an operational mode where charging took place at 20 °C, and discharging took place at elevated temperatures (T=50 and 80 °C). Applying elevated temperatures during the discharging stage was motivated by previous studies[142, 86]. In the third mode, we investigated thermal effects in a dynamic matter. Here, we applied a variable temperature profile during the charging phase. The temperature profile applied to the cell was chosen to enable constant chemical potential operation during the charging and discharging stage. As was motivated earlier, constant chemical potential ion separations/mixing in a chemical engine is analogous to isothermal heat addition process in a heat engine. Furthermore, the use of constant chemical potential separations/mixing has been shown to minimize/maximize the work per number of ion[142, 84].

The simulations were subject to an initial voltage of 0.1 V, and charged at constant concentration until a final voltage of 1.0 V. A maximum of 1.0 V was chosen to mitigate

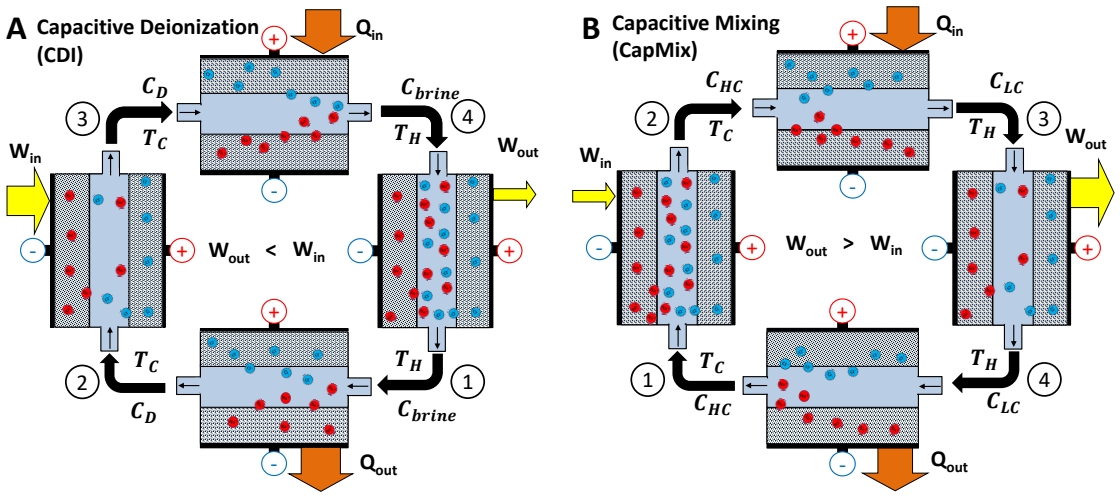

Figure 5.1: Physical depiction of thermal and electrical energy conversion processes for (a) CDI, and (b) CapMix cycles. Note that both the CapMix and the CDI cycles are operated in a continuous (single-pass) mode during all four stages, and the processes are only depicted in a cyclic manner to demonstrate the energy transfers of work and heat.

issues associated with electrolysis (e.g. side reactions). Maintaining the discharge voltage at 0.1 V enabled energy recovery during the cycle which is necessary when looking for optimal thermodynamic efficiency in CapMix and CDI systems. For CDI, the maximum (brine) concentration is determined by the C_{feed}, water recovery α, and minimum (dilute) concentration $C_{diluate}$:

$$C_{brine} = \frac{C_{feed} - \alpha C_{diluate}}{1 - \alpha} \tag{5.1}$$

For CDI cycles, the thermodynamic efficiency (TEE) is the ratio of the Gibbs energy of mixing $\Delta G_{mix,\,CDI}$ to the input cycle work W_{cycle}, measured by $\oint V\, d\sigma$. To equate units with the Gibbs energy of mixing, σ is represented as a volumetric-based charge after dividing by 2x the pore length L_e. The Gibbs energy of mixing and TEE is defined as:

$$\Delta G_{mix,CDI} = nRT\left(\frac{C_{feed}}{\alpha} ln\left(\frac{C_{feed} - \alpha C_{diluate}}{C_{feed}(1-\alpha)}\right) - C_{diluate} ln\left(\frac{C_{feed} - \alpha C_{diluate}}{C_{diluate}(1-\alpha)}\right)\right) \tag{5.2}$$

$$TEE = \frac{\Delta G_{mix}}{W_{cycle}} \tag{5.3}$$

where n is the vanFLt Hoff Factor, which for $1:1$ electrolytes assumes a value of 2. For CapMix, an equivalent efficiency is developed. This thermodynamic efficiency considers the maximum work that can be extracted by the cycle $\Delta G_{mix,CapMix}$:

$$\Delta G_{mix,CapMix} = -2RT\Big(\frac{C_{mix}}{\phi} ln\Big(\frac{C_{mix}}{C_{H_2O}}\Big) - (C_{LC}) ln\Big(\frac{C_{LC}}{C_{H_2O}}\Big) - \frac{1-\phi}{\phi} C_{HC} ln\Big(\frac{C_{HC}}{C_{H_2O}}\Big)\Big) \tag{5.4}$$

where ϕ is the volume fraction of low concentration water used during the CapMix process. C_{mix} is the mixture solution, and the volume fraction is fixed at ϕ = 0.5. This indicates that the same amount of water is mixed during both of the switching stages. We have also assumed activity coefficients as unity values. Thus the thermodynamic efficiency for CapMix is:

$$\eta_{th} = \frac{W_{cycle}}{\Delta G_{mix,CapMix}}. \tag{5.5}$$

The detailed development and analysis for ΔG_{mix} at alternating temperatures is discussed in the Appendix (Figure B.1).

Chemical potential in chemical systems is the analog to temperature in thermal energy systems, and is represented by

$$\mu = RTln\Big(\frac{C}{C_{ref}}\Big) \tag{5.6}$$

where T is temperature, R is the universal gas constant, and C_{ref} represents a reference concentration for the dead/surrounding environment state, taken as 1 M [141]. It can be seen that chemical potential varies as a function of both temperature and concentration. Thus, if the operation CapMix/CDI cycle operation is isothermal, then a constant concentration

process will result in the desired constant chemical potential. If CapMix/CDI cycle operation is non-isothermal, in order to maintain constant chemical potential with variable temperature the concentration must be varied.

We also consider the effects of temperature changes during the charging/discharging stages as well as during switching stages. Here, constant chemical potential is enabled through varying temperature and concentration [141, 171]. Operating cycles under variable temperature conditions may provide insight into more realistic means to achieve constant chemical potential operations in experiments. During variable temperature operation, the temperature was limited to 0°C to 100°.

Changes in the number of ions in the cell (N) is indicated by the following.

$$N = \Gamma + CL_eN_{av} \tag{5.7}$$

where Γ is the buildup of ions in the cell from charging, and $\mathrm{CL}_e\mathrm{N}_{av}$ is ions directly in the body of the cell (See Supporting Information). When this number of ions in transport is reduced, cycles can operate under conditions closer to Carnot operation [141]. We will explore the ideal steady-state conditions (infinitely slow reversible cycles), then consider transient mode to simulate more realistic operation.

It is important to note that these reversible cycles are only theoretical, and transient transport limitations still need to be considered. For instance, the infinitely slow model neglects all cell ohmic resistances since current magnitude is assumed negligible. In actuality, the cell exhibits concentration-dependent internal resistances, along with a constant external resistance. The internal resistance within the electrolyte channel is inversely related to the cell conductivity, which depends on both concentration of electrolyte and temperature (Figure B.2A). Additionally, effects of diffusion will also influence transport when current is considered. Temperature strongly influences diffusion (Figure B.2B) due to the increase in thermal vibrations within the electrolyte at higher temperatures, which can further aid in effective ion transport. All other important operational parameters for the transient analy-

sis, such as properties and geometries (see Table S5.1).

5.4 Results and Discussion

5.4.1 CDI and CapMix cycles operated with isothermal input streams

To evaluate the effect input solution temperature has on system level performance (energy production, consumption and thermodynamic efficiency) we initially investigated CDI and CapMix cycles which occur under infinitely slow conditions. Through neglecting kinetic effects we can evaluate the impact of solution temperature under theoretically ideal (reversible) system operation (Fig 5.2A). For CapMix operation, the high concentration (C_{HC}) is 600 mM, the low concentration (C_{LC}) at 20 mM, and the volume ratio is fixed at ϕ =50%. For CDI, the inlet feed concentration is 20 mM (C_{feed}), the diluate concentration is 5 mM ($C_{diluate}$), and the water recovery is fixed at $\alpha = 50\%$. The voltage limit in all cases is 0.1 to 1 V. We also expanded the GCS CDI model to evaluate kinetic and ohmic–based irreversibilites (Fig 5.2B and C).

During the reversible and isothermal CapMix cycles, increasing the cell temperature (from 20°C to 80°C), results in an decrease in the accumulated surface charge (from 0.24 to 0.22 #/nm^2) at fixed voltage (V=1V). Despite this slight reduction in the maximum charge obtained, the cell discharge voltage rises due to a 5 mV jump in the thermal voltage as temperature increases from 20°C to 80°C. As a result, the net-work extracted from the CapMix cycle increases from 0.18 to 0.27 kWh per m^3 of solution mixed, as temperature increases from 20°C to 80°C. Graphically, the greater electrical energy generation is represented by an increase in the area of the μ-N diagram (Figure 5.2A) and σ-V diagrams (Figure B.3A). Thus, the increase in net-work equates to 1.0 Wh per m^3 per °C of mixed solution. The theoretical cycle thermodynamic efficiency also increased from 39% to 43%. We note that reversible net-work and thermodynamic efficiency correspond to a cell operated at zero current(Figure 5.2B and C).

During the reversible and isothermal CDI cycles, increasing the cell temperature (from

20°C to 80°C), again results in an increase in the surface charge during charging (from 0.19 to 0.21 #/nm^2) at fixed voltage (V=1.0V). Again the increase in surface charge results in an increase in net-work, indicated by the larger area on both μ-N (Figure 5.2D) and V-σ diagrams (Figure B.3B). However, this net-work is consumed by the cell, rather than produced. Thus the work input for the same separations, increased from 0.28 to 0.32 kWh per m^3 of solution separated, as the solution temperature increased from 20°C to 80°C (Figure 5.2E). This results in an increase in energy which corresponds to 0.65 Wh per m^3 per °C. Despite the increase in energy consumed for the separation process, higher temperatures also increase the Gibbs energy of mixing. As a result, the cycle thermodynamic efficiency actually increased slightly from 6.1 and 6.4% as the cell temperature increased to 80°C (Figure 5.2F – Current = 0 mA).

When the CDI and CapMix cycles are operated irreversibly, the performance (net-work and thermodynamic efficiency) is dependent on the cell operating current. Ideally, CapMix cycles need to operate under conditions which minimize resistive losses. When comparing irreversible cycles directly with reversible cycles, a voltage discontinuity exists during solution switching (Figure B.4A-C). This abrupt transition increases the cell voltage due to changes in the structure of the EDL (Debye Length). As the switching stage proceeds, the voltage spike decreases as the effluent cell concentration approaches that of the recently introduced diluate stream. This spike has been observed experimentally [171, 159]. As the operating current increases, the net-work generated from the mixing process decreases due to resistance–based irreversibilities. Nevertheless, at all current values, the net-work for CapMix increases with temperature. At the maximum value of 25 mA, the net-work output was 0.09, 0.11, and 0.12 kWh per m^3 for 20, 50, and 80°C. This corresponded to thermodynamic efficiency values of 19, 21, and 22% (Figure 5.2C). We attribute the increase in the η_{th} with temperature due to the gradual nonlinear increase in the net cycle work output (Figure B.5).

For irreversible CDI cycles, higher temperature increased the work required up to a

3-5 mA threshold; however, the thermodynamic efficiency also increased with temperature (Figure 5.2E and F). Increasing current decreased the maximum attainable thermodynamic efficiency due to a greater amount of irreversibilities (ohmic resistance) present at high current. Therefore, while increasing the temperature during isothermal operation does augment system performance for CapMix (increased energy recovery), it degraded system performance for CDI (increased energy consumed). This indicates that if system operation is to occur at a fixed temperature with minimal charging current, elevated temperatures are preferred for CapMix whereas low temperatures are preferred for CDI.

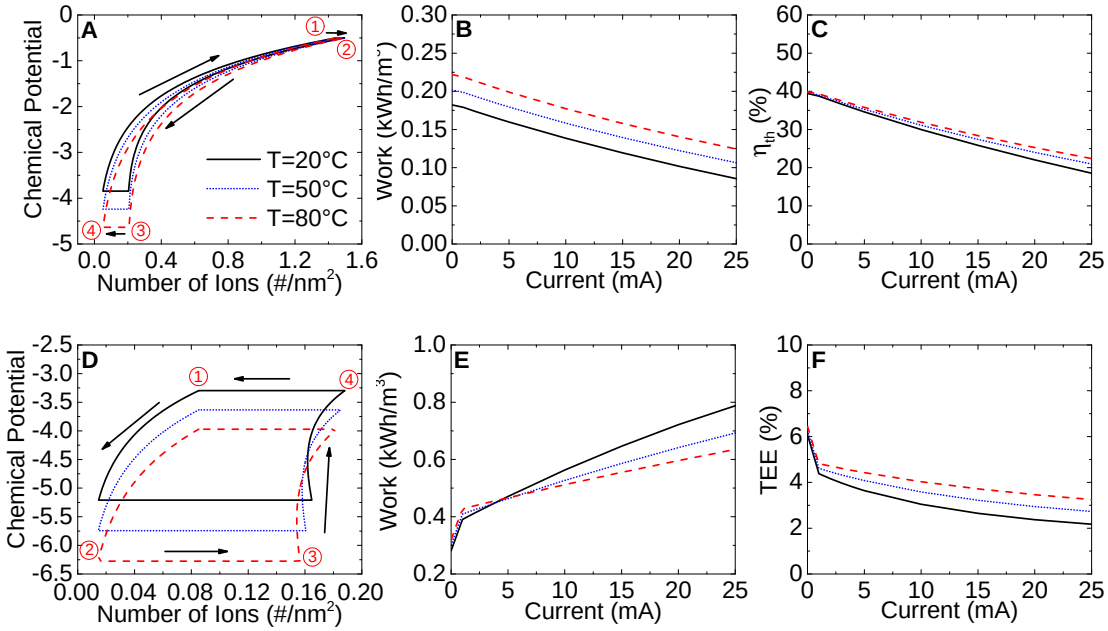

Figure 5.2: Cycles operated on two isotherms. (A) CapMix μ-N Diagram, (B) net-work extracted from CapMix cycle, (C) CapMix Thermodynamic efficiency, (D) CDI μ-N Diagram,(E) net-work consumed from CDI cycle, (F) CDI Thermodynamic efficiency.

5.4.2 CDI and CapMix cycles operated with nonisothermal input streams

To evaluate the effect input solution temperature has on system level performance (energy production, consumption and thermodynamic efficiency) we initially investigated CDI and CapMix cycles which occur under infinitely slow conditions. Through neglecting kinetic effects we can evaluate the impact of solution temperature under theoretically ideal (re-

versible) system operation (Fig 5.3A). For CapMix operation, the high concentration (C_{HC}) is 600 mM, the low concentration (C_{LC}) at 20 mM, and the volume ratio is fixed at ϕ =50%. For CDI, the inlet feed concentration is 20 mM (C_{feed}), the diluate concentration is 5 mM ($C_{diluate}$), and the water recovery is fixed at $\alpha = 50\%$. The voltage limit in all cases is 0.1 to 1 V. We also expand the GCS CDI model to evaluate kinetic and ohmic-based irreversibilites (Fig 5.3B and C).

During the reversible and isothermal CapMix cycles, increasing the cell temperature (from 20°C to 80°C), results in a decrease in the accumulated surface charge (from 0.24 to 0.22 #/nm^2) at fixed voltage (V=1V). Despite this slight reduction in the maximum charge obtained, the cell discharge voltage rises due to a 5 mV jump in the thermal voltage from 20°C to 80°C. As a result, the net-work extracted from the CapMix cycle increases from 0.18 to 0.27 kWh per m^3 of solution mixed, as temperature increases from 20°C to 80°C. Graphically, the greater electrical energy generation is represented by an increase in the area of the μ-N diagram (Fig 5.3A) and σ-V diagrams (Figure B.3A). Thus, the increase in net-work equates to 1.0 Wh per m^3 per °C of mixed solution. The theoretical cycle thermodynamic efficiency also increased from 39 to 43%. We note that reversible net-work and thermodynamic efficiency correspond to a cell operated at zero current(Figure 5.3B and C).

During the reversible and isothermal CDI cycles, increasing the cell temperature (from 20°C to 80°C), again results in an increase in the surface charge during charging (from 0.19 to 0.21 #/nm^2) at fixed voltage (V=1V). Again the increase in surface charge results in an increase in net-work, indicated by the larger area on both μ-N (Figure 5.3D) and V-σ diagrams (Figure B.3B). However, this net-work is consumed by the cell, rather than produced. Thus the work input for the same separations, increased from 0.28 to 0.32 kWh per m^3 of solution separated, as the solution temperature increased from 20°C to 80°C (Figure 5.3E). This results in an increase in energy which corresponds to 0.65 Wh per m^3 per °C. Despite the increase in energy consumed for the separation process, higher temperatures

also increase the Gibbs energy of mixing. As a result, the cycle thermodynamic efficiency actually increased slightly from 6.1% and 6.4% as the cell temperature increased to 80°C (Figure 5.3F - Current = 0 mA).

For irreversible CDI cycles, similar to the case with isothermal input streamshigher temperature increased the work required up to a 3-5 mA threshold. However, TEE increased with temperature (Figure 5.3E and F). Increasing current also reduced maximum attainable TEE due to higher ohmic drops.

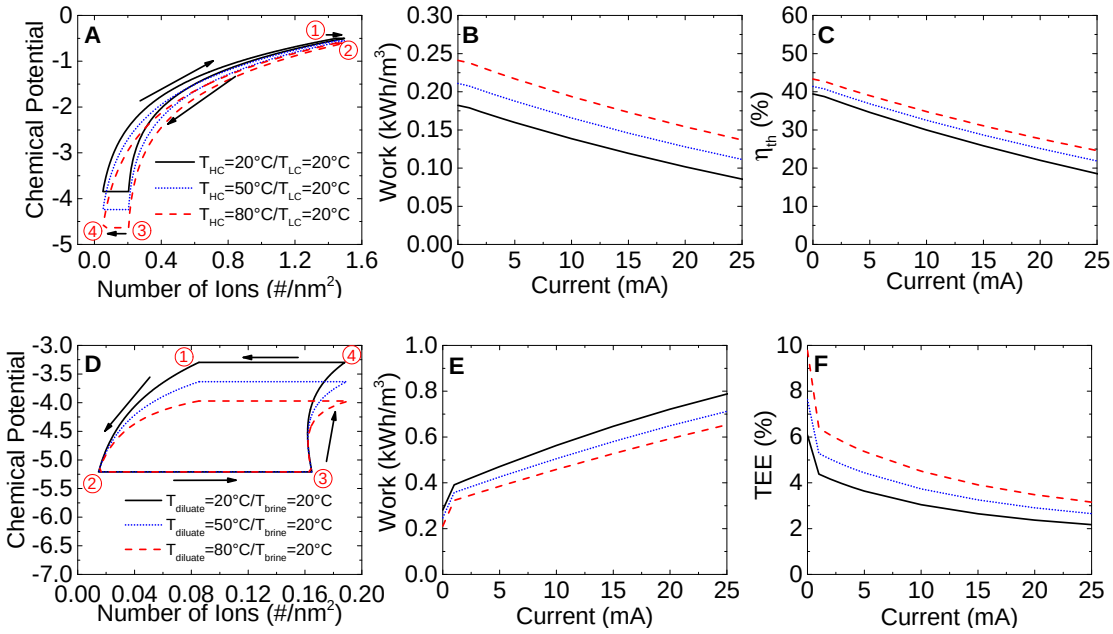

Figure 5.3: Cycles operated on two isotherms. (A) CapMix μ-N Diagram, (B) net-work extracted from CapMix cycle, (C) CapMix Thermodynamic efficiency, (D) CDI μ-N Diagram,(E) net-work consumed from CDI cycle, (F) CDI Thermodynamic efficiency. Chemical potential is normalized by RT_0, where T represents the dead state temperature at 20°C , resulting in its value as unitless, as consistent with [141].

5.4.3 CDI and CapMix cycles operated with input streams with varying temperatures

Finally, for both CapMix and CDI cycles, we consider the performance of a cycle where charging and discharging occur with a variable temperature profile. Like the previously investigated cycles, charging and discharging occurs while chemical potential is fixed (iso-

μ), resembling the Carnot-like ion separations/mixing[84]. However, in order to maintain a constant chemical potential while temperature is varied, here the concentration profile must also vary (Eq. 5.6). Note that the cycle also maintains a constant number of ions (iso-N) during solution switching.

For the CapMix system, we start by charging (Process 1–2) at room temperature (20°C), and cool the stream to a minimum temperature of 0°C (Figure 5.4A - black line). During the switching stage (Process 2-3), the cell is gradually heated to a temperature of 50°C. During the discharging stage (Process 3–4), the cell will continue to be gradually heated to a maximum temperature of 100°C. Finally, in the switching stage (process 4-1), the reactor is cooled and returns to a temperature of 20°C. Note that this operation is both a cycle with respect to the chemical engine, and with respect to the heat engine. The temperature profiles described and graphically shown in Figure 5.4 are the same for the CDI cell; however, the stages are different (Figure 5.4 - Top x-axis).

To illustratively compare this unique mode of temperature-based operation, three alternative cases are considered in which temperature changes occur in the switching stage only, while the charge/discharge processes are isothermal (Figure 5.4A). The lowest temperature range assumes that T_{charge} = 20°C and $T_{discharge}$ = 50°C (ΔT=30°C, T_{avg}=35°C). The high range assumes the T_{charge} = 0°C and $T_{discharge}$ = 100°C (ΔT=100°C and T_{avg}=50°C). A third case considers the averaged temperatures between the high range and low range T_{charge} = 75°C, $T_{discharge}$ = 10°C (ΔT=65°C and T_{avg}=42.5°C).

For the mid range, we show the corresponding cycle variations in concentration, which also coincides with the high and low temperature ranges. When the variable temperature cycle is compared to the cycles with temperature changes in the switch stage only, concentration changes in the CapMix cycles vary only by up to 25 mM, or 5% of C_{HC} (Figure 5.4B). The switching stage only requires recovery to the initial concentration, and during discharging, the concentration is returned to brine (Figure 5.4C). For these iso-chemical potential studies, we only consider the reversible cycle.

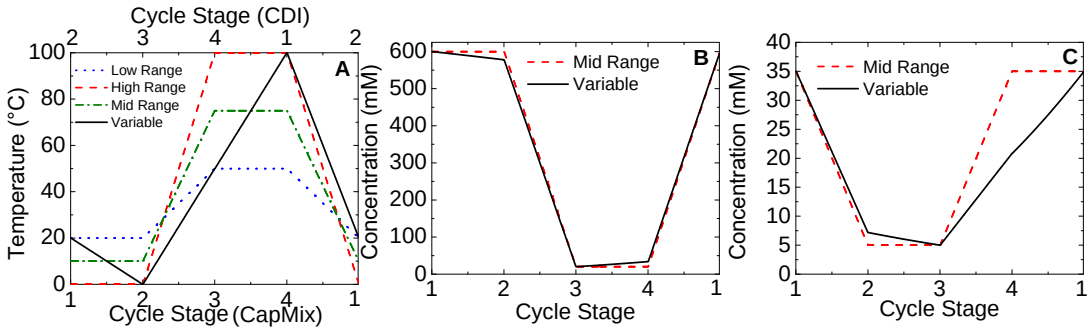

Figure 5.4: (A) Variable temperature profiles applied to CDI/CapMix cycles. (B) Resulting concentration profile of the CapMix and (C) CDI cells.

The quantitative effect of the variable temperature-based operation is illustrated on charge-voltage (σ-V) and chemical potential-number of ions (μ-N) diagrams. For CapMix, the the variable temperature does not increase the cycle output work (Figure 5.5A and B). For each of the cycles studied, the overall cycle work is: 0.21 kWh/m^3 for the low range, 0.27 kWh/m^3 for the high range, 0.24 kWh/m^3 for the mid range, and 0.21 kWh/m^3 for the variable temperature. Subsequently, the efficiencies for each of the cycles are 41.4% (low range), 43.5% (high range), 45.6% (mid range), and 41.3% (variable temperature). Additionally, the work output per number of ions exchanged were 0.15 (low range), 0.19 (high range), 0.17 (mid range), and 0.15 (variable temperature) kWh/m^3/#/nm^2. Thus, for CapMix, maximizing the temperature range between charge and discharge improved performance, while employing variable temperatures offered minimal overall benefit for the cycle. This is despite the fact that the variable temperature is more Carnot-like.

For CDI, the the variable temperature did aid in decreasing the net-work consumed by the cycle (Figure 5.5C and D). The cycle net work is only 0.14 kWh/m^3 for the variable cycle operation, whereas the temperature-averaged mid range was 0.20 kWh/m^3, the maximum temperature range 0.15 kWh/m^3, and the low range 0.20 kWh/m^3. The cycle TEE comparison follows with values of 7.6%, 14.9%, 10.3%, and 10.0% for the tested temperature ranges of low, high, mid, and variable. Furthermore, the range in the number of ions was the smallest (0.15 #/nm^2) for the variable range of all cycles (Figure 5.5C), with 0.17, 0.18, and 0.18 #/nm^2 reported for the cycles operated with a high, low, and mid tem-

perature ranges. The nearly 0.02 #/nm^2 over the cycle may appear small, but is a nearly 15% reduction in total in the number of ions. Furthermore, the change in number of ions during this switching process in nearly four times less than that of all of the other temperature cases, suggesting that the variable temperature operation may be valuable in future applications for simulating Carnot conditions experimentally. While savings do exist from operating at elevated temperatures, the energy benefits are small compared to the quantity of the thermal energy input to the system (Tables SI2-SI3). Thus, increased temperature during isothermal processes must be achieved through waste heat. The maximum energy savings relative to the maximum theoretical Carnot cycle efficiency is 2.37% which occurs for irreversible cycles at 50°C and 25 mA (Table SI3).

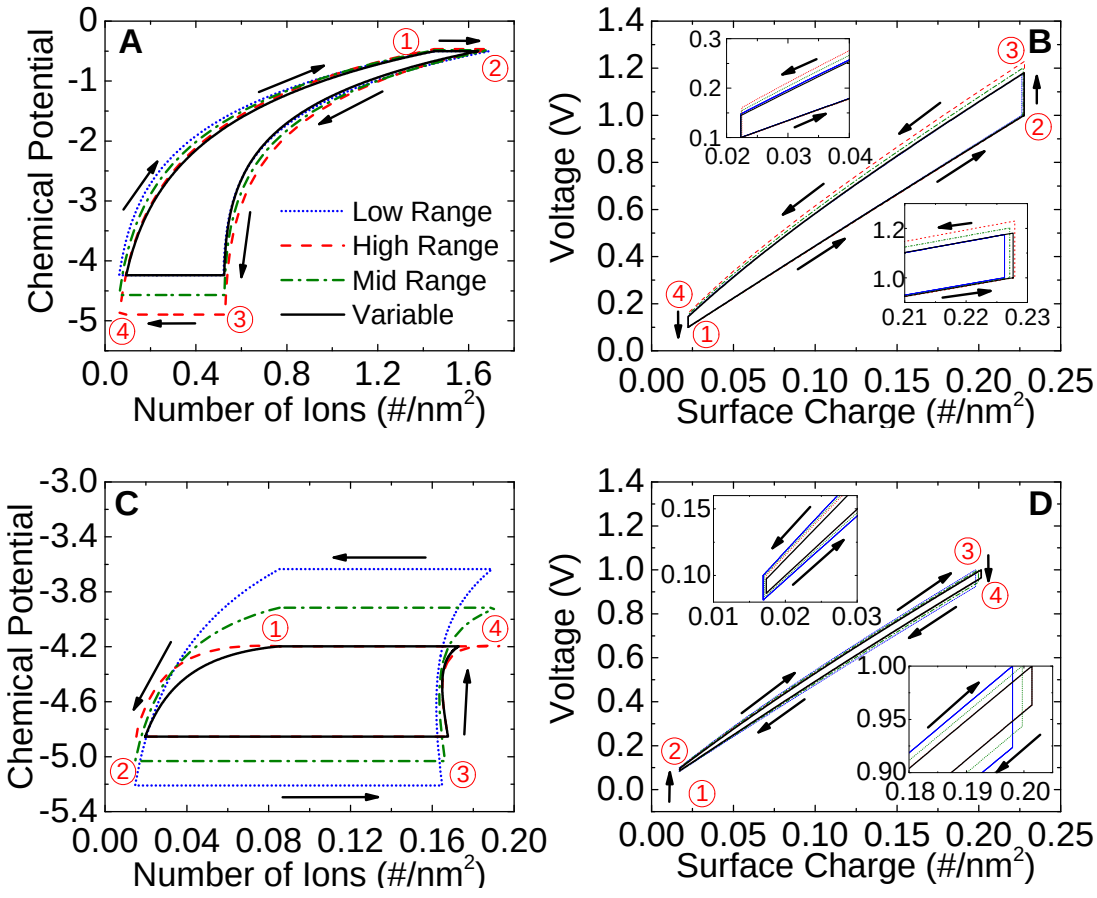

Figure 5.5: (A)-N diagram for CapMix, (B)-V diagram for CapMix,(C)-N diagram for CDI, (D)-V diagram for CDI for systems operated with the variable temperature profile.

5.5 Conclusions

We show how through tuning the temperature of the input solutions to a CapMix and CDI system, system performance can be enhanced (energy production, energy consumed and thermodynamic efficiency). When operating CapMix and CDI isothermally, increasing the operating temperature aids in maximizing the net-work output from the CapMix system by up to 50%. Conversely, increasing the operating temperatures has an adverse effect on CDI operation, increasing energy consumption by $\sim$15%. Additional cycles whereby input solution temperature is individually varied (e.g. $T_{HC} \neq T_{LC}$ and $T_{Diluate} \neq T_{Brine}$), resulted in enhanced CDI performance. However, CapMix performance never exceeded that attained under high temperatures with isothermal temperature values (T_{HC}=T_{LC}=$T_{high\ temp}$). Specifically, by charging in a low temperature feed, and discharging in a high temperature brine, we show that thermodynamic efficiencies can exceed 9%. This is in contrast to isothermal operation which only obtains maximum thermodynamic efficiencies of $\sim$6%. We note that thermodynamic efficiency, in addition to being dependent on temperature, is also dependent on the feed concentration and percent of salt removed. Finally, a variable temperature profile is explored as a means to operate a CDI and CapMix cycle with Carnot-like electrosorption behaviour (iso-μ). Again, performance improvements did not result in benefits for CapMix, but CDI performance increased with temperature up to almost 10% for the conditions tested. Ion mixing and separation–based technologies provide new approaches toward harvesting energy and performing ionic separations using only electrical energy input. However, system performance improvements must occur in order for implementation to take place. Through gaining an understanding regarding the role various system level properties play, one can begin to design system level operational modes which most closely mimic theoretical optimal performance.

CHAPTER 6
INFLUENCE OF FEED-ELECTRODE CONCENTRATION DIFFERENCES IN FLOW-ELECTRODE SYSTEMS FOR CAPACITIVE DEIONIZATION

6.1 Abstract

The common performance metrics ascribed to flow electrode capacitive deionization systems can vary significantly depending on the mode of operation and initial system conditions. Through varying the flow electrolyte ionic strength, performance values such as average salt adsorption rate and energy consumption can vary by as much as 51% and 55%. This variability from cycle to cycle is in part due to changes in electrical conductivity (ohmic) but is also due to the introduction of competing transport processes. Diffusive transport can enhance or diminish the rate of desalination and energy recovery, creating a larger degree of error in reported values. Here, we propose a dimensionless ratio comparing diffusion and electromigration-based transport to measure performance stability. Unstable system performance is most prominent when the feed ionic strength does not match the flow electrode ionic strength. In this scenario, the ratio of the diffusion to electromigration transport reached a maximum. Conversely, stable operation occurs when the ionic strength of the feed matches the ionic strength in the flow electrode. With the growing interest to move flow electrode capacitive deionization into treatment regimens which operated with high contaminant concentration feedwater, characterizing and quantifying diffusive flux is important for assessing true electrochemical system performance.

6.2 Introduction

Capacitive deionization (CDI) has shown promise for treating brackish waters [86]. The low projected cost and antifouling surfaces provide valuable advantages when compared

with state of the art technologies such as reverse osmosis (RO) [172] and flash stage distillation [135] CDI is limited to low saline solutions, as traditional film electrodes have a finite surface area available for ion removal. Flow electrode capacitive deionization (FCDI) overcomes this limitation through transforming the static electrodes into flow electrodes, which are stored in tanks outside of the flow cell. This allows for much higher surface area per flow cell volume, permitting the treatment of higher saline waters (e.g., seawater).

The flow electrode consists of solid active material (activated carbon) mixed with a salt-based electrolyte. To date, most efforts aim to improve system performance through evaluating new materials, system configurations, and innovative ways to increase carbon loading in the electrode [173, 174, 120, 118]. The flow electrode-supporting electrolyte has received less attention with the majority of researchers using various concentrations (0-0.5 M) of sodium chloride [172, 79, 175, 112]. Increasing the salt concentration reduces the whole cell solution ohmic resistance and consequently can improve the electrochemical cell performance. Yet, increasing the ionic strength has been shown to increase the desalination efficiency only up until 0.4 M sodium chloride ($E_{cell} < 1.2$ V) and decreases beyond this point [121]. Higher saline electrolytes (0.5 M $NaSO_4$) were observed to improve the rate of desalination only at elevated voltages ($E_{cell} > 1.5$ V), but side reactions at these voltages can limit charge efficiency. Varying the electrolyte and feed ionic concentration also has a significant impact of membrane ionic resistance, which ultimately can limit system performance [176, 177, 178, 179, 180]. Thus, understanding and quantifying all transport-based processes occurring between the electrode and electrolyte will aid in overcoming performance limitations.

Here, we investigate the ability to obtain stable performance metrics (desalination and energy recovery) in a FCDI. We evaluate the interactions between the feed and the electrode by quantifying the charge efficiency, salt removal efficiency, energy input, and average salt adsorption rate during a series of charge-discharge cycles. In addition, we developed a transport model that decouples and quantitatively compares the various modes of ion

transport (diffusion and migration) with a dimensionless ratio. This ratio is able to serve as a predictive measure for reporting the degree of stability within a given electrochemical FCDI performance measurement.

6.3 Materials and Methods

The FCDI system is comprised of a Model 857 Redox Flow Cell Test System (Scribner Associates, Inc., Southern Pines, North Carolina) (Figure 6.1). Tanks for the flow electrode contain stir plates to enable continuous mixing of the electrode during testing. The flow cell (area A_{cell} = 25 cm^2) contains a polycarbonate flow channel (clear polycarbonate, 0.47 cm thickness) and gold-plated copper current collectors. The carbon slurries flow through two graphite plates with channels (1 mm width x 5 cm length x 1 mm depth, 33 channels total in a triple serpentine flow pattern), and the feed flows vertically through the center of the cell. Cation exchange membranes (CEM) and anion exchange membranes (AEM) separate the feed from electrode (Selemion AMV/CMV, Chiba, Japan).

The feed and electrode flow rates used during the experiment were 5 and 10 mL/min. The flow electrode (100 mL) consisted of 5 wt % activated charcoal Norit (Sigma-Aldrich, St. Louis, Missouri) with a variable concentration of sodium chloride salt (Sigma-Aldrich, St. Louis, Missouri, ACS reagent, 99%). The feed (25 mL) was prepared with three different salt concentrations: 10 mM, 500 mM, and 1 M. The cell was charged and discharged for 1.5 h at a voltage of 1.2 V to limit water splitting [121]. The feed conductivity was measured using an Orion Fisher Scientific 013005MD Versa Star Pro Benchtop conductivity meter, and the current through the cell was collected from the Flow Cell software. The data obtained for conductivity and current were used as inputs for the transport-based model.

The average salt adsorption rate (ASAR) was calculated to determine overall salt re-

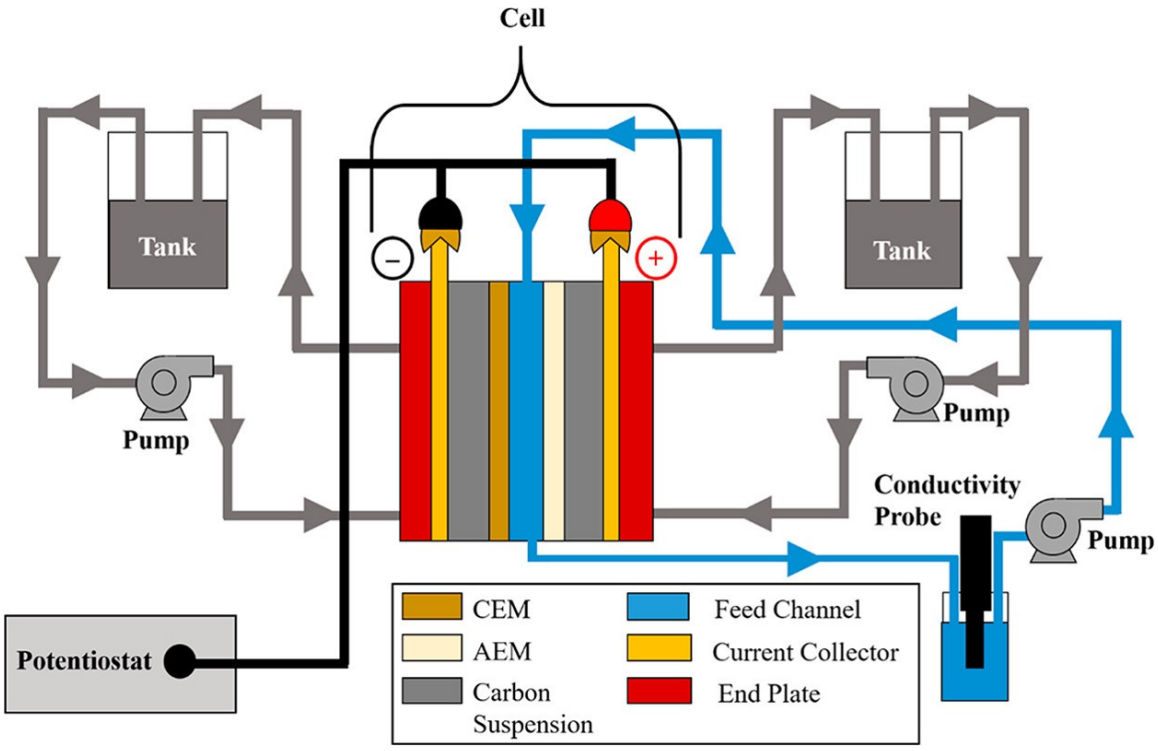

Figure 6.1: Schematic of FCDI cell setup.

moval during each of the cycles:

$$ASAR = \frac{\int_0^T (C_i - C_f)\phi_f M_{NaCl} dt}{m_{AC} T} \tag{6.1}$$

where C_f is the feed concentration at any given time, C_i is the initial concentration in the feed, ϕ_f is the feed flow rate, M_{NaCl} is the molar mass of NaCl, m_{AC} is the total mass of activated carbon in both electrodes, and T is time. Charge efficiency (CE) was calculated to determine salt removal in relation to energy input during charging stage [181, 116, 182]:

$$CE = \frac{(C_{f,i} - C_{f,f}) V_f F}{\int_0^T I dt} \tag{6.2}$$

where $C_{f,i}$ represents the initial concentration in the feed, $C_{f,f}$ represents the final concentration in the feed, V_f is the feed volume, I is the current, F is Faradays constant, and t

is the time. The salt removal efficiency (SRE) was calculated using the following:

$$SRE = \frac{(C_{f,i} - C_{f,f})}{C_{f,i}} \tag{6.3}$$

The study considered six different cases for feed and electrolyte concentrations. Three feed concentrations were examined: a dilute feed solution (10 mM), a moderate saline solution that was an approximate for seawater (0.5 M), and high concentration (1 M) which was meant to approximate a modest brine stream. In all of the matched tests, the electrode electrolyte concentration used was equivalent to that of the electrode electrolyte. In the mismatched tests, the electrode electrolyte concentration was fixed (100 mM), while the feed was varied. FCDI testing was conducted in a batch mode to discern the degree of reversibility between cycles [118].

6.4 Theory

The diffusion–migration ratio (DMR) was developed using the Nernst-Planck equation [161, 153]

$$\frac{\partial C_i}{\partial t} = -\nabla N_i \tag{6.4}$$

where C_i represents cell concentration and N represents the flux. The subscript i describes the i_{th} species (e.g Cl^- or Na^+). The flux, N_i, includes migration, diffusion, and convection terms:

$$N_i = -zu_i F C_i \nabla \phi_i - D\nabla C_i + C_i \nu \tag{6.5}$$

where D_i is the diffusivity of ions in the feed. The diffusivity in the feed and electrolyte was approximated to be the same because the major component in both chambers was saline water. ∇ C_i is the concentration gradient across the membrane, z is the ion valence, u_i is the ionic mobility, and ∇ ϕ_i is the potential gradient across the membrane. The ionic

mobility u_i can also be expressed as $u_i = D_i/RT$.

With this 1-D model, the ratio of the diffusion to electromigration can be written as:

$$DMR = \frac{|N_{diffusion}|}{|N_{migration}|} = \frac{|-D_i \nabla C_i|}{|z u_i F C_i \nabla \phi_i|} = \frac{|RT \frac{\partial C}{\partial x}|}{|zFC_f \nabla \frac{\partial V}{\partial x}|} \tag{6.6}$$

where $N_{diffusion}$ is the diffusion flux, $N_{migration}$ is the electromigration flux, R is the universal gas constant, and T is the operating temperature.

The diffusion to migration ratio can be calculated using experimentally obtained data (e.g., current, voltage, and conductivity (concentration). In the model, we neglect convection as the magnitude of the fluid velocity is negligible compared to diffusion and electromigration. We also assume the 1-D field is symmetric. Ions electroadsorbed from the salt solution are stored in the activated carbon slurry rather than in bulk. Thus, the overall electrode electrolyte ionic strength experiences relatively little change during the experiment. This is unlike the feed solution that varies during the desalination test.

The concentration gradient used to estimate diffusive transport is the difference in concentration between electrode (C_e) and feed (C_f) over the membrane thickness, δ:

$$\frac{\partial C}{\partial x} = \frac{C_e - C_f}{\delta} \tag{6.7}$$

Similarly, the electromigrative term in Eq. 5 encompasses information regarding the ohmic drop across the membrane (Figure 6.2A). The ohmic drop varies in magnitude based on surrounding electrolyte and feed concentrations. The ohmic drop ∇V_{mem} also varies as a function of the current density of the membrane and the membrane resistance:

$$\Delta V_{mem} = iR"_{mem} \tag{6.8}$$

where i is current density in A/cm^2, and R is the membrane resistance in Ωcm^2. Experiments conducted at constant voltage result in current density profiles for Eq 6.8. An

approximation for the membrane resistance is

$$R"_{mem} \approx a + \frac{b}{(C_e/C_{ref})} \tag{6.9}$$

where C_{ref} is a reference concentration to nondimensionalize the electrolyte concentration C_e (C_{ref} = 1 M). To account for variable concentration on either side (henceforth referred to as C_e and C_f), the study considers a power-law profile for the concentration across the membrane and averages the local resistance over the membrane to obtain the total resistance:

$$C(x) = min(C_e, C_f) + |C_e - C_f|\left(\frac{x}{\delta}|\right)^n \tag{6.10}$$

$$R"_{mem} = \frac{1}{\delta}\left(a + \frac{b}{C_e(x)/C_{ref}}\right) \tag{6.11}$$

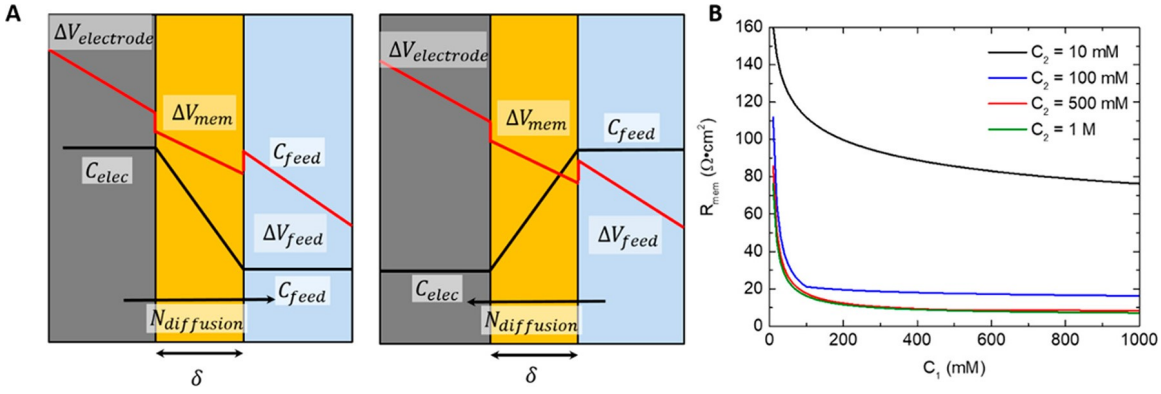

Figure 6.2: (A) Schematic depicting concentration and voltage drops across the membrane. (B) Variations in predicted membrane resistance as a function of varying concentrations in both the feed and the electrode.

The three fitting parameters (a, b, and n) are membrane dependent and obtained from ex situ membrane testing. Here, a = 5.59, b = 1.55, and n = 5.5 (C_f = 10 mM and C_e = 1 M). Membrane resistances calculated from Eqs. 10 and 11) demonstrated that especially large variations occur if the concentration of either the feed or electrolyte is low (Figure 6.2B). This is consistent with prior ex situ membrane testing [177]. Generally, AMV resistances

for Selemion membranes are lower than the CMV; here, we assume that the AEM is 80% of the CEM resistance [177].

In considering migration into the feed, the electromigration term in Eq. 5 simplifies to

$$N_{migration} = \frac{DF}{RT} C_{feed} \frac{iR"_{mem}}{\delta} \tag{6.12}$$

Thus, when taking a ratio of diffusive and electromigrative fluxes, the diffusivity term and membrane thickness effectively cancels. The final expression for the diffusion-migration ratio (DMR) is

$$DMR = \frac{|C_{electrode} - C_{feed}|}{\frac{F}{RT} C_{feed} iR"_{mem}} \tag{6.13}$$

where temperature, feed concentration, and current density are experimentally obtained. In-line measured conductivity is converted to concentration using a calibration curve (Eq. S8 in the Supporting Information). Further details are provided in the Supporting Information (eqs S1-S8).

6.5 Results and Discussion

One of the primary advantages of electrochemical separations is the ability to target and remove the minority component (ions) rather than majority component (water) in a mixture. This ability to remove the ionic species can promote low energy water treatment through unique system operation. Low energy consumption is possible because one can have control over the composition of the produced water, and hence, complete desalination is not necessary. Desired separation is achievable through changing the charging voltage (current) or time (Figure 6.3). Control over produced water salinity is increasingly becoming important for water treatment, as energy consumption takes place during the post-treatment phase through the reintroduction of minerals. A certain degree of mineral composition is required to minimize corrosion and for taste. The introduction of minerals during post

treatment processes also adds to the cost and complexity of a treatment system.

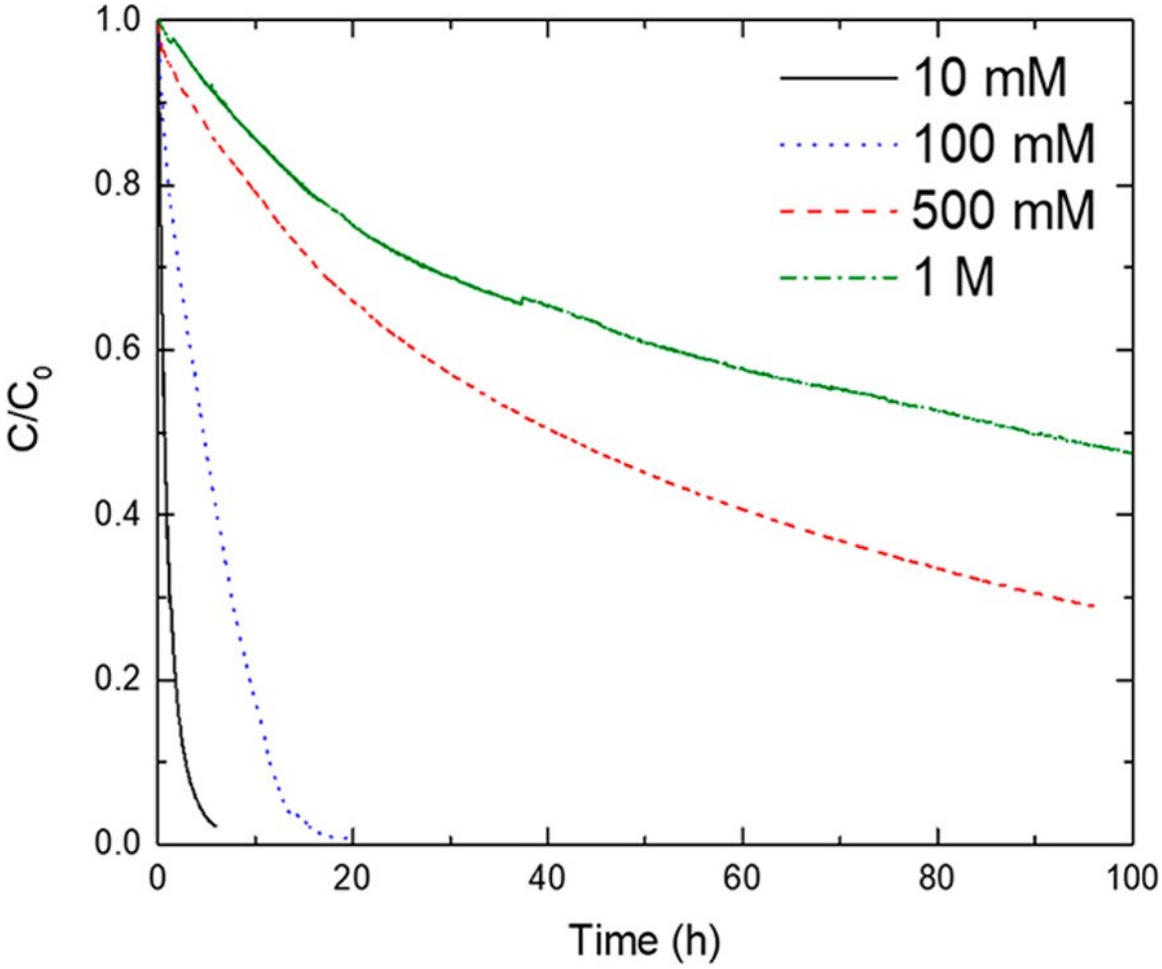

Figure 6.3: Flow electrodes can achieve various degrees of salt removal depending on the charging time, voltage and initial feed concentration.

This potential advantage associated with electrochemical-based separations technologies is important for FCDI systems that often operate with a range of feed solutions. For instance, a flow electrode with a modest carbon loading (5 wt %) is capable of achieving a range of exit salinities (Figure 6.3). With low saline feeds (10-100 mM), the percent of salt removed can easily be tuned from 0 to 100% by simply increasing the charge (desalination) time. This ability to control the exit salinity (or total salt removed) is most likely an even more favorable characteristic with higher concentration feed solutions. Here, the flexibility in exit salinity is also observed with a similar flow electrode (5 wt %), with total

salt removed ranging from zero to 60% (C_{feed} = 0.5-1 M) (Figure 6.3), albeit at longer time scales. Therefore, a desalination test with an FCDI system would not necessarily operate solely to complete salt removal ($C/C_0 = 0$), but rather desalination would be cut off once a desired salinity is reached. This desalination process would correspond to the charging phase. Next, the electrodes could be regenerated and ideally returned to the initial state ($C_e = C_{e,i}$) using a discharge process. By returning the flow electrode ionic strength back to the initial condition, repeatable operation exists within the system.

However, the complete reversal of a flow electrode back to the initial conditions is not always possible. For instance, when a flow electrode (5 wt percent carbon in 100 mM NaCl) is operated with a range of feeds, there is a lack of reversibility observed from cycle to cycle during batch operation (Figure 6.4a). Completely reversible system performance would entail removing a certain number of ions from a feed and discharging the same number of ions into a brine. In addition, electrical reversibility would entail recovering during discharge the same number of electrons introduced during the charging phase. Graphically, reversible cycle-to-cycle performance occurs if the feed solution returns to the initial condition ($C_0 = 1$) after regeneration (discharge), and this did not occur in any test where the feed ionic strength was different than the electrode electrolyte ion concentration ($C_f \neq C_e$) (Figure 6.4a).

This lack of reversibility is not due to changes in electrochemical performance but to the presence of a concentration gradient between the feed and the electrode. This gradient causes a general trend whereby a portion of the ionic transport occurs via diffusive processes (Figure 6.4A, black line). This results in a greater degree of resalination per cycle than desalination. This excess resalination is exhibited by the feed increasing by nearly 2x following the first complete desalination-resalination (charge-discharge) process. Despite the overall increasing feed concentration, the total salt removed remained consistent at 75% notwithstanding the increasing initial feed concentration. The consistency in the total salt removed aligns with the fixed time scale and similar currents observed from cycle

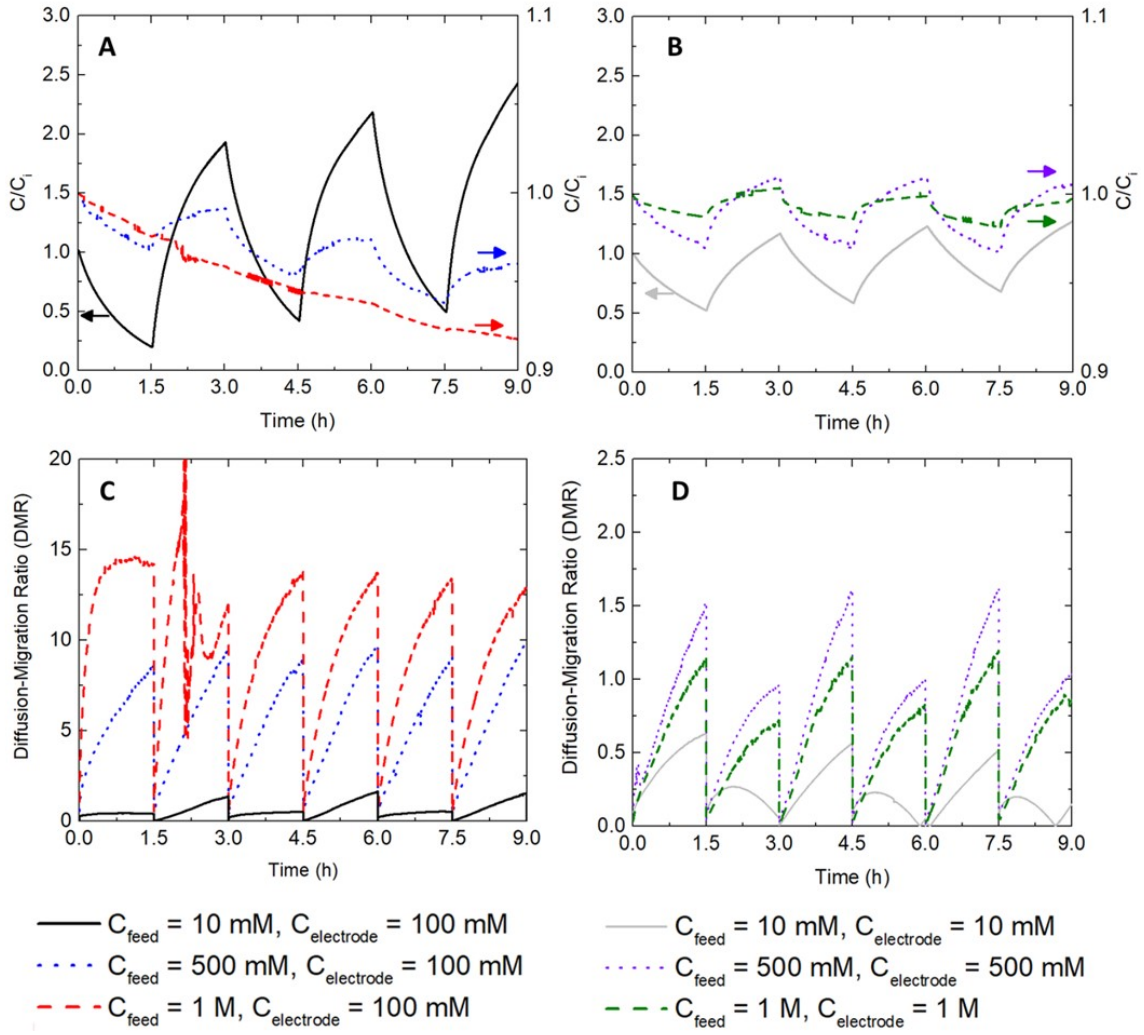

Figure 6.4: (A) Relative conductivity for mismatched feed and electrolyte, and (B) relative conductivity matching feed and electrolyte. (C) DMR for mismatched feed and electrolyte, and (D) DMR for matched feed and electrolytes.

to cycle. The electrochemical performance was stable (repeatable) in each cycle (Figure C.1). This indicates that attributing the increase in resalination is not due to an increase in current passing through the cell. Furthermore, the volume of each flow electrode and feed solutions did not change throughout the experiment, excluding effects such as leakage and/or osmotic transport. All tests were also conducted multiple times with various volume of flow electrodes (100, 300, and 500 mL). In each series of experiments, the observations remained the same (Figure SC.2).

When the concentration gradient was reversed ($C_f > C_e$), a decreasing trend was ob-

served in the feed concentration post each desalination-resalination cycle (Figure 6.4A, red/blue lines). Therefore, in these tests, the degree of desalination was greater than the degree of resalination. This trend appears to be valuable as the ultimate goal of the technology is to remove ions through electrochemical forces. By removing ions through a diffusive transport process, the impact of electrochemical separations may be overestimated. This is important when trying to compare and access the practicality of a certain separations process for water treatment and when comparing results to predicted thermodynamic models.

In addition to maintaining repeatable charge-discharge desalination performance, there are numerous other benefits to operating FCDI in a stable near equilibrium regime. Operating at an equilibrium will allow for an increase in energy recovery and could enhance the rate of desalination. Thus, energy recovery improves, as any resalination that occurs through diffusion limits the number of ions that transport across the membranes for the sole purpose of balancing charge. It is still uncertain if energy recovery will be required within FCDI systems; however, if it is a desired characteristic, resalination must occur solely through electromigration. Enhancement in the rate of desalination is also probable, especially in the case where the feed solution is less saline than the electrolyte. In this scenario, the ion transport processes during desalination are in opposite directions (diffusion and electromigration), which may result in partial resalination during the desalination process.

Evaluation of the ratio of the observed diffusion to migration (DMR)-based transport can be a means to access the propensity for diffusion to play an active role during either the desalination and/or resalination process. During each process (desalination or resalination), the DMR increases with time and with an increase in the feed concentration (Figure 6.4C). As described above, an estimate of the electromigration-based transport is accomplished through the use of the 1-D-based model, where experimentally observed current density serves as the primary input. An estimate of the potential magnitude of diffusive-based

transport uses the experimentally obtained feed concentration as the model input.

When the feed and electrode ionic strength differed ($C_f \neq C_f$), the DMR ratio ranged from 10 to 20 (Figure 6.4C). Conversely, during the matched experiments ($C_f = C_e$), DMR never exceeded four, and only approached this value at the end of a process, whereby the experiment is known not to be at an ionic equilibrium. The significance of the DMR reaching 20 (Figure 6.4C, red line) represents an electrochemical cell whereby the diffusive ionic transport is 20x greater than the electromigration-based transport. We do not anticipate that the diffusive transport is dominant across the ion-exchange membrane, yet when a large enough potential exists, the likelihood for partial transport through diffusion increases. In the matched experiments, the diffusive ionic transport only ever approached 4x that of electromigration. This low value promotes limited diffusive transport, and therefore nearly all observed ionic transport occurs through electromigration.

As stated above, this additional transport of ions through diffusion results in a direct reduction in energy recovery, and furthermore inhibits the system from achieving purely electrochemical separations. It should be noted that the total salt removed under the identical electrochemical conditions appears to be greater when $C_f \neq C_e$ rather than when $C_f = C_e$. Therefore, if the sole goal is the remove ions and reversible flow electrode performance is not required, the diffusive transport can appear as an advantageous effect. However, one should be careful to note the exact mode of separations (electrochemical and diffusive) when reporting performance values. Therefore, the DMR provides a means to assess if the performance can be attributed to electrochemical forces (e.g., electromigration) or if additional transport processes may play a role in mediating desalination or resalination. To mitigate any diffusive transport, we suggest operating and collecting performance metrics in cells where the DMR is less than five.

In addition to the diffusion effects associated with mismatched electrolyte and feed solutions, the concentration gradient across the membrane can alter the resistance of the membrane during operation. With a large gradient across the cell, resistance can vary

tremendously, reaching a maximum of 600 cm^2 (Figure C.3a) with the low concentration feed solution (10 mM). It is difficult to limit the resistance of a membrane in a low saline solution, but the gradient across the membrane can exacerbate the resistance. For ideal electrochemical performance, whereby low energy consumption is required, membrane resistance should be low.

The membrane resistance appears to decrease substantially when moving toward higher saline feed waters; however, in testing where the membrane was exposed to a gradient, the membrane resistance was almost 2x greater than that in testing with the ionic strengths matched (Figure C.3b). In addition to reducing the membrane resistance, the variability in the membrane resistance decreases. Variable membrane resistance can contribute to a decrease in performance over time.

An additional consequence of the mismatched electrode and electrolyte ionic strength is the potential to overestimate system performance values. During testing with elevated DMR values where C_f C_e, the ASAR was consistently greater than in testing with matched ionic strength $C_f = C_e$ (Figure 6.6A). The transport attributed to diffusion therefore overestimates the ASAR for the given electrochemical conditions. In particular, this is evident with the 1 M mismatch test, which displays by far the largest concentration difference between feed and electrode at the start of the cycle (ΔC = 900 mM). This led to both unusually high values for ASAR and CE (Figures 6.5A and C). In future cycles, as the system moves toward an equilibrium, the ASAR approaches a more reasonable value. When the cell moves away from an ionic equilibrium, accentuated performance values can be obtained, but are not true measures of the electrochemical desalination performance. Due to the emerging nature of FCDI systems, there is a need for performance metrics that accurately depict the potential advantages or disadvantages of electrochemical-based separation technologies. For these tests, maintaining tests near ionic equilibrium will allow performance metrics to access the separations potential of FCDI.

Finally, in addition to ionic gradients within the flow electrode cell, there are large pH

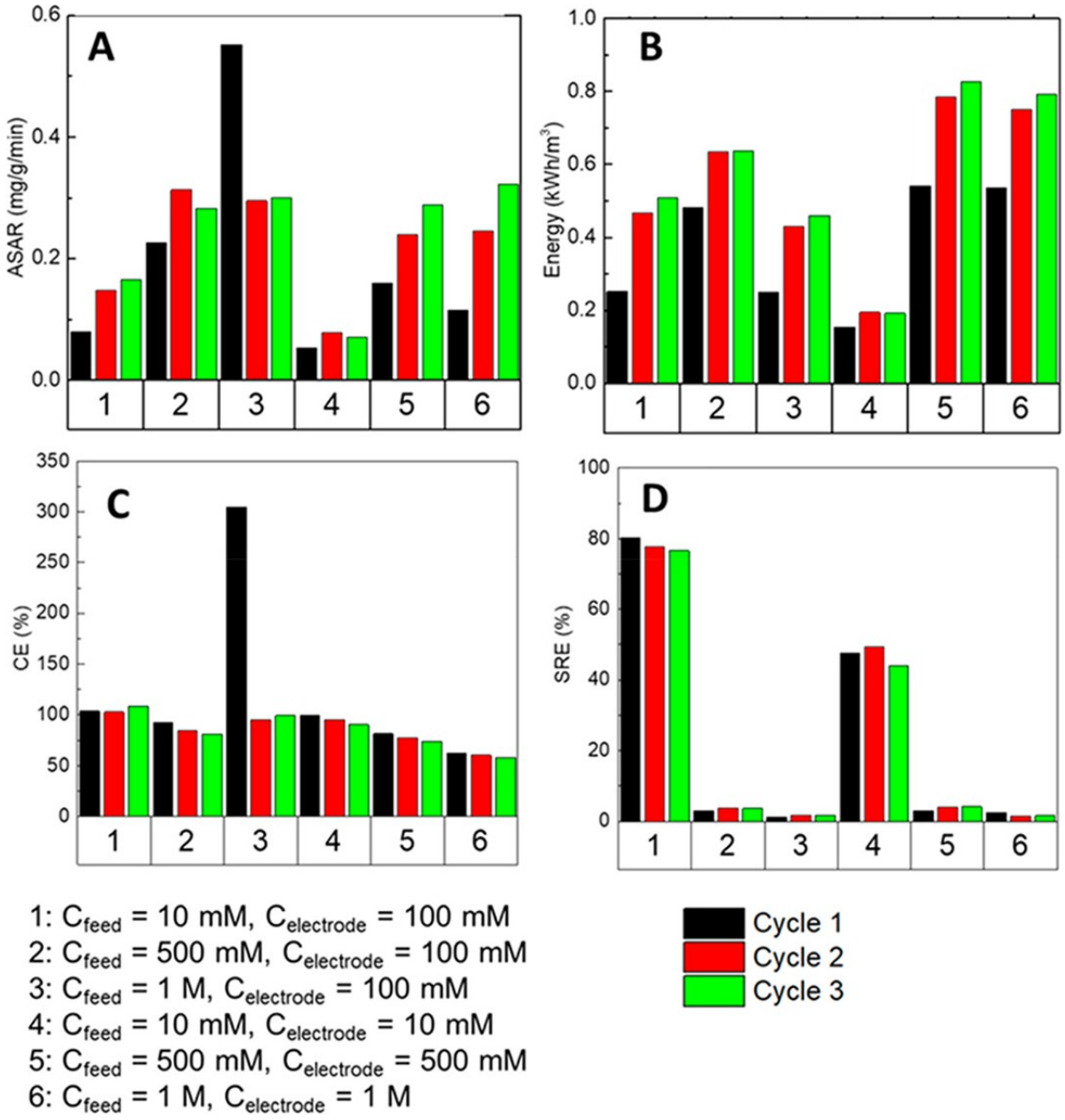

Figure 6.5: FCDI performance metrics: (A) ASAR, (B) energy consumed, (C) CE, and (D) SRE.

gradients that also can contribute to some of the performance variability. Generally, lower feed solutions (C_f = 10 mM) result in a negligible change in pH within the feed and/or electrolyte (Figure 6.6a), while larger saline feed solutions (C_f = 0.1-1 M) can result in a significant drop or rise in pH (Figures 6.6bd). The change in pH correlates with the current or total charge that passes through the circuit. Side reactions, namely water splitting, are the source of the proton consumption and production and are hard to mitigate in

a FCDI system operated with two electrodes. While the pH stabilizes, the pH change in the feed by as much as four to eight pH units can be disadvantageous for water treatment and membrane resistance and ultimately can also aid in moving the system away from an ionic equilibrium. The change in pH could therefore promote the transport of alternative ionic species (proton or hydroxide ions) rather than transport of ionic species (Na^+ or Cl^-). Previous investigations have eliminated this pH gradient through recirculating the two flow electrodes in one reservoir, but this is at the expense of energy recovery.

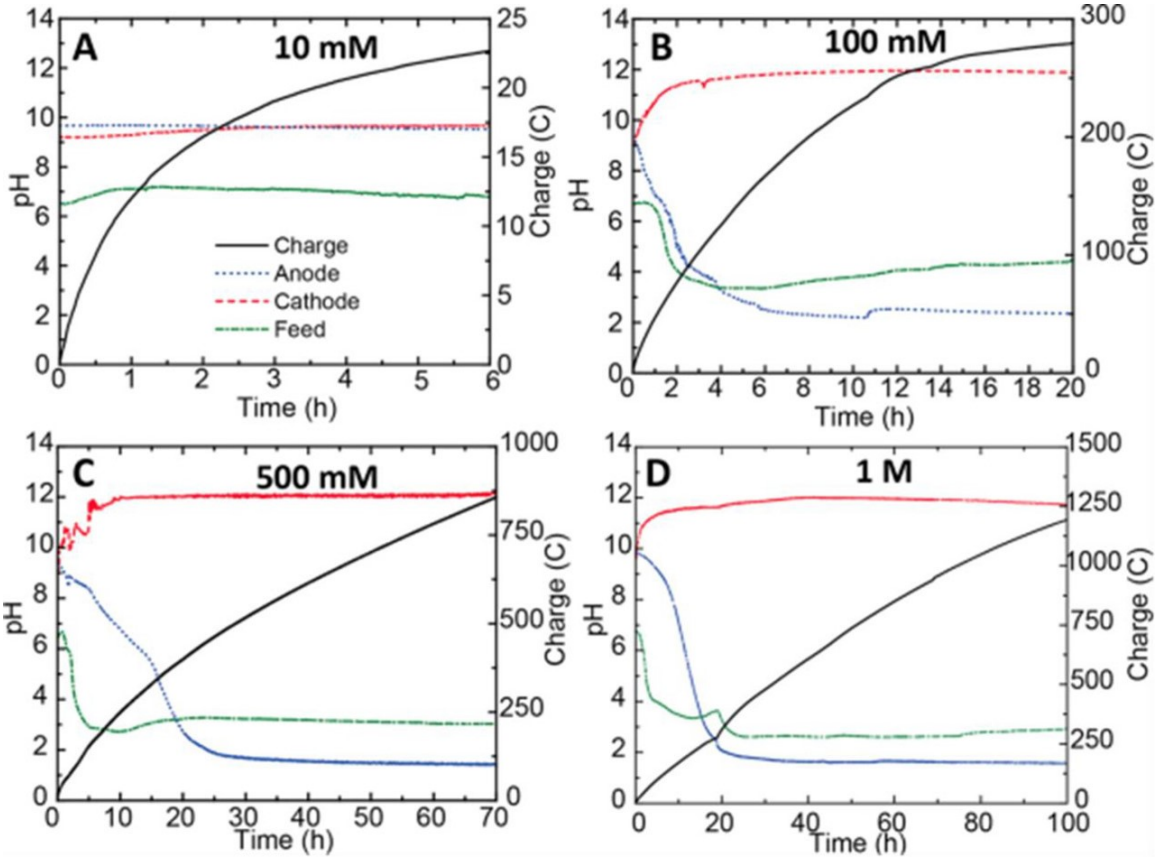

Figure 6.6: pH fluctuations and accumulated charge in the anode, cathode, and feed with (A) 10 mM feed, (B) 100 mM feed, (c) 500 mM feed, and (d) 1 M feed solutions.

The results obtained here offer some suggestions regarding the role variable ionic strength ($C_f \neq C_e$) plays on enhancing or diminishing long-term desalination performance within a FCDI system. The variable concentrations can exist due to experimental conditions or can arise through the production or consumption of protons due to side reactions. In either

case, the impact is the addition of potential transport of ionic species through diffusion rather than purely electromigration-based transport. Because the ultimate goal with electrochemical separations is to move ions via electrochemical forces, diffusion should be limited. Matching the feed-electrolyte concentrations can mitigate this issue, but doing so requires greater energy input and limits the apparent salt removal.

6.6 Conclusion

Matching the ionic strength of the electrode and electrolyte to that of the feed promotes greater reliability in the reported desalination performance metrics (salt removal and ASAR, energy) in a FCDI system. For more dilute feeds, mismatched electrodes with a higher ion concentration can appear to improve desalination performance through minimizing ohmic resistances, but a gradual increase in the feed solution is disadvantageous for promoting reversible system performance. When the feed concentration was much greater than that of the electrode, higher concentration gradients hindered the ability to divert salt into a waste stream, preventing full energy recovery. Therefore, characterizing the degree of diffusive transport between the feed and electrode is imperative for understanding and predicting the true electrochemical performance of FCDI systems. This will also become increasingly important as researchers move toward treating high saline solutions (seawater/produced) with FCDI systems.

CHAPTER 7
THERMODYNAMIC EVALUATION OF ELECTRODE STORAGE FOR CAPACITIVE DEIONIZATION IN BATCH AND CONTINUOUS MODE

7.1 Abstract

We examine and quantitatively compare capacitive deionization (CDI) processes which do not a have a chemical charge, which have a fixed chemical charge, and those that have variable chemical charge due to redox-active electrode. The main focal points from this research are: (1) evaluating ideal, equilibrium-based cycles to determine thermodynamically if Faradaic CDI (FaCDI) can attain higher thermodynamic efficiency, (2) evaluating short-term cycles in continuous mode as well as through a new means for predicting batch-mode performance, and (3) extending batch-mode performance over a range of porous electrodes to determine fitting isotherms as well as free energy, entropy, and enthalpy. From this study, we conclude that FaCDI can be utilized to reduce energy consumption by as much as 12%, can double charge efficiencies when operated in short-term continuous mode, and can increase full adsorption capabilities by approximately 1.5 x over traditional CDI. This study builds on research on redox-active species that has been previously developed, and provides new insight into the computational analysis of predicted Gibbs free energy, entropy, and enthalpy of adsorption.

7.2 Introduction

The operating principle of capacitive deionization (CDI) involves electrosorption of aqueous ions onto porous electrodes, effectively desalinating either a continuous or a batch feed stream [183]. Porous electrodes are by far the most commonly investigated CDI electrodes for charge storage, owing to their high specific surface area, along with their good chem-

ical and thermal stability. Among the materials used to construct these carbon electrodes include activated carbon fibers, aerogels, mesoporous, and carbon nanotubes [28, 40, 44, 45]. The electrosorption process is governed by the formation of an electrical double layer (EDL) at the electrodes. EDL theory is commonly described using one of two models: Either the Gouy-Chapman-Stern (GCS) model, or the more recently developed modified Donnan (mD) model, which takes into account overlapping double layers in regions with a sufficiently small pore size [94]. The mD model is typically employed at lower concentrations, $C < 50$ mM, which is of greater interest for CDI studies.

One new technique that has recently been explored is implementing chemical charges on surfaces of the electrodes [184], such as sulfonic, amine, or carboxylic groups on the micropores of the electrode materials [185, 186, 187]. If the chemical charges are introduced at the electrodes with the same sign of surface charge (i.e. opposite cell terminal), cell performance can be enhanced (ECDI). However, this chemical charge can be further modified by using redox-active materials [188], such as surface-modified with redox-active polymers. By incorporating such redox-active species, chemical charges are not fixed, but vary based on cell voltage and other related operating conditions. This allows for an effective tuning of the CDI process to enable even more optimized performance. As the redox-active species promote Faradaic reactions but maintain traditional capacitor-like behavior, the charges were initially termed pseudocapacitive separation [188]. However, some pseudocapacitors typically involve a separate mechanism through which ions are stored, the process has been more recently called Faradaic CDI, a terminology which we will use in this study. Intercalation-based materials, such as manganese oxide (MnO_2), ruthenium oxide (RuO_2), cannot be modeled similarly to FaCDI process, since the redox reactions do not take place on the surface or the electrode, but rather with the porous electrode structure, thus requiring a full 1-D analysis of charge storage inside the electrode [189, 190, 191].

Previously, the performance of CDI, ECDI, and FaCDI had been developed and compared in short term continuous mode desalination cycles; these studies also examined and

compared ion concentration and point of zero charge (PZC) [192]. In this study, we seek to expand the comparison of electrochemical sorption processes by looking at equilibrium conditions to examine ideal, fully reversible cycles, and compared theoretical performance based on the different charge mechanisms. Secondly, we will examine (computationally) performance in short-term batch mode simulations to examine adsorption isotherms and compare standard values of adsorption. By examining these terms of adsorption, we can determine spontaneity, randomness, and whether the process is exothermic or endothermic. This has been previously done experimentally in published literature for various adsorption processes, including CDI [73, 71]. As computational studies are not typically done for evaluating these characteristics of adsorption processes, we hope that the results obtained and discussed can be of future benefit for studying a wide range of different adsorption processes.

7.3 Theory

7.3.1 Modified Donnan theory

We consider a CDI cell with a monovalent salt (in this case NaCl, such that valencies z_- and z_+ are assumed as unity). The carbon electrode consists of two primary regions: macroporous and microporous. A charge balance within the electrode consists of three different types of charge: ionic, electronic, and chemical charge:

$$\sigma_{ionic} + \sigma_{elec} + \sigma_{chem} = 0 \tag{7.1}$$

Thus, if σ_{chem}=0, as in traditional CDI, the magnitudes of charges are equal, and they are commonly assigned a singular value σ. The charges are volume based, averaged by the micropore volume. If divided by the Faradaic constant, then the charges will be in units of mol/m^3, or mM, the same unit as ion concentration C. All types of charge values will henceforth be referred to as in units of molar concentration.

We will consider three different cases for CDI testing: Traditional CDI (Figure 7.1A), in which no chemical charge is used (σ_{chem}=0), enhanced CDI (ECDI) (Figure 7.1B), in which a chemical charge value σ_{chem} is fixed to alter the point of zero charge (PZC) of the system at equilibrium, and Faradaic CDI (FaCDI) (Figure 7.1C), in which chemical charge σ_{chem} varies based on redox reactions taking place at the electrode surface.

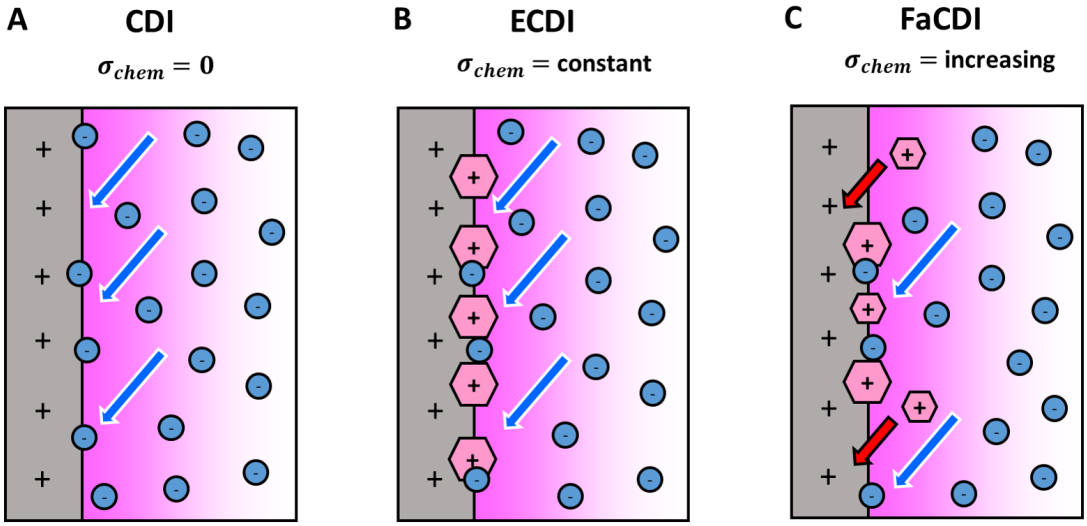

Figure 7.1: Schematic of the charging of micropores of a CDI cell, depicting (A) traditional CDI process with no chemical charge, (B) enhanced CDI process with fixed/immobile chemical charge, and (C) Faradaic CDI process with variable chemical charge which increases during the charging stage, and decreases during discharging.

As we are mainly interested in how the governing behavior for these electrodes affect overall cell performance, we will neglect the spatial variations within the electrode structure and the feed. This is a very important simplification to make, and is reasonable if we assume mass transfer limitations are negligible and the fluid is well mixed within the cell. With the mD model, if we assume a symmetric cell, then we can determine the total cell voltage by:

$$V_{cell} = 2(\Delta V_S + \Delta V_D) + IR \tag{7.2}$$

where V_S represents the potential in the Stern layer and V_D is the potential in the Donnan layer. The cell voltage also comprises the ohmic drop IR, in which the resistance varies as

a function of cell concentration as well as geometry and electrode/electrolyte properties. The Stern layer voltage varies with the electronic charge:

$$\Delta V_S = \frac{\sigma_{elec} F}{C_{St}} \tag{7.3}$$

where C_{St} represents the Stern layer capacitance, given in units of F/m^3. This capacitance is also given as a parabolic variation, based on approximate curve fitting to a parabolic shape [93]:

$$C_{St} = C_{St,vol} + \alpha {\sigma_{elec}}^2 \tag{7.4}$$

Here, we will use $C_{St,vol}$ = 150 F/m^3 and α = 30 F m^3/mol^2. The differences between Eq 7.4 and constant Stern layer capacitance are negligible but still do exist (Figure D.1). The Stern layer capacitance has also been reported to display some variations with the operating temperature, but the exact variation has been somewhat unclear in the literature [193, 194, 156]. Furthermore, since we are considering only small temperature variations, this contribution will be neglected.

For the diffuse layer, the mD model assumes that the micropore diameter is much smaller than the Debye length λ_D, and as such, the Debye length is not explicitly needed in the calculation of diffuse layer potential. Instead of a Debye length, the mD model, assumes that there exists a Donnan potential located at the macropore-micropore interface. This Donnan potential is given as [93]:

$$\Delta V_D = -sinh^{-1}\Big(\frac{\sigma_{ionic}}{2C_{mA}e^{\mu_{att}}}\Big) \tag{7.5}$$

where μ_{att} is an ionic-based attraction term between charges in the porous carbon structure. This is usually much more significant for examining CDI at higher concentration values and has been used for enabling mD to function for both high and low ranges for CDI. However, since only lower concentration values for CDI have been examined, the

value and contribution of μ_{att} will be neglected in this study.

The primary difference between CDI, ECDI, and FaCDI is the presence of the chemical charge σ_{chem}, which alters the performance of the double layer as given by equations 7.3 - 7.5 (Figure 7.1). The micropore concentration is related to macropore concentration using the Boltzmann distribution:

$$C_{mi} = C_{mA}(exp(-\Delta V_D + \mu_{att}) + exp(\Delta V_D + \mu_{att})) \tag{7.6}$$

where again we neglect the attractive term μ_{att} for this study.

If the cell is assumed symmetric, then the redox active polymer undergoes a single electron exchange during the charging process: e.g. O + e^- $\rightarrow$ R^- for oxidant O and reductant R. For the Faradaic reactions, the chemical charge σ_{chem} varies as a function of the Stern layer voltage C_{St} and other properties constant based on the characteristics of the electrode. The equilibrium (dimensionless) Stern layer voltage $\Delta V^0_{S,eq}$ is given as:

$$\Delta V^0_{S,eq} = V_T ln(\frac{k_{R,A}}{k_{O,A}}) \tag{7.7}$$

7.3.2 Transient-based considerations

For the transient analysis, we follow the setup of [192] similarly, but make a few new additions. Mass balance over the cell is given as:

$$V_{tot}\frac{dC_{mA}}{dt} = \phi(C_{in} - C_{mA}) - \frac{1}{2}J_{ions} \tag{7.8}$$

where the ionic fluxes are assumed equivalent for the anode and the cathode, and here are approximated as:

$$J_{ions} = \frac{I}{F} \tag{7.9}$$

For the Faradaic reactions in FaCDI, chemical charges change over time according to:

$$\frac{d\sigma_{chem}}{dt} = -R_F \tag{7.10}$$

The chemical charge generation follows first-order kinetics with reaction-rate R given as:

$$R_F = k_R \sigma_{chem} exp\Big(-\frac{\Delta_{S,eq}}{2}\Big) - k_O\Big(\Gamma - \sigma_{chem}\Big) exp\Big(\frac{\Delta_{S,eq}}{2}\Big) \tag{7.11}$$

where Γ represents the maximum chemical charge that may exist at the electrode surface (a constant), and ΔS,eq is the Stern layer voltage. The current within the cell, I, is related to the ionic charge by:

$$\frac{d\sigma_{ionic}}{dt} = -\frac{I}{m_e v_{mi,e} F} \tag{7.12}$$

where m_e and $v_{mi,e}$ represent the mass and gravimetric micropore volume of the electrode. Finally, the electrical charge magnitude at the surface can be related to chemical and ionic charges using the electroneutrality condition by Eq. 7.1. When considering batch mode tests, the most important modification to make is that to the mass balance (Eq. 7.8). In batch mode, the inlet concentration is not constant, but will change gradually as a function of the total batch volume, the outlet feed concentration, and the total volume that passes through the cell at an instant in time. As such, we make the approximation for the updated inlet concentration as:

$$C_{in,i+1}(V_{batch} + V_{tot}) = C_{mA,i+1}\phi\Delta t + V_{tot}C_{mA,i} + (V_{batch} - \phi\Delta t)C_{in,i} \tag{7.13}$$

where Δt represents the change during one instant in time.

Unless where explicitly stated, all constant parameters, material, and operational pa-

rameters were borrowed and replicated from the previous studies [184, 192] and examined to fit our new evaluation and cycle developments.

7.3.3 Adsorption thermodynamics

Most adsorption isotherms studied have been gas adsorption isotherms, but isotherms can also be used for liquid solutions, varying as a function of concentration. Adsorption isotherms have been modeled in several desalination studies [195, 196, 197, 198, 199]. Of the models that exist to predict the variation of electroadsorption as a function of equilibrium concentration, the two most commonly cited in literature are the Langmuir isotherm and the Freundlich isotherm.

The Langmuir isotherm model, while initially developed for gas-solid adsorbent pairs [67], is also applicable to liquid solutions. In such solutions, the adsorption varies as a function of concentration at equilibrium, C_{eq}, typically given in mg/L. The Langmuir model assumes fully homogeneous, monolayer adsorption with no interaction of the adsorbed species in the plane of the surface. Furthermore, the model assumes that there is a limit to the maximum quantity of total adsorption by the adsorbate. The governing equation for the Langmuir adsorption isotherm is given as:

$$q_e = q_{max} \frac{K_L C_{eq}}{1 + K_L C_{eq}} \tag{7.14}$$

where K_L is the Langmuir constant, given in units of q_{max}, which represents this maximum adsorption. The concentration C_{eq} is determined as the equilibrium concentration for the adsorption process. In continuous mode processes this can be assumed as the inlet concentration, but if the process is done in batch mode with a finite volume constantly circulated during adsorption, the equilibrium concentration is given as the average between inlet and dilute concentration.

A second isotherm that can be used to determine ion sorption capabilities is the Freundlich isotherm. This model extends beyond monolayer adsorptions of the Langmuir

model and assumes that multiple layers exist through which sorbent can be stored within sorbate. Unlike the Langmuir model, however, the Freundlich isotherm is semi-empirical [68] and does not have a purely theoretical basis behind its values. The Freundlich isotherm is preferred when lower concentrations of solute are used [69], and commonly for desalination it is directly compared with the Langmuir adsorption process. The Freundlich isotherm is given as a power relation:

$$q_e = K_L {C_{eq}}^{1/n} \tag{7.15}$$

where K_F is a constant, related to heat of adsorption, given in units of $(L/mg)^{1/n}$, and 1/n is a constant power parameter, which indicates the heterogeneity of the solution and indicates the tendency for which the sorbent readily adsorbs.

For desalination processes, the adsorption isotherms can be developed by examining salt removal with experimental operating conditions as the control and the initial feed concentration as the variable. A plot of C_e vs. q_{eq} can be fitted to the Langmuir and/or Freundlich adsorption isotherms to predict the extent to which monolayer or multilayer adsorption holds under the given conditions based on R^2 values [69]. The chosen equilibrium constant K_{eq} is then multiplied by appropriately related parameters to make its value dimensionless. Regardless of which isotherm is used, it is important to perform this unit conversion correctly, as it has been cited as a source of error in various adsorption isotherm literature [70].

If evaluating a range of different temperatures as well as concentrations, isotherms can further identify further characteristics of the adsorption process. The equilibrium constant K_{eq} can be related to Gibbs free energy of adsorption by [72]:

$$ln(K_{eq}) = -\frac{\Delta G}{RT} \tag{7.16}$$

When $\Delta G < 0$, the process is said to be spontaneous; positive values are considered

non-spontaneous. The Gibbs energy can also be used to calculate related enthalpies and entropies of adsorption:

$$\Delta G = \Delta H - T\Delta S \tag{7.17}$$

The relationship between ΔG, ΔH, and ΔS can be plotted as a linear variation with T. More specifically, the variation of ln(K_{eq}) vs. 1/T can be used to determine ΔH and ΔS via linear regression. Thus, ΔH and ΔS can be used to further characterize the adsorption process. If ΔH is positive, it is indicative of an endothermic reaction; if it is negative, it is indicative of an exothermic reaction. Furthermore, the magnitude of the enthalpy of adsorption allows for prediction of characteristics for some adsorption processes: If the enthalpy values are below 84 kJ/mol, the adsorption is considered physiosorption; whereas values from approximately 80 - 420 kJ/mol are considered chemisorption [67, 71]. Alternatively, it has been suggested that chemisorption process can occur if the ΔH values are negative, regardless of their magnitude [73]. The entropy of adsorption indicates the affinity between sorbent and sorbate. If the value is higher, there is more favorable adsorption due to greater degrees of freedom from the sorbate. If the entropy value is negative, the activity of sorbent at the solid-liquid interface is reduced, essentially making the adsorption process more difficult [74].

The determination of ΔH and ΔS experimentally has been done for salt water desalination on various electrodes, for NaCl sorbent as well as other ions in aqueous solutions [73, 71]. However, the breadth of experimental data collected is limited since ranges of both concentrations and temperatures are required to determine a single ΔH and ΔS value. As a result, the viability of exploring fundamental adsorption processes with different values/ranges of multiple parameters is further challenged. Computational studies can relieve the arduous task of running many experiments, and more importantly, can easily assess the sensitivity of ΔH, ΔG, and ΔS to a wide range of operating conditions.

In short-term batch and continuous mode desalination tests, we will evaluate thermo-

dynamic energy efficiency (TEE) and Coulombic efficiency (CE) among the three CDI storage mechanisms.

7.4 Results and Discussion

7.4.1 Steady-state based cycles

The cycle demonstrated in Figure 7.2 is for a case of C_0 = 20 mM, C_D = 1 mM, water recovery ratio α=0.5. The cycle operated using four stages: Initial charging from initial concentration C_0 to diluate concentration C_D, switching to return to initial concentration C_0 while maintaining constant ionic charge σ_{ionic}, discharging to a brine concentration, and switching back to the initial concentration C_0, again at constant σ_{ionic}. This operation is thus similar to the processes described in Chapter 5.

The benefits of Faradaic CDI cycles is the reduction of work through the tuning of chemical charge during cycling. With enhanced CDI, the voltage range is kept nearly constant, a magnitude of 0.05 #/nm^2 of surface charge. This charge is similar to what had been previously observed [192], where ECDI shifted the PZC to approximately 0.5 V. The ECDI cycle reduces the maximum charge reached, it could limit work relative to CDI, but this comes at the expense of ionic charge values dropping below zero as the cycle is further discharged. This negative charge is the result of the fixed chemical charges which remain active during the discharging stage, when they are not needed, resulting in an increase in unnecessary input work to compensate for the inclusion of these fixed charges. This issue is resolved when the redox active chemical charges are introduced in Faradaic CDI. The chemical charge composition increases gradually during the charging stage to take advantage of the reduced charge during ECDI (oxidation process). During the discharge, the reverse reaction occurs in which the minimum cycle charge returns to the value of nearly zero for CDI. While the voltage ranges remain the same as defined for this steady-state based cycle, the charge range is decreased by nearly 12%, corresponding to a total 10% reduction in the net work for this particular cycle.

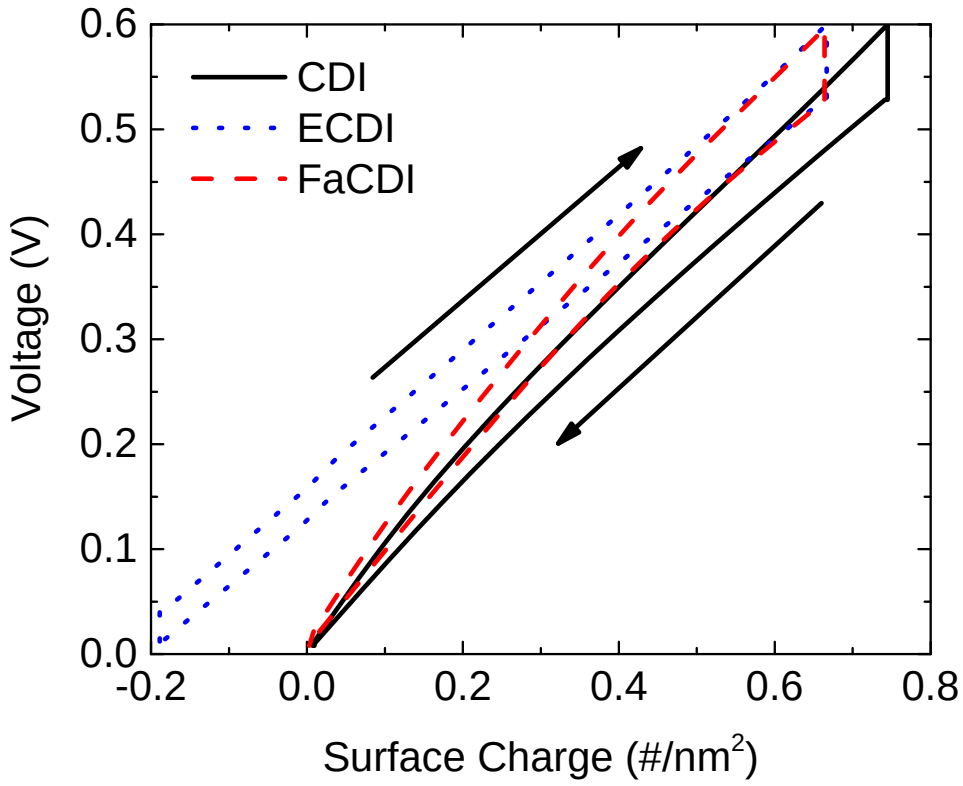

Figure 7.2: Depiction of a four-stage CDI cycle taking into account variations in cell charge with applied voltage and concentration. For this cycle C_0 = 20 mM, C_D = 1 mM, and water recovery ratio α = 0.5.

Next, we examine and compare the variations in cycle performance with different degrees of desalination for the different cycles tested. Examining the TEE as functions of salt removal ratio as well as water recovery ratio have been commonly examined in literature [146, 162]. With a constant water recovery ratio of 0.5, the benefits of FaCDI are present, but marginal (Figure 7.3A). Due to the presence of surface charges, ECDI performs below CDI when no chemical charge is implemented, unless in the cases where $\Delta C/C_0$ approaches unity; CDI approaches up to 4.6% TEE whereas Faradaic CDI only reaches 3.7% and CDI approaches 3.5%.

Examining the effect of water recovery ratio displays similar trends with FaCDI receiving a boost in TEE (Figure 7.3B), and this boost is increased further, when water recovery

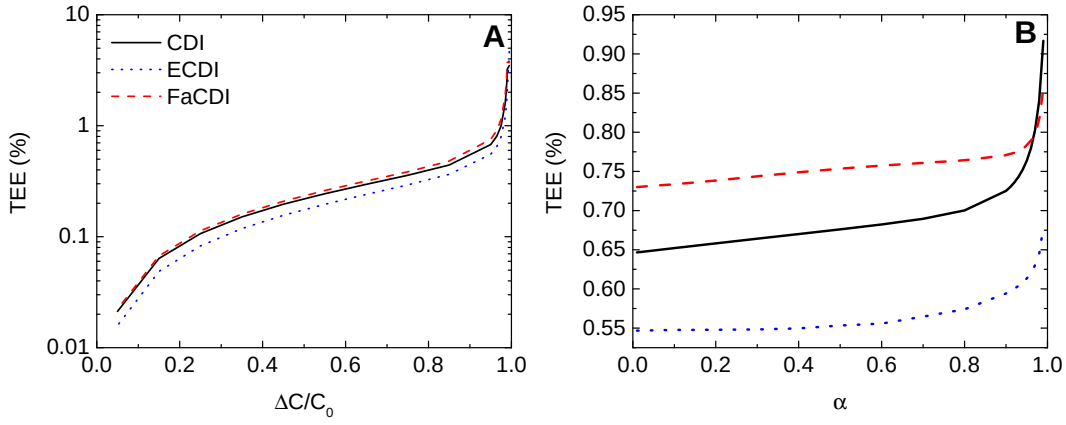

Figure 7.3: Effect of thermodynamic energy efficiency (TEE) as functions of (A) relative salt removal ratio (C_0 = 20 mM, C_D = 1 mM) and (B) water recovery ratio (C_0 = 20 mM, C_D = 1 mM).

ratios approach unity. Normally, it is not realistic for water recovery ratios to obtain values as high as 0.99, although recent literature has shown feasibility in achieving 90% water recovery ratios experimentally [200]. However, we must note that water recovery ratios above 80% should be handled with caution as the brine concentrations obtained, while smaller in volume, consist of concentration values not adequately suited for the modified Donnan model. Including considerations such as the attractive ion force coefficient μ_{att} may allow for more reliable estimates of values that can be compared with both modified Donnan as well as Gouy-Chapman-Stern models.

7.4.2 Short-term batch and continuous mode

Short-term tests run in continuous mode and batch mode will determine the practicality of implementation as well as consideration regarding appropriate storage mechanisms. Both sets of tests run in continuous mode (Figure 7.4A) and batch mode (Figure 7.4B) are shown after charging at 0.6 V and discharging at 0 V for three cycles, to ensure that cycling stability is reached. The continuous mode conditions mirror those of [192], but we further examine some of the performance parameters of this particular cycle. Here, FaCDI demonstrates a clear benefit in the minimum salt capable of removal, but this also comes with

the trade-off of higher brine concentrations and higher current values (Figure D.2A). Regardless, the FaCDI case as well as the CDI case exceed CDI for both TEE and CE: In continuous mode, the CDI cycle attains a TEE of 0.008%, but the TEE of FaCDI is nearly 10x as much due to greater overall dilute concentration in the system, at nearly 0.07% (for ECDI here, TEE = 0.0007%; thus, no benefit in the performance is obtained). The variable chemical charges enable the decaying current to be retained longer (Figure D.2B), but this does not display a positive input on the cell's overall performance as demonstrated by the TEE. Additionally the FaCDI cycle nearly doubles the overall cell charge efficiency; CDI results yielded an overall CE of 49% while FaCDI approached 98%. ECDI showed an improvement in this case over CDI, reaching a CE of 65%. The reason why ECDI increased in CE but not TEE is due to Gibbs free energy of mixing, which is dependent on influent and dilute concentration; the slightly lower diluate for ECDI displayed a clearer benefit for the integrated salt removal over time than for the logarithmically-dependent TEE.

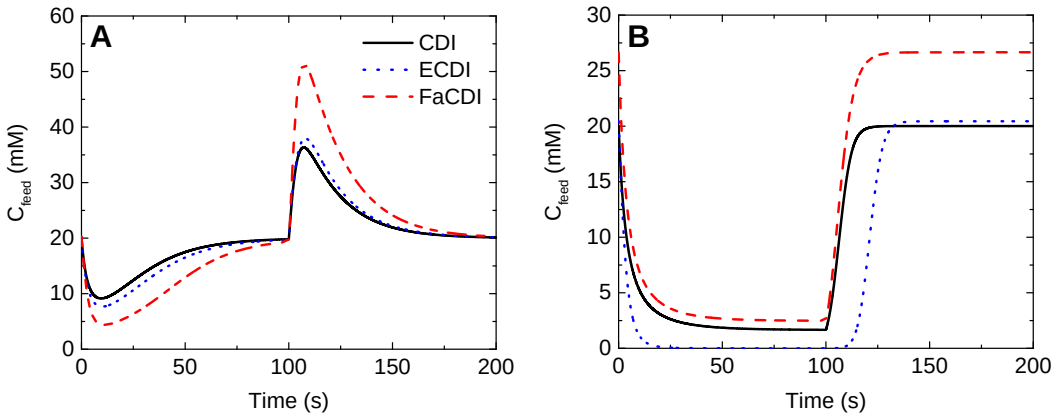

Figure 7.4: Comparison of effluent salt concentration for adsorption desorption cycles in (A) batch mode, (B) continuous mode.

In batch mode, the higher current for the FaCDI cycle again demonstrates a clear benefit; in this case, that all of the salt within the solution is removed while recovering to nearly the same initial concentration. The CDI tests are not able to approach 100% removal due to the poorer retention of the current. Regarding the ECDI case, the concentration values are

offset due to an increase in the calculated concentration value after the discharging stage in the first cycle, which was re-examined in all continuing cycles. Also, since we only consider constant voltage and the charge/discharge times are short, the excess discharging seen by ECDI in Figure 7.2 is eliminated.

In addition to the higher salt removal, another subtle benefit of the FaCDI cycle is the delayed recovery during the discharging stage by about 10% of the discharging time. This allows for a further boost in the desalination performance of FaCDI in batch mode: thermodynamic efficiency reaches 0.12% for CDI and 0.58% for CDI and ECDI; comparable with values to the steady-state cases shown in Figure 7.2. Due to the increased retention of nearly 0 V during initial discharge stage, TEE is increased to 4.4% for FaCDI, a nearly 8x increase over ECDI. Furthermore, CE values still demonstrate a slight increase while batch mode tests under nearly perfect conditions produce 95% efficiency for CDI and 94% for ECDI, FaCDI peaks at 98%. Thus, if appropriately tuned with the right electrode material properties, redox-active electrodes exhibit clear benefits for both short-term and long-term tests with nearly ideal conditions.

7.4.3 Development of isotherms and adsorption characteristics in batch mode

Tests using parameters from short-term batch mode studies

The batch mode tests from Figure 7.4B were taken and subsequently examined over a larger range of cycles. By increasing the influent salt concentration while keeping all other parameters constant, an adsorption isotherm can be generated and then compared with the Langmuir and Freundlich theoretical predictions. Adsorption isotherms shown in Figure 7.5 vary in order to obtain adsorption enthalpy and entropy values. It is predicted that in batch mode tests, temperature should exhibit increases in salt removal due to benefits of increased thermal voltage (in addition to, while not present in this model, higher ionic conductivity with temperature).

In Figure 7.5 the results are plotted out of concentrations of 100 mM or approximately

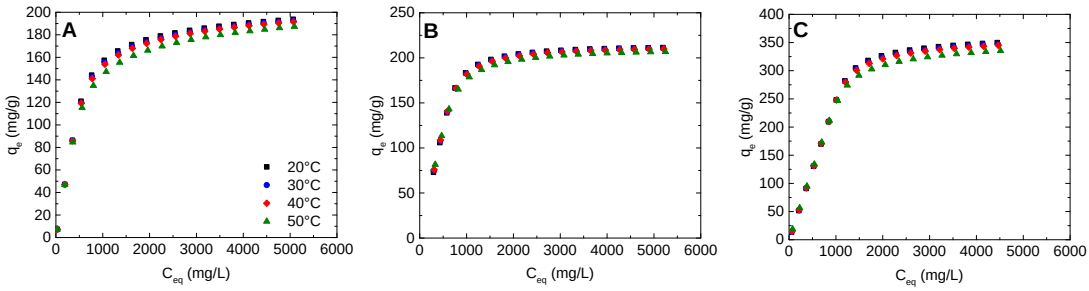

Figure 7.5: Batch-mode Langmuir adsorption isotherms. (A) CDI, (B) ECDI, (C) FaCDI.

6 g/L. The equilibrium concentrations are not the same across electrode considerations or even temperature, because it is dependent on the total cycle desalination performance (as described in Eq. 7.14 for the definition of equilibrium concentration) and not just the inlet concentration. Since FaCDI exhibited the greatest short-term salt removal, it follows for it to have lower salt concentration. While adsorption isotherms previously have not attained values higher than 20 mM with CDI, here it is necessary to estimate reasonable fitting parameters for the Langmuir and Freundlich adsorption isotherm. In all graphs it is clear the adsorption limit is approached when C $\rightarrow$ 100 mM; however, its value is notably different for each of the CDI cases tested. The ECDI case is about 20 mg/g higher than CDI, a benefit corresponding to short term tests in continuous mode as well as batch mode, with higher removal relative to the starting concentration.

For FaCDI, the perceived adsorption limit is higher, at over 350 mg/g, but the performance still appears to show a clearer leveling off appropriate for the Langmuir isotherm.

All of the results presented here are confirmed through the performance of an appropriate regression analysis as shown in Tables 7.1-7.3. On average, R^2 for the Langmuir isotherm proved to be a much better fit than for the Freundlich isotherm. We also notice that the perceived q_m values are substantially higher than those which have been previously shown for adsorption isotherms in CDI literature. We hypothesize that it is because of the larger removal capabilities of a theoretical cell, as opposed to one experimentally designed. Further, the total volume assumed for the carbon is relatively low, without taking into ac-

count additional challenges that can arise in its ion storage during charging, such as cell resistance, ion mixing instability, and tortuosity.

Table 7.1: Fitting parameters for Langmuir and Freundlich isotherms and regression coefficients of CDI, short-term.

Parameter	20°C	30°C	40°C	50°C
K_L	0.00149	0.00153	0.00157	0.00171
K_F	0.2805	0.2759	0.2716	0.2562
q_m	265.71	262.57	259.56	248.73
n	0.3240	0.3208	0.3178	0.3079
R^2 (Langmuir)	0.9289	0.9295	0.9304	0.9361
R^2 (Freundlich)	0.7573	0.7602	0.7633	0.7781

Table 7.2: Fitting parameters for Langmuir and Freundlich isotherms and regression coefficients of ECDI, short-term.

Parameter	20°C	30°C	40°C	50°C
K_L	8.4406E-4	8.5862E-4	8.7336E-4	9.3366E-4
K_F	0.5472	0.5463	0.54551	0.5429
q_m	303.13	298.06	293.08	274.10
n	1.0999	1.1025	1.1058	1.1251
R^2 (Langmuir)	0.9981	0.9981	0.9982	0.9984
R^2 (Freundlich)	0.8557	0.8575	0.8594	0.8673

Table 7.3: Fitting parameters for Langmuir and Freundlich isotherms and regression coefficients of FaCDI, short-term.

Parameter	20°C	30°C	40°C	50°C
K_L	2.4801E-4	2.5649E-4	2.6542E-4	3.0577E-4
K_F	0.7023	0.6948	0.6871	0.6554
q_m	1021.4367	989.7618	958.6854	841.8838
n	3.0896	2.6861	2.3700	1.5955
R^2 (Langmuir)	0.9982	0.9979	0.9976	0.9961
R^2 (Freundlich)	0.9113	0.9094	0.9075	0.9002

With the Langmuir isotherm values obtained, we can now generate van't Hoff plots to analyze variations in sorption values with temperature. We non-dimensionalize the Langmuir isotherm constant K_L (in L/mg) by multiplying it by a factor of 10^6 (10^6 mg/L for density of water) and plot its logarithm vs. the inverse of temperature as a van't Hoff

plot. Steeper slopes indicate larger adsorption enthalpies, and more positive values of K will indicate larger adsorption entropies. When only the range 1-20 mM is considered, the Faradaic CDI deviates significantly. In this case, ECDI has nearly the same slope as CDI, but offset by a value of about ln(K) = 2, indicating the entropy values may differ but enthalpy values (determined by the slope) should remain nearly the same. When using the full concentration range to create adsorption isotherms from Figure 7.5, the behavior of FaCDI is more closely aligned with CDI and ECDI, differing by magnitude of ln(K) = 2 at most. We conclude that the prediction of adsorption isotherms is strongly dependent on the concentration range chosen, if the cycle's overall performance is nearly optimized. Thus, it may be appropriate to consider expanding higher concentrations of salt removal capabilities to verify how closely maximum adsorption capabilities are approached.

Using the van't Hoff plots presented in Figure 7.6, enthalpy, entropy, and Gibbs energies of adsorption are predicted via a linear fit. To fully visualize the sensitivity of these parameters, we scanned over the applied cycle potential from 0.5 to 1.5 V. Again, we remind the readers that the nominal value for voltages during batch and continuous mode short-term tests up to this point was 0.6 V.

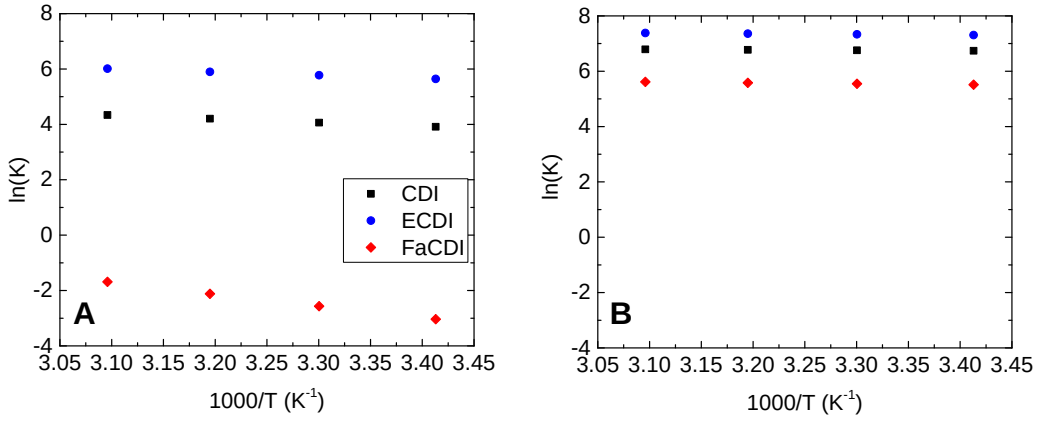

Figure 7.6: van't Hoff plots for ion electrosorption. (A) Over concentration range $1 < C_{feed} < 20$ mM, (B) Over concentration range $1 < C_{feed} < 100$ mM.

When considering only the range from 1 to 20 mM (Figure 7.7), a nearly linear trend

is shown by the input voltage and the enthalpy of adsorption, which indicated that greater applied potential would make the reaction more endothermic. The value of DH indicates if a sorption-based process is physiosorption ($<$ 80 kJ/mol) or chemisorption (80 kJ/mol - 420 kJ/mol). While none of the values shown in Figure 7.7A appear to exceed that threshold potential, which is consistent with experimental results that suggest FaCDI is primarily a sorption-based process. Thus, it may be concluded that FaCDI may still be able to achieve greater salt removal even while still a physiosorption-based process.

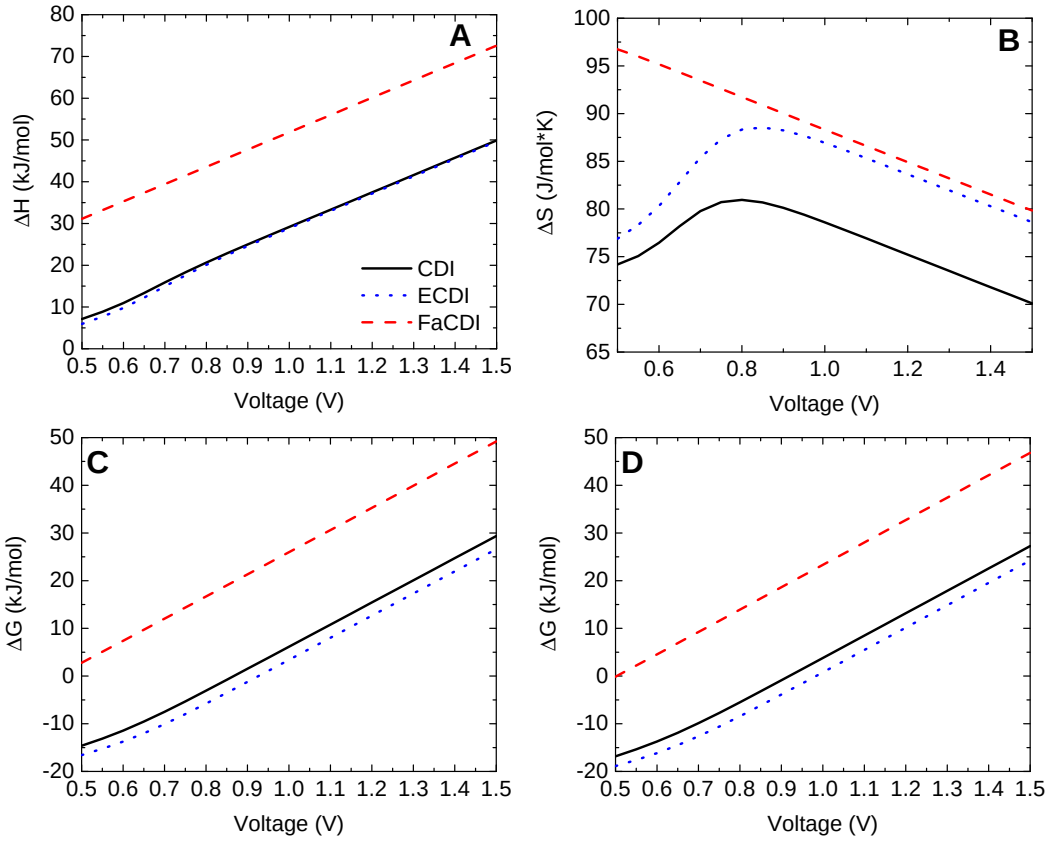

Figure 7.7: Plot of adsorption values as a function of the input voltage applied to the cell, 1 mM $<$ C_{feed} $<$ 20 mM. (A) Enthalpy of adsorption DH, (B) Entropy of adsorption DS, (C) Gibbs energy of adsorption, at 20°C, (D) Gibbs energy of adsorption, at 50°C.

Entropy, however, displays notably different results in all cases except FaCDI. At voltages below $\approx$ 0.9 V, the entropy term decreases with decreasing voltage indicating that adsorption in this lower voltage regions is more challenged in the short term. The decrease

is not seen for FaCDI, which only continues to rise at higher concentrations. This complements with strong increases in performance for FaCDI in both batch and continuous mode.

Gibbs energy is also plotted at two reference temperatures: The minimum evaluated temperature at 20°C and the maximum temperature at 50°C. The Gibbs energy ΔG determines thermodynamically the spontaneity feasibility of achieving such reactions, and in almost all cases for investigation. From the Langmuir adsorption isotherms its value is negative. ΔG has also suggested ranges for physisorption of between -20 and 0 kJ/mol. Thus, for CDI, physiosorption may be inferred for voltages of up to 0.9 at 20°C, or 1.0 V at 50°C. ECDI expands this window for chemisorption (and assurance of a truly spontaneous process) by about +50 extra mV. As for FaCDI, we cannot make any conclusions about its thermodynamic feasibility as its ΔG is always above 0 kJ/mol, yet it had been demonstrated in the batch modes as well as continuous.

If we consider the expanded voltage that was for the Langmuir isotherms previously shown (C_{feed} = 1 - 100 mM), the thermodynamic results will display reduced values (Figure 7.8). One most notable change is the enthalpy of adsorption, which never sees values above 7 kJ/mol, nowhere near the predicted chemisorption region of 80 kJ/mol. Here the value of ΔH is higher for ECDI than for CDI, the reverse is as shown in Figure 7.8A. The values in Figure 7.8A now in fact coincide with the increasing adsorption limits observed when the temperature range is increased.

The results here thus reaffirm in Figure 7.7B that at sufficiently higher voltage, adsorption is challenged by reduced affinity to electrode surfaces. Entropy values now all follow consistent downward trends, but FaCDI appears to stabilize as the maximum tested voltage of 1.5 V is approached. A closer inspection of batch mode tests run at the higher concentrations is needed to fully understand the trend in the results, in particular why FCDI would be the minimum value at ECDI the highest. It may suggest that in this operating regime the ECDI performance becomes diminished relative to just regular CDI.

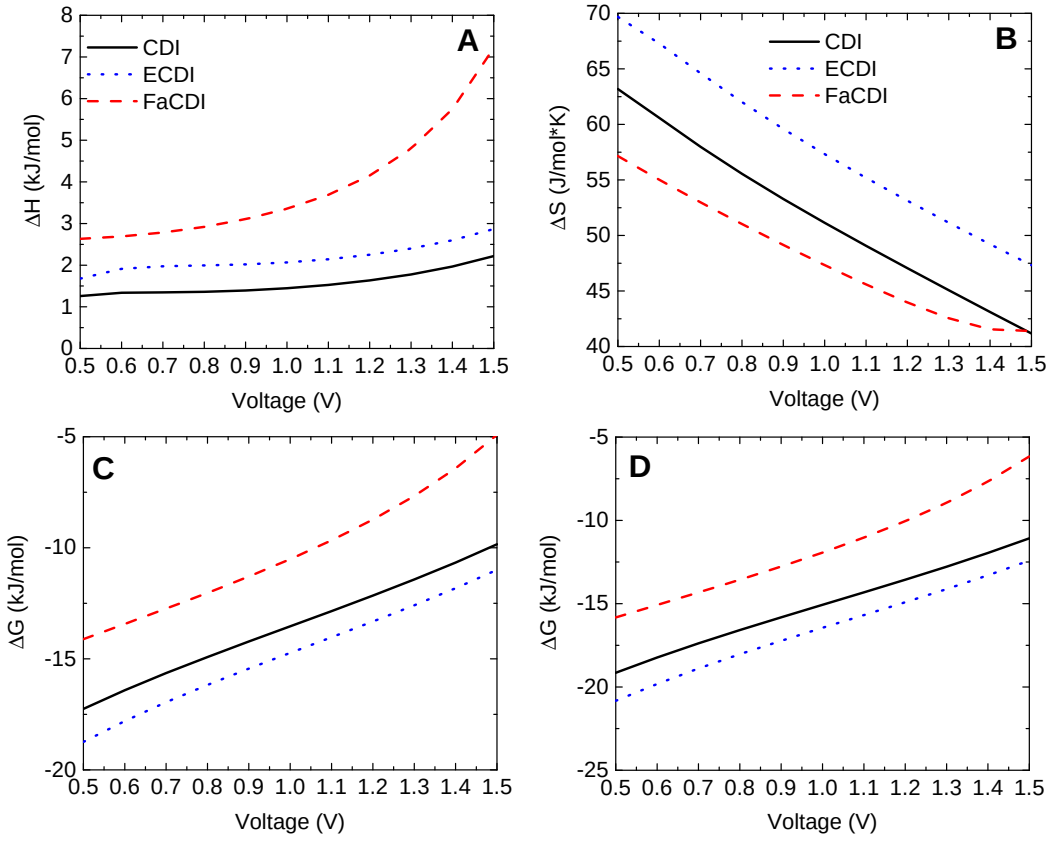

Figure 7.8: Plot of adsorption values as a function of the input voltage applied to the cell, 1 mM $< C_{feed} <$ 100 mM. (A) Enthalpy of adsorption ΔH, (B) Entropy of adsorption ΔS, (C) Gibbs energy of adsorption, at 20°C, (D) Gibbs energy of adsorption, at 50°C.

Gibbs energies (from Figure 7.8C-D) all display negative values, indicating that all reactions are spontaneous. The sensitivity of the results to concentration and temperature may indicate that some continued scanning of geometric/operating conditions, assumptions, and geometry may be necessary to see if results will show less variation with the chosen ranges. Furthermore, the reaction range -20 - 0 kJ/mol is confirmed, reaffirming that all processes run under such conditions can be assumed as physioadsorption. Furthermore, the adsorption tests considered here were only short term, as stability was reached quickly; examining other batch or continuous mode models may help to determine the best considerations for assumptions to make on computational development and prediction of thermodynamic adsorption values.

Tests using parameters from longer-term batch mode studies

The results from Figures 7.5 - 7.8, while able to achieve high adsorption values as had been developed from electrode storage mechanisms, do not accurately reflect the adsorption ranges shown in the CDI experiments. Most notably, the adsorption values for all three mechanisms are an order of magnitude higher than had been shown through previous isotherm literature. To obtain adsorption values that correlate closer, we evaluate the system under a different set of parameters. Here, we will use a charging voltage of 0.6 V, but with a total charging and discharging time of 3600 seconds (1 hour). Discharging voltage will be kept at 0 V to avoid inputting extra energy during this process. The total bulk volume of the solution is 200 mL, with 25 mL used as the volume in direct contact with the cell. The cross-sectional area of the cell will be kept at 25 cm^2, with the same input mass used of 1 g. The flow rate, however, will be increased to 20 mL/min, a value more comparable with previous batch for tests for CDI as well as various adsorption processes. The larger volume and higher flow rate will complicate the salt removal akin to a more realistic operation that would be employed in practice, which should yield values that are more comparable to those previously seen experimentally.

Under the conditions chosen, and using the same modified Donnan theory for the EDL structure, adsorption values reach ranges that would much more likely be observed experimentally. Scanned from concentrations ranging from 1 to 100 mM, traditional CDI approaches a maximum adsorption limit of 18-19 mg/g (Table 7.4). ECDI retains the same benefits as previously shown in Figure 7.4 - 7.5 and reaches a maximum adsorption values of 19.9 - 20.6 mg/g, a nearly 10% advantage (Table 7.5). FaCDI, however, still achieves a nearly 1.5x advantage over traditional CDI, approaching maximum adsorption values of 39-40 mg/g (Table 7.6).

The temperature dependence for the results, however, is notably weaker. While the graphs in Figure 7.9 depict temperature values closer to one another, real metric is in the van't Hoff plot used to predict thermodynamic adsorption values. As the values depicted in

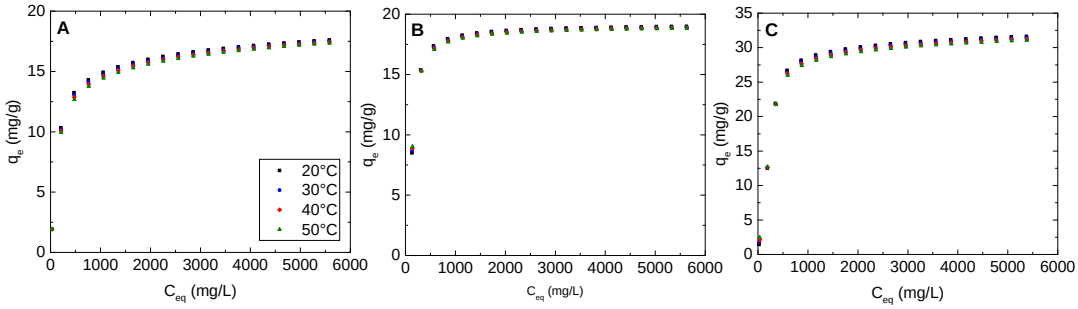

Figure 7.9: Plot of adsorption values as a function of the input voltage applied to the cell, 1 mM $<$ C_{feed} $<$ 100 mM. (A) Enthalpy of adsorption ΔH, (B) Entropy of adsorption ΔS, (C) Gibbs energy of adsorption, at 20°C, (D) Gibbs energy of adsorption, at 50°C.

Table 7.4: Fitting parameters for Langmuir and Freundlich isotherms and regression coefficients of CDI, long-term.

Parameter	20°C	30°C	40°C	50°C
K_L	0.0039	0.0039	0.004	0.004
K_F	0.3322	0.3333	0.3344	0.3356
q_m	18.76	18.57	18.38	18.20
n	5.61	6.18	6.89	7.82
R^2 (Langmuir)	0.9970	0.9973	0.9976	0.9979
R^2 (Freundlich)	0.7911	0.7968	0.8024	0.8081

Table 7.5: Fitting parameters for Langmuir and Freundlich isotherms and regression coefficients of ECDI, long-term.

Parameter	20°C	30°C	40°C	50°C
K_L	0.0061	0.0062	0.0064	0.0065
K_F	0.1398	0.1369	0.1345	0.1322
q_m	20.26	20.13	20.01	19.90
n	0.551	0.5454	0.5408	0.5369
R^2 (Langmuir)	0.9411	0.9433	0.9457	0.9484
R^2 (Freundlich)	0.6439	0.6508	0.6580	0.6654

Figure 10 are much closer in range ($7 <$ ln(K) < 9) to the range shown in Figure 7.6, this predicts that changes in adsorption entropy may not be as significant, but enthalpy values will be much smaller due to the lower direct temperature impact. The conclusion that we draw from this set of results demonstrates that values can replicate ranges given from experimental data, but a clear sensitivity persists which affects the adsorption behavior.

Table 7.6: Fitting parameters for Langmuir and Freundlich isotherms and regression coefficients of FaCDI, long-term.

Parameter	20°C	30°C	40°C	50°C
K_L	0.0017	0.0017	0.0018	0.0018
K_F	0.4452	0.4240	0.4061	0.3918
q_m	42.14	41.34	40.55	39.82
n	-12.68	13.19	4.85	3.24
R^2 (Langmuir)	0.9971	0.9957	0.9941	0.9925
R^2 (Freundlich)	0.7739	0.7678	0.7637	0.7612

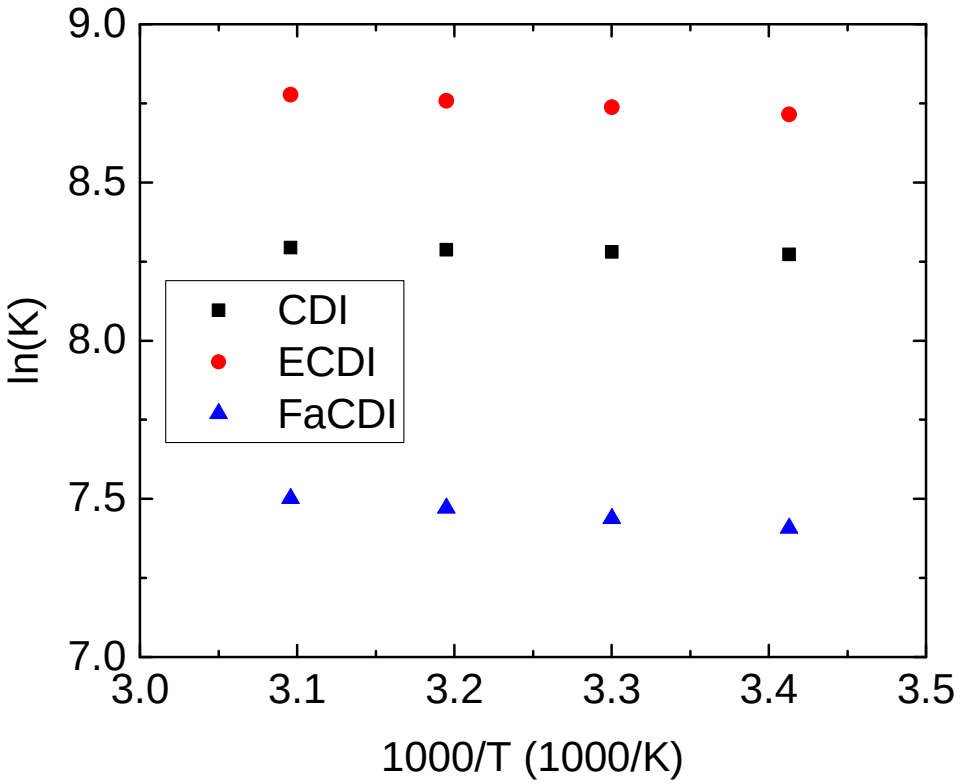

Figure 7.10: Plot of adsorption values as a function of the input voltage applied to the cell, 1 mM $<$ C_{feed} $<$ 100 mM. (A) Enthalpy of adsorption ΔH, (B) Entropy of adsorption ΔS, (C) Gibbs energy of adsorption, at 20°C, (D) Gibbs energy of adsorption, at 50°C.

The adsorption metrics are again evaluated over two concentration ranges: 1- 100 mM to cover the full adsorption isotherm range, and 1 - 20 mM to more closely focus the range to what had been explored experimentally. Under both ranges, the trends appear

more irregular than under the previous testing conditions, with both ΔH and ΔS values exhibiting peak values as opposed to mostly clear linear trends.

When only considering the reduced range of 20 mM, we are now able to more accurately replicate the thermal adsorption parameters used for studies with activated carbon ([71]) as carbon nanotube structures ([196]). Enthalpy of adsorption values increase from CDI to ECDI to FaCDI (higher SAC), as well as with higher voltage. The irregularity in the curve shapes may be indicative of inaccuracies with R^2 fits, or of different effects of temperature dependence on the electrode storage mechanisms. At 1.2 V, ΔH approaches 7 kJ/mol for CDI seen in [71], while the value for ECDI is nearly twice as much at 14 kJ/mol, and for FaCDI is at almost 17 kJ/mol. Nevertheless, the adsorption values all remain far below the feasible range for chemisorption-based processes, even for FaCDI.

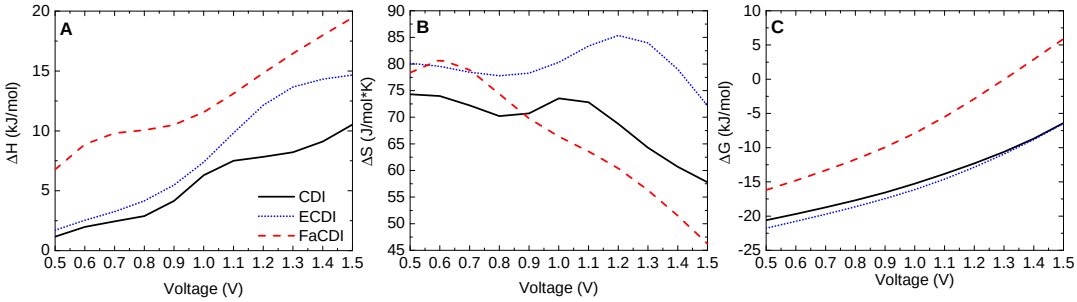

Figure 7.11: Plot of adsorption values as a function of the input voltage applied to the cell, 1 mM $< C_{feed} <$ 100 mM. (A) Enthalpy of adsorption ΔH, (B) Entropy of adsorption ΔS, (C) Gibbs energy of adsorption, at 20°C, (D) Gibbs energy of adsorption, at 50°C.

The unusual peaks in Figure 7.11 are also reflected in the adsorption entropy values, at nearly the same locations at which the notable features of the enthalpy curves are seen. As entropy decreases, the randomness of the adsorption processes decreases, which occurs at higher applied voltages. The lower amount of disorder corresponds to greater work applied to the cell. As Faradaic reactions are not accounted for in the model, it would be of great future interest to observe experimentally if adsorption capabilities and thermodynamic parameters changed notably above the limits or electrolysis or other possible reactions.

The Gibbs energy, however, does follow the trend that is most logically consistent with

decreasing randomness (entropy) at lower adsorption values leading to lower spontaneity; thus, the values approach zero.

When considering the maximum concentration range (1 - 100 mM), the enthalpy of adsorption notably never exceeds 4 kJ/mol (Figure 7.12. While the values are higher for ECDI and FaCDI, the magnitudes are too low to exhibit much insight. For CDI and ECDI, maximum adsorption enthalpy occurs at 1.2 V - For FaCDI, this maximum occurs much lower, at around 0.6 V, but this peak is nearly 2x lower than the peak adsorption enthalpy for ECDI. Thus, the maximum adsorption enthalpies seen here may be indicative of the optimal voltage to use for each electrode storage mechanism, and the justification of the lower CDI cycle voltage of 0.6 V, shown in Figure 7.2.

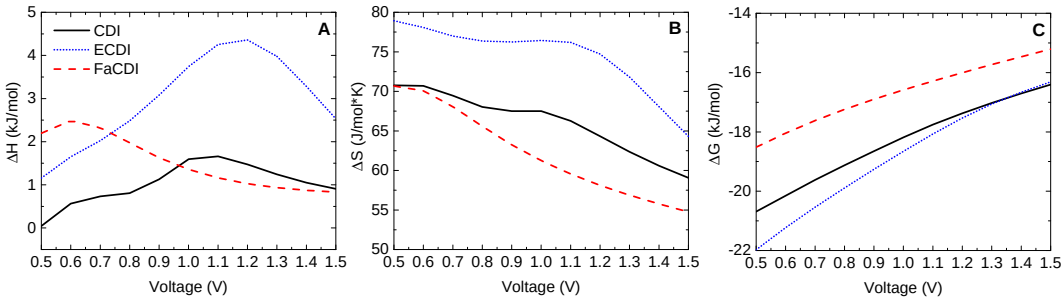

Figure 7.12: Plot of adsorption values as a function of the input voltage applied to the cell, 1 mM $< C_{feed} <$ 100 mM. (A) Enthalpy of adsorption ΔH, (B) Entropy of adsorption ΔS, (C) Gibbs energy of adsorption, at 20°C, (D) Gibbs energy of adsorption, at 50°C.

Tests using Gouy-Chapman-Stern model

A final case study examined here is looking at traditional CDI only using the Gouy-Chapman-Stern (GCS) model. We employ GCS to provide a more direct link to the majority of the other studies conducted in this thesis, and determine if appropriate isotherm fits can be performed similarly. The testing conditions used for the GCS batch mode study nearly mimic the operating conditions, with inlet parameters given as follows:

The deviations from the simulations using the mD model were enacted to enable more direct connection to operational conditions which could be replicated on a given experi-

mental setup. The lower concentration ranges tested demonstrated several similar trends; in this case, the GCS model, less restrictive than mD, enabled over 2x maximum adsorption capabilities for CDI (Figure 7.13. Additionally, temperature dependence is much more clearly visible, and transition of q_e with temperature remains, as in 7.13. When the equilibrium constant is directly related to temperature in the van't Hoff plot (Figure 7.10), the temperature dependence is notably higher here when compared to CDI mD models.

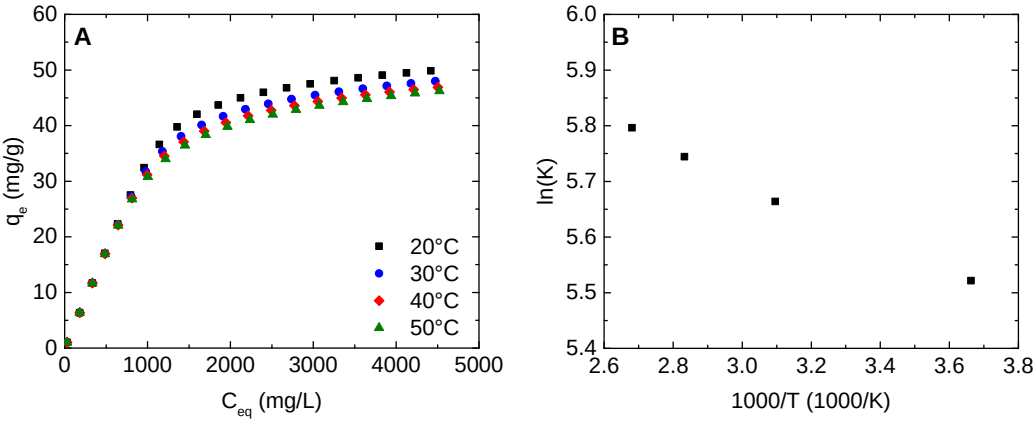

Figure 7.13: Plot of adsorption values as a function of the input voltage applied to the cell, 1 mM $< C_{feed} <$ 100 mM. (A) Enthalpy of adsorption ΔH, (B) Entropy of adsorption ΔS, (C) Gibbs energy of adsorption, at 20°C, (D) Gibbs energy of adsorption, at 50°C.

Lastly, the adsorption values with voltage tell a similar story with previous observations. While the values increase greatly with voltage, chemisorption range (ΔH ¿ 80 kJ/mol) is not reached for maximum voltage of 1.5 V. DH at 1.2 V is higher than experimental observations, so it could indicate that a further refinement between GCS and mD models could be observed. Entropy values display a similar decrease with increasing input voltage, but a maximum is attained when the input voltage is 1.2 V. The high DG values indicate that further investigation should be conducted with this GCS adsorption model, as the DG values below zero indicate that the adsorption process is non-spontaneous, and as such will not be able to proceed.

In summary, evaluating the three case studies shown in this discussion indicate that accurate prediction of adsorption parameters is sensitive to geometric and operating con-

ditions used, as well as the ranges of concentration and temperature that are considered in the parametric sweeps for curve fitting This research into computational-based adsorption models is extremely helpful to reduce the need to run many experiments to collect a limited number of adsorption parameters with questionable accuracy. A more in-depth sensitivity analysis of the adsorption values to the operating conditions needs to be conducted to gain more reliable criteria for choosing different kinds of electrodes. Ranges of concentrations and temperatures studied are of particular interest as they directly determine the equilibrium constant to obtain enthalpy, entropy, and Gibbs free energy of adsorption.

7.5 Conclusion

We demonstrate thermodynamically the influence of redox-active electrodes on the performance of both redox-active electrodes on the performance of both-term and long-term cycles. Thermodynamically, by limiting the range of electronic charge during cycling, a FaCDI cell can reduce work consumption by as much as 12%. Furthermore, we demonstrate that FaCDI can increase Coulombic efficiency by as much as 2x in continuous mode, and thermodynamic efficiency by over 7x in batch mode, the latter due to delayed discharging which maintains production of diluate for slightly longer (1/10 of cycle length). Finally, we evaluate batch mode results by generating computational-based adsorption isotherms, which had not previously been employed for CDI processes. Likewise, FaCDI has demonstrated 1.5x greater maximum salt adsorption capacity relative to CDI and ECDI, and also demonstrated by greater values of enthalpy of adsorption and Gibbs energy of adsorption. In summary, investigating this unique method of evaluating adsorption provides guidance in the future design and operational considerations for various processes.

CHAPTER 8

CONCLUSIONS AND RECOMMENDATIONS FOR FUTURE WORK

The research explored in this dissertation examined a set of new tools and operating considerations to make for capacitive-based mixing and energy processes. We began in Chapter 3 by analyzing and quantitatively comparing the thermodynamic performance of two kinds of CDI cycles: a traditional operation with constant current and voltage modes, and a proposed Carnot-like cycle with constant chemical potential charging and constant number of ions switching. The Carnot-like cycle demonstrates greater work consumption over the traditional cycle under the brackish water concentration. If the initial concentration is raised to 100 mM, we can show TEEs that would be expanded from the realistic operation to over 30%. This TEE achieved is higher than previous experimental TEEs reported which have only gone to around 10%.

In Chapter 4, building on the principles of thermodynamic cycles operations for capacitive-based cycling technologies, we developed analogies for 4-stage thermodynamic heat engines to CapMix cycles. We developed equivalencies to each of the major types of 4-stage thermodynamic cycles using appropriate terms and evaluated/tested under different conditions to assess performance. While Carnot-like operation for CapMix does not display the same immediate benefits as for CDI, efficiency per number of ions exchanged during cycling is over 10x higher. Developing such thermodynamic analogies can improve our understanding and performance of a wide range of cyclic energy processes. Up to this point, however, the studies conducted have only been assumed to be theoretical. As the cycles assume no losses such as irreversible mixing inefficiencies or ohmic drops, real world conditions are not yet covered. As such, an economic analysis was not yet considered, but will serve as a key point of interest to focus on for future CapMix studies involving alternative cycle operations.

In Chapter 5, we evaluated how temperature profiles impact the thermodynamic efficiency of CDI and CapMix cycles operated under both infinitely slow and current dependent conditions. We showed that the limit of infinity slow steady-state operation was approached as current and corresponding flow rate values approached zero. With CapMix, operational efficiencies went up to 43%. For CDI, optimal TEE was attained through the use of non-isothermal temperature profile, with maximum value approaching 10%. Variable temperature conditions resulted in a reduction of number of ions exchanged by nearly 15%, enabling closer approximation to Carnot-like behavior. One important consideration to make for future studies would be to determine if temperature could be varied as a means of facilitating or more closely approximating a constant number of ions operation. If temperature can be altered in a manner that would make sense realistically without compromising performance parameters such as thermodynamic efficiency, benefits of this mode of operations can be expanded to other modes of cycling operation previously explored in this dissertation. Experimental work looking at the feasibility of varying temperatures using appropriate heat transfer considerations and control schemes for the temperature would confirm the significance of the results seen during this study.

Chapter 6 explored the use of alternative storage means using slurry-based flow electrodes to increase the salt adsorption capabilities of higher concentration inlet feeds. We specifically studied the influence of concentration gradients in FCDI, and confirmed their influence on overall desalination performance. In evaluating the influence of diffusion for various electrolyte and feed concentrations we developed a new dimensionless parameter to qualitatively relate diffusive transport to electromigration from cell potential during operation. Results from this study highlighted the importance that diffusion has in processes where the gradient between feed and electrode is high: It can enhance salt removal, but makes the salt recovery process more difficult, limiting stability. In the future, this work can be compared to theoretical models to more appropriately design scalable flow electrode CDI systems, based on the available/desired input parameters. Additionally, when

considering the benefits of thermally-assisted CDI cycles, we could examine the effects of thermal gradients on flow electrode CDI performance, based on studies previously conducted with film CDI. From there, we may also be able to predict if thermal effects will have an influence on ion selectivity in certain aqueous transport systems.

In Chapter 7, we examined computational-based adsorption isotherms in relation to different electrode storage processes for CDI with enhanced (ECDI) and Faradaic (FaCDI) charge modifications. Thermodynamically, by limiting the range of electronic charge during cycling, a FaCDI cell can reduce work consumption by as much as 12%. Furthermore, we demonstrate that FaCDI can increase thermodynamic efficiency by over 7x in batch mode, in part due to delayed discharging which maintains production of diluate for slightly longer (1/10 of cycle length). Finally, we evaluated batch-mode results by generating computational-based adsorption isotherms, which had not previously been employed for CDI processes. FaCDI demonstrated 1.5x greater maximum salt adsorption capacity relative to CDI and ECDI, and also demonstrated by greater values of enthalpy of adsorption and Gibbs energy of adsorption. The unique method of evaluation adsorption values provides guidance in the future design and operational considerations for various processes. Future work in dilatometry to assist in obtaining the thermodynamic properties of different electrode structures can further corroborate the computational results obtained.

This research conducted in this dissertation integrated thermodynamic and transport principles with theory from electrochemistry and double layer capacitors, along with experiments. The findings indicate that certain means of improving CDI/CapMix cycles exist following proper considerations of thermodynamic cycling modes, temperature conditions, concentration ranges, and electrode storage mechanisms. This research can be extended to a wide range of applications for physical and chemical-based adsorption processes.

Appendices

APPENDIX A

SUPPORTING INFORMATION FOR: EVALUATING EFFICIENCY OF CARNOT AND CONVENTIONAL CAPACITIVE DEIONIZATION CYCLES

A.1 Constraints on Carnot-analog cycles

As discussed within the context of Chapter 3, while the proposed Carnot-analog cycles provide a new means of looking at salt water desalination, constraints arise due to the use of the constant number of ions criteria. In particular, during the discharging stage, the ion recovery is limited by the brine concentration that is needed based on the chosen water recovery ratio.

As mentioned in Chapter 3, the excess surface charge, Γ (given in units of #/m^2), is determined as a function of both the electrode surface charge σ and additional crossover charge σ^*:

$$\Gamma = \sqrt{\sigma^2 + \sigma^{*2}} - \sigma^* \tag{A.1}$$

From A.1 it is clear that the value of Γ cannot be less than zero, meaning that under the constraints for a Carnot analog, the cell cannot over-discharge below zero Coulombs (can also be expressed in units of #/nm^2).

To determine whether we have reached this limit, we determine the total number of ions in the cell at the maximum charge value. This depends on only two criteria, the minimum salt concentration and the maximum cell voltage. These two parameters can be used to solve for the maximum charge in the cell, which can then be used to determine total excess charge, and thus the total number of ions.

As this value will remain constant during the first discharging stage, we only need to ensure that the minimum charge reached within the cycle does not go below zero. This can

be done by setting $\Gamma = 0$, and solving for the concentration in the cell C_{min} where this would occur. From the definition of number of ions given in #/nm^2, this concentration C_{max} can be written as:

$$N_2 = 2C_{max}L_eN_{av} \tag{A.2}$$

where N_2 is the total number of ions in the cell after stage 2, which remains constant until stage 3. L_e is the pore length of the electrode (which we assume to be the total electrode volume normalized by its surface area), and N_{Av} is Avogadro's constant. This limit can be expressed as a function of the starting concentration, the dilute concentration, and water recovery ratio. To better qualitatively compare between different salt concentrations, we display this maximum concentration as a function of the amount of salt removed relative to the starting concentration, ΔC_{feed} (Figure A.1a). At 100 mM initial concentration, the limit of around 285 mM implies that these modes of operation are not reliable for higher saline solutions, when a higher brine concentration must be created.

The limit on brine concentration for the theorized cycles also implies a limit for the maximum recovery ratio allowed at different concentrations (Figure A.1b). This limit becomes much more restricted with larger concentration differences. However, as shown in Chapter 3, more input energy is easily recovered during discharging, particularly for a 100 mM feed. At only a 20 mM concentration, the limit is not reached at $\alpha = 0.75$ when $C_{min} = 1$. However, when C_0 is raised to 100 mM, the maximum allowable removal is only around 40%, which is near the maximum for where data is shown in Figure 3.3c (blue line). For 100 mM feeds, as this limit is approached, TEE increases sharply, which suggests that operating closer to the minimum charge limit can yield optimal performance. This operating limit may not completely restrict the operation of a cycle, however; as seen for Figure 3.4a (black line) that cyclic operation could be performed to yield a thermodynamic efficiency. As the Carnot analog cycle examined here is only theoretical, our performance does not consider values too close to this limit as they would likely not be practical. Future stud-

ies considering this theoretical cycle in greater detail should examine the behavior of CDI cycles operating closer to these limits.

A.2 Detailed calculation of chemical exergy values

For an aqueous NaCl solution, The Szargut model [149] defines chemical exergy B_{Ch} as:

$$B^s_{ch} = n_{H_2O}e_{H_2O} + n_{NaCl}e_{NaCl} + RT(n_{H2O}ln(a_{H2O}) + n_{NaCl}ln(m_{NaCl}\gamma_{NaCl})) \quad \text{(A.3)}$$

The intrinsic reference chemical exergy values used here are e_{H2O} = 0.9 kJ/mol and e_{NaCl} = 14 kJ/mol. The number of moles of n can be rewritten as molar concentrations, thus converting the units to energy per volume, consistent with Gibbs energy of mixing and input energy as defined in Chapter 3. Thus, Eq. A.1 is given in units of J/m^3. For H_2O, the molar concentration is the quotient of its density and molar mass, or 55.56 M.

$$B^s_{Ch} = C_{H_2O}e_{H_2O} + C_{NaCl}e_{NaCl} + RT(C_{H_2O}ln(a_{H_2O}) + C_{NaCl}ln(m_{NaCl}\gamma_{NaCl})) \quad \text{(A.4)}$$

The activity coefficient of water, a_{H_2O}, is based on the molar fraction of water within the aqueous solution. The salt molality m_{NaCl} is expressed in units of moles solute/kg of solution. For an ideal solution,this can be calculated directly as a function of the molar fraction of the solute[201]. Since mostly dilute solutions are considered in this study, this serves as a reasonable approximation:

$$a_{H_2O} = 1 - X_{NaCl} \quad \text{(A.5)}$$

where X_{NaCl} is the mole fraction of solution in the total solution. This results in activity coefficients close to, but not equal to 1. Thus the terms in Eq. A.2 with C_{H_2O} coefficients

will not cancel given the magnitude of C_{H_2O} relative to C_{NaCl}. Activity coefficient for NaCl was calculated more carefully using the Pitzer equation to account for non-ideal behavior of Na^+ and Cl^- ions [50]:

$$ln(\gamma) = -A_0\Big(\frac{\sqrt{I}}{1+b\sqrt{I}} + (2/b)ln(1+b\sqrt{I}) + m\frac{2\nu_m\nu_x}{\nu}\Big) + \Big(2B_{0,mx} + 2\frac{\beta_{1,mx}}{\alpha^2 I}(1-(1+\alpha\sqrt{I}-\frac{\alpha^2 I}{2})e^{-\alpha\sqrt{I}})\Big) + (3m^2/2)\Big(2\frac{(\nu_m\nu_x)^{3/2}}{\nu}C_{0,mx}\Big) \tag{A.6}$$

where I is the ionic strength given as a function of the salt molality [202], the terms A_0 and b are constants which vary with atmospheric conditions. At room temperature of 293 K and ambient pressure, the values of α = 2, b = 1.2, and A_0 = 0.3882. Likewise, the constants $B_{0,MX}$,$B_{1,MX}$, and $C_{0,MX}$ are similarly found under these conditions, as 0.0714, 0.2723, and 0.002, at salt concentrations of up to 6 M[202]. The number of ions ν dissociated for NaCl are ν_m=1 for Na^+, ν_x=1 for Cl^-, and ν = 2 total ions.

Combining the above equations A.2–A.4, chemical exergy for a given salt concentration can be obtained. Since we are primarily interested in the changes in chemical exergy, we consider the total change in chemical exergy between different concentrations as:

$$\Delta B_{ch} = |B_{ch,0} - B_{ch,min}| + |B_{ch,b} - B_{ch,0}| \tag{A.7}$$

Since the brine concentration C_b is set by the water recovery ratio, ΔB_{Ch} can be examined as a function of three different operating parameters. In comparison with Gibbs energy [81], we plot ΔB_{Ch} as a function of initial concentration and water recovery ratio at a dilute stream value of C_{min} = 1 mM (Figure A.2). While it can be seen that chemical exergy changes grow substantially higher at lower salt concentrations, achieving such a large salt removal for a CDI cell will likely not be possible without inputting a similarly high amount of excess work.

A.3 Validation of Helmholtz Integral

In order to ensure that both of the thermodynamic cycles run were truly complete cycles, equivalence of both the work integral $\int V d\sigma$ and free energy integral $\int \mu dN$ terms was checked. For the cycle to be complete, the two terms must cancel each other, resulting in no net increase in the Helmholtz energy, $\int dF$. Figure A.3 demonstrates that for both cycles, this integral is verified at varying ranges of feed concentrations.

A.4 Effect of voltage on cycle constraints

One way to address this limit at higher concentrations is to raise the maximum allowable charging voltage. Increasing the maximum charging voltage enables higher ranges for brine concentration/water recovery, but this increase becomes much more limited for higher voltages (Figure A.4). Furthermore, operating at higher voltages in actuality could produce unwanted side reactions, such as electrolysis, which could disrupt the performance of desalination.

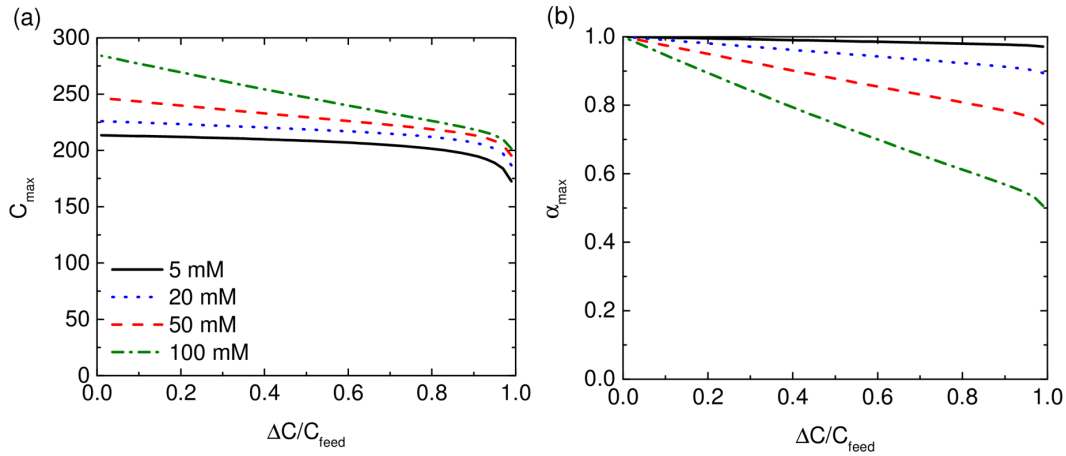

Figure A.1: (a) Maximum allowable brine concentration, and (b) maximum allowable recovery ratio, as a function of initial concentration and salt removal percentage, based on Carnot analog constraints.

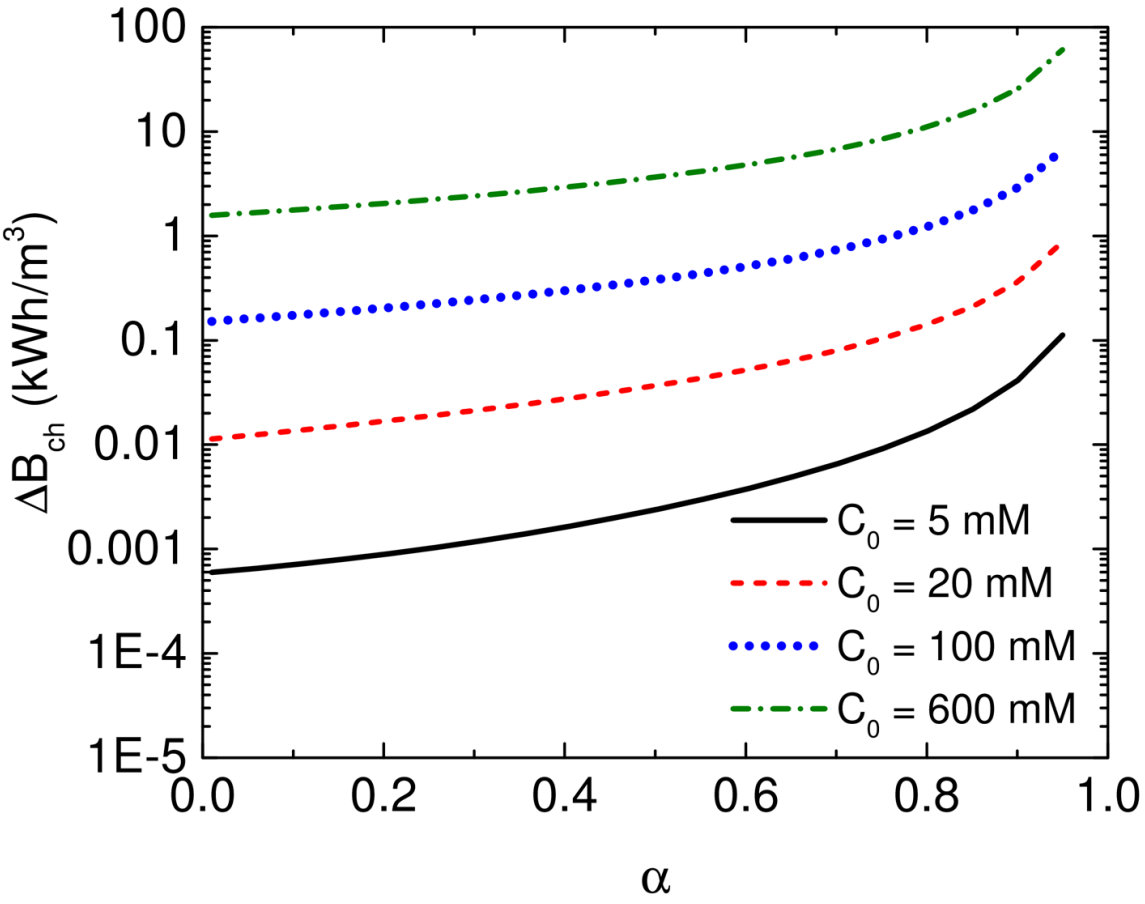

Figure A.2: Variation in the chemical exergy change as a function of starting concentration C_{feed} and water recovery ratio α, according to the Szargut model. In all cases minimum concentration C_{min} = 1 mM.

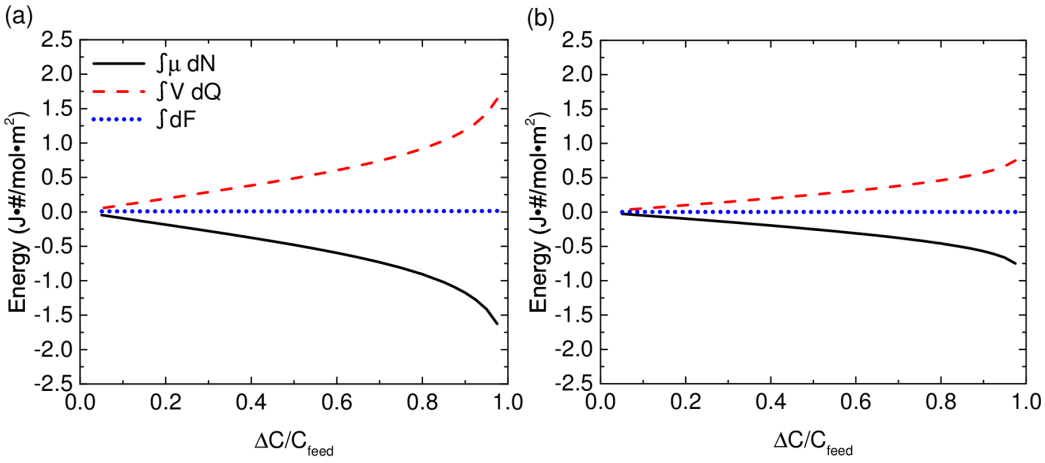

Figure A.3: Confirmation of zero change in Helmholtz energy at the completion of each cycle. (a) Carnot analog, (b) Traditional cycle. C_{feed} = 20 mM, α = 0.5.

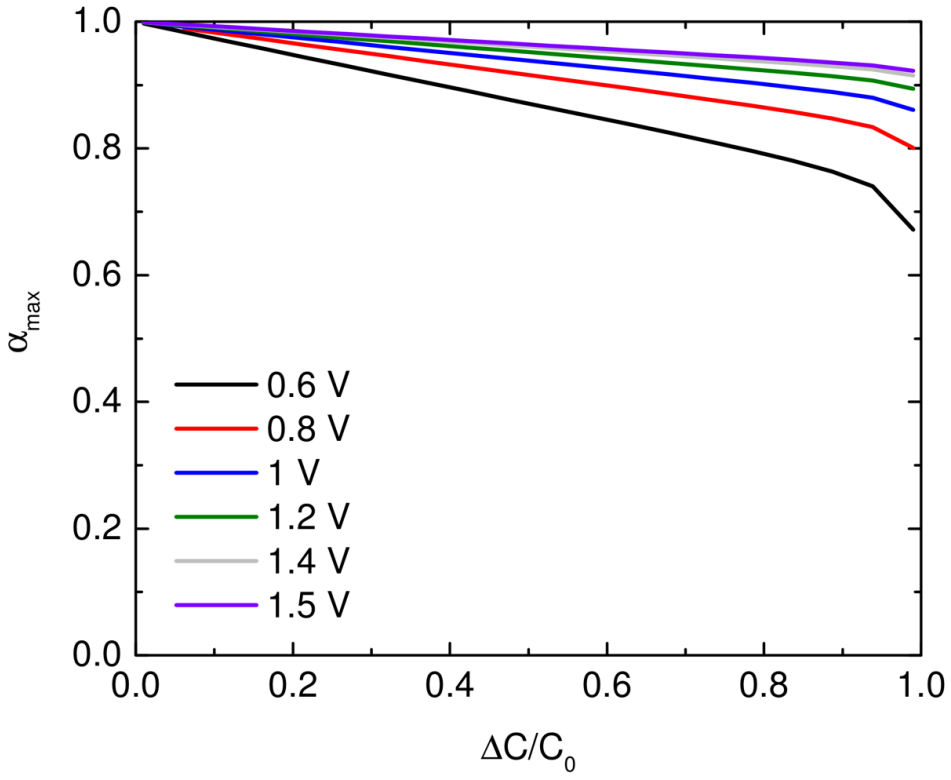

Figure A.4: Variation in maximum allowable water recovery ratio as a function of input voltage and salt removal percentage, for C_{feed} = 20 mM.

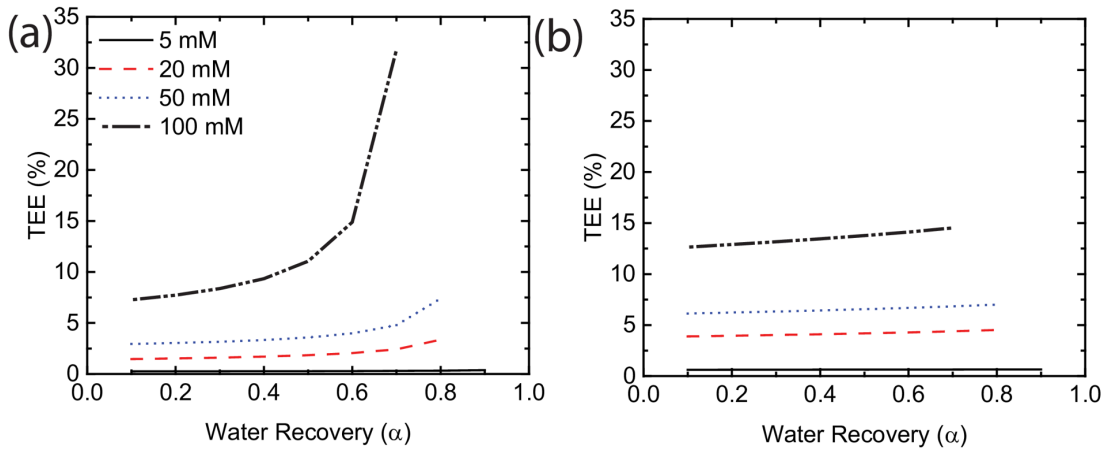

Figure A.5: Thermodynamic energy efficiency for different feed concentrations as a function of water recovery ratio, at 95% salt removal. (a) Carnot analog and, (b) conventional operation cycles.

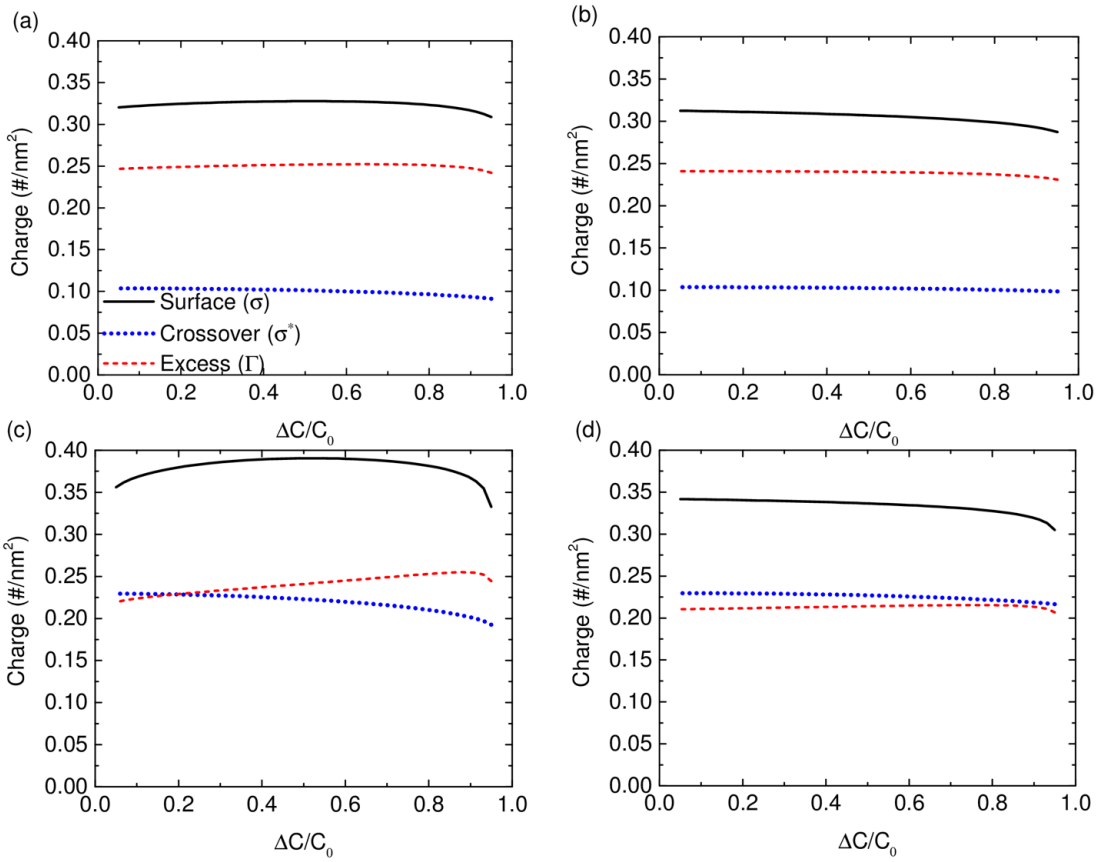

Figure A.6: A study of the effect of the average charge under varying concentrations used for the Carnot and conventional operation mode cycles. (a) Carnot analog, C_{feed} = 20 mM, (b) Conventional operation, C_{feed} = 100 mM, (c) Carnot analog, C_{feed} = 20 mM, (d) Conventional operation, C_{feed} = 100 mM.

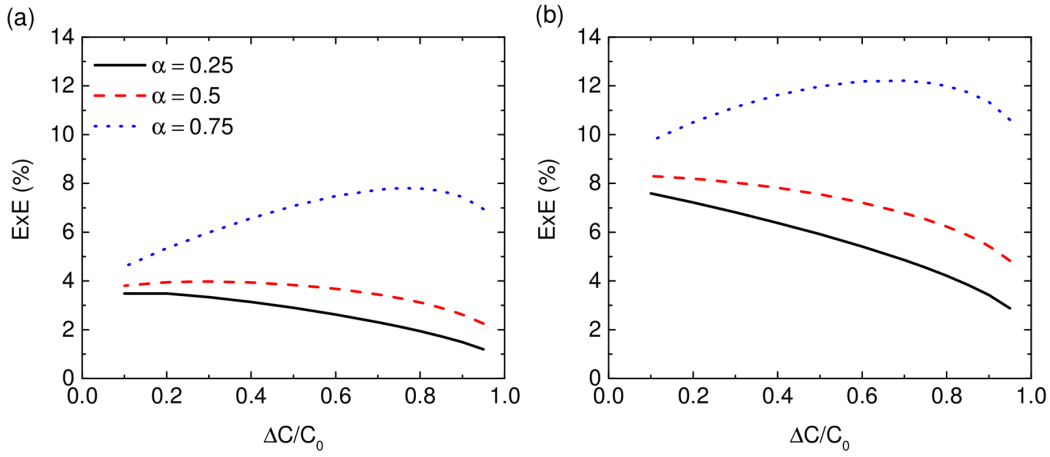

Figure A.7: Evaluation of exergetic efficiency for the (a) Carnot analog cycle, and (b) conventional operation cycle with C_{feed}=20 mM.

APPENDIX B

SUPPORTING INFORMATION FOR: EFFICIENCY OF THERMALLY ASSISTED CAPACITIVE MIXING AND DEIONIZATION SYSTEMS

B.1 Maximum extractable CapMix energy under isothermal conditions

First, we consider a control volume around a mixing stream similar to the one derived from previous exergy analysis [203]. In this scenario we equate the mixing processes to the discharging process a CapMix cycle, in which energy is extracted. The analysis assumes perfectly isothermal and isobaric conditions, and this neglects the need for additional heat exchange during this process. This analysis holds in an insulated process without heat loss to the surroundings. The analysis is not perfect for the cases where temperature changes during the discharge stage, and as such, we will assume averaged temperature throughout the cycle here to neglect any additional contributions to include for the analysis.

The analysis considers a stream of high concentration C_{HC} and low concentration C_{LC} which form a mixed concentration C_{Mix}. By conservation of the total moles of salt, we have:

$$\dot{n_{Mix}} = \dot{n_{HC}} + \dot{n_{CL}} \tag{B.1}$$

where n represents the molar flow rate of each stream. The fraction ϕ indicates the total fraction of the volumetric flow rate for each stream. For an arbitrary stream i:

$$\dot{n_i} = C_i \dot{V_i} \tag{B.2}$$

where the volume balance in this analysis is given as simply $\dot{V}_{HC} + \dot{V}_{LC} = \dot{V}_{M}$. Thus, if the volumetric flow rate fractions are used, corresponding to $\dot{V}_{HC} = (1\text{-}\phi)\dot{V}$, $\dot{V}_{LC} = \phi\ \dot{V}$, and $\dot{V}_{M} = \dot{V}$, we can obtain the formula for the mixing concentration C_{Mix}:

$$C_{HC}(1-\phi) + C_{LC}(\phi) = C_{Mix} \tag{B.3}$$

Next, we apply a molar exergy balance to the system, as described above:

$$\dot{n_{HC}}e_{HC} + \dot{n_{LC}}e_{LC} - \dot{n_{Mix}}e_{Mix} - \dot{E}_d - \dot{W} = 0 \tag{B.4}$$

Here each of the extensive exergies are calculated as functions of intensive exergies multiplied by the corresponding molar flow rate. Using the notation $\dot{E}_{\mathrm{i}} = \dot{n}_{\mathrm{i}}\ \mathrm{e_i}$, we can rewrite Eq. B.4 for the reversible work, which neglects the exergy destruction $\dot{E}_{\mathrm{d}}$:

$$\dot{n_{HC}}e_{HC} + \dot{n_{LC}}e_{LC} - \dot{n_{Mix}}e_{Mix} - \dot{W} = 0 \tag{B.5}$$

To obtain the total work in terms of J/m^3 of water, we write an appropriate balance for Eq. B.5. Then, The total work per volume of water can be written as:

$$\dot{W} = (1-\phi)C_{HC}e_{HC} + \phi C_{LC}e_{LC} - C_{Mix}e_{Mix} \tag{B.6}$$

The intensive exergies e each account for mechanical, thermal, and chemical contributions. If the mechanical-based kinetic and potential exergy contributions are neglected, then we can get each of the exergy values $\mathrm{e_i}$ as:

$$e_i = h_i - h_0 - T_i(s_i - s_0) \tag{B.7}$$

where all values marked with the subscript 0 denote values at the dead state. If assuming specific heat capacities that are independent of temperature, then the intensive exergy term can be expanded as:

$$e_i = c_P(T_i - T_0) - T_i\Big(C_P ln\Big(\frac{T_i}{T_0}\Big) - Rln\Big(\frac{C_i}{C_{H_2O}}\Big)\Big) \tag{B.8}$$

where $\mathrm{c_P}$ is the specific heat of water, taken here as 4186 J/kg*K, and R is the universal gas constant. To ensure that the logarithmic arguments are all dimensionless, the associated concentrations are all divided by the molar concentration of water $\mathrm{C_{H_2O}}$, 55.5 M.

If temperatures are all assumed equal, then it can be shown that all c_P-dependent terms for exergy in Eq. B.6 will cancel, and we will be left with the resulting Gibbs energy of mixing given by Eq. 5.4. If we do not assume uniform temperature, then the analysis can become more complicated as the assumption of no heat exchange within the system as shown by Figure B.1 cannot be valid.

B.1.1 Theory

For the Gouy-Chapman-Stern model, the EDL voltage is divided into two components, diffuse layer voltage for mobile regions of ions and fixed Stern layer for immobile ions, to neutralize some of the surface charge.

The diffuse layer voltage difference ΔV_D is given by:

$$\Delta V_D = 2V_T sinh^{-1}\sigma\sqrt{\frac{\pi\lambda_B}{2C_{feed}N_{av}}} \tag{B.9}$$

where λ_B is the Bjerrum length. The charge σ is henceforth referred to as a surface charge. The thermal voltage V_T is defined as $V_T = RT/F$, where F is Faraday's constant. For the Stern layer voltage ΔV_{st}, Gauss law is used:

$$\Delta V_{st} = \sigma e/C_{st} \tag{B.10}$$

where C_{st} is the Stern capacity and *e* is the elementary charge. For this study, we will employ a Stern layer capacitance of C_{st} = 0.08 F/m^2 [155, 156]. Assuming a symmetric cell configuration, the diffuse and Stern layer potentials can be summed and then doubled for each electrode to provide the total voltage ΔV_{cell} through the cell:

$$\Delta V_{cell} = 2V_T(\Delta V_{st} + \Delta V_D) \tag{B.11}$$

For the number of ions N in the cell, the surface charge Γ is determined as a function of both the electrode surface charge σ and additional crossover charge σ^*:

$$\sigma^* = \frac{1}{2\pi\lambda_B\lambda_D} \tag{B.12}$$

where the Debye and Bjerrum lengths for the electrolyte, λ_B and λ_D determine the crossover charge[66]. Taking the volume of the electrolyte outside of the electrode as negligible to the volume inside the electrode, the pore length then represents 2x the electrolyte's volume

normalized by its surface area.

For the transient-based considerations, we will adapt from a previously published GCS EDL model for CDI employing transient considerations. The model also considers the use of membranes to aid in the ion transport. For appropriate mass/charge balance, the given transport equations are:

$$\frac{dC_{feed}}{dt} = \frac{\phi}{V_{tot}}(C_0 - C_{feed}) - jJ_{lim}A_{cell} \tag{B.13}$$

$$\frac{d\sigma}{dt} = jJ_{lim}N_{av}\frac{A_{cell}}{\alpha} \tag{B.14}$$

where ϕ represents the volumetric flow rate through the channel, V_{tot} is the total liquid volume contained within the cell, j is a dimensionless current value, A_{cell} is the macroscopic cross-sectional area of the cell, and a is the total surface area of the electrode. J_{lim} is a current-limited ion flux, defined in the model based on the feed concentration and diffusion coefficient of ions across the membrane, D:

$$J_{lim} = \frac{2DC_{feed}}{L_{SDL}} \tag{B.15}$$

where L_{SDL} is the stagnant diffusion layer that characterizes transport through the membrane, assumed constant in this study (L_{SDL} = 40 μm). The cell area A^{cell} is 25 cm^2 for CDI, and 4000 cm^2 for CapMix. Essentially, the CapMix cell can be thought of as a 16-stacked cell with each stack having the same area as the cell for CDI. The high contact area of CapMix was used to facilitate extraction of ions on the cell when larger current values are used. If A_{cell} were too small, then the CapMix cell would not be able to reliably obtain net energy extracted, due to increased resistance values.

The total cell voltage V_{cell} now considers ohmic losses as well as a transport-based

potential term:

$$\Delta V_{cell} = 2V_T(\Delta V_{st} + \Delta V_D + \Delta V_{tr} + \Delta V_{loss}) \tag{B.16}$$

where Δ V_{loss} denotes the ohmic loss term, given as Δ V_{loss} = I($R_{internal}$ + $R_{external}$)/V_T. The external resistance $R_{external}$ for both CDI and CapMix was assumed at 5 Ω. The transport potential ΔV_{tr} is given by [145]:

$$\Delta V_{tr} = -2ln(1-j) + 2j\frac{C_{feed}}{C_{m,app}} - ln\Big(\frac{C_{feed}}{C_{m,app}}\Big) \tag{B.17}$$

where $C_{m,app}$ is a membrane-based concentration parameter, which we will take in this study as $C_{m,app}$ = 2 mM [145]. Manipulating the aforementioned equations enables a solution for the current through the cell, based on the dimensionless current and limiting ion flux:

$$I = jJ_{lim}A_{cell} \tag{B.18}$$

The internal resistance in the cell $R_{internal}$ is determined as a function of both electrolyte concentration and temperature. Typically, experiments are required to determine the exact nature of temperature/concentration dependence. We will take data previously obtained from an Orion Benchtop conductivity meter to estimate the cell concentration. From there, we will employ a calibration to alter the cell's conductivity at temperatures deviating from the conductivity meter's equilibrium temperature (25°C). This variation is a 2% maximum deviation from each degree away from 25°C, with the maximum conductivity of around 1.6x at 50°, and a minimum of 0.4x around 0°C. Combining this temperature dependence with a quadratic calibration fit based on concentration results in the following product solution for the full conductivity dependence:

$$\kappa = (2x10^{-5}{C_{feed}}^2 + 0.1062C_{feed} + 0.0086)\frac{1}{2}\Big(\frac{T}{25} + 1\Big) \tag{B.19}$$

where the conductivity κ is in units of mS/cm, the feed concentration C_{feed} is in mM, and the temperature T is in °C. As higher temperatures increase conductivity, cell resistance is reduced. To the best of the author's knowledge, this effect has not explicitly been captured computationally in previous models.

In considering transport-based effects, diffusion also exhibits a strong dependence on temperature, governed by the Arrhenius relation:

$$D = D_0 exp\Big(\frac{\Delta E_0}{R}\Big(\frac{1}{298} - \frac{1}{T}\Big)\Big) \tag{B.20}$$

with activation energy Δ E_0 and standard temperature diffusivity D_0 as empirical constants based on the ions and the solution. Temperature-based experiments and molecular dynamics (MD) simulations have shown strong changes in diffusion coefficients with temperature suggested by the above Arrhenius relation. We will borrow from experimental data on diffusion coefficients for Na+ cations and Cl- anions, and average them together to determine overall diffusion coefficients for a symmetric cell. To connect to a best fit for replicating the tabulated data, linear coefficients were determined by relating ln(D) with 1/T. These parameters for Na^+ are given as ΔE^0 = 12.4 kJ and D_0 = 1.32 x 10^{-9} m^2/s. For Cl^- the constants were determined as ΔE_0 = 12.4 kJ and D_0 = 1.74 x 10^{-9} m^2/s. Taking an inverted average for both ions (Cussler Equation) enables a best estimate of the diffusion coefficient to use in the symmetric cell (shown in Figure B.1b):

$$D = \frac{2D_{Na^+}D_{Cl^-}}{D_{Na^+} + D_{Cl^-}} \tag{B.21}$$

For the changes in temperature that occur during cycling, we will consider a constant heat input, into the cell and assume only losses by natural convection. Mass fluxes for the salt streams in/out will not be considered since fluid flow rates are sufficiently small enough to maximize ion capture in the cell. This results in a simple lumped model for the

temperature changes in the cell:

$$\rho C_P V_{ext} \frac{dT}{dt} = \dot{Q} - hA_s(T - T_0) \tag{B.22}$$

Property values were averaged based on the averaged weight percentage of each of the materials composed of in the cell (see Table SI1). The averaged density ρ was calculated as 4030 kg/m^3, and averaged specific heat C_P was 810 J/kgK. The total surface area was estimated at A_s = 448 cm^2, and total volume as V_{ext} = 610 cm^3 (Parameters from Table SI1). Convection coefficients were approximated for natural convection based on film temperature of the surrounding air (average of cell and ambient temperatures) and an appropriate correlation for natural convection around a cube [204], resulting in values of approximately 1-5 W/m^{2}K for convection coefficients.

Further details of the experimental setup can be found in [152, 160].

B.2 Calculation of thermal energy conversion efficiency

To calculate the energy savings/gains during CapMix/CDI, we take the difference between work input and work outputs in CDI and CapMix cycles. For a non-isothermal process where a heating stage is necessary between charging and discharging, we assume the heat input as:

$$Q_{in} = \rho C_P (T_{discharge} - T_{charge}) \tag{B.23}$$

where ρ represents density and C_P represents specific heat for water. In this analysis, we neglect the variation in salinity on the molar heat of water and assume simply a constant specific heat.

When the temperature is raised between the charging and discharging stages, we define the thermal energy which is converted into useful work by η_{Carnot}. This is the percent of the theoretical thermal energy which is converted into electricity, and for CapMix is:

$$\eta_{Carnot,CM} = \frac{\frac{(W_{out,T>20C}) - (W_{out,T=20C})}{Q_{in}}}{\frac{T_H - T_C}{T_H}} \tag{B.24}$$

Likewise, η_{carnot} for CDI is defined as:

$$\eta_{Carnot,CDI} = \frac{\frac{(W_{in,T=20C}) - (W_{in,T>20C})}{Q_{in}}}{\frac{T_H - T_C}{T_H}} \tag{B.25}$$

where W_{out} represents the net energy extracted for CapMix, and W_{in} represents the net energy input for CDI. This energy is then compared to the Carnot limit which is defined by the thermal properties of the high and low temperature reservoir (T_H and T_C). A summary of the tabulated results is shown in Table B.2 and B.3. The data is taken from Figures 5.3B, 5.3C, 5.3E, and 5.3F in the Chapter 5.

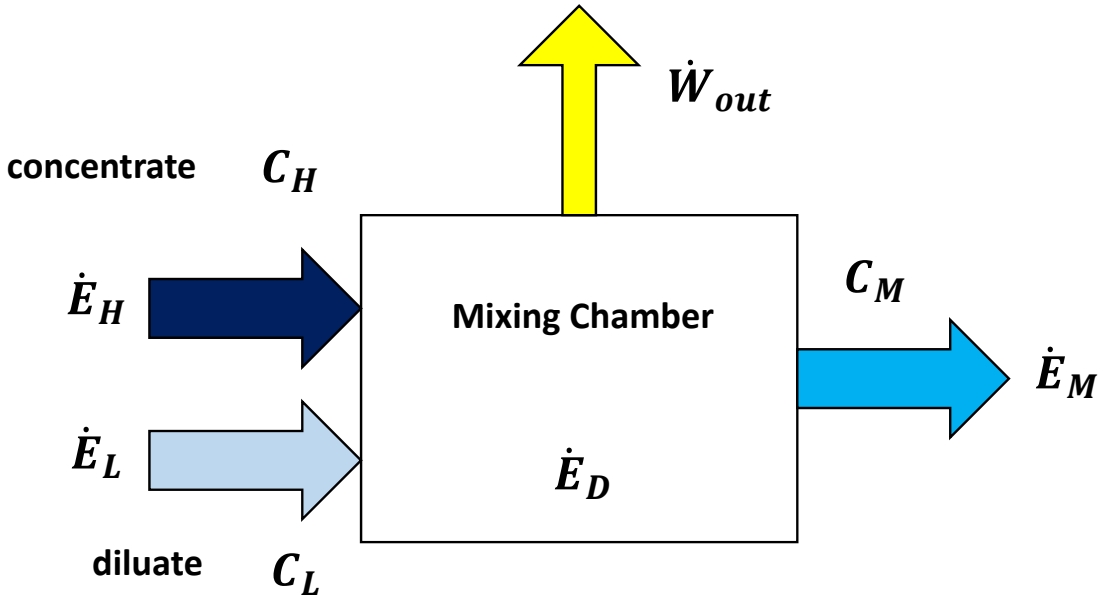

Figure B.1: Schematic of system to produce work from salinity gradient.

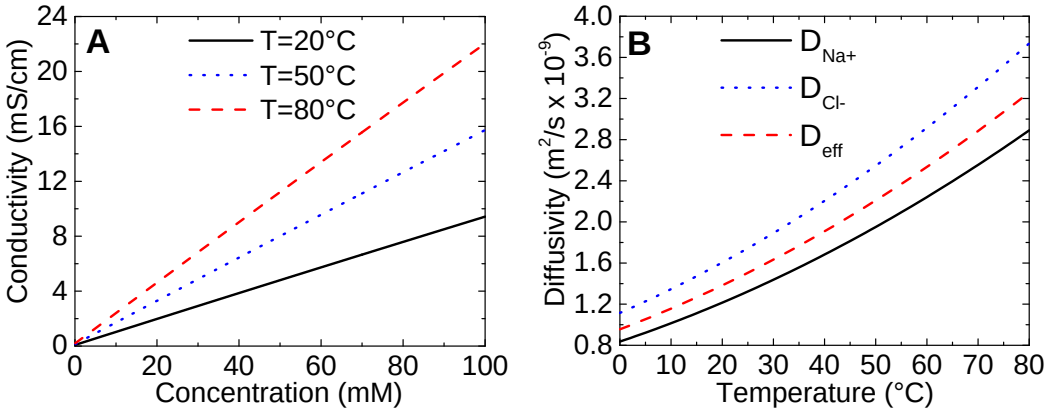

Figure B.2: (a) Effect of electrolyte conductivity for varying feed concentrations and temperatures, (b) Effect of temperature on diffusion coefficients, with both Na^+ and Cl^- ions shown independently and then averaged together using Cussler's relation.

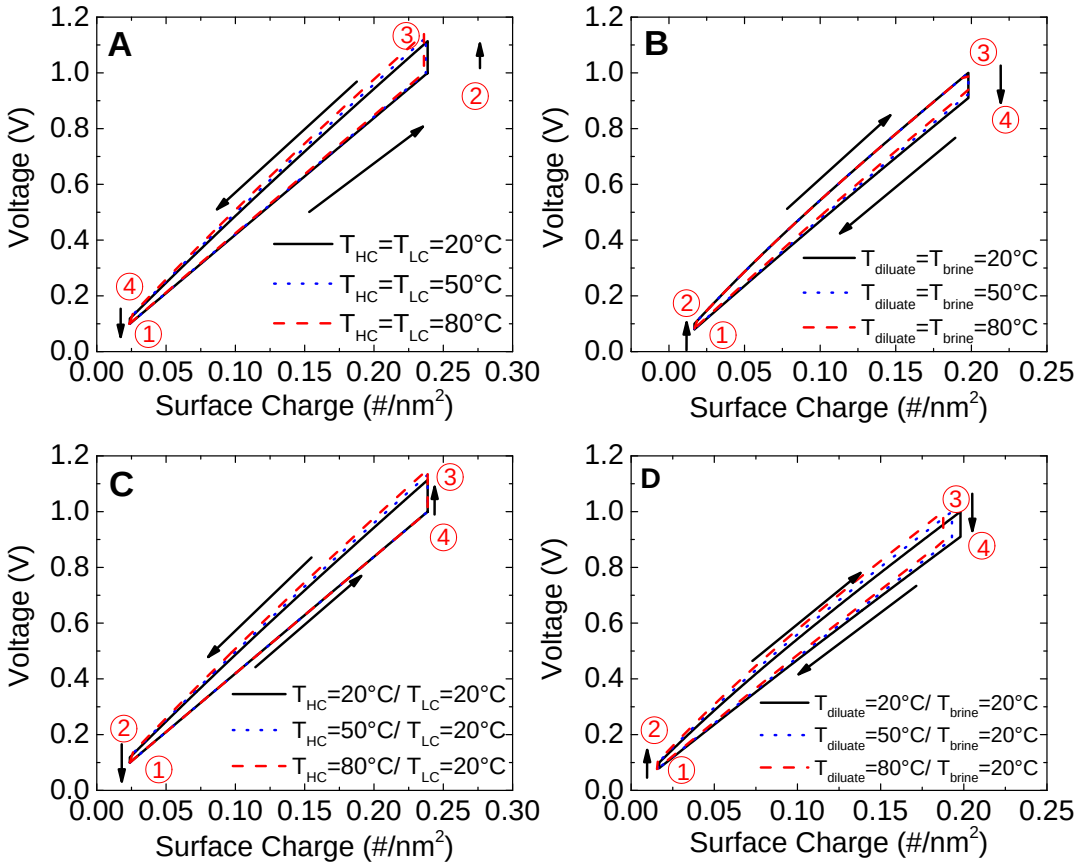

Figure B.3: (A) σ-V diagram for isothermal and reversible CapMix cycles (T_{HC}=T_{LC}) (B) σ-V diagram for isothermal and reversible CDI cycles (T_{feed}=T_{brine})(C) σ-V diagram for isothermal and reversible CapMix ($T_{HC}\neq T_{LC}$) (D) σ-V diagram for isothermal and reversible CDI cycles (T_{feed}=T_{brine}).

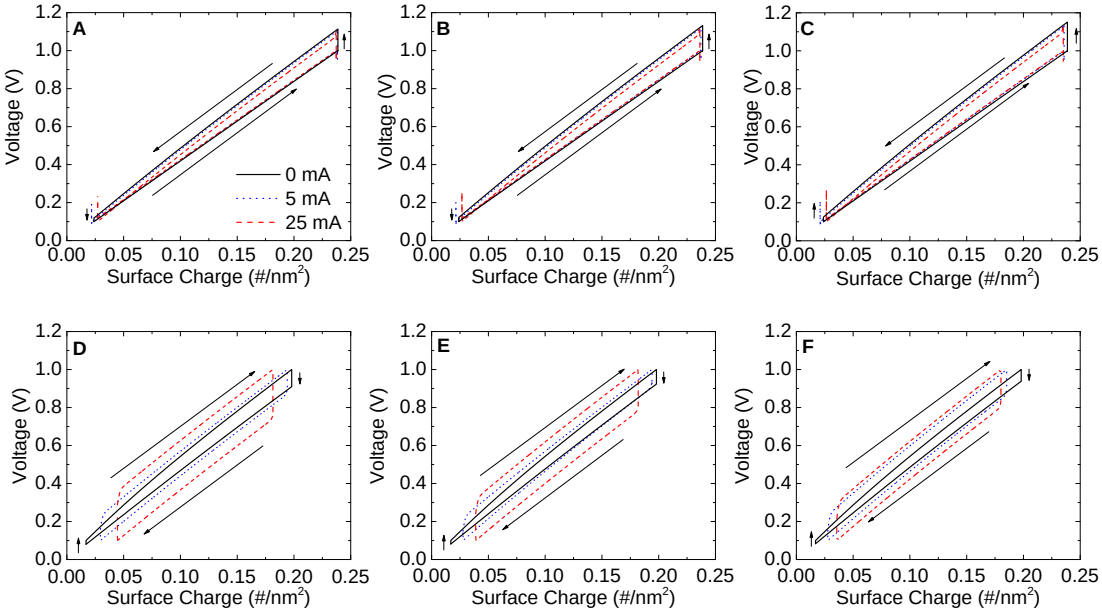

Figure B.4: CapMix σ-V diagrams for isothermal and irreversible operation at (A) 20°C, (B) 50°C, and (C) 80°C. CDI σ-V diagrams for isothermal and irreversible operation at (D) 20°C, (E) 50°C, and (F) 80°C.

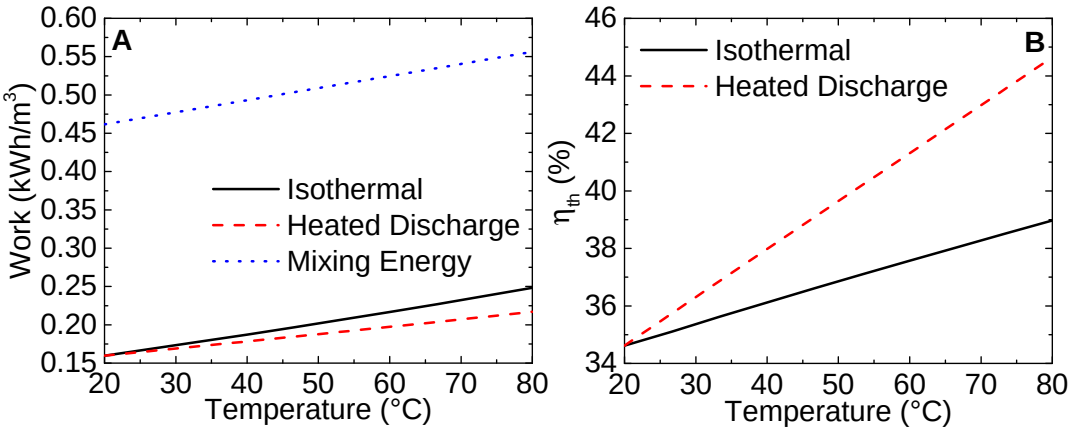

Figure B.5: (A)Net cycle work extracted from reversible and isothermal CapMix cycles, and (B) thermal efficiency from reversible and isothermal CapMix cycles.

Table B.1: Parameters assumed for model to determine convection coefficient.

Part	Material	Thickness (cm)	Area (cm^2)	Density (kg/m^3)	Specific Heat (J/kg*K)	Mass (kg)
End plate	Aluminum	3.8	109	2700	900	1.13
Flow field	Graphite	2.5	58	2500	720	0.37
Channel	Water	0.47	25	999	4200	0.01
Gasket	Viton Fluoroelastomer	0.3	33	1900	180	0.02
Current collector	Copper	3	130	8790	385	0.34
Channel case	Propylene	4	33	900	1920	0.01

Table B.2: Tabulated work extracted, thermodynamic efficiency, and exchange efficiency for CapMix processes.

$T_{discharge}(^{\circ}C)$	Current (mA)	Work Extracted (kWh/m^3)	$\eta_{th}(\%)$	$\eta_{Carnot}(\%)$
20	Reversible	0.18	39.42	–
50	Reversible	0.21	41.38	0.86
80	Reversible	0.24	43.32	0.47
20	5 mA	0.16	34.65	–
50	5 mA	0.19	36.86	0.86
80	5 mA	0.22	38.97	0.47
20	10 mA	0.14	30.05	–
50	10 mA	0.17	32.53	0.86
80	10 mA	0.19	34.80	0.47
20	15 mA	0.12	25.90	–
50	15 mA	0.15	28.65	0.86
80	15 mA	0.17	31.07	0.47
20	20 mA	0.10	22.11	–
50	20 mA	0.13	25.11	0.86
80	20 mA	0.15	27.69	0.47
20	25 mA	0.09	18.55	–
50	25 mA	0.11	21.87	0.75
80	25 mA	0.14	24.59	0.41

Table B.3: Tabulated work extracted, thermodynamic efficiency, and exchange efficiency for CDI processes.

$T_{discharge}(^{\circ}C)$	Current (mA)	Work Input (kWh/m^3)	TEE (%)	$\eta_{Carnot}(\%)$
20	Reversible	0.28	6.09	–
50	Reversible	0.25	7.63	1.08
80	Reversible	0.21	9.78	0.59
20	5 mA	0.16	3.64	–
50	5 mA	0.19	4.44	1.40
80	5 mA	0.22	5.36	0.71
20	10 mA	0.14	3.04	–
50	10 mA	0.17	3.73	1.72
80	10 mA	0.19	4.50	0.88
20	15 mA	0.12	2.65	–
50	15 mA	0.15	3.26	2.05
80	15 mA	0.17	3.91	1.00
20	20 mA	0.10	2.37	–
50	20 mA	0.13	2.91	2.26
80	20 mA	0.15	3.48	1.06
20	25 mA	0.09	2.17	–
50	25 mA	0.11	2.65	2.37
80	25 mA	0.14	3.16	1.12

APPENDIX C

SUPPORTING INFORMATION FOR: INFLUENCE OF FEED-ELECTRODE CONCENTRATION DIFFERENCES IN FLOW-ELECTRODE SYSTEMS FOR CAPACITIVE DEIONIZATION

C.1 Detailed operating parameters

Table C.1 shows the detailed parameters that were used during the experiments.

Table C.1: Parameters used in experiments.

Parameter (Units)	Symbol	Value
Cell Area (cm^2)	A_{cell}	25
Flow Channel Thickness (cm)	t_f	0.47
AEM thickness (μm)	t_{AEM}	110 - 150
CEM thickness (μm)	t_{CEM}	130 - 150
Flow electrode thickness (cm)	t_e	0.1
Activated Charcoal Surface Area (m^2/g)	SA"$_{AC}$	708
Activated Charcoal Density (g/mL)	ρ_{AC}	0.5
AEM Resistance (m^2)	R"$_{AEM}$	1.5 - 3.0
CEM Resistance (m^2)	R"$_{CEM}$	2.0 - 3.5

C.2 Estimation of electrode concentration during experiment

While it is not known exactly whether more of the adsorbed ions are stored in the activated carbon vs. the bulk solution, here, an estimate will be made to relate the concentration in the activated carbon (here assumed to be an average of all of the different pore sizes) to the salt adsorption capacity (SAC) of the electrode:

$$\rho C_{AC} = \frac{m_{AC}(SAC)}{V_f M_{NaCl}} \tag{C.1}$$

where m_{AC} is the mass of the carbon electrode, V_f is the feed volume, and M_{NaCl} is the

molar mass of NaCl. In order to relate the different concentrations, the definition of SAC based on salt removal during experimentation, shown in Eq. C.2, will be used:

$$SAC = \frac{(C_{f,i} - C_{f,f})V_f M_{NaCl}}{m_{AC}} \tag{C.2}$$

where $C_{f,i}$ represents the initial concentration of the feed, and $C_{f,f}$ the final volume of the feed. In this model, it will be assumed that the starting concentration of ions present is uniform throughout the entire slurry. In the entire electrodefeed system, an ion balance needs to be maintained at all times within feed and electrode. This balance can be represented by Eq. C.3, with all of the lefthand terms representing the total number of moles of NaCl initially:

$$C_{f,i}V_f + C_{bulk,i}V = C_{AC}V_{AC} + C_{bulk,f}V_{bulk} \tag{C.3}$$

In Eq. C.3, $C_{bulk,i}$ is the initial concentration of the bulk electrolyte solution in the flow electrode, and $C_{bulk,f}$ is the final volume of the bulk electrolyte solution in the flow electrode. The volume V represents the total volume of the flow electrode, comprising both the carbon particle volume and the bulk electrolyte volume:

$$V = V_{AC} + V_{bulk} \tag{C.4}$$

The volume of the activated carbon region, V_{AC} is best estimated using both the AC itself as well as a thin region outside of the electric double layer (EDL), which forms around the entire surface area of the carbon particles:

$$V_{AC} = m_{AC}SA"_{AC}t_{EDL} + \frac{m_{AC}}{\rho_{AC}} \tag{C.5}$$

where the EDL thickness t_{EDL}, is approximated as:

$$t_{EDL} = \left(\frac{\epsilon_r \epsilon_0 RT}{F^2 C_0 z^2}\right)^{1/2} \tag{C.6}$$

where ϵ_r is the relative static permittivity of the solution (dimensionless, a function of both concentration and temperature 5), ϵ_0 is the permittivity of free space (in F/m), R is the universal gas constant (in J/molK), T is the temperature of solution (in K), F is the fundamental Faraday constant, and C_0 is the concentration of the solution (in mM or mol/m3). z represents the valence, which is always taken to be unity in this study. Strictly speaking, the concentration as well as the EDL may change slightly as the AC is being adsorbed into the electrode. For simplicity, this value can be assumed to be constant and equivalent to the starting values. This allows us to ensure that the sizes of the two regions of the electrode remain constant through the desalination process.

This volume can generally be assumed to be relatively small compared to the bulk volume. The electrode conductivity and concentration can thus be assumed to change relatively little in comparison to the feed. Some of the ions can still go to the bulk, which can slightly increase the measured conductivity in the electrode overall.

Resistances were determined using the conductivities obtained/calculated, the cell area A_{cell}, and the given thickness in each region (t_e or t_f), with R_e representing the resistance for the electrode and R_f representing the resistance for the feed:

$$R_e = \frac{t_e}{(\kappa_e + \kappa_c) A_{cell}} \tag{C.7}$$

$$R_f = \frac{t_f}{\kappa_f A_{cell}} \tag{C.8}$$

where κ_e represents the ionic conductivity of the electrode, κ_f, the ionic conductivity of the feed, and κ_c the electrical conductivity of the activated carbon. However, in most cases, κ_c proved to be small enough that it did not make a significant difference.

While carbon particles allow for the conduction of electrons, electron transport occurs from the current collector to the particles, rather than from the membrane to the particle. For electron transfer to occur through the bulk of the flow electrode, a percolation threshold must be met. In all experiments conducted in this study, we are well below the percolation threshold as we only had 5% carbon particles. A significant amount of work has been conducted to evaluate this threshold, but typically, it has been shown that 5% weight is not significant enough to enable electric charge percolation within the cell 67. Therefore the resistance of flow electrode is quite high, independent of the carbon.

As needed during the calculations, conductivity was related to solution concentration using established correlations available. For a 20°C operating temperature (approximately equal to the room temperature obtained in actual experiments for this study), Eq. C.9 was obtained by extrapolating collected data for different salt concentrations:

$$\kappa = -(2x10^{-5})(C^2) + 0.1062C + 0.0886 \tag{C.9}$$

Eq. C.9 is valid when F is in units of mS/cm and C is in mM. Properties for the electrode were not directly measured during the experiment, but based on molar balance, their values can be estimated. First, we need to consider the volume of the AC relative to the electrode. This is best approximated by considering both its density and the electric double layer (EDL) surrounding its surface.

C.3 Plot of current density data

Plots of current density clearly illustrate that matching the electrode concentration to a more saline feed results in higher current magnitudes (Figure C.1). However, in the case of the 10 mM feed, it is seen that matching the electrode and feed concentrations reduces the overall current, as would be expected due to lower conductivity through the cell. Additionally, since the plots are extremely similar in Figure C.1A, this is a possible indicator that

current through the cell is much more sensitive to resistances from the electrode than it is to resistances from the feed under these conditions.

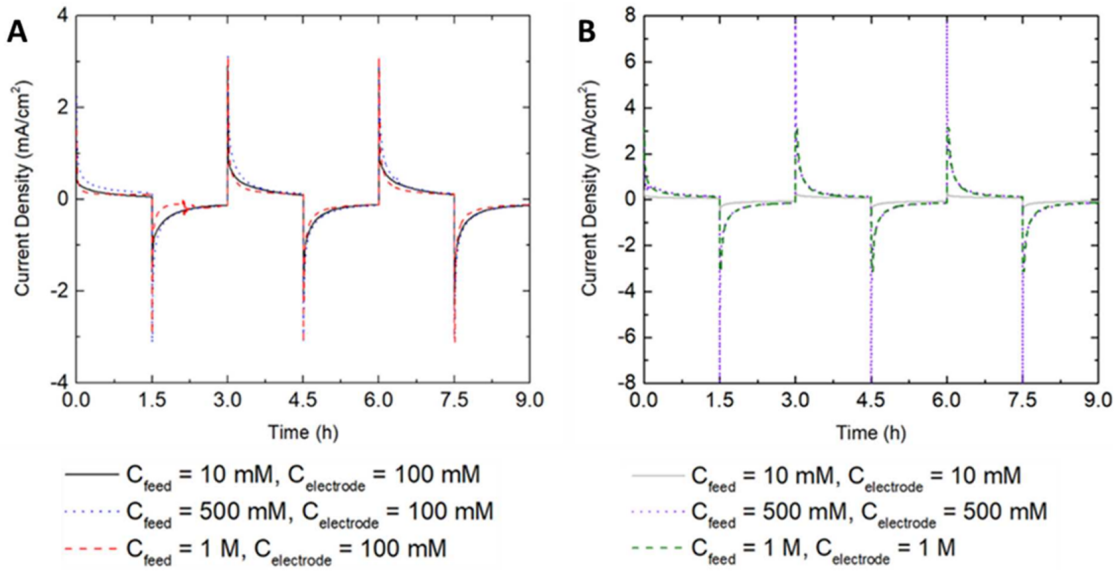

Figure C.1: Plot of current density vs. time for (A) mismatched and (B) matched concentrations.

It is unclear exactly why the current for the 500 mM test is maximized, although the difference may be insignificant. Additional cycling would help to rectify this to give results with greater certainty. It is worth noting, however, that the maximum only occurs during the first few seconds of testing with each cycle, then quickly drops off. This may be due to the higher influence of diffusion during the 1 M tests, which could possibly reduce some of the extent of the current.

C.4 Additional tests for high concentration feeds at greater electrode volumes

Additional data is presented for the 500 mM mismatch, 500 mM match, 1 M mismatch, 1 M match tests. These flow electrode volumes tested were 300 mL and 500 mL, while all other parameters are kept the same as with the 100 mL tests. These results support the data from Figure 6.4, but there does not appear to be any significant influence on the electrode volume alone.

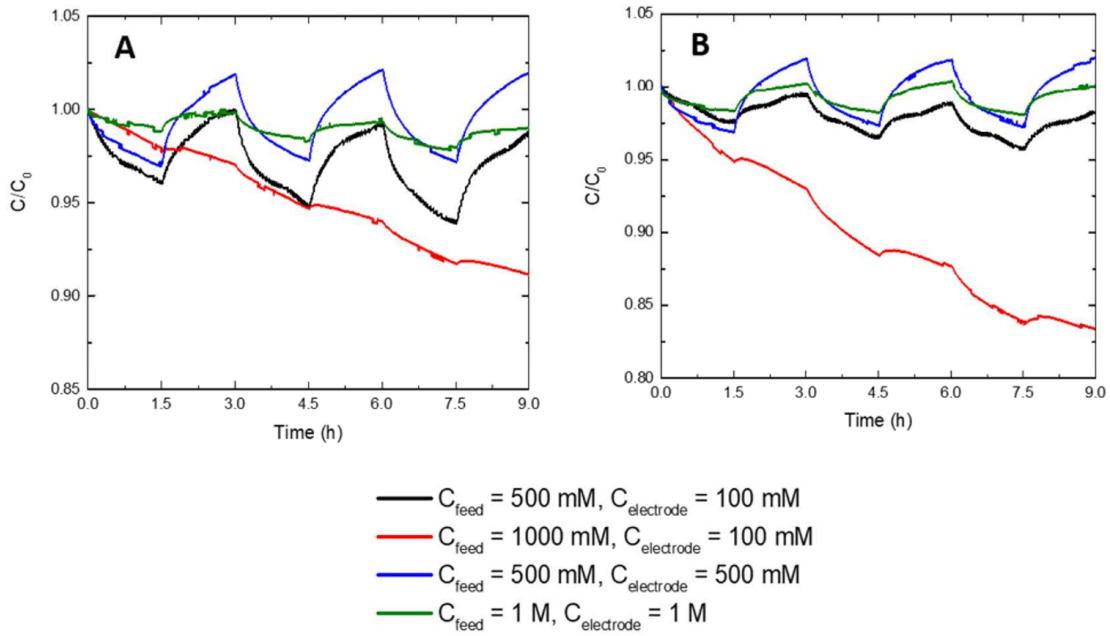

Figure C.2: Concentration vs. time for varying flow electrode volumes. (a) 300 mL, (b) 500 mL.

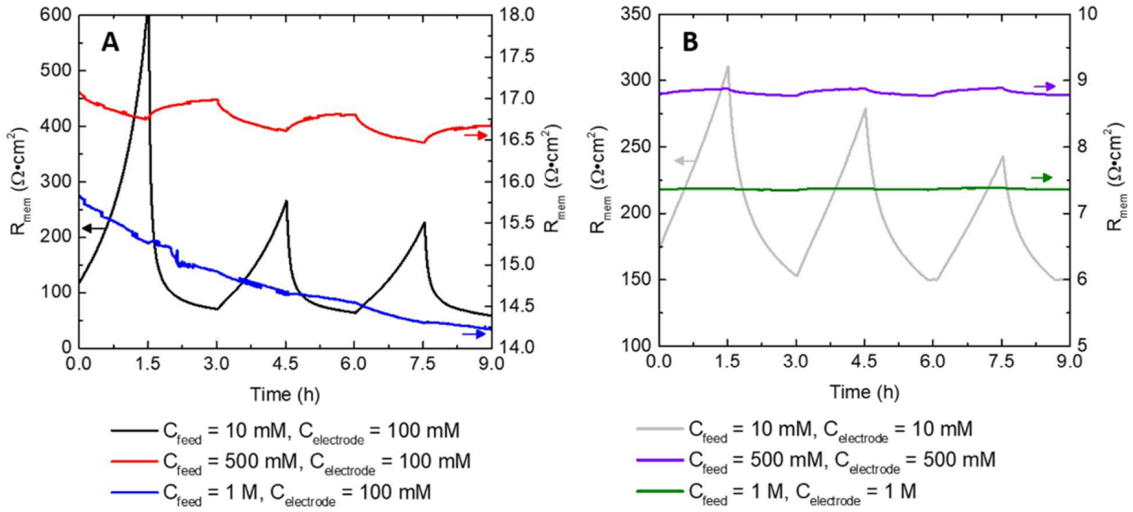

Figure C.3: Resistance directly calculated as a function of feed/electrolyte concentrations for (a) mismatched cases, (b) matched cases.

C.5 Long-term testing

Long-term experiments were run to ensure that the concentrations studied in this test would not be limited by the flow electrode volume. In all of these tests the flow electrode volume

used was 100 mL. (Figure 6.3 in Chapter 6)

APPENDIX D

SUPPORTING INFORMATION FOR: THERMODYNAMIC EVALUATION OF TRADITIONAL, FIXED-CHARGE, AND REDOX-ACTIVE POROUS ELECTRODES FOR CAPACITIVE DEIONIZATION IN BATCH AND CONTINUOUS MODE

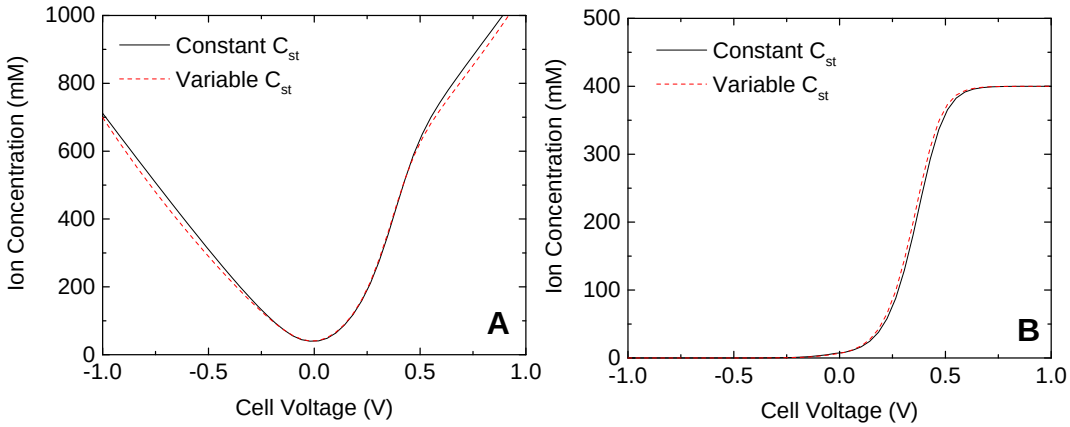

Figure D.1: Evaluation of (A) micropore concentration and (B) chemical charge when the Stern layer capacitance is considered as a constant or variable to account for effects of compression.

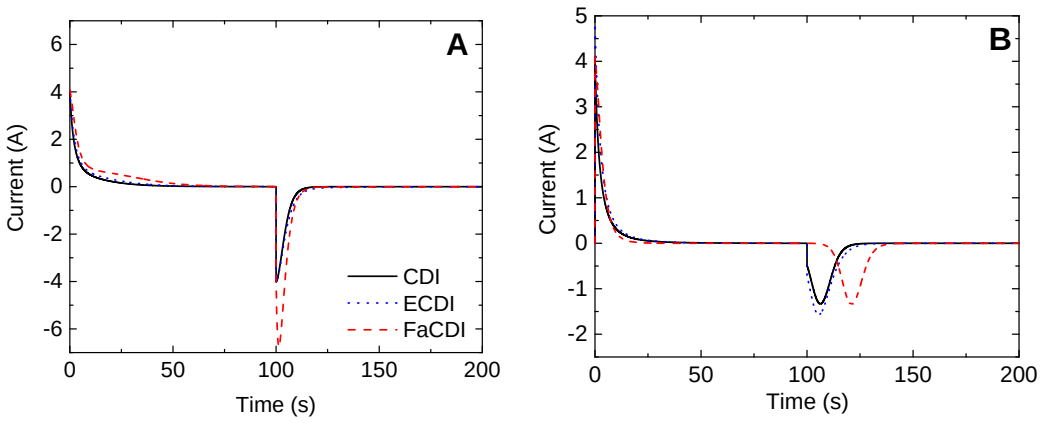

Figure D.2: Plots of current for (A) continuous and (B) batch mode short-term desalination.

REFERENCES

[1] T Buerkle, "Making every drop count," *Food and Agriculture Organization of the United Nations*, 2007.

[2] W. U.N.W.W. A. Program, "The united nations world water development report 2014," *Water and Energy*, 2014.

[3] M. Elimelech and W. A. Phillip, "The future of seawater desalination: Energy, technology, and the environment," *Science*, vol. 333, no. 6043, pp. 712–717, 2011.

[4] T. W. Hartley, "Public perception and participation in water reuse," *Desalination*, vol. 187, no. 1-3, pp. 115–126, 2006.

[5] N. H. Tran, M. Reinhard, and K. Y.-H. Gin, "Occurrence and fate of emerging contaminants in municipal wastewater treatment plants from different geographical regions-a review," *Water research*, vol. 133, pp. 182–207, 2018.

[6] J. S. Stanton, D. W. Anning, C. J. Brown, R. B. Moore, V. L. McGuire, S. L. Qi, A. C. Harris, K. F. Dennehy, P. B. McMahon, J. R. Degnan, *et al.*, "Brackish groundwater in the united states," US Geological Survey, Tech. Rep., 2017.

[7] D. Bauer, M. Philbrick, B. Vallario, H. Battey, Z. Clement, F. Fields, *et al.*, "The water-energy nexus: Challenges and opportunities," *US Department of Energy2014*, 2014.

[8] T. A. Bauder, R. Waskom, P. Sutherland, J. Davis, R. Follett, and P. Soltanpour, "Irrigation water quality criteria," *Service in action; no. 0.506*, 2011.

[9] M. Howells and H.-H. Rogner, "Water-energy nexus: Assessing integrated systems," *Nature Climate Change*, vol. 4, no. 4, p. 246, 2014.

[10] A. Plappally *et al.*, "Energy requirements for water production, treatment, end use, reclamation, and disposal," *Renewable and Sustainable Energy Reviews*, vol. 16, no. 7, pp. 4818–4848, 2012.

[11] R. Connor, *The united nations world water development report 2015: Water for a sustainable world*. UNESCO Publishing, 2015, vol. 1.

[12] P. Friedlingstein, R. M. Andrew, J. Rogelj, G. Peters, J. G. Canadell, R. Knutti, G. Luderer, M. R. Raupach, M. Schaeffer, D. P. van Vuuren, *et al.*, "Persistent growth

of co 2 emissions and implications for reaching climate targets," *Nature geoscience*, vol. 7, no. 10, p. 709, 2014.

[13] T. Welgemoed and C. Schutte, "Capacitive deionization technology: An alternative desalination solution," *Desalination*, vol. 183, no. 1-3, pp. 327–340, 2005.

[14] A. Cipollina, G. Micale, and L. Rizzuti, *Seawater desalination: Conventional and renewable energy processes*. Springer Science & Business Media, 2009.

[15] O. Buros, *The abcs of desalting*. International Desalination Association Topsfield, MA, 2000.

[16] H. Cooley, P. H. Gleick, and G. Wolff, "Desalination, with a grain of salt," *Pacific Institute. June*, 2006.

[17] H. T. El-Dessouky, H. M. Ettouney, and Y. Al-Roumi, "Multi-stage flash desalination: Present and future outlook," *Chemical Engineering Journal*, vol. 73, no. 2, pp. 173–190, 1999.

[18] D. M. Warsinger, K. H. Mistry, K. G. Nayar, H. W. Chung, and J. H. Lienhard V, "Entropy generation of desalination powered by variable temperature waste heat," *Entropy*, vol. 17, no. 11, pp. 7530–7566, 2015.

[19] T. Mezher, H. Fath, Z. Abbas, and A. Khaled, "Techno-economic assessment and environmental impacts of desalination technologies," *Desalination*, vol. 266, no. 1-3, pp. 263–273, 2011.

[20] R. Raluy, L Serra, J Uche, and A Valero, "Life-cycle assessment of desalination technologies integrated with energy production systems," *Desalination*, vol. 167, pp. 445–458, 2004.

[21] K. C. Ng, K. Thu, Y. Kim, A. Chakraborty, and G. Amy, "Adsorption desalination: An emerging low-cost thermal desalination method," *Desalination*, vol. 308, pp. 161–179, 2013.

[22] L. F. Greenlee, D. F. Lawler, B. D. Freeman, B. Marrot, and P. Moulin, "Reverse osmosis desalination: Water sources, technology, and today's challenges," *Water research*, vol. 43, no. 9, pp. 2317–2348, 2009.

[23] C. Fritzmann, J. Löwenberg, T. Wintgens, and T. Melin, "State-of-the-art of reverse osmosis desalination," *Desalination*, vol. 216, no. 1-3, pp. 1–76, 2007.

[24] L. Malaeb and G. M. Ayoub, "Reverse osmosis technology for water treatment: State of the art review," *Desalination*, vol. 267, no. 1, pp. 1–8, 2011.

[25] S. Avlonitis, K Kouroumbas, and N Vlachakis, "Energy consumption and membrane replacement cost for seawater ro desalination plants," *Desalination*, vol. 157, no. 1-3, pp. 151–158, 2003.

[26] M. W. Shahzad, M. Burhan, L. Ang, and K. C. Ng, "Energy-water-environment nexus underpinning future desalination sustainability," *Desalination*, vol. 413, pp. 52–64, 2017.

[27] M. Mintz, "Electrodialysisprinciples of process design," *Industrial & Engineering Chemistry*, vol. 55, no. 6, pp. 18–28, 1963.

[28] T. Humplik, J Lee, S. Ohern, B. Fellman, M. Baig, S. Hassan, M. Atieh, F Rahman, T Laoui, R Karnik, *et al.*, "Nanostructured materials for water desalination," *Nanotechnology*, vol. 22, no. 29, p. 292 001, 2011.

[29] T. G. Hurd, S. Beyhaghi, and M. Nosonovsky, "Ecological aspects of water desalination improving surface properties of reverse osmosis membranes," in *Green Tribology*, Springer, 2012, pp. 531–564.

[30] N. C. Wright *et al.*, "Justification for community-scale photovoltaic-powered electrodialysis desalination systems for inland rural villages in india," *Desalination*, vol. 352, pp. 82–91, 2014.

[31] M. Fidaleo and M. Moresi, "Electrodialysis applications in the food industry," *Advances in food and nutrition research*, vol. 51, pp. 265–360, 2006.

[32] K. M. Chehayeb *et al.*, "Entropy generation analysis of electrodialysis," *Desalination*, vol. 413, pp. 184–198, 2017.

[33] K. Dorfner, *Ion exchangers*. Walter de Gruyter, 2011.

[34] J. W. Blair and G. W. Murphy, "Saline water conversion," *Adv Chem Ser*, vol. 27, p. 206, 1960.

[35] G. Murphy and D. Caudle, "Mathematical theory of electrochemical demineralization in flowing systems," *Electrochimica Acta*, vol. 12, no. 12, pp. 1655–1664, 1967.

[36] A. Johnson and J. Newman, "Desalting by means of porous carbon electrodes," *Journal of the Electrochemical Society*, vol. 118, no. 3, pp. 510–517, 1971.

[37] A. M. Johnson and W. VENOLIA, "The electrosorb process for desalting water," 1970.

[38] A Soffer and M Folman, "The electrical double layer of high surface porous carbon electrode," *Journal of Electroanalytical Chemistry and Interfacial Electrochemistry*, vol. 38, no. 1, pp. 25–43, 1972.

[39] Y Oren and A Soffer, "Electrochemical parametric pumping," *Journal of the Electrochemical Society*, vol. 125, no. 6, pp. 869–875, 1978.

[40] J. C. Farmer, D. V. Fix, G. V. Mack, R. W. Pekala, and J. F. Poco, "The use of capacitive deionization with carbon aerogel electrodes to remove inorganic contaminants from water," in *Low Level Waste Conference*, 1995.

[41] J. Farmer, D. Fix, G. Mack, R. Pekala, and J. Poco, "Capacitive deionization of nacl and nano3 solutions with carbon aerogel electrodes," *Journal of the Electrochemical Society*, vol. 143, pp. 159–169, 1996.

[42] L. Li, L. Zou, H. Song, and G. Morris, "Ordered mesoporous carbons synthesized by a modified sol–gel process for electrosorptive removal of sodium chloride," *Carbon*, vol. 47, no. 3, pp. 775–781, 2009.

[43] S Porada, L Borchardt, M Oschatz, M Bryjak, J. Atchison, K. Keesman, S Kaskel, P. Biesheuvel, and V Presser, "Direct prediction of the desalination performance of porous carbon electrodes for capacitive deionization," *Energy & Environmental Science*, vol. 6, no. 12, pp. 3700–3712, 2013.

[44] K. Dai, L. Shi, J. Fang, D. Zhang, and B. Yu, "Nacl adsorption in multi-walled carbon nanotubes," *Materials Letters*, vol. 59, no. 16, pp. 1989–1992, 2005.

[45] D. Zhang, L. Shi, J. Fang, K. Dai, and X. Li, "Preparation and desalination performance of multiwall carbon nanotubes," *Materials Chemistry and Physics*, vol. 97, no. 2-3, pp. 415–419, 2006.

[46] L. Zou, "Developing nano-structured carbon electrodes for capacitive brackish water desalination," in *Expanding Issues in Desalination*, InTech, 2011.

[47] C. Yan, L. Zou, and R. Short, "Single-walled carbon nanotubes and polyaniline composites for capacitive deionization," *Desalination*, vol. 290, pp. 125–129, 2012.

[48] J. H. Lienhard, K. H. Mistry, M. H. Sharqawy, and G. P. Thiel, "Thermodynamics, exergy, and energy efficiency in desalination systems," 2017.

[49] J. A. Carballo, J. Bonilla, L. Roca, A. De la Calle, P. Palenzuela, and D. C. Alarcón-Padilla, "Optimal operating conditions analysis for a multi-effect distillation plant according to energetic and exergetic criteria.," *Desalination*, vol. 435, pp. 70–76, 2018.

[50] P. A. Fritz, F. Zisopoulos, S Verheggen, K Schroën, and R. Boom, "Exergy analysis of membrane capacitive deionization (mcdi)," *Desalination*, 2018.

[51] P. Debye and E. Hückel, "Zur theorie der elektrolyte. ii," *Das Grenzgesetz für die elektrische Leitfähigkeit. Phys*, no. 24, p. 305, 1923.

[52] C. W. Davies, "397. the extent of dissociation of salts in water. part viii. an equation for the mean ionic activity coefficient of an electrolyte in water, and a revision of the dissociation constants of some sulphates," *Journal of the Chemical Society (Resumed)*, pp. 2093–2098, 1938.

[53] D. Brogioli, F. La Mantia, and N. Y. Yip, "Thermodynamic analysis and energy efficiency of thermal desalination processes," *Desalination*, vol. 428, pp. 29–39, 2018.

[54] B. M. Fabuss and A Korosi, "Boiling point elevations of sea-water and its concentrates.," *Journal of Chemical and Engineering Data*, vol. 11, no. 4, pp. 606–609, 1966.

[55] A. Nafey, H. Fath, and A. Mabrouk, "Exergy and thermoeconomic evaluation of msf process using a new visual package," *Desalination*, vol. 201, no. 1-3, pp. 224–240, 2006.

[56] K. H. Mistry, M. A. Antar, and J. H. Lienhard V, "An improved model for multiple effect distillation," *Desalination and Water Treatment*, vol. 51, no. 4-6, pp. 807–821, 2013.

[57] M Blahušiak, A. A. Kiss, S. R. Kersten, and B. Schuur, "Quick assessment of binary distillation efficiency using a heat engine perspective," *Energy*, vol. 116, pp. 20–31, 2016.

[58] N. Kahraman and Y. A. Cengel, "Exergy analysis of a msf distillation plant," *Energy Conversion and Management*, vol. 46, no. 15-16, pp. 2625–2636, 2005.

[59] S. Kaushik, V. S. Reddy, and S. Tyagi, "Energy and exergy analyses of thermal power plants: A review," *Renewable and Sustainable energy reviews*, vol. 15, no. 4, pp. 1857–1872, 2011.

[60] Y. Cerci, *Improving the thermodynamic and economic efficiencies of desalination plants: Minimum work required for desalination and case studies of four working plants*, ser. Desalination and Water Purification Research and Development Program Report. U.S. Department of the Interior, Bureau of Reclamation: Denver, USA, 2003.

[61] B. A. Qureshi and S. M. Zubair, "Exergetic analysis of a brackish water reverse osmosis desalination unit with various energy recovery systems," *Energy*, vol. 93, pp. 256–265, 2015.

[62] G. P. Thiel, R. K. McGovern, S. M. Zubair, *et al.*, "Thermodynamic equipartition for increased second law efficiency," *Applied energy*, vol. 118, pp. 292–299, 2014.

[63] E. R. Reahl, "Half a century of desalination with electrodialysis," *GE Water & Process Technologies, General Electric Company*, 2006.

[64] K. Walha, R. B. Amar, L. Firdaous, F. Quéméneur, and P. Jaouen, "Brackish groundwater treatment by nanofiltration, reverse osmosis and electrodialysis in tunisia: Performance and cost comparison," *Desalination*, vol. 207, no. 1-3, pp. 95–106, 2007.

[65] R. K. McGovern, A. M. Weiner, L. Sun, C. G. Chambers, S. M. Zubair, *et al.*, "On the cost of electrodialysis for the desalination of high salinity feeds," *Applied Energy*, vol. 136, pp. 649–661, 2014.

[66] P. Biesheuvel, "Thermodynamic cycle analysis for capacitive deionization," *Journal of colloid and interface science*, vol. 332, no. 1, pp. 258–264, 2009.

[67] S. D. Faust and O. M. Aly, *Adsorption processes for water treatment*. Elsevier, 2013.

[68] S. K. Milonjić, "A consideration of the correct calculation of thermodynamic parameters of adsorption.," *Journal of the Serbian chemical society*, vol. 72, no. 12, 2007.

[69] H. Li, T. Lu, L. Pan, Y. Zhang, and Z. Sun, "Electrosorption behavior of graphene in nacl solutions," *Journal of Materials Chemistry*, vol. 19, no. 37, pp. 6773–6779, 2009.

[70] P. S. Ghosal and A. K. Gupta, "Determination of thermodynamic parameters from langmuir isotherm constant-revisited," *Journal of Molecular Liquids*, vol. 225, pp. 137–146, 2017.

[71] M. Mossad and L. Zou, "Evaluation of the salt removal efficiency of capacitive deionisation: Kinetics, isotherms and thermodynamics," *Chemical engineering journal*, vol. 223, pp. 704–713, 2013.

[72] Y. Liu, "Is the free energy change of adsorption correctly calculated?" *Journal of Chemical & Engineering Data*, vol. 54, no. 7, pp. 1981–1985, 2009.

[73] H. Li, L. Pan, Y. Zhang, L. Zou, C. Sun, Y. Zhan, and Z. Sun, "Kinetics and thermodynamics study for electrosorption of nacl onto carbon nanotubes and carbon nanofibers electrodes," *Chemical Physics Letters*, vol. 485, no. 1-3, pp. 161–166, 2010.

[74] P. Saha and S. Chowdhury, "Insight into adsorption thermodynamics," in *Thermodynamics*, InTechOpen, 2011.

[75] M. J. Moran, H. N. Shapiro, D. D. Boettner, and M. B. Bailey, *Fundamentals of engineering thermodynamics*. John Wiley & Sons, 2010.

[76] A Al-Zahrani, J Orfi, Z Al-Suhaibani, B Salim, and H Al-Ansary, "Thermodynamic analysis of a reverse osmosis desalination unit with energy recovery system," *Procedia engineering*, vol. 33, pp. 404–414, 2012.

[77] M. J. Suess, "Reverse osmosis. a thermodynamic analysis and exercise," *Journal of Chemical Education*, vol. 48, no. 3, p. 190, 1971.

[78] M. C. Hatzell, K. B. Hatzell, and B. E. Logan, "Using flow electrodes in multiple reactors in series for continuous energy generation from capacitive mixing," *Environmental Science & Technology Letters*, vol. 1, no. 12, pp. 474–478, 2014.

[79] K. B. Hatzell, M. C. Hatzell, K. M. Cook, M. Boota, G. M. Housel, A. McBride, E. C. Kumbur, and Y. Gogotsi, "Effect of oxidation of carbon material on suspension electrodes for flow electrode capacitive deionization," *Environmental science & technology*, vol. 49, no. 5, pp. 3040–3047, 2015.

[80] R Willemse, "Blue energy (salinity power) in the netherlands," *Energy Research Centre of the Netherlands, Petten, The Netherlands, Technical Report No. ECN-E–07-058. http://www. esteem-tool. eu/fileadmin/esteem-tool/docs/CASE_27_def. pdf*, 2007.

[81] M. C. Hatzell and K. B. Hatzell, "Blue refrigeration: Capacitive de-ionization for brackish water treatment," *Journal of Electrochemical Energy Conversion and Storage*, vol. 15, no. 1, p. 011 009, 2018.

[82] D. Brogioli, "Extracting renewable energy from a salinity difference using a capacitor," *Physical review letters*, vol. 103, no. 5, p. 058 501, 2009.

[83] R. van Roij *et al.*, "Statistical thermodynamics of supercapacitors and blue engines," *Electrostatics of Soft and Disordered Matter*, vol. 263, 2014.

[84] N. Boon and R. Van Roij, "blue energyfrom ion adsorption and electrode charging in sea and river water," *Molecular Physics*, vol. 109, no. 7-10, pp. 1229–1241, 2011.

[85] P. Biesheuvel and A Van der Wal, "Membrane capacitive deionization," *Journal of Membrane Science*, vol. 346, no. 2, pp. 256–262, 2010.

[86] J. Zhang, K. B. Hatzell, and M. C. Hatzell, "A combined heat-and power-driven membrane capacitive deionization system," *Environmental Science & Technology Letters*, vol. 4, no. 11, pp. 470–474, 2017.

[87] J. Zhang, M. Nazemi, and M. C. Hatzell, "Evaluation of non-adiabatic thermodynamic cycles for electroadsorption based deionization," in *Meeting Abstracts*, The Electrochemical Society, 2017, pp. 2262–2262.

[88] J. Zhang, *Experimental investigation of combined heat and power capacitive deionization*, 2017.

[89] A. J. Bard, L. R. Faulkner, J. Leddy, and C. G. Zoski, *Electrochemical methods: Fundamentals and applications*. wiley New York, 1980, vol. 2.

[90] H. v. Helmholtz, "Ueber einige gesetze der vertheilung elektrischer ströme in körperlichen leitern, mit anwendung auf die thierisch-elektrischen versuche (schluss.)," *Annalen der Physik*, vol. 165, no. 7, pp. 353–377, 1853.

[91] G. Ehrenstein, "Surface charge," *Biophysics textbook on-line. Biophysical Society, Bethesda, Maryland. Available at: Http:/www. biophysics. org/btol*, 2001.

[92] O. Stern, "The theory of the electrolytic double-layer," *Z. Elektrochem*, vol. 30, no. 508, pp. 1014–1020, 1924.

[93] P. Biesheuvel, S Porada, M Levi, and M. Z. Bazant, "Attractive forces in microporous carbon electrodes for capacitive deionization," *Journal of solid state electrochemistry*, vol. 18, no. 5, pp. 1365–1376, 2014.

[94] P. Biesheuvel, Y. Fu, and M. Z. Bazant, "Diffuse charge and faradaic reactions in porous electrodes," *Physical Review E*, vol. 83, no. 6, p. 061 507, 2011.

[95] P. Biesheuvel and M Van Soestbergen, "Counterion volume effects in mixed electrical double layers," *Journal of Colloid and Interface Science*, vol. 316, no. 2, pp. 490–499, 2007.

[96] C. Outhwaite and L. Bhuiyan, "A modified poisson–boltzmann equation in electric double layer theory for a primitive model electrolyte with size-asymmetric ions," *The Journal of chemical physics*, vol. 84, no. 6, pp. 3461–3471, 1986.

[97] E. Sambriski, D. Schwartz, and J. De Pablo, "A mesoscale model of dna and its renaturation," *Biophysical journal*, vol. 96, no. 5, pp. 1675–1690, 2009.

[98] P. Sharma and T. Bhatti, "A review on electrochemical double-layer capacitors," *Energy conversion and management*, vol. 51, no. 12, pp. 2901–2912, 2010.

[99] E. Frackowiak and F. Beguin, "Carbon materials for the electrochemical storage of energy in capacitors," *Carbon*, vol. 39, no. 6, pp. 937–950, 2001.

[100] L. Jianming and C. Xiaomei, "Ruo2/mno2 composite materials for high-performance supercapacitor electrodes," *Journal of Semiconductors*, vol. 36, no. 8, p. 083 006, 2015.

[101] R. L. Spyker and R. M. Nelms, "Classical equivalent circuit parameters for a double-layer capacitor," *IEEE transactions on aerospace and electronic systems*, vol. 36, no. 3, pp. 829–836, 2000.

[102] R. De Levie, "On porous electrodes in electrolyte solutions: I. capacitance effects," *Electrochimica Acta*, vol. 8, no. 10, pp. 751–780, 1963.

[103] B. Pillay and J. Newman, "The influence of side reactions on the performance of electrochemical double-layer capacitors," *Journal of the Electrochemical Society*, vol. 143, no. 6, pp. 1806–1814, 1996.

[104] V. Srinivasan and J. W. Weidner, "Mathematical modeling of electrochemical capacitors," *Journal of the Electrochemical Society*, vol. 146, no. 5, pp. 1650–1658, 1999.

[105] J. R. Miller and P. Simon, "Electrochemical capacitors for energy management," *Science Magazine*, vol. 321, no. 5889, pp. 651–652, 2008.

[106] A. d'Entremont and L. Pilon, "First-principles thermal modeling of electric double layer capacitors under constant-current cycling," *J. Power Sources*, vol. 246, pp. 887–898, 2014.

[107] A. L. d'Entremont and L. Pilon, "Thermal effects of asymmetric electrolytes in electric double layer capacitors," *J. Power Sources*, vol. 273, pp. 196–209, 2015.

[108] H. K. Mutha, "Carbon nanotube electrodes for capacitive deionization," PhD thesis, Massachusetts Institute of Technology, 2013.

[109] S.-i. Jeon, H.-r. Park, J.-g. Yeo, S. Yang, C. H. Cho, M. H. Han, and D. K. Kim, "Desalination via a new membrane capacitive deionization process utilizing flow-electrodes," *Energy & Environmental Science*, vol. 6, no. 5, pp. 1471–1475, 2013.

[110] K. B. Hatzell, M. Boota, and Y. Gogotsi, "Materials for suspension (semi-solid) electrodes for energy and water technologies," *Chemical Society Reviews*, vol. 44, no. 23, pp. 8664–8687, 2015.

[111] M. Wang, S. Hou, Y. Liu, X. Xu, T. Lu, R. Zhao, and L. Pan, "Capacitive neutralization deionization with flow electrodes," *Electrochimica Acta*, vol. 216, pp. 211–218, 2016.

[112] S Porada, D Weingarth, H. Hamelers, M Bryjak, V Presser, and P. Biesheuvel, "Carbon flow electrodes for continuous operation of capacitive deionization and capacitive mixing energy generation," *Journal of Materials Chemistry A*, vol. 2, no. 24, pp. 9313–9321, 2014.

[113] M Boota, K. Hatzell, M Alhabeb, E. Kumbur, and Y Gogotsi, "Graphene-containing flowable electrodes for capacitive energy storage," *Carbon*, vol. 92, pp. 142–149, 2015.

[114] H.-r. Park, J. Choi, S. Yang, S. J. Kwak, S.-i. Jeon, M. H. Han, and D. K. Kim, "Surface-modified spherical activated carbon for high carbon loading and its desalting performance in flow-electrode capacitive deionization," *RSC Advances*, vol. 6, no. 74, pp. 69 720–69 727, 2016.

[115] X. Xu, M. Wang, Y. Liu, T. Lu, and L. Pan, "Ultrahigh desalinization performance of asymmetric flow-electrode capacitive deionization device with an improved operation voltage of 1.8 v," *ACS Sustainable Chemistry & Engineering*, vol. 5, no. 1, pp. 189–195, 2016.

[116] T. Kim and J. Yoon, "Cdi ragone plot as a functional tool to evaluate desalination performance in capacitive deionization," *RSC Advances*, vol. 5, no. 2, pp. 1456–1461, 2015.

[117] S. Yang, S.-i. Jeon, H. Kim, J. Choi, J.-g. Yeo, H.-r. Park, and D. K. Kim, "Stack design and operation for scaling up the capacity of flow-electrode capacitive deionization technology," *ACS Sustainable Chemistry & Engineering*, vol. 4, no. 8, pp. 4174–4180, 2016.

[118] Y. Gendel, A. K. E. Rommerskirchen, O. David, and M. Wessling, "Batch mode and continuous desalination of water using flowing carbon deionization (fcdi) technology," *Electrochemistry Communications*, vol. 46, pp. 152–156, 2014.

[119] J. Ma, D. He, W. Tang, P. Kovalsky, C. He, C. Zhang, and T. D. Waite, "Development of redox-active flow electrodes for high-performance capacitive deionization," *Environmental science & technology*, vol. 50, no. 24, pp. 13 495–13 501, 2016.

[120] A. Rommerskirchen, Y. Gendel, and M. Wessling, "Single module flow-electrode capacitive deionization for continuous water desalination," *Electrochemistry Communications*, vol. 60, pp. 34–37, 2015.

[121] P. Liang, X. Sun, Y. Bian, H. Zhang, X. Yang, Y. Jiang, P. Liu, and X. Huang, "Optimized desalination performance of high voltage flow-electrode capacitive deionization by adding carbon black in flow-electrode," *Desalination*, vol. 420, pp. 63–69, 2017.

[122] K. S. Spiegler and Y. M. El-Sayed, "The energetics of desalination processes," *Desalination*, vol. 134, no. 1-3, pp. 109–128, 2001.

[123] Y. Oren, "Capacitive deionization (cdi) for desalination and water treatment-past, present and future (a review)," *Desalination*, vol. 228, no. 1-3, pp. 10–29, 2008.

[124] I. C. Karagiannis and P. G. Soldatos, "Water desalination cost literature: Review and assessment," *Desalination*, vol. 223, no. 1-3, pp. 448–456, 2008.

[125] S. S. Kremen, "Reverse osmosis makes high quality water now," *Environ. Sci. Technol.*, vol. 9, no. 4, pp. 314–318, 1975.

[126] R. K. McGovern and J. H. Lienhard, "On the potential of forward osmosis to energetically outperform reverse osmosis desalination," *J. Membr. Sci.*, vol. 469, pp. 245–250, 2014.

[127] E. S. Hrayshat, "Brackish water desalination by a stand alone reverse osmosis desalination unit powered by photovoltaic solar energy," *Renew. Energy*, vol. 33, no. 8, pp. 1784–1790, 2008.

[128] M Wilf, M Konstantin, and A Chencinsky, "Evaluation of an ion exchange system regenerated with seawater for the increase of product recovery of reverse osmosis brackish water plant," *Desalination*, vol. 34, no. 3, pp. 189–197, 1980.

[129] M. Alghoul, P Poovanaesvaran, K. Sopian, and M. Sulaiman, "Review of brackish water reverse osmosis (bwro) system designs," *Renew. Sust. Energ. Rev.*, vol. 13, no. 9, pp. 2661–2667, 2009.

[130] Y. Cerci, "Exergy analysis of a reverse osmosis desalination plant in california," *Desalination*, vol. 142, no. 3, pp. 257–266, 2002.

[131] I. H. Aljundi, "Second-law analysis of a reverse osmosis plant in jordan," *Desalination*, vol. 239, no. 1-3, pp. 207–215, 2009.

[132] H.-J. Lee, F Sarfert, H Strathmann, and S.-H. Moon, "Designing of an electrodialysis desalination plant," *Desalination*, vol. 142, no. 3, pp. 267–286, 2002.

[133] R Zhao, S Porada, P. M. Biesheuvel, and A Van der Wal, "Energy consumption in membrane capacitive deionization for different water recoveries and flow rates, and comparison with reverse osmosis," *Desalination*, vol. 330, pp. 335 –341, 2013.

[134] M. E. Suss, S. Porada, X. Sun, P. M. Biesheuvel, J. Yoon, and V. Presser, "Water desalination via capacitive deionization: What is it and what can we expect from it?" *Energy Environ. Sci.*, vol. 8, no. 8, pp. 2296–2319, 2015.

[135] M. A. Anderson, A. L. Cudero, and J. Palma, "Capacitive deionization as an electrochemical means of saving energy and delivering clean water. comparison to present desalination practices: Will it compete?" *Electrochimica Acta*, vol. 55, no. 12, pp. 3845–3856, 2010.

[136] P. M. Biesheuvel, M. Z. Bazant, R. D. Cusick, T. A. Hatton, K. B. Hatzell, M. C. Hatzell, S. Liang P.; Lin, S. Porada, and J. G. Santiago, "Et al. capacitive deionization–defining a class of desalination technologies," *ArXiv preprint arXiv:1709.05925* ***2017***.,

[137] R Zhao, P. M. Biesheuvel, and V. der Wal A, "Energy consumption and constant current operation in membrane capacitive deionization," *Energy Environ. Sci.*, vol. 5, no. 11, pp. 9520 –9527, 2012.

[138] J. E. Dykstra, R Zhao, P. M. Biesheuvel, and V. der Wal A, "Resistance identification and rational process design in capacitive deionization," *Water Res.*, vol. 88, pp. 358–370, 2018.

[139] X Shang, R. D. Cusick, and K. C. Smith, "A combined modeling and experimental study assessing the impact of fluid pulsation on charge and energy efficiency in capacitive deionization," *J. Electrochem. Soc.*, vol. 164, no. 14, ES53–547, 2016.

[140] A. Hemmatifar, A. Ramachandran, K. Liu, D. I. Oyarzun, M. Z. Bazant, and J. G. Santiago, "Thermodynamics of ion separation by electrosorption," *Environ. Sci. Technol.*, In Press, 2018.

[141] N. Boon and R. van Roij, "'blue energy' from ion adsorption and electrode charging in sea and river water.," *Mol. Phys.*, vol. 109, pp. 1229–1241, 2011.

[142] M. Janssen, A. Härtel, and R. Van Roij, "Boosting capacitive blue-energy and desalination devices with waste heat," *Physical review letters*, vol. 113, no. 26, p. 268 501, 2014.

[143] T. Markovich, D. Andelman, and R. Podgornik, "Charged membranes: Poisson-boltzmann theory, dlvo paradigm and beyond," *ArXiv preprint arXiv:1603.09451*, 2016.

[144] R. A. Rica, R. Ziano, D. Salerno, F. Mantegazza, R. van Roij, and D. Brogioli, "Capacitive mixing for harvesting the free energy of solutions at different concentrations," *Entropy*, vol. 15, no. 4, pp. 1388–1407, 2013.

[145] P. M. Biesheuvel and A van der Wal, "Membrane capacitive deionization," *J. Membr. Sci.*, vol. 346, no. 2, pp. 256–262, 2010.

[146] L. Wang, P. M. Biesheuvel, and S. Lin, "Reversible thermodynamic cycle analysis for capacitive deionization with modified donnan model," *J. Colloid Interface Sci.*, vol. 52, pp. 522–528, 2018.

[147] L. Wang and S. Lin, "Membrane capacitive deionization with constant current vs. constant voltage charging: Which is better?" *Environ. Sci. Technol.*, vol. 13, pp. 4051–4060, 2018.

[148] S. I. Sandler, *Chemical, biochemical, and engineering thermodynamics*. John Wiley & Son, 2006.

[149] J. Szargut, D. R. Morris, and F. R. Steward, *Exergy analysis of thermal, chemical, and metallurgical processes*. Hemisphere Publishing, New York, NY, 1987.

[150] K. S. Pitzer, "Thermodynamics of electrolytes. i. theoretical basis and general equations," *J. Phys. Chem.*, vol. 77, no. 2, pp. 268–277, 1973.

[151] K. B. Hatzell, J. Eller, S. L. Morelly, M. H. Tang, N. J. Alvarez, and Y. Gogotsi, "Direct observation of active material interactions in flowable electrodes using x-ray tomography," *Faraday discussions*, vol. 199, pp. 511–524, 2017.

[152] D. Moreno and M. Hatzell, "The influence of feed-electrode concentration differences in flow-electrode systems for capacitive deionization," *Industrial & Engineering Chemistry Research*, 2018.

[153] P. Biesheuvel, B Van Limpt, and A Van der Wal, "Dynamic adsorption/desorption process model for capacitive deionization," *The journal of physical chemistry C*, vol. 113, no. 14, pp. 5636–5640, 2009.

[154] A. Härtel, M. Janssen, D. Weingarth, V. Presser, and R. van Roij, "Heat-to-current conversion of low-grade heat from a thermocapacitive cycle by supercapacitors," *Energy & Environmental Science*, vol. 8, no. 8, pp. 2396–2401, 2015.

[155] M. Marino, L. Misuri, M. L. Jiménez, S. Ahualli, O. Kozynchenko, S. Tennison, M. Bryjak, and D. Brogioli, "Modification of the surface of activated carbon electrodes for capacitive mixing energy extraction from salinity differences," *Journal of colloid and interface science*, vol. 436, pp. 146–153, 2014.

[156] M. Simoncelli, N. Ganfoud, A. Sene, M. Haefele, B. Daffos, P.-L. Taberna, M. Salanne, P. Simon, and B. Rotenberg, "Blue energy and desalination with nanoporous carbon electrodes: Capacitance from molecular simulations to continuous models," *Physical Review X*, vol. 8, no. 2, p. 021 024, 2018.

[157] A. P. Straub, A. Deshmukh, and M. Elimelech, "Pressure-retarded osmosis for power generation from salinity gradients: Is it viable?" *Energy & Environmental Science*, vol. 9, no. 1, pp. 31–48, 2016.

[158] F. Liu, T. F. Donkers, R. M. Wagterveld, O. Schaetzle, M. Saakes, C. J. Buisman, and H. V. Hamelers, "Parallel up-scaling of capacitive mixing (capmix) system enhances the specific performance," *Electrochimica Acta*, vol. 187, pp. 104–112, 2016.

[159] D Brogioli, R Ziano, R. Rica, D Salerno, and F Mantegazza, "Capacitive mixing for the extraction of energy from salinity differences: Survey of experimental results and electrochemical models," *J. Colloid Interface Sci.*, vol. 407, pp. 457–466, 2013.

[160] D. Moreno, Y. Bootwala, W.-Y. Tsai, Q. Gao, F. Shen, N. Balke, K. B. Hatzell, and M. C. Hatzell, "In situ electrochemical dilatometry of phosphate anion electrosorption," *Environmental Science & Technology Letters*, vol. 5, no. 12, pp. 745–749, 2018.

[161] M. Z. Bazant, K. Thornton, and A. Ajdari, "Diffuse-charge dynamics in electrochemical systems," *Physical review E*, vol. 70, no. 2, p. 021 506, 2004.

[162] D. Moreno and M. C. Hatzell, "Efficiency of carnot and conventional capacitive deionization cycles," *The Journal of Physical Chemistry C*, vol. 122, no. 39, pp. 22 480–22 486, 2018.

[163] A. dEntremont and L. Pilon, "Scaling laws for heat generation and temperature oscillations in edlcs under galvanostatic cycling," *Int. J. Heat Mass Transfer*, vol. 75, pp. 637–649, 2014.

[164] H. Gualous, H. Louahlia-Gualous, R. Gallay, and A. Miraoui, "Supercapacitor thermal modeling and characterization in transient state for industrial applications," *IEEE Trans. Ind. Appl.*, vol. 45, no. 3, pp. 1035–1044, 2009.

[165] F. Rafik, H. Gualous, R. Gallay, A. Crausaz, and A. Berthon, "Frequency, thermal and voltage supercapacitor characterization and modeling," *J. Power Sources*, vol. 165, no. 2, pp. 928–934, 2007.

[166] J. Schiffer, D. Linzen, and D. U. Sauer, "Heat generation in double layer capacitors," *J. Power Sources*, vol. 160, no. 1, pp. 765–772, 2006.

[167] A. L. d'Entremont, H.-L. Girard, H. Wang, and L. Pilon, "Electrochemical transport phenomena in hybrid pseudocapacitors under galvanostatic cycling," *J. Electrochem. Soc.*, vol. 163, no. 2, A229–A243, 2016.

[168] P. Guillemet, Y Scudeller, and T. Brousse, "Multi-level reduced-order thermal modeling of electrochemical capacitors," *J. Power Sources*, vol. 157, no. 1, pp. 630–640, 2006.

[169] B. B. Sales, O. S. Burheim, S. Porada, V. Presser, C. J. Buisman, and H. V. Hamelers, "Extraction of energy from small thermal differences near room temperature using capacitive membrane technology," *Environ. Sci. Technol. Lett.*, vol. 1, no. 9, pp. 356–360, 2014.

[170] S. Ahualli, M. M. Fernández, G. Iglesias, Á. V. Delgado, and M. L. Jiménez, "Temperature effects on energy production by salinity exchange," *Environ. Sci. Technol.*, vol. 48, no. 20, pp. 12 378–12 385, 2014.

[171] R. A. Rica, D. Brogioli, R. Ziano, D. Salerno, and F. Mantegazza, "Ions transport and adsorption mechanisms in porous electrodes during capacitive-mixing double layer expansion (cdle)," *The Journal of Physical Chemistry C*, vol. 116, no. 32, pp. 16 934–16 938, 2012.

[172] S Porada, R Zhao, A Van Der Wal, V Presser, and P. Biesheuvel, "Review on the science and technology of water desalination by capacitive deionization," *Progress in Materials Science*, vol. 58, no. 8, pp. 1388–1442, 2013.

[173] H. Cohen, S. E. Eli, M. Jõgi, and M. E. Suss, "Suspension electrodes combining slurries and upflow fluidized beds," *ChemSusChem*, vol. 9, no. 21, pp. 3045–3048, 2016.

[174] A. Rommerskirchen, B. Ohs, K. A. Hepp, R. Femmer, and M. Wessling, "Modeling continuous flow-electrode capacitive deionization processes with ion-exchange membranes," *Journal of Membrane Science*, vol. 546, pp. 188–196, 2018.

[175] K. B. Hatzell, E. Iwama, A. Ferris, B. Daffos, K. Urita, T. Tzedakis, F. Chauvet, P.-L. Taberna, Y. Gogotsi, and P. Simon, "Capacitive deionization concept based on suspension electrodes without ion exchange membranes," *Electrochemistry Communications*, vol. 43, pp. 18–21, 2014.

[176] K. Urano, Y. Masaki, and M. Kawabata, "Electric resistances of ion-exchange membranes in dilute solutions," *Desalination*, vol. 58, no. 3, pp. 171–176, 1986.

[177] G. M. Geise, A. J. Curtis, M. C. Hatzell, M. A. Hickner, and B. E. Logan, "Salt concentration differences alter membrane resistance in reverse electrodialysis stacks," *Environmental Science & Technology Letters*, vol. 1, no. 1, pp. 36–39, 2013.

[178] A. Galama, D. Vermaas, J Veerman, M. Saakes, H. Rijnaarts, J. Post, and K Nijmeijer, "Membrane resistance: The effect of salinity gradients over a cation exchange membrane," *Journal of membrane science*, vol. 467, pp. 279–291, 2014.

[179] F. Q. Mir and A. Shukla, "Sharp rise in resistance of ion exchange membranes in low concentration nacl solution," *Journal of the Taiwan Institute of Chemical Engineers*, vol. 72, pp. 134–141, 2017.

[180] J.-H. Choi, S.-H. Kim, and S.-H. Moon, "Heterogeneity of ion-exchange membranes: The effects of membrane heterogeneity on transport properties," *Journal of colloid and interface science*, vol. 241, no. 1, pp. 120–126, 2001.

[181] R Zhao, P. Biesheuvel, and A Van der Wal, "Energy consumption and constant current operation in membrane capacitive deionization," *Energy & Environmental Science*, vol. 5, no. 11, pp. 9520–9527, 2012.

[182] S. A. Hawks, J. M. Knipe, P. G. Campbell, C. K. Loeb, M. A. Hubert, J. G. Santiago, and M. Stadermann, "Quantifying the flow efficiency in constant-current capacitive deionization," *Water research*, vol. 129, pp. 327–336, 2018.

[183] N.-L. Liu, S.-H. Sun, and C.-H. Hou, "Studying the electrosorption performance of activated carbon electrodes in batch-mode and single-pass capacitive deionization," *Separation and Purification Technology*, 2019.

[184] P. Biesheuvel, H. Hamelers, and M. Suss, "Theory of water desalination by porous electrodes with immobile chemical charge," *Colloids and Interface Science Communications*, vol. 9, pp. 1–5, 2015.

[185] M. Andelman, "Ionic group derivitized nano porous carbon electrodes for capacitive deionization," *Journal of Materials Science and Chemical Engineering*, vol. 2, no. 03, p. 16, 2014.

[186] X Gao, S Porada, A Omosebi, K.-L. Liu, P. Biesheuvel, and J Landon, "Complementary surface charge for enhanced capacitive deionization," *Water research*, vol. 92, pp. 275–282, 2016.

[187] T. Wu, G. Wang, Q. Dong, B. Qian, Y. Meng, and J. Qiu, "Asymmetric capacitive deionization utilizing nitric acid treated activated carbon fiber as the cathode," *Electrochimica Acta*, vol. 176, pp. 426–433, 2015.

[188] D. S. Achilleos and T. A. Hatton, "Selective molecularly mediated pseudocapacitive separation of ionic species in solution," *ACS applied materials & interfaces*, vol. 8, no. 48, pp. 32 743–32 753, 2016.

[189] P. Guillemet, T. Brousse, O. Crosnier, Y Dandeville, L. Athouel, and Y Scudeller, "Modeling pseudo capacitance of manganese dioxide," *Electrochimica Acta*, vol. 67, pp. 41–49, 2012.

[190] K. C. Smith and R. Dmello, "Na-ion desalination (nid) enabled by na-blocking membranes and symmetric na-intercalation: Porous-electrode modeling," *Journal of The Electrochemical Society*, vol. 163, no. 3, A530–A539, 2016.

[191] K Singh, H. Bouwmeester, L. de Smet, M. Bazant, and P. Biesheuvel, "Theory of water desalination with intercalation materials," *Physical Review Applied*, vol. 9, no. 6, p. 064 036, 2018.

[192] F. He, P. Biesheuvel, M. Z. Bazant, and T. A. Hatton, "Theory of water treatment by capacitive deionization with redox active porous electrodes," *Water research*, vol. 132, pp. 282–291, 2018.

[193] D Brogioli, R Ziano, R. Rica, D Salerno, O Kozynchenko, H. Hamelers, and F Mantegazza, "Exploiting the spontaneous potential of the electrodes used in the capacitive mixing technique for the extraction of energy from salinity difference," *Energy & environmental science*, vol. 5, no. 12, pp. 9870–9880, 2012.

[194] B. Shapira, I. Cohen, E. Avraham, and D. Aurbach, "Anion-exclusion carbon electrodes for energy storage and conversion by capacitive mixing," *Journal of The Electrochemical Society*, vol. 164, no. 9, A1933–A1938, 2017.

[195] H. Li and L. Zou, "Ion-exchange membrane capacitive deionization: A new strategy for brackish water desalination," *Desalination*, vol. 275, no. 1-3, pp. 62–66, 2011.

[196] H. Li, L. Pan, T. Lu, Y. Zhan, C. Nie, and Z. Sun, "A comparative study on electrosorptive behavior of carbon nanotubes and graphene for capacitive deionization," *Journal of Electroanalytical Chemistry*, vol. 653, no. 1-2, pp. 40–44, 2011.

[197] Z. Chen, C. Song, X. Sun, H. Guo, and G. Zhu, "Kinetic and isotherm studies on the electrosorption of nacl from aqueous solutions by activated carbon electrodes," *Desalination*, vol. 267, no. 2-3, pp. 239–243, 2011.

[198] X. Quan, Z. Fu, L. Yuan, M. Zhong, R. Mi, X. Yang, Y. Yi, and C. Wang, "Capacitive deionization of nacl solutions with ambient pressure dried carbon aerogel microsphere electrodes," *RSC Advances*, vol. 7, no. 57, pp. 35 875–35 882, 2017.

[199] X. Gu, M. Hu, Z. Du, J. Huang, and C. Wang, "Fabrication of mesoporous graphene electrodes with enhanced capacitive deionization," *Electrochimica Acta*, vol. 182, pp. 183–191, 2015.

[200] A. Ramachandran, D. I. Oyarzun, S. A. Hawks, M. Stadermann, and J. G. Santiago, "High water recovery and improved thermodynamic efficiency for capacitive deionization using variable flowrate operation," *Water research*, vol. 155, pp. 76–85, 2019.

[201] O. Miyawaki, A. Saito, T. Matsuo, and K. Nakamura, "Activity and activity coefficient of water in aqueous solutions and their relationships with solution structure parameters," *Biosci. Biotechnol. Biochem*, vol. 61, no. 3, pp. 466–469, 1997.

[202] L. Fitzsimons, B. Corcoran, P. Young, G. Foley, and F. Regan, "Modelling the activity of seawater and implications for desalination exergy analyses," vol. 444, 2012.

[203] R. Labrecque, "Exergy as a useful variable for quickly assessing the theoretical maximum power of salinity gradient energy systems," *Entropy*, vol. 11, no. 4, pp. 798–806, 2009.

[204] E. Sparrow and A. Stretton, "Natural convection from variously oriented cubes and from other bodies of unity aspect ratio," *International journal of heat and mass transfer*, vol. 28, no. 4, pp. 741–752, 1985.